Reflectarray with Variable-patch-and-slot Size

The Nan Chang and Bor-Tsong Chen
Tatung University, Taipei, Taiwan R. O. C.

Abstract— Reflectarray using a variable-patch-and-slot (VPS) size method is presented. A slot as a new variable is added to the original variable patch (VP) size configuration. The slot plays a role to modify the original phase diagram. In some cases, it optimizes both sensitivity and bandwidth of a reflectarray. Based on this observation, we designed a reflectarray on an FR4 substrate. Experimental results show a maximum gain of 24.5 dB at 11.4 GHz with an aperture size of 19.5 cm×25 cm. It has a 1.5 dB bandwidth of 19.3% and has an aperture efficiency of 31.48%. The cross-polarization level is bellow 25 dB.

1. INTRODUCTION

Reflectarray has been extensively studied in the literature. A common step in designing such an array is to adjust phase among elements when it is illuminated by a primary source [1]. Progressive phase shift methods for a microstrip reflectarray have been extensively studied in the literature. The methods include identical microstrip patch elements with variable length delay line [2], variable size microstrip patches [3, 4], and identical microstrip patch elements with angular rotations [5]. In this paper, a modification to the variable size reflectarray of [4] is proposed. A slot as a new variable is added to the conventional design.

Phase adjustment from 0° to 360° in a reflectarray is required. A smoother phase variation versus element change is also important to relax manufacture sensitivity. In [4], a smoother phase variation within a range larger than 360° was obtained by stacking two or more arrays. In [4], a multilayer printed reflectarray based on patches of variable size was built on a low dielectric constant material. In [6, 7], performances of reflectarrays based on variable delay line method were checked by the authors. In this paper, stacked variable patch size reflectarray on FR4 substrate will be investigated with an intension to make an improvement.

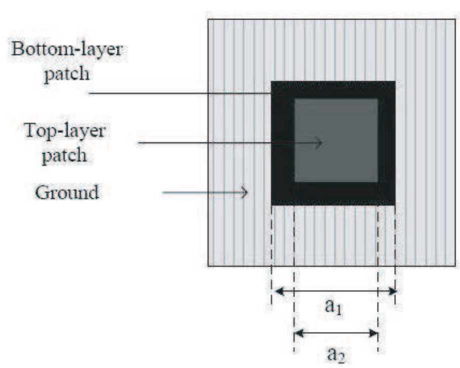

(a)

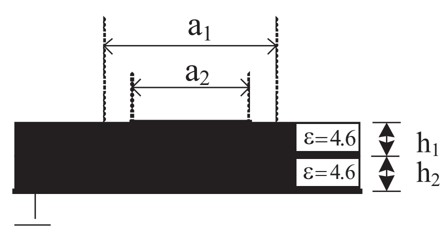

(b)

Figure 1: The unit cell of a reflectarray with variable patch size (a) top view (b) side view ($h_1 = h_2 = 1.6$ mm).

The unit cell of the structure, denoted by "VP", is shown in Fig. 1. In this configuration, the top and bottom layer patches are square. The relative size of the stacked patches is considered fixed in the design process ($a_2 = 0.65a_1$), the substrate thickness is 3.2 mm ($h = h_1 + h_2 = 3.2$ mm, $h_1 = h_2$), and the unit cell occupies an area of 15×15 mm. The commonly used substrate materials could be Rohacell ($\varepsilon_r = 1.05$) [4], Duroid ($\varepsilon_r = 2.2$), FR4 ($\varepsilon_r = 4.4$) and Arlon ($\varepsilon_r = 6$). As a comparison, we adjusted patch size to obtain phase diagram based on a similar approach of [7] for each material. The results are shown in Fig. 2 (at 11 GHz). It shows that relatively lower sensitivity can be obtained using Rohacell and Duroid rather than using FR4 and Arlon. As dielectric constant gets higher, the equivalent wavelength gets shorter. Therefore, the change rate of phase per mini-meter (not in terms of wavelength) is faster. Fig. 3 shows that the sensitivity value is 166 degrees/mm for FR4 material adopting the definition of [8]. From this study, it is

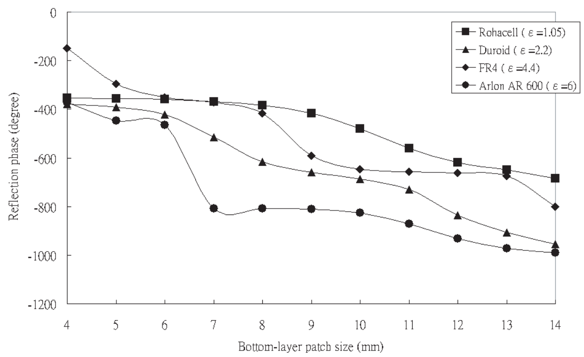

Figure 2: Phase versus patch size for a reflectarray with different materials.

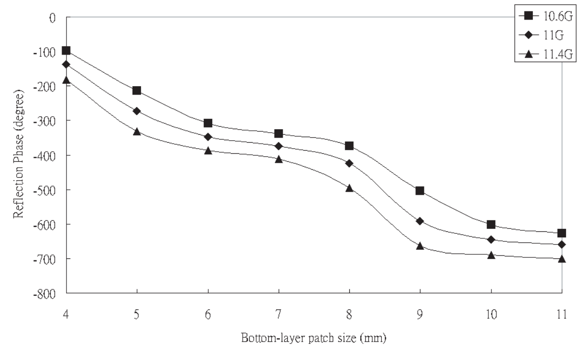

Figure 3: Phase versus patch size at different frequencies.

clear that although the "VP" approach of [4] was successfully implemented using low dielectric constant material, it may not work for high dielectric constant material. We also note that a thick (6 mm) substrate was used in [4]. For a thinner substrate, it is expected that the sensitivity will also increase for a fixed dielectric constant.

With a fixed-thickness substrate, it was studied the phase curve also has a high slope near resonance. Therefore, reflectarray with a high dielectric constant or a thin substrate is very sensitive to manufacture tolerances. Our motivation is to present a method to modify the phase curve of "VP" structure when it is applied to the FR4 material with a relative thinner substrate.

2. VARIABLE-PATCH-AND-SLOT SIZE REFLECTARRAY

In this section, we propose a new structure by etching a slot on the bottom-layer patch of the previous "VP" configuration. The new construction unit cell is called by "VPS". VPS is different from VP by adding a slot of length L as shown in Fig. 4. The width of the slot is W. We keep $W = 0.2a_1$ and $a_2 = 0.65a_1$ as we tune the slot length L. Four different slot lengths to patch size ratios for each material were studied. In Figures 5 to 8, the curves marked by $s1$, $s2$, $s3$, and $s4$ refer to $L = 0.2a_1$, $L = 0.4a_1$, $L = 0.6a_1$, and $L = 0.8a_1$ respectively. These curves are all analyzed at 11 GHz.

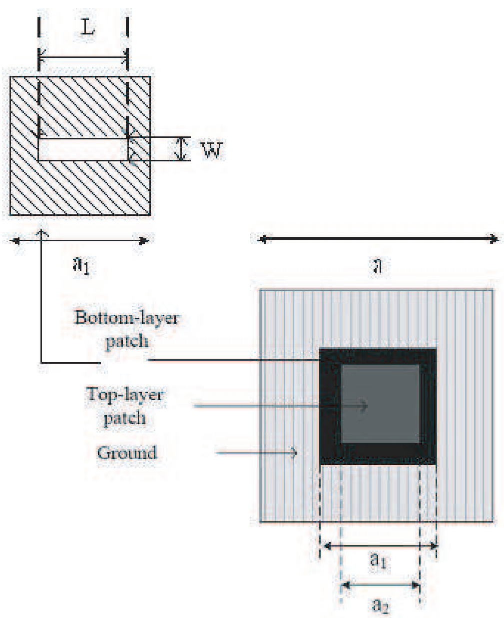

Figure 4: Unit cell of a variable patch and slot size reflectarray (Its side view is the same as shown in Fig. 1(b).

The roles played by the slot depend on the employed material. In [4], thick substrate (thickness is 6 mm) with low dielectric constant ($\varepsilon_r = 1.05$) was used. In this case, we found from Fig. 5 that it is not necessary to introduce the slot. In fact, the slot makes a steeper slope than the original design for a low dielectric constant material. However, it is clear that the slot introduces additional phase delay. For an original less smooth VP-based phase diagram, we may use the slot to modify the high-slope region. For example, we may use the $s4$ curve in Fig. 8 or use the $s3$ or $s4$ curve in Fig. 7 to replace the conventional design. As for Fig. 6, no apparent advantage can be obtained from VPS design. In experiment, we use the "layout curve" which is a straight line in Fig. 9 to approximate the $s3$ curve in Fig. 7 to design a reflectarray on an FR4 substrate.

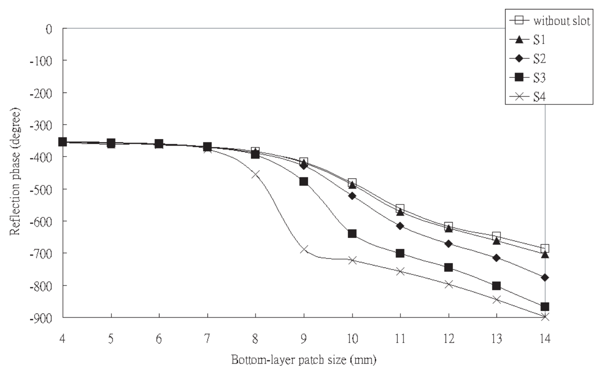

Figure 5: Phase diagram of VP (with no slot) and VPS in Rohacell material ($\varepsilon_r = 1.05$).

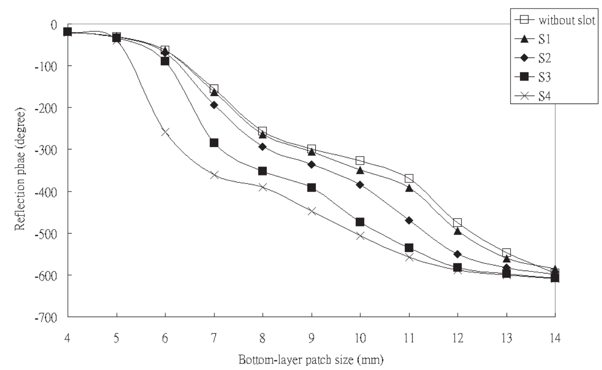

Figure 6: Phase diagram of VP (with no slot) and VPS in Duroid material ($\varepsilon_r = 2.2$).

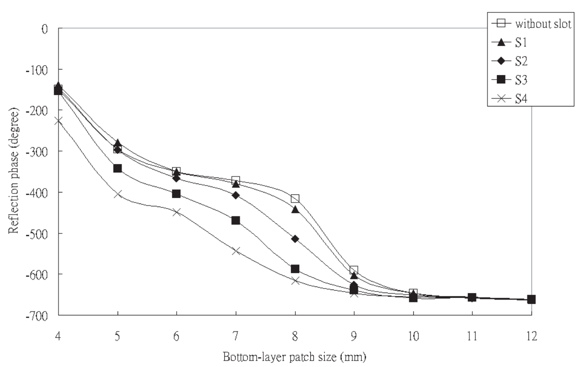

Figure 7: Phase diagram of VP (with no slot) and VPS in FR4 material ($\varepsilon_r = 4.4$).

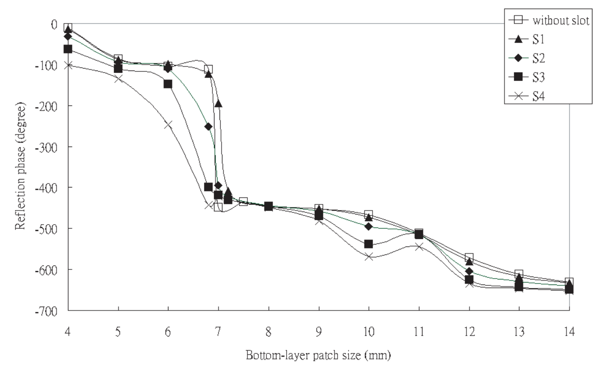

Figure 8: Phase diagram of VP (with no slot) and VPS in Arlon material($\varepsilon_r = 6$).

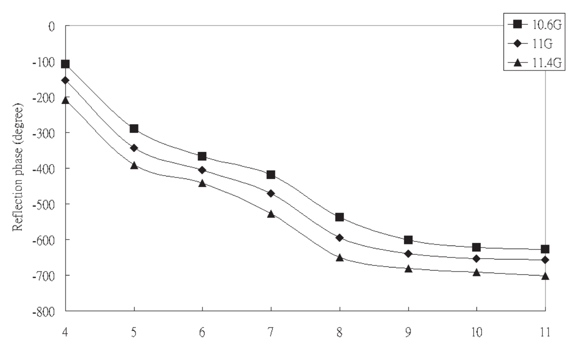

Figure 9: Phase diagram of VPS at different frequencies in FR4 material.

3. EXPERIMENTS

The reflectarray is composed of 320 elements with an area of 19.5 cm × 25 cm. It is a center-fed array with a feed horn at a distance of 20 cm away from the reflecting board. In [4], the substrate thickness is 6 mm. In this design, only 3.2 mm thickness is needed. Low efficiency of the present array is due to the losses of the FR4 substrate. It has been checked in [6] that the FR4 material may cause 2.5 dB loss in this frequency range. Besides this unavoidable loss, other performances such as bandwidth and cross polarization level are all comparable to each other. A measured H-plane pattern at 11 GHz is shown in Fig. 11.

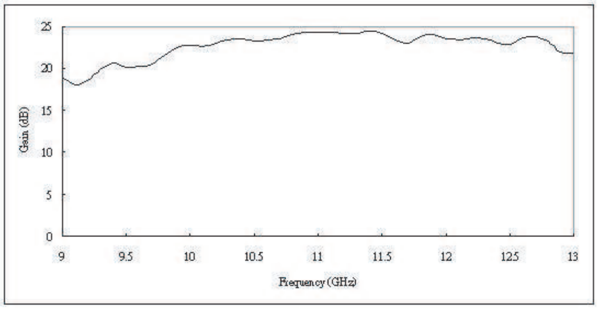

Figure 10: Measured gain of a VPS reflectarray.

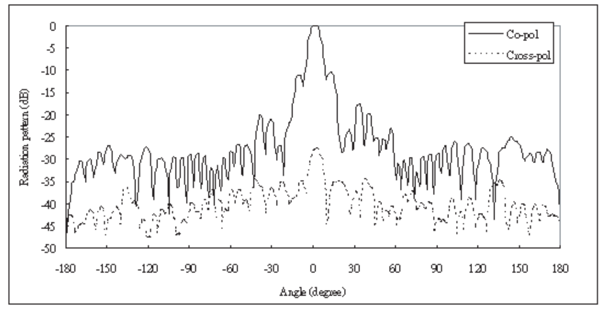

Figure 11: Measured H-plane pattern of a VPS reflectarray at 11 GHz.

4. CONCLUSION

In this paper, we first investigate a conventional stacked variable patch size reflectarray. The phase diagram shows that the configuration can lead to a phase change greater than 360°. Therefore, thick substrate with low dielectric constant can be used in order to optimize both sensitivity and bandwidth. To further extend application of the stacked variable patch size method to a relatively thin substrate with high dielectric constant, we propose a VPS structure. It is obtained by etching rectangular slot on bottom-layer patch of the original array. The slot introduces additional phase delay to modify the high slope region which is commonly seen on a reflectarray built on a high dielectric constant material. Therefore, more design flexibilities can be obtained. However, we should know that as dielectric constant gets higher, the equivalent wavelength gets shorter. Therefore, the change of phase per mini-meter (not in terms of wavelength) is faster. This should be a general restriction for any phase-changing scheme in design of a reflectary. What we present here is to show that we may possibly lower down the changing rate at least to some degrees. The method is demonstrated using FR4 as the substrate. Experiments show that we can account on the new modified phase diagram to design a reflectarray. Without this modification, the original curve shown in Fig. 7 suggests that as bottom-layer patch size ranges from 8 mm to 9 mm, only 200° phase shift yields. It is easy to see that the proposed VPS method can relax manufacture sensitivity in this example.

Reflectarrary on high dielectric constant substrates can be made more compact. The disadvantage of doing so is sensitivity limitations even for a VP array. The use of a variable-patch-and-slot size (VPS) element can potentially solve this problem. For a reflectarray built on FR4 substrate, experiment showed that we can get 1.5 dB gain bandwidth of 19.3% with an aperture efficiency of 31.48%.

REFERENCES

1. Munson, R. E. and H. Haddad, "Microstrip reflectarray for satellite communication and RCS enhancement or reduction," U.S. Patent 4,684,952, Washington, D.C., August 1987.
2. Javor, R. D., X.-D. Wu, and K. Chang, "Design and performance of a microstrip reflectarray antenna," *IEEE Trans. Antennas Propagat.*, Vol. 43, No. 9, 932–939, Sep. 1995.
3. Targonski, S. D. and D. M. Pozar, "Analysis and design of a microstrip reflectarray using patches of variable size," *IEEE Int. Symp. Antennas Propagat. Seattle*, 1820–1823, WA, June 1994.
4. Encinar, J. A., "Design of two layer printed reflectarrays using patches of variable size," *IEEE Antennas and Propagation*, Vol. 49, No. 10, 1403–1410, Oct. 2001.
5. Huang, J. and R. J. Pogorzelski, "A Ka-band microstrip reflectarray with elements having variable rotation angles," *IEEE Trans. Antennas Propagat.*, Vol. 46, 650–656, May 1998.
6. Chang, T. N. and Y. C. Wei, "Proximity-coupled reflectarray," *IEEE Transactions on Antennas and Propagation*, Vol. 52, No. 2, 631–635, Feb. 2004.

7. Chang, T. N. and H. Suchen, "Microstrip reflectarray with QUAD-EMC element," *IEEE Transactions on Antennas and Propagation*, Vol. 53, No. 6, 1993–1996, June 2005.
8. Bozzi, M., S. Germani, and L. Perregrini, "Performance comparison of different element shapes used in printed reflectarrays," *IEEE Antennas and Wireless Propagation Letters*, Vol. 2, 219–222, 2003.

Design of an UWB Antenna with Band-rejection Characteristic

H. J. Lee, Y. H. Jang, and J. H. Choi

Department of Electrical and Computer Engineering, Hanyang University
17 Haengdang-Dong, Seongdong-Gu, Seoul 133-791, Republic of Korea

Abstract— This paper proposes the design of an ultra-wideband (UWB) antenna with band-rejection characteristic. By inserting a notch on the ground, extremely wide impedance bandwidth is obtained. The band-rejection characteristic is achieved by embedding the spur-lines on the ground. The designed antenna has a rejection band from 4.7 GHz to 5.9 GHz while maintaining the wide impedance bandwidth from 3 GHz to 10.6 GHz for VSWR less than 2.0.

1. INTRODUCTION

The recent ultra-wideband (UWB) system has become one of the most fascinating technologies for various communication services. The UWB system requires a compact antenna providing wideband characteristic over operating band from 3.1 GHz to 10.6 GHz. Due to attractive features of wide impedance bandwidth, simple structure and ease of fabrication, planar monopole antennas have been studied for UWB communication system [1, 2]. However, the band-rejection technique needs to be employed to avoid the possible interference between UWB system and wireless local area network(WLAN) service since frequency band from 5.15 GHz to 5.825 GHz has been allocated for WLAN. To satisfy such a requirement, various band-rejection methods applicable to planar antenna structures have been reported recently [3, 4].

In this paper, a new UWB antenna with band-rejection characteristic is proposed. The band-rejection characteristic is achieved by embedding the spur-lines [5] on the ground. With the change of the length of the spur-lines, the center frequency of rejection band can be easily adjusted. Experimental and simulated results of the designed antenna are presented.

2. ANTENNA DESIGN

The geometrical configuration of the proposed antenna is shown in Fig. 1. The antenna of height 50 mm and width 40 mm is fabricated on the FR4 substrate with thickness of 1.6 mm and dielectric constant of 4.4. A 50 Ω microstrip feed line is designed with a width of 3 mm. Basically, the antenna structure is a circular patch which has a radius of 12.5 mm and the size of the ground plane, which has a notch of 5×1.5 mm on the other side of the microstrip line, is 22.5×40 mm. In addition, the $\lambda/4$ spur-lines are embedded on the ground. In this design, the notch on the ground plane leads

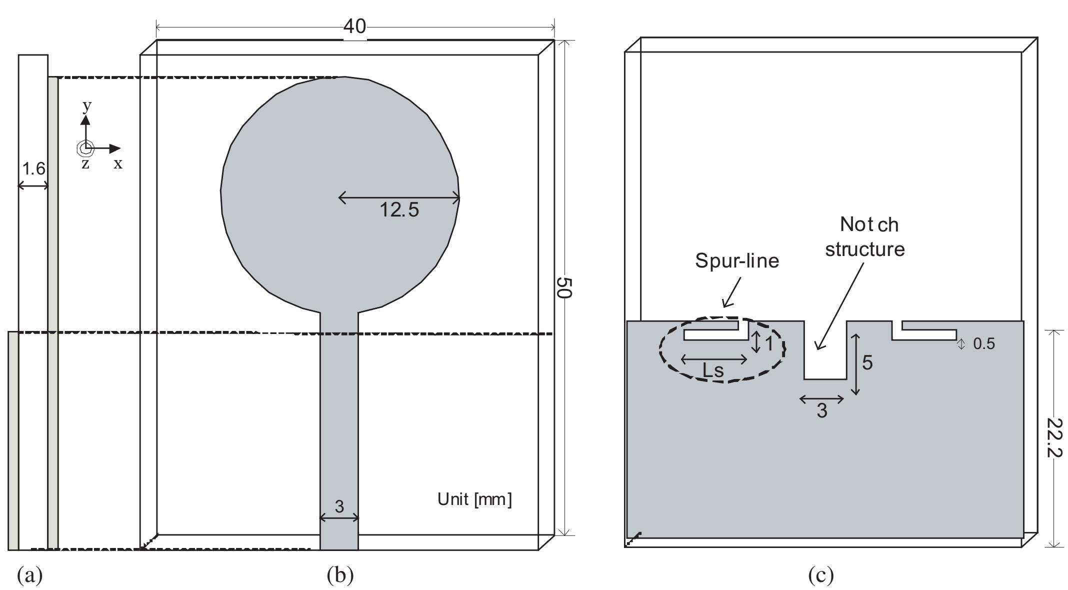

Figure 1: Geometry of proposed antenna. (a) Side view, (b) Top view, (c) Bottom view.

to enhance the impedance bandwidth of the proposed antenna. The spur-lines are used to attain the band-reject characteristic in 5.15 to 5.825 GHz frequency band of WLAN service. The length (Ls) of the spur-line is an important parameter to design band-rejection structure. The spur-line originally operates as a band-rejection filter when the length becomes a quarter-wavelength at the desired frequency.

3. EXPERIMENTAL RESULTS

The performance of proposed antenna was analyzed using the simulation software, Ansoft High Frequency Structure Simulator (HFSS) [6]. The simulated VSWR characteristics for various spur line lengthes are illustrated in Fig. 2. As shown in Fig. 2, by controlling the length (Ls) of a pair of about quarter wavelength long spur-lines, the band-rejection performance can be obtained. Fig. 3 shows the simulated and measured VSWR characteristics of the proposed antenna. It is observed that the rejection band of 4.7 GHz to 5.9 GHz is achieved by embedding the spur-lines while the required performance is satisfied in operating frequency band of 3.1 to 10.6 GHz. Fig. 4 shows the measured radiation patterns at 3.5, 6.5, and 9 GHz. Radiation patterns and antenna gains are illustrated in Fig. 4 and Fig. 5, respectively.

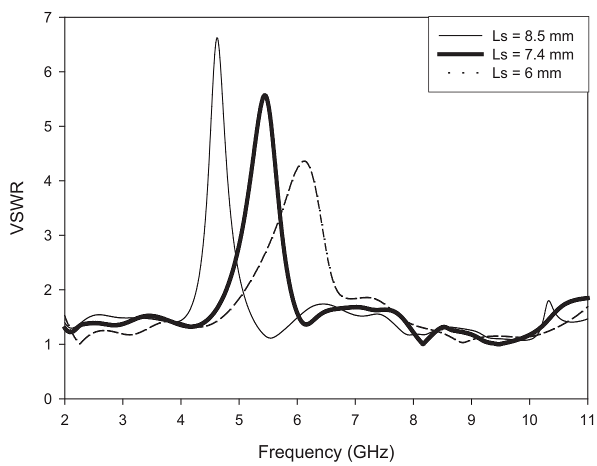

Figure 2: Simulated VSWR for various length of a pair of spur-lines.

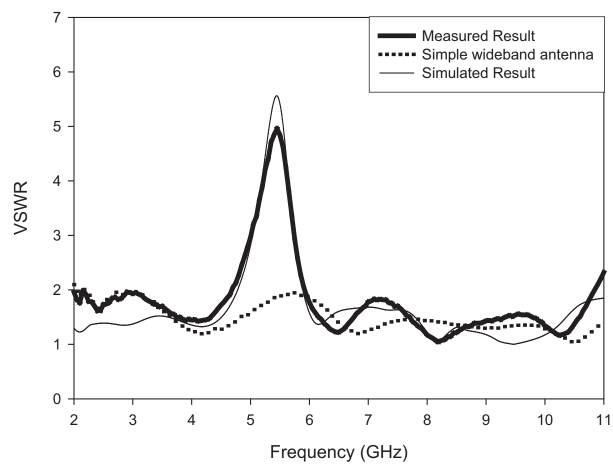

Figure 3: Comparison of simulated and measured VSWR.

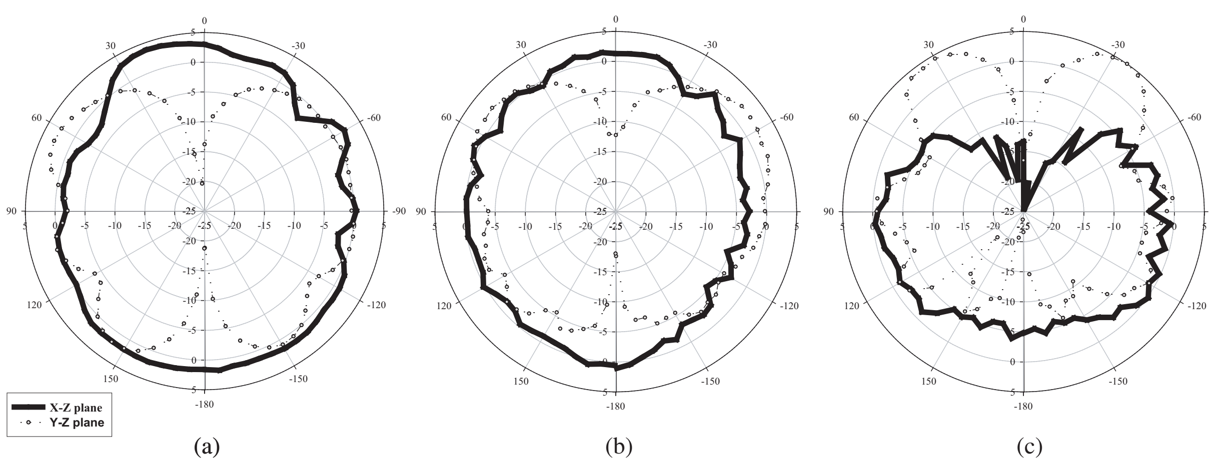

Figure 4: Measured radiation patterns at (a) 3.5 GHz, (b) 6.5 GHz, and (c) 9 GHz.

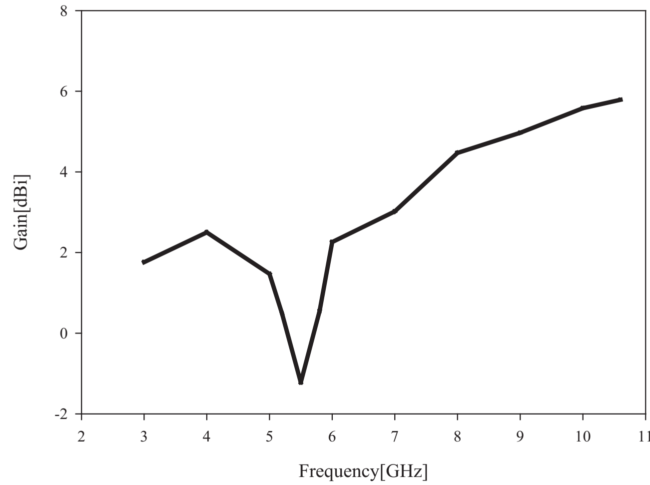

Figure 5: Measured antenna gain.

4. CONCLUSION

A new UWB antenna with band-rejection characteristic has been proposed and manufactured. The notch structure on the ground is used to improve the impedance bandwidth over UWB frequency band. In addition, to reject the WLAN service since frequency band from 5.15 GHz to 5.825 GHz, a pair of spur-lines are embedded on the ground. The proposed antenna has the bandwidth from 3.1 GHz to 10.6 GHz for VSWR less than 2.0 except for the rejection band from 4.7 GHz to 5.9 GHz. The manufactured antenna has good impedance bandwidth and radiation pattern. Simulated and measured results show that the proposed antenna could be a good candidate for UWB system applications.

ACKNOWLEDGMENT

This work was supported by HY-SDR Research Center at Han-yang University, Seoul, Korea, under the ITRC Program of IITA, Korea.

REFERENCES

1. Ammann, M. J. and Z. N. Chen, "A wide-band shorted planar monopole with bevel," *IEEE Trans. on Antennas and Propagation*, Vol. 51, No. 4, 901–903, 2003.
2. Liang, J., C. C. Chiau, X. Chen, and C. G. Parini, "Printed circular disc monopole antenna for ultra-wideband applications," *Electronic Letters*, Vol. 40, No. 20, 1246–1247, 2004.
3. Yoon, H. K., H. Kim, K. Chang, Y. J. Yoon, and Y. H. Kim, "A Study on the UWB antenna with band-rejection characteristic," *IEEE Antennas and Propagation Society International Symposium*, Vol. 2, 1784–1787, 2004.
4. Kerkhoff, A. and H. Ling, "A parametric study of band-notched UWB planar monopole antennas," *IEEE Antennas and Propagation Society International Symposium*, Vol. 2, 1768–1771, 2004.
5. Sanchez-Hernandez, D. and I. D. Robertson, "Analysis and design of a dual-band circularly polarized microstrip patch antenna," *IEEE Trans. Antennas Propagation*, Vol. 43, No. 2, 201–205, 1995.
6. Ansoft High Frequency Structure Simulator (HFSS), Ver. 10.1, Ansoft Corporation.

A Novel Antenna Design for UHF RFID Tag on Metallic Objects

Youngman Um[1], **Uisheon Kim**[1], **Wonmo Seong**[2], **and Jaehoon Choi**[1]

[1]Department of Electrical and Computer Engineering, Hanyang University, Republic of Korea
[2]E.M.W. Antenna Co., Ltd., Gasan-dong, Geumcheon-gu, Seoul 459-2, Republic of Korea

Abstract— A novel microstrip patch RFID tag antenna with wideband characteristic is proposed. It has less sensitive characteristic against size of metallic object, wide impedance bandwidth and long reading distance. The antenna consists of shorting strip, open stubs, tag IC and radiating patch having I-shaped slits. The proposed antenna is located on the finite ground plane and is constructed on FR4 substrate ($\varepsilon_r = 4.4, \tan\delta = 0.02$). Overall dimension of the antenna is 100 mm×26 mm×6 mm. The tag IC has input impedance of $43 - j800\,\Omega$ at 915 MHz. The −3 dB impedance bandwidth is from 696 MHz to 978 MHz. When the antenna is placed in free space and mounted on 200 mm×200 mm, 400 mm×400 mm and 600 mm×600 mm metallic plates, the peak gains are 4.7 dBi, 2.4 dBi, 2.3 dBi and 1.7 dBi, respectively. The radiation efficiencies are 69%, 40%, 38% and 38%, respectively, and the maximum reading distances are 5.13 m, 6 m, 5.75 m and 4.75 m, respectively.

1. INTRODUCTION

Recently, radio frequency identification (RFID) in the UHF band has gained popularity in many applications, since it provided a broad readable range, fast reading speed, and large information storage capability. In RFID system, tags are usually attached to objects having various material properties. Among them, metallic objects strongly affect the performance of antenna including radiation efficiency, gain, etc.. Planar inverted-F and microstrip patch antennas have been proposed for RFID tag application. However, these antennas have narrow impedance bandwidth and resonant frequency can be easily shifted due to the characteristics of objects that tag antennas are attached to.

In this paper, a novel microstrip patch RFID tag antenna with wideband characteristic is proposed. It has a less sensitive characteristic against size of metallic object, wide impedance bandwidth and a long reading distance. The resonant frequency and impedance bandwidth can be controlled by adjusting the lengthes of I-shaped slits and open stubs, and a gap distance between the open stub and feed line. High radiation efficiency and peak gain are achieved by using shorting strip.

2. STRUCTURE AND DESIGN

The geometry of the proposed antenna is shown in Fig. 1. The antenna consists of shorting strip, open stubs, tag IC and radiating patch having I-shaped slits. The values of parameters are listed in Table 1. The width of open stubs and I-Shaped slits is 1 mm. The radiating patch is a metal plate with length L_2 and width W_1. The length L_1, L_2 and width W_1 are optimized to a tag chip with an impedance $Z_c = (43 - j800)\,\Omega$ at 915 MHz. It means that the load antenna impedance should be $43 + j800\,\Omega$ for conjugate matching and to transmit the maximum power between the antenna and the microchip. The tag chip feed is placed at one end of the feed line, and the other end is terminated by shorting strip and ground. The radiating patch is constructed on FR4 substrate ($\varepsilon_r = 4.4$, $\tan\delta = 0.02$) with thickness H. Thickness H is used to achieve a high gain and less

Table 1: Final design parameters (Unit: mm).

Parameters	Values	Parameters	Values
L_1	100	W_1	26
L_2	69	W_2	5.5
L_3	22	W_3	8
L_4	11	W_4	3.5
L_5	9.5	H	6

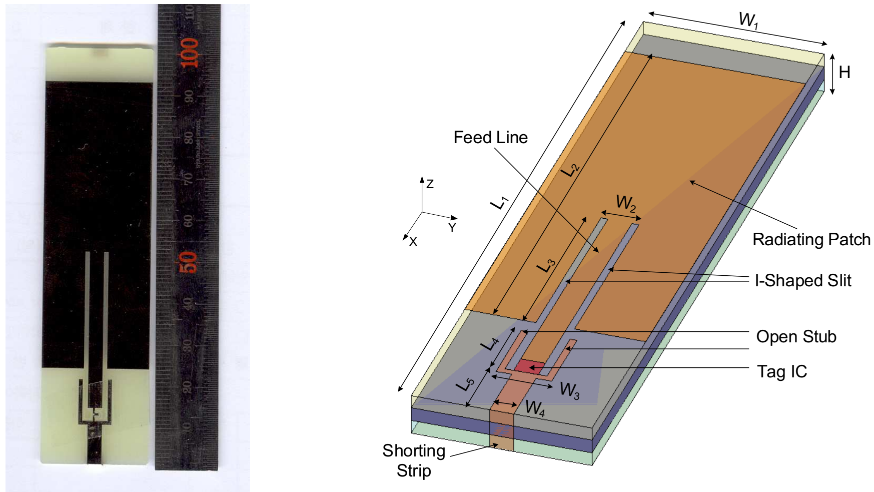

(a) (b)

Figure 1: Proposed RFID tag antenna: (a) fabricated antenna, (b) 3D view.

sensitive characteristic against size of a metallic object. The microstrip feed line is inset into the patch. Generally, the edge-coupled feed suffers from a limitation of impedance mismatch because the input impedance of the patch at its radiating edge is very high compared to that of the feed line. Therefore, an inset microstrip feed line is used in radiating patch to mitigate this problem. The open stubs are used for impedance matching. Resonant frequency can be controlled by adjusting the gap length between feed line and open stub, and the length of open stub.

3. RESULTS AND MEASUREMENT

The antenna performance is analyzed by Ansoft HFSS simulator. Return loss, peak gain, radiation pattern, radiation efficiency and maximum reading distance are simulated and measured in free space, on 200 mm×200 mm, 400 mm×400 mm and 600 mm×600 mm metallic plates. The maximum reading distance is measured in RFID Test Bed, E.M.W Antenna Co., Ltd..

Figure 2 shows return loss characteristic of the antenna. The bandwidth is measured to be about 282 MHz (696 MHz ∼ 978 MHz) which satisfies UHF band (908 MHz ∼ 914 MHz) of RFID system. I-shaped slits and open stubs can control resonant frequency of antenna. Length of I-shaped slits and open stubs can be interpreted as series inductance. Therefore, the longer their lengthes are, the lower resonant frequency of the antenna becomes. Fig. 3 shows radiation patterns. As listed in Table 2, radiation patterns, peak gains and radiation efficiencies are less sensitive against metallic sizes.

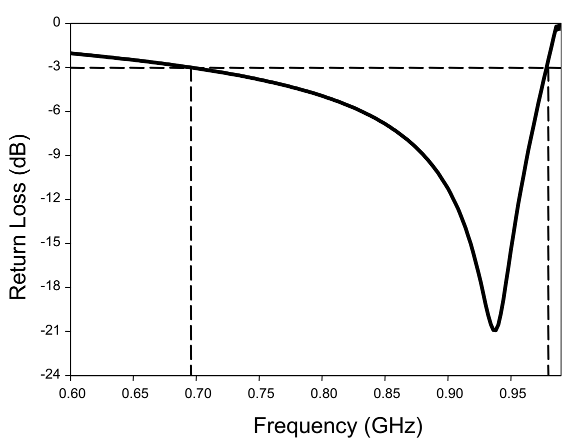

Figure 2: Return loss characteristic.

The proposed antenna is combined with the commercial tag chip. Then, using the commercial

Table 2: Peak gain and radiation efficiency.

Metallic Plate Size	Free Space	200 mm×200 mm	400 mm×400 mm	600 mm×600 mm
Peak Gain (dBi)	4.7	2.4	2.3	1.7
Radiation Efficiency (%)	69	40	38	38

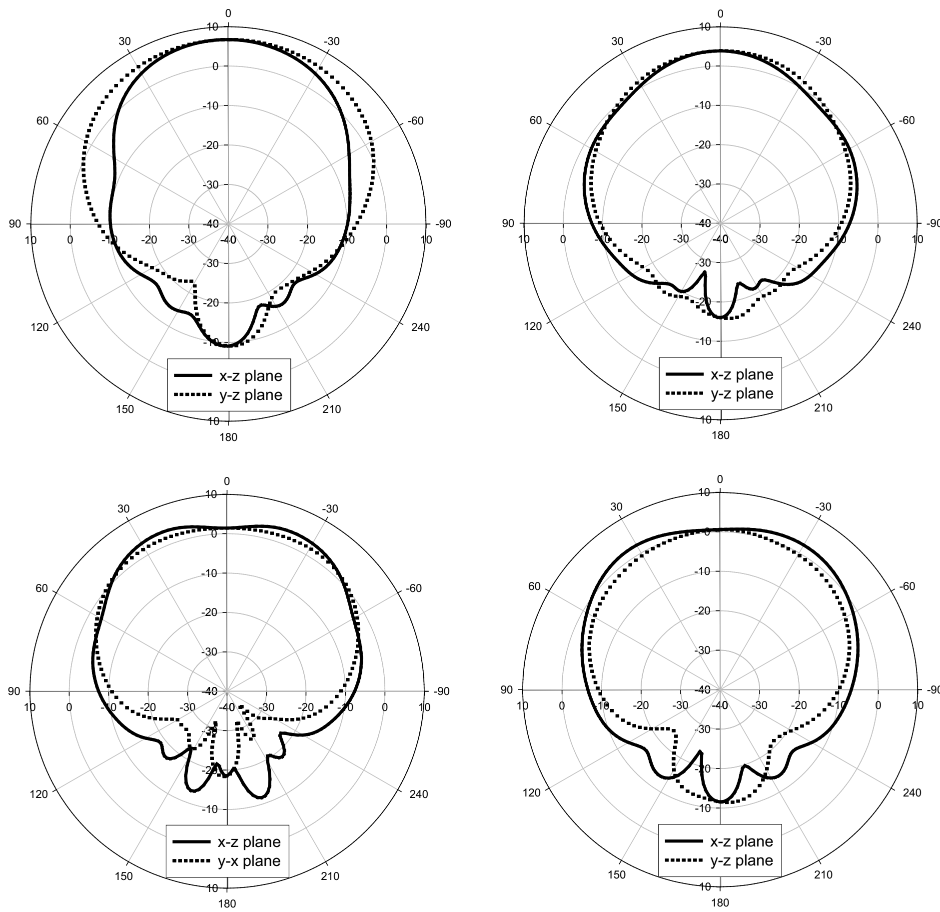

Figure 3: Radiation pattern at 910 MHz.

RFID reader, its performances are measured based on the back-scattering method in an RFID Test bed. The measurement setup consists of the transmission and receiving parts. The transmission part includes a computer, RFID reader (ALIEN, ALR-9800-KOR), reader antenna (EMW Antenna, FSDC-07) and variable attenuator. The minimum power signal from the reader is sent to wake up the tag. The reader output power is 32 dBm. The maximum reading distances of the proposed antenna are listed in Table 3.

Table 3: Measured maximum reading distance for metallic plate sizes (Unit: m).

	Sample 1	Sample 2	Average
Free Space	5	5.25	5.13
200 mm×200 mm	5.5	6.5	6
400 mm×400 mm	5.5	6	5.75
600 mm×600 mm	4.5	5	4.75

4. CONCLUSION AND FUTURE WORK

In this paper, a novel microstrip patch RFID tag antenna with wideband characteristic is proposed. It has a less sensitive characteristic against size of metallic objects, wide impedance bandwidth and a long reading distance. The performance of proposed antenna is not sensitive to the metallic size of object and can be applied to RFID systems whose tags are mounted on metallic objects. In the future, the height and size of the proposed antenna will be further reduced.

REFERENCES

1. Cho, C. H., H. S. Choo, and I. M. Park, "Design of novel RFID tag antennas for metallic objects," *Antennas and Propagation Society International Symposium 2006 IEEE*, 3245–3248, 2006.
2. Ukkonen, L., L. Sydanheirno, and M. Kivikoski, "A novel tag design using inverted-F antenna for radio frequency identification of metallic objects," *2004 IEEE/Sarnoff Symposium on Advances in Wired and Wireless Communication*, 91–94, 26–27 Apr., 2004.
3. Kim, S. J., H. Rhyu, S. H. Baek, F. J. Harackiewicz, and B. J. Lee, "UHF Band RFID tag antenna with a symmetric structure mountable on metallic platforms," *Asia-Pacific Microwave Conference Proceedings*, 3–6, 2005.
4. Son, H. W., G. Y. Choi, and C. S. Pyo, "Design of wideband RFID tag antenna for metallic surfaces," *Electronics Letters*, Vol. 42, No. 5, 263–265, 2 March, 2006.
5. Ukkonen, L., L. Sydanheirno, and M. Kivikoski, "Effects of metallic plate size on the performance of microstrip patch-type tag antennas for passive RFID," *IEEE Antennas and Wireless Propagation Letters*, Vol. 4, 410–413, 2005.
6. Wong, K. L., *Compact and Broadband Microstrip Antennas*, 163–191, Wiley-Interscience, New York 2002.
7. Ramesh, G., B. Prakash, B. Inder, and I. Apisak, *Microstrip antenna Design Handbook*, 19–27, Artech House, 2001.

A Neural Network Approach to the Prediction of the Propagation Path-loss for Mobile Communications Systems in Urban Environments

S. P. Sotiroudis, K. Siakavara, and J. N. Sahalos
Radiocommunications Lab, Department of Physics, School of Sciences
Aristotle University of Thessaloniki, Thessaloniki 54124, Greece

Abstract— This paper presents an alternative procedure for the prediction of propagation path loss in urban environments. It is based on Neural Network (NN) algorithms and uses the detailed environment profile instead of the mean values of its structural parameters. The general performance of the NN shows its effectiveness to yield results with satisfactory accuracy in short time. The received results are compared to the respective ones yielded by the Ray-Tracing model and exhibit satisfactory accuracy either for uniform or for non-uniform distribution of the manmade structured environment.

1. INTRODUCTION

The prediction of electromagnetic wave propagation is of great importance in the design and planning of a cellular-network both for mobile and fixed wireless-access systems. A prediction, based on theoretical models, is really valuable since it offers the capability of determining optimum base locations, in order to obtain suitable data rates, to estimate their coverage and evaluate the quality of the wireless network without the need of expensive and time consuming measurements.

The theoretical models used for the estimation of the path-loss in various urban or suburban areas, even within buildings, are grouped in two categories [1]: the empirical or statistical models (e.g., the COST-231-Walfisch-Ikegami model, the Hata model, etc.) and the site-specific or deterministic ones (e.g., the Ray Tracing technique, the Image Method, the FDTD or the Moment Method, etc.). The models of the former category are easier to implement and require less computational effort but are less sensitive to the environment's physical and geometrical structure. Those of the latter category have a certain physical basis and are more accurate but at the cost of more computations and at the necessity of more detailed information about the coverage area.

In the present work, a prediction model based on Neural Network (NN)-architectures is proposed. Published works have introduced the NN-methodologies as efficient techniques for indoor and outdoor estimation of path-loss propagation. They have given solutions, using measured or theoretically produced data and feeding the input of the NN by the values of some of the geometry parameters of the environment, e.g., the mean height and mean dimensions of the buildings and the mean width of the roads [2–6]. In the work at hand a Multiple Layer Perceptron (MLP) neural network was composed, and the collections of data, by which it was trained, include the detailed environment profile. These data were produced using the Ray Tracing technique. Although the calculation for the training collections were made for simple and uniform distribution of the manmade structures, the appropriate grid modeling of the built-up area as well as the way by which the input data were presented to the NN made it efficient to give, in the generalization phase, results for arbitrary environments, if their profile is provided.

2. FORMULATION

The propagation of radio waves in built-up areas is strongly influenced by the nature of the environment, in particular by the size and the density of the buildings. Urban areas are dominated by tall building blocks with high density and non uniform distribution. Empirical prediction models use mean values for the parameters of the manmade terrain (meanly the mean values of the roads' widths or of the buildings' height). Many proposed NN models use also these parameters as information for the NN. The present work suggests an alternative approach for the prediction of path loss based on a NN-methodology which uses detailed description of the entire coverage area. The used Neural Network was composed via a Multiple Layer Perceptron (MLP) architecture. The input layer consists of a large number of nodes that accept analytical information for the structure of the built-up environment as well as for the coordinates of the position at which the path-loss is going to be estimated. A single node output layer gives the value of this path loss.

A virtual grid of a $N \times N$ cell that covers the area under investigation is supposed (Fig. 1). The center of each cell may lay on a built block of the area or on a street, depending on the specific distribution of the buildings, and it is described via three numbers. If the point lays on a block, then the numbers are the values of W and L (Fig. 1(a)) as well the height of the block. If the center point is on a street two of the numbers are set equal to zero and the third one is set equal to the value of the street's width. Therefore the terrain of the area under consideration is described via $3N^2$ numbers. All this information must be presented to the network during the training, testing and generalization phases.

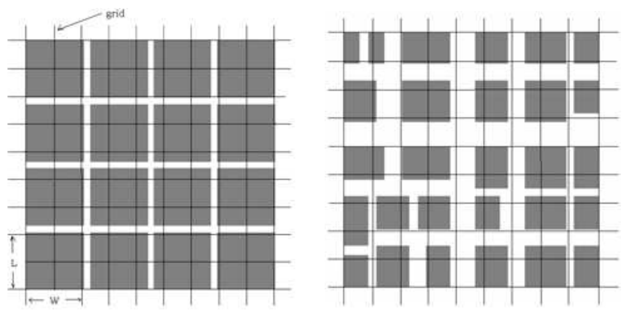

(a) (b)

Figure 1: The scheme of the urban environment with (a) uniform and (b) non-uniform built-up profile.

The general form of an MLP-NN is depicted in Fig. 2. The input layer consists of I nodes, M hidden layers exist each one having m_i nodes and the output is a layer of N_{out} nodes. In this work the input layer has $I = 3N^2 + 2$ nodes. The first $3N^2$ nodes accept the above mentioned information about the area under study and the last two ones accept the coordinates of the point at which the path loss is predicted. The output is a single node layer ($N_{\text{out}} = 1$) and exhibits the path loss value. The number of hidden layers is collected under the criterion of the best convergence of the results.

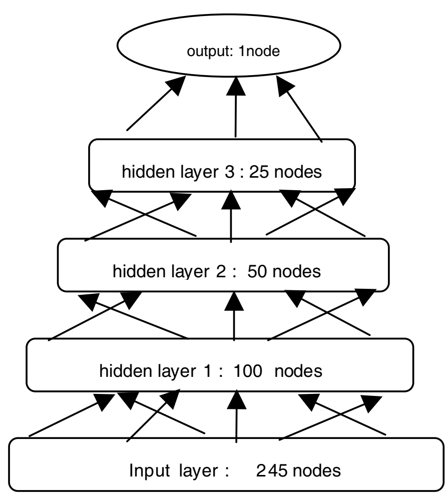

Figure 2: The composed MLP neural network.

For the training of the NN, a collection of N_{tr} input-output data sets is used. These data would come from measurements or calculations via one of the theoretical path loss prediction techniques. For the test of the NN a set of input patterns and the respective output set containing the a priori calculated path loss values is created. The results, yielded from the phase of NN testing, show if the NN is efficiently trained. If so, it is ready to accept at its input the terrain information of the area of interest as well as the coordinates of the point at which the estimation of the path loss is needed and to exhibit at its output this path loss value. Fig. 2 shows the configuration of the

MLP-NN. The NN's output is described by the following equation

$$y_o(p) = F_o\left[\sum_{\ell=1}^{m3} w_3^{\ell}\left(F_3^h\left(\sum_{k=1}^{m2} w_2^{k\ell}\left(F_2^h\sum_{j=1}^{m1} w_1^{jk}\left(F_1^h\sum_{i=1}^{I} w_{in}^{ij}x_i^p\right)\right)\right)\right)\right] \tag{1}$$

where w_q^{nt} represents the synaptic weight from nth neuron of the qth layer towards the tth neuron of the next layer, x_i^p represents the ith element of the pth input pattern and F_m^h is the activation function of the mth layer. The error function, used for the control of NN'S convergence, is $E(p) = (1/2)[d(p) - y_p(p)]^2$ where $d(p)$ is the desired value of the pth output pattern and $y_o(p)$ is the output of the NN when the pth input pattern is presented to its input. During the training phase the network changes its weights so that the above function is minimized. It is realized by the gradient descent procedure [7] via which the weights change by an amount proportional to the negative gradient of the error function, that is $\Delta w(p) = -\eta\nabla E_p(w) + \alpha\Delta w(p-1)$. The constant of proportionality, η, is the learning rate and α is the momentum constant. When the error function is minimized the learning process is terminated and the network can be tested by the test data set.

3. RESULTS

The target of the total procedure was to make the composed NN capable to yield accurate path loss prediction for a non uniformly built-up area Two issues that condition the successfulness of the procedure are the proper selection of the training set and the appropriate configuration of the MLP-NN. A collection of $N_{tr} = 7700$ training patterns (Train 1) was prepared. Their calculation was made via the Ray-tracing prediction model for a large number of uniformly manmade surroundings (Fig. 1(a)). The heights of the built blocks were ranging between 12 m and 27 m, the size of coverage areas was ranging from 500 m×500 m to 1300 m×1300 m and various sizes were considered for the blocks' sectoral plans and the widths of the roads. Two test sets were prepared using the Ray Tracing model: A test set ($\text{Test}_{\text{unif}}$) of 1200 patterns coming from uniformly structured areas and a second set ($\text{Test}_{\text{non-unif}}$) of 580 patterns calculated for non uniformly built-up environments.

The optimum configuration of the MLP-NN was obtained with $M = 3$ hidden layers (see Fig. 2). The learning rates were 0.3 and 0.15 for the hidden and output layers respectively, the values of the momentums were 0.1 for the hidden and 0.2 for the output layer. The activation function for the hidden layers was the hyperbolic tangent function and for the output layer was the linear one. At first it was trained with the Train 1 set and was tested with the $\text{Test}_{\text{unif}}$ set. In this case the best satisfactory convergence was achieved using 8 epochs. The convergence process as a function of the number of iterations, is presented in Fig. 3. For each number of iterations the NN was tested with the $\text{Test}_{\text{unif}}$ set and the absolute value of the difference D, between the expected and the received path-loss values for all the 1200 data, was calculated. The statistical manipulation of these differences yielded an absolute mean value that is depicted in Fig. 3(a), as a function of the number of iterations. It is observed that the mean value of the difference D is reducing by the increase of the number of iterations converging to the value of 2.46 dB, for 7 10^7 iterations. For this case, after statistical processing over the results produced by the set of 1200 patterns, analytical results are presented in Figs. 3(b) and 3(c). In Fig. 3(b) we see the path loss values

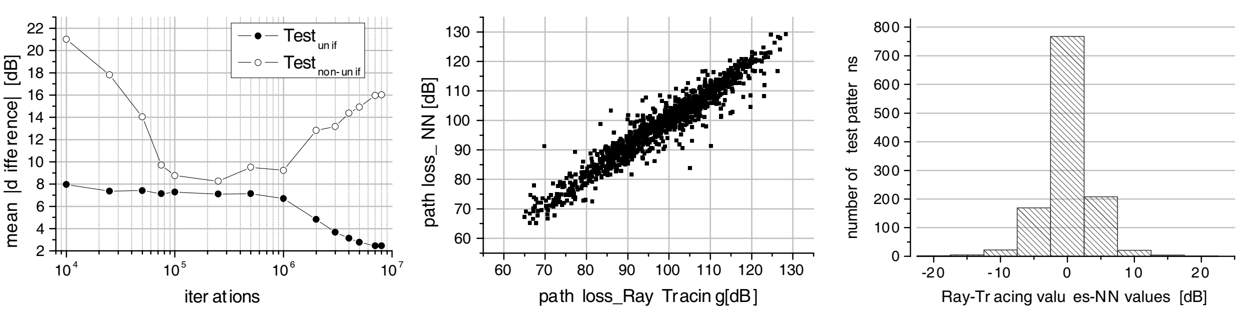

(a) (b) (c)

Figure 3: Results received by the NN when trained via the Train 1 set. (a) the mean value of the difference $D = |\text{expected value-received value}|$ of the path loss, versus the number of iterations (b) results for 8 10^6 iterations (c) statistical distribution of the difference D, mean value 2.46 dB, mean error 2.56%.

yielded by the MLP-NN, versus the expected values in accordance with the Ray Tracing model. The respective histogram of the difference D is presented in Fig. 3(c). The mean value of this statistical distribution is 2.46 dB and the estimated mean error 2.6%.

The respective results received when the NN was tested via the $\mathrm{Test}_{\mathrm{non-unif}}$ set, are presented also in Fig. 3(a). It is shown that the mean value of the difference D remains larger than 8 dB for every iteration value, so the NN fails to closely approximate the expected path loss values. It is also observed that the above divergence is large even for small numbers of iterations or for large ones. This is due to the fact that few iterations are not enough for the learning of the NN and a large number of them make the NN over-adapted. This over-adaptation is enforced also by the large amount of information about the uniform environment given to the NN. This concept explains also the fact that either for moderate number of iterations(Fig. 3(a)) the divergence is large. The NN memorizes the training examples and can not generalize the non-uniform situation.

In order to avoid this over-adaptation a smaller training subset (Train 2) was created. The NN was trained by the new set and initially was tested with the $\mathrm{Test}_{\mathrm{nonunif}}$ using various epoch sizes and number of iterations. In each case the results were statistically processed and are presented in Fig. 4. It is shown that the best results have mean value of the difference D equal to 4.89 dB and are obtained with epoch size 32 and 10^5 iterations. For lower iteration values the NN seems to have not been trained sufficiently and for more than 10^5 iterations it is rather over-adapted. The latter concept is verified by the results of Fig. 4(b) where it is confirmed that the best result for the convergence between the expected and the received path loss value is about 4.9 dB for epoch size 32 and 10^5 iterations. For this case statistical processing over the results of the 580 patterns of the $\mathrm{Test}_{\mathrm{nonunif}}$ set, was made and they are depicted in Fig. 5. In Fig. 5(a) we see the path loss values yielded by the MLP-NN, versus the expected values in accordance with the Ray Tracing model. The respective histogram of the difference D is presented in Fig. 5(b). The mean value of this statistical distribution is 4.89 dB and the estimated mean error is 5.3%.

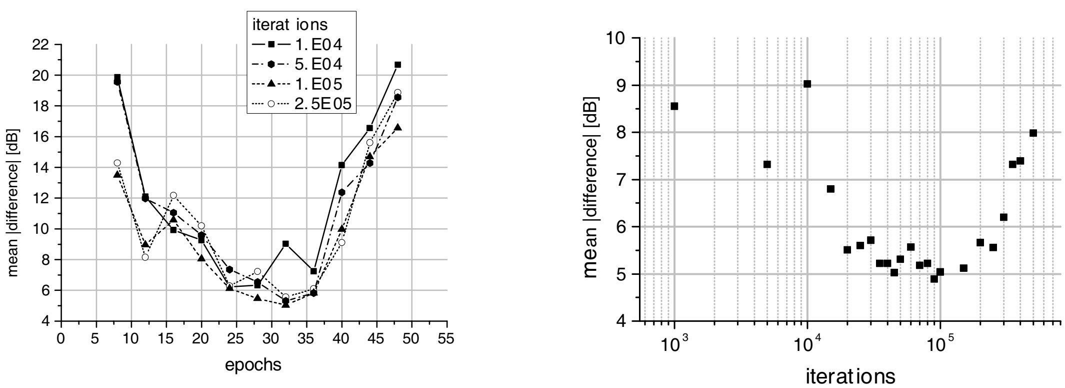

(a) (b)

Figure 4: Results received by the NN when trained via the Train 2 set. (a) the mean value of difference D versus the number of epochs (b) results as a function of the number of iterations, for epoch size equal to 32.

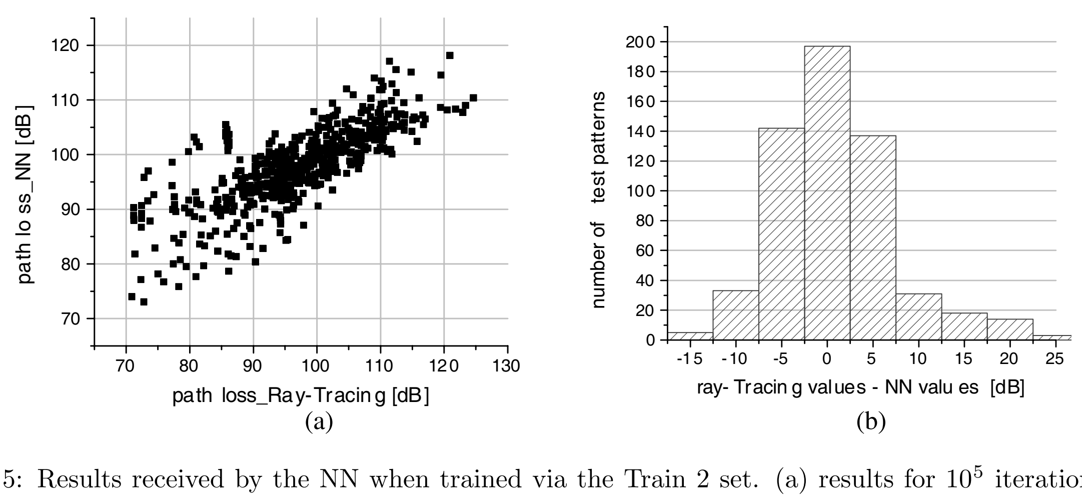

(a) (b)

Figure 5: Results received by the NN when trained via the Train 2 set. (a) results for 10^5 iterations with epoch size equal to 32 (b) statistical distribution of the difference D, mean value 4.89 dB, mean error 5.3%.

4. CONCLUSION

An alternative NN based procedure for the prediction of the path loss in urban environment is proposed. The basic idea is to yield results via the NN, giving to it detailed information about the profile of the built-up environment. This information is obtained, using a virtual grid covering the area under investigation and creating by this an approximate scheme of the terrain of the area. The MLP architecture is proposed for the procedure. In the present work the NN was trained using theoretically calculated data for uniform built-up surroundings and using the Ray Tracing model. The methodology is general and can be used for any type of environment employing training data which come from measurements or from theoretical calculations by other predicting models. However, we believe that when training with the Ray-Tracing method we inherently insert to the procedure a certain physical basis which make the NN more flexible to adapt to arbitrary environments. The results show that a large number of training patterns, epochs of small size and a large number of iterations are necessary to ensure the accurate prediction for uniform environments. This accuracy is approximately equal to ± 2.5 dB. For the prediction of the path loss in non-uniform built-up areas, small training sets, moderate size of epoch and moderate number of iterations are indicated. In this case the accuracy is about 4.9 dB. A better approximation would be obtained if the NN is trained using data calculated for non-uniform built-up areas and this would be the issue of a future investigation.

REFERENCES

1. Sarkar, T. K., J. I. Zhong, K. Kyungjung, A. Medouri, and M. Salazar-Palma, "A survey of various propagation models for mobile communications systems," *IEEE Antennas and Propagation Magazine*, Vol. 45, No. 3, 51–78, 2003.
2. Popescu, I., A. Kanstas, E. Angelou, L. Nafornita, and P. Constantinou, "Applications of generalized RBF-NN for path loss prediction," *Proceedings of the 13th International Symposium on Personal Indoor and Mobile Radiocommunications*, Vol. 1, 484–488, Sept. 2002.
3. Popescu, I., D. Nikitopoulos, P. Constantinou, and L. Nafornita, "ANN prediction models for outdoor environment," *Proceedings of the 17th International Symposium on Personal Indoor and Mobile Radio Communications*, 1–5, Sept. 2006.
4. Barkhatov, N. A., S. E. Revunov, V. P. Uryadov, G. G. Vertogradov, and V. G. Vertogradov, "Forecasting of the propagation with use of artificial neural networks," *Proceedings of XXVIIIth General Assembly of U.R.S.I*, paper GP1.82(01727), India, 2005.
5. Chang, P.-R. and W.-H. Yang, "Environment-adaptation mobile radio propagation prediction using radial basis function neural networks," *IEEE Trans. on Vehicular Technology*, Vol. 46, No. 1, 155–160, 1999.
6. Popescu, I., L. Nafornita, and P. Constantinou, "Comparison of neural network models for path prediction," *Proceedings of the IEEE International Wireless and Mobile Computing, Networking and Communications*, Vol. 1, 44–49, Aug. 2005.
7. Christodoulou, C. and M. Georgiopoulos, *Applications of Neural Networks in Electromagnetics*, Artech House, 2001.

Calculation of EM Characteristics of a Cellular Phone Handset by Time-domain MoM

R. Sarraf[1], **R. Moini**[1], **S. H. H. Sadeghi**[1], **and A. Farschtschi**[2]

[1]Amirkabir University of Technology, Iran
[2]Chemnitz University of Technology, Germany

Abstract— The effect of cellular phone handset dimensions on radiation pattern, impedance and resonance frequency is investigated. The handset body is modeled by an appropriate three-dimensional wire-grid structure with a $\lambda/4$ monopole antenna as its radiating source. The governing electric field integral equation (EFIE) is solved in the time domain, using the method of moments (MoM). The validity of the model is demonstrated by comparing the wide-band results of the antenna input impedance with those available in the literature. It is shown that at current operating frequencies, a regular handset dimensions has minimal effect on the antenna radiation pattern and impedance, and hence modeling of a handset by its antenna (monopole) is sufficient.

1. INTRODUCTION

In the last decade, there has been an enormous growth in the wireless communication usage and there are more than two thousand millions cellular users are reported at the end of 2005 [1]. Biological effects of a handset close range radiation on human body and its medical consequences are of great concern. Therefore, we need a model showing the radiated field of an antenna in the presence of the cellular phone main body. The trend for small size phones necessitates the study of the antenna pattern with different handset body dimensions. Due to irregular shape of a handset, numerical methods are best suited for analysis of electromagnetic fields. Recently, the FDM in time domain (FDTD) has been preferred by many researchers [2–5]. The FDTD method is not efficient for analyzing metallic structures such as antennas due to its large computer time and memory requirements [6]. In contrast, the MoM has been efficiently used for analyzing thin-wire structures [7, 8]. Here, we use the MoM for analyzing electromagnetic field distributions around a radiating cellular phone handset. In particular, we focus on how the physical dimensions of the handset can affect the radiation pattern, resonance frequency and input impedance of the antenna.

2. THEORY

The time-dependent Maxwell's equations are the starting point of derivation:

$$\nabla\times\mathbf{E}=-\mu_0\frac{\partial}{\partial t}\mathbf{H}\qquad \nabla\times\mathbf{H}=-\epsilon_0\frac{\partial}{\partial t}\mathbf{E}+\mathbf{J}\qquad \nabla\cdot\mathbf{J}+\frac{\partial}{\partial t}\rho=0\qquad \nabla\cdot\mathbf{H}=0 \tag{1}$$

The required integral equation may be derived by the vector Green's identity combined with (1). This equation relates $\mathbf{J}$ and $\mathbf{E}$ on the surface of considered structure. It is assumed that the structure is wire like with a circular cross section small compared with the wavelength of the highest significant frequency component of the excitation spectrum. The filamentary current density flows on the path along which the length variable is (Fig. 1). It produces electric field given below:

$$\mathbf{E}(\mathbf{r},t) = -\nabla\Phi(\mathbf{r},t)-\frac{\partial}{\partial t}\mathbf{A}(\mathbf{r},t) \tag{2}$$

$$\mathbf{A}(\mathbf{r},t) = \frac{\mu_0}{4\pi}\int_C\frac{\mathbf{I}(\mathbf{r},t-R/\nu)}{R}ds' \tag{3}$$

$$\Phi(\mathbf{r},t) = \frac{1}{4\pi\epsilon_0}\int_C\frac{q(\mathbf{r},t-R/\nu)}{R}ds' \tag{4}$$

where $\mathbf{s}=\mathbf{s}(\mathbf{r})$, $\mathbf{s}'=\mathbf{s}(\mathbf{r}')$, $ds'=ds(\bar{\mathbf{r}}')$, $R=|\mathbf{R}|=|\mathbf{r}-\mathbf{r}'|$ and the unprimed coordinates $\mathbf{r}$ and t denote the observation point location and the primed coordinates $\mathbf{r}'$ and $t'=t-R/c$ the source location. The differential operators in (2) are with respect to the observation coordinate. If

$\mathbf{s} = \mathbf{s}(\mathbf{r})$ and $\mathbf{s}' = \mathbf{s}(\mathbf{r}')$ are unit tangential vectors to $C(\mathbf{r})$ at $\mathbf{r}$ and $\mathbf{r}'$ the required terms in (2) can be written in the following way:

$$\frac{\partial}{\partial t}\mathbf{A}(\mathbf{r},t) = \frac{\mu_0}{4\pi}\int_C \frac{\mathbf{s}'}{R}\frac{\partial}{\partial t'}I(\mathbf{r}',t)ds' \tag{5}$$

$$\nabla\Phi(\mathbf{r},t) = \frac{1}{4\pi\epsilon_0}\int_C \left[-q(\mathbf{r}',t')\frac{\mathbf{R}}{R^3} + \frac{\mathbf{R}}{R^2\,c}\frac{\partial}{\partial s'}I(\mathbf{r}',t')\right]ds' \tag{6}$$

using

$$\nabla q(\mathbf{r}',t') = \frac{\partial}{\partial s'}I(\mathbf{r}',t')\frac{\mathbf{R}}{R\,c}$$

and

$$\frac{\partial}{\partial s'}I(\mathbf{r}',t') = -\frac{\partial}{\partial t'}q(\mathbf{r}',t')$$

Upon noting that $I(\mathbf{r}',t') \equiv I(\mathbf{s}',t')$ and $q(\mathbf{r}',t') \equiv q(\mathbf{s}',t')$ and combining (5) and (6) with (2) the integral equation form of the electric field due to a filamentary current is derived:

$$\mathbf{E}(\mathbf{r},t) = -\frac{\mu_0}{4\pi}\int_C \left[\frac{\mathbf{s}'}{R}\frac{\partial}{\partial t'}I(s',t') + c\frac{\mathbf{R}}{R^2}\frac{\partial}{\partial s'}I(s',t') - c^2\frac{\mathbf{R}}{R^3}q(s',t')\right]ds' \tag{7}$$

This equation for all space and time except the source region is valid. In fact the source region is a conductor of nonzero cross section. Applying the standard thin wire approach it is assumed that $I(s',t')$ and $q(s',t')$ are confined to the conductor axis and that the boundary condition on the tangential electric field at the conductor surface is known. For a perfect conductor the relation $\mathbf{s}\cdot\left(\mathbf{E}+\mathbf{E}^A\right) = 0$ is fulfilled. $\mathbf{E}$ and $\mathbf{E}^A$ are the applied and generated fields respectively. By applying the boundary condition on the tangential electric field at the conductor surface of Equation (7) the electric field integral equation for thin conducting wires is obtained

$$\mathbf{s}\cdot\mathbf{E}^A(\mathbf{r},t) = \frac{\mu_0}{4\pi}\int_C \left[\frac{\mathbf{s}\cdot\mathbf{s}'}{R}\frac{\partial}{\partial t'}I(s',t') + c\frac{\mathbf{s}\cdot\mathbf{R}}{R^2}\frac{\partial}{\partial s'}I(s',t') - c^2\frac{\mathbf{s}\cdot\mathbf{R}}{R^3}q(s',t')\right]ds',\ \mathbf{r}\in C(\mathbf{r})+a(\mathbf{r}) \tag{8}$$

where q can be expressed in terms of I as $q(s',t') = -\int_{-\infty}^{t'}\frac{\partial}{\partial s'}I(s',\tau)d\tau$ and $a(\bar{\mathbf{r}})$ denotes the wire radius at point $\bar{\mathbf{r}}$. Since the integration path in Equation (8) is along $C(\bar{\mathbf{r}})$ while the wire radius displaces the field evaluation path, it is always true that $R > 0$ and the integral in Equation (8) thus has no singularity. This displacement of the observation and source locations by the wire radius is the essence of the thin wire approximation. To solve (8) by MoM, the first step is to divide the thin wire in to N_S elementary segment of length Δ_i. In addition, the time is divided into N_t equal step Δ_t. Next, a set of rectangular basis function is defined for expressing the known current in each of the segment:

$$I(s_0,t_0) = \sum_{i=1}^{N_S}\sum_{j=1}^{N_T} I_{i\,j}(S''_i,t''_j)\,U(s''_j)\,V(t''_j),\quad s''_i = s_0 - s_i,\quad t''_i = t_0 - t_i \tag{9}$$

$$U(s''_j) = \begin{cases} 1 & |s''_i| \le \Delta_i/2 \\ 0 & \text{otherwise}\end{cases} \qquad V(t''_i) = \begin{cases} 1 & |t''_i| \le \Delta_i/2 \\ 0 & \text{otherwise}\end{cases} \tag{10}$$

A second order polynomial representation is used to evaluate the current $I_{i\,j}(s''_i,t_j)$ and the interpolation is chosen to be Lagrangian:

$$I_{i\,j}(s''_i,t''_j) = \sum_{l=-1}^{+1}\sum_{m=\nu}^{\nu+1} B_{i\,j}^{(l,\,m)} I_{i+1,j+1} \tag{11}$$

$$B_{i\,j}^{(l,\,m)} = \prod_{p=-1}^{+1}\prod_{q=\nu}^{\nu+2}\frac{(s_0-s_{i+p})(t_0-t_{j+q})}{(s_{i+1}-s_{i+p})(t_{j+m}-t_{j+q})} \tag{12}$$

$$\nu = \begin{cases} -1 & \Delta R = \frac{R}{c\cdot(t_j-t_{j-1})} > 0.5 \\ -2 & \Delta R < 0.5\end{cases} \tag{13}$$

where $I_{i+1,j+m}$ is the current value at the center of the $(l+1)$th space segment and the $(j+m)$th time step. The last step involves selection of the test function in order to get a system of linear equations. The point matching method, based on Dirac distributions, is used, i.e., $\delta(t-t_u)$ in space and $\delta(t-t_\nu)$ in time. The following system of equations is solved at every time step $\nu\Delta_t$ to obtain the vector $(I_{i,\nu})$ $(i=1,\ldots,N_S;\ u=1,\ldots,N_S;\ \nu=1,\ldots,N_T;\ x=1,\ldots,\nu-1)$:

$$(I_{i,\nu}) = \{(Z_{u\nu})\}^{-1}\{(e^a_{uv}) - (e^d_{ux})\} \tag{14}$$

where (Z_{iu}) is the matrix of the mutual interactions between the segments. This matrix has the advantage of being time independent.

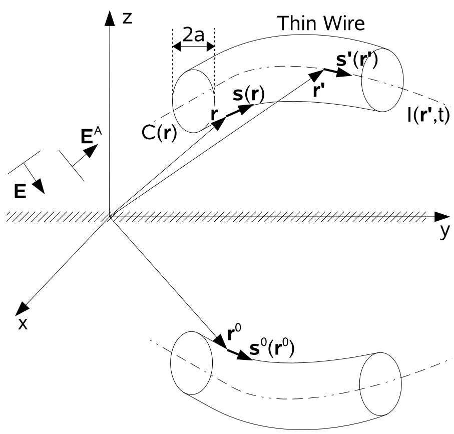

Figure 1: Thin wire geometry.

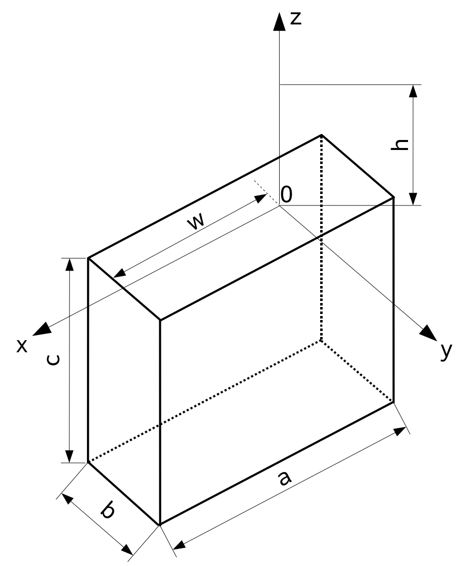

Figure 2: The geometric structure of the handset body together with its radiating monopole antenna.

3. RESULTS

The model described above is used to compute the electromagnetic field intensity around the handset. The handset body is approximated by a metallic box of dimension $a \times b \times c$ (Fig. 2).

A $\lambda/4$ monopole wire antenna of length h and radius r is placed at the top center of the handset body along the z-axis ($w = 3\,\text{cm}$). It should be noted that since the technique is general, the model can be used for more complex the handset geometries as well. To study the effect of the working frequency, we assume that the source is a modulated Gaussian pulse whose magnitude, $\nu(t)$ is defined as:

$$\nu(t) = \sin(2\cdot\pi\cdot f_z(t-t_{max}))\cdot e^{-a_n^2\cdot(t-t_{max})^2} \tag{15}$$

where t_{max}, a_n and f_z define the pulse shape. It should be noted that the Fourier transform of such a waveform is also a Gaussian function with a central frequency f_z.

Table 1: Physical dimensions of the handset body and its monopole antenna used in the case studies.

$a = 6.7\,\text{cm}$	$b = 1.2\,\text{cm}$	$c = 5\ldots 12\,\text{cm}$
$h = 5\,\text{cm}$	$w = 3\,\text{cm}$	$r = 0.1\,\text{mm}$

Table 2: Parameters of the source excitation voltage.

$t_{max} = 4.58333\cdot 10^{-10}\,\text{s}$	$a_n = 4.68131\cdot 10^9\,\text{s}^{-1}$
$f_z = 1500\,\text{MHz}$	

Table 1 lists the handset and antenna dimensions. The parameters of the source excitation voltage are given in Table 2. Fig. 3 shows the source waveform in time and frequency domains.

The validity of this approach is verified by comparing our simulated results by those reported by Luebbers et al. [6]. Fig. 4 shows the input impedance of the antenna when $c = 5\,\text{cm}$. The operating frequency varies from 0 to 2 GHz. The results are in good agreement with each other. Fig. 5 depicts the variation of impedance versus frequency for the cases of single monopole ($c = 5, 7, 12\,\text{cm}$) with

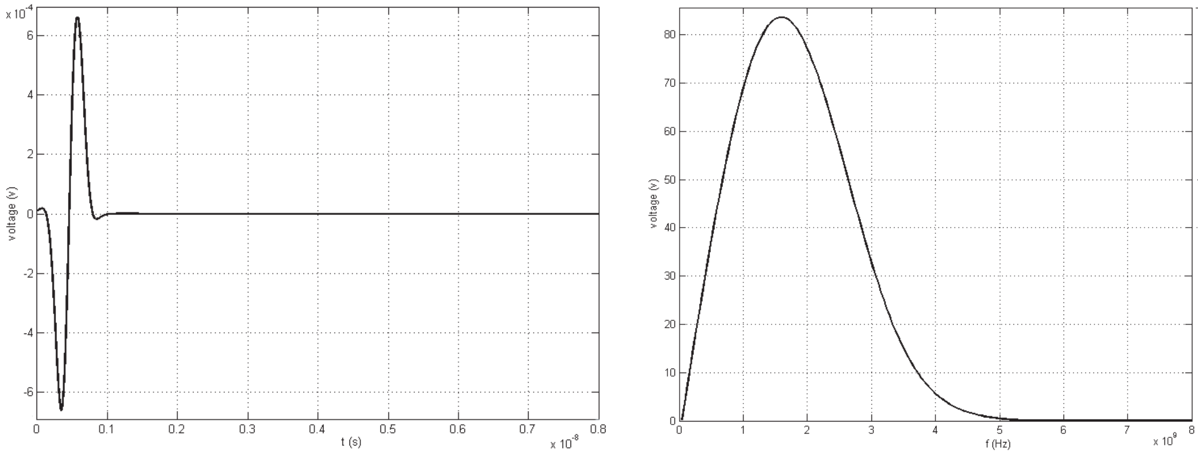

Figure 3: Source excitation voltage (left picture: time domain, right picture: frequency domain).

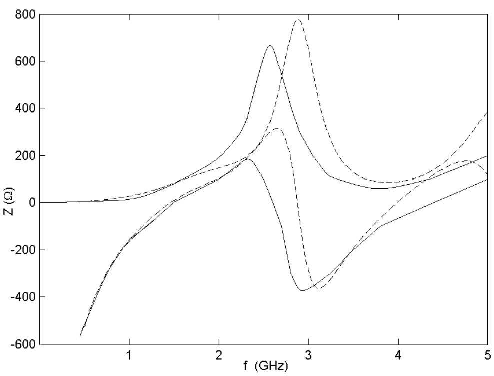

Figure 4: Computed input impedance of the monopole antenna mounted on the handset with height $c = 5\,\mathrm{cm}$ for the proposed method (—) and the method given in [6] (- - -).

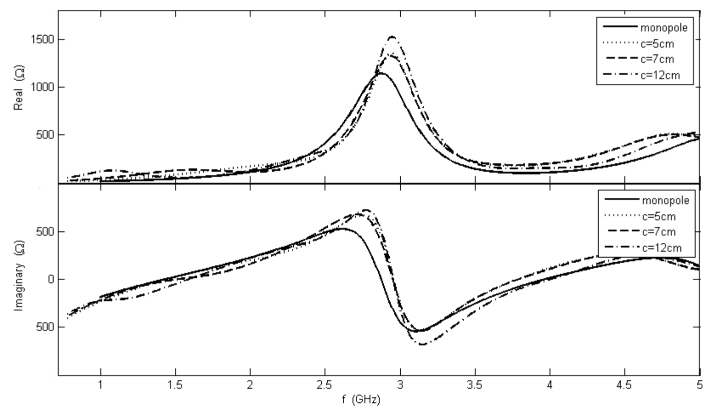

Figure 5: Input impedance of the monopole antenna without conducting box (—) and with conducting box: $c = 5\,\mathrm{cm}$ ($\cdots$), $c = 7\,\mathrm{cm}$ (- - -), $c = 12\,\mathrm{cm}$ (-· -·).

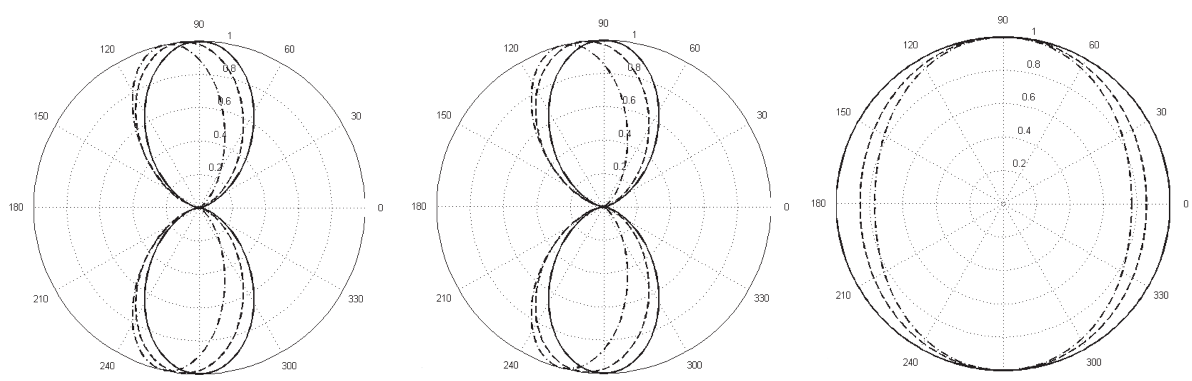

Figure 6: Radiation pattern of monopole antenna (—) and mounted antenna on the headset with $c = 7\,\mathrm{cm}$ (- - -), $c = 12\,\mathrm{cm}$ (-·-·). (a) y-z plane ($\Phi = 0°$), (b) x-z plane ($\Phi = 0°$), (c) x-y plane ($\theta = 90°$).

the resonant frequencies of 1450, 1470 and 1580 MHz respectively. As vividly seen in this figure, except for the case of $c = 12\,\mathrm{cm}$, the first resonant frequency (first occurrence of the imaginary part being zero) appears to be in the close vicinity of our design frequency (i.e., 1.5 GHz). This exception is most likely due to the induced currents on the surface of the box that affect the input impedance and radiation patterns of the antenna. The radiation patterns of the antenna in xy, yz, and xz planes are shown in Fig. 6, respectively. Fig. 6 demonstrates that the handset height has a slight effect on the antenna radiation pattern, particularly when compared with the case where the antenna is placed on an infinite planar perfect conductor. The increasing of the handset height results in the one sided downward radiated lobes which could possibly be used to deter the radiation from the human body. Fig. 7 shows variations of the input impedance at different handset widths and lengths. These variations have no significant affect on the input impedances in the working frequency range (i.e., $0 \ldots 1.5\,\mathrm{GHz}$). Fig. 8 illustrates the impact of the monopole position w on the radiation pattern. The position of the monopole antenna shifts the main lobe of the antenna to the side. This affect could be used to reduce the amount of the radiation reaching human brain which is considered to be the most harmful.

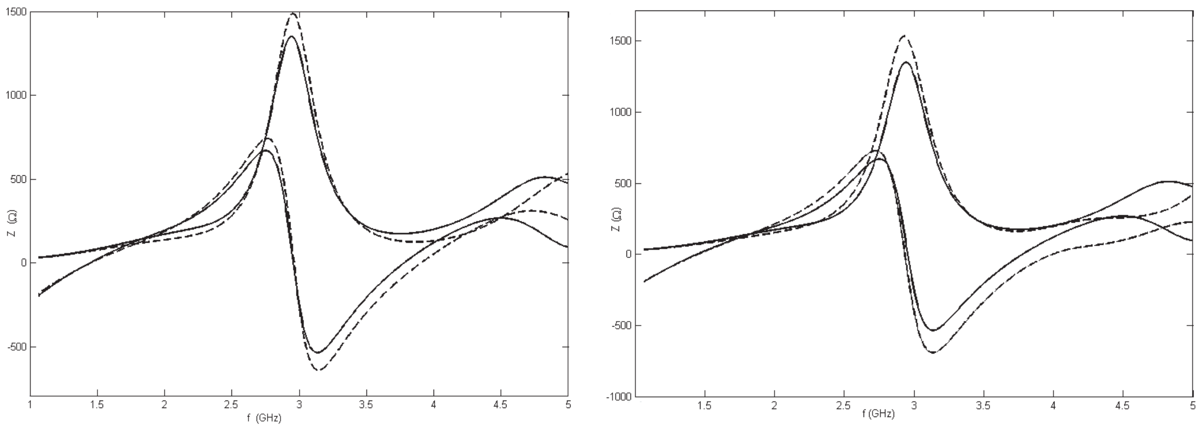

Figure 7: Input impedance of the monopole antenna with different box widths. (a) $b = 1\,\mathrm{cm}$ (—), $b = 2\,\mathrm{cm}$ (- - -), (b) $b = 6\,\mathrm{cm}$ (—), $b = 7\,\mathrm{cm}$ (- - -).

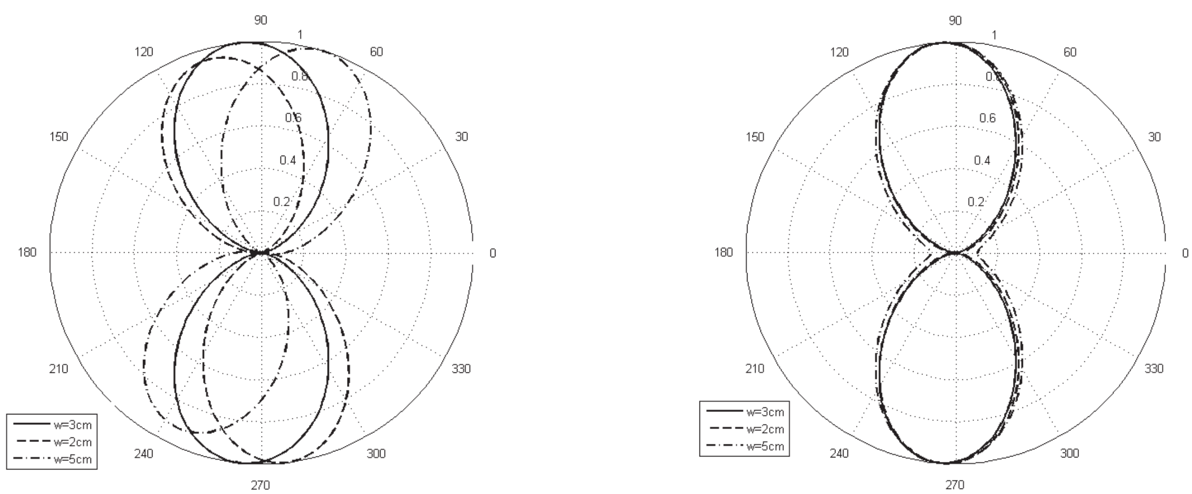

Figure 8: Radiation pattern of the monopole mounted on the headset with $w = 3\,\mathrm{cm}$ (—), $w = 2\,\mathrm{cm}$ (- - -) and $w = 5\,\mathrm{cm}$ (-·-·-). (a) x-z plane ($\Phi = 0°$), (b) y-z plane ($\theta = 90°$)

REFERENCES

1. Johansen, C., J. D. Boice, et al., "Cellular telephones and cancer — a nationwide cohort study in Denmark," *J. Natl. Cancer. Inst.*, Vol. 93, 203–207, 2001.
2. Jensen, M. A. and Y. Rahmat-Samii, "EM interaction of handset antennas and a human in personal communications," *Proc. IEEE*, Vol. 83, No. 1, 7–17, Jan. 1995.
3. Gandhi, O. P., G. Lazzi, and C. M. Furse, "Electromagnetic absorption in the human head and neck for mobile telephones at 835 and 1900 MHz," *IEEE*, MIT, Vol. 44, No. 10, Oct. 1996.

4. Kunz, K. S. and R. J. Luebbers, *The Finite-Difference Time-Domain Method in Electromagnetics,* Boca Raton, CRC, FL, 1993.
5. Taflove, A., *Computational Electrodynamics: The Finite-Difference Time-Domain Method*, Dedham, Artech House, MA, 1995.
6. Luebbers, R., L. Chen, T. Uno, and S. Adachi, "FDTD calculation of radiation patterns, impedance, and gain for a monopole antenna on a conducting box," *IEEE Trans. Ant. and Propagat.*, Vol. 40, No. 12, 1992.
7. Li, Y., D. Tao, and X. Xu, "Study of the characteristics of a portable hand-held phone antenna by MoM," *Proc. of the 3'rd International Conference on Microwave and Millimeter Wave Technology*, 2000.
8. Sarraf, R., R. Moini, and S. H. H. Sadeghi, "Analysis of electromagnetic fields due to a cellular phone handset, using the electric field integral equation method in time domain," *Proc. of 6's International Conference on Computational Methods in Electrical Engineering and Electromagnetics (ELECTROCOMP)*, Vol. 53, No. 61, Sep. 2003.

Topology Finite Element Method for Field Calculation Problems

Shizuo Li[1] and Yong Lu[2]

[1]College of Electrical Engineering, Guangxi University, Nanning 530004, China
[2]Guangxi Electric Power Institute of Vocational Training, Nanning 530007, China

Abstract— The paper introduces topology finite element method and its advantages firstly, then presents a new approach combining topology finite element method with a new preconditioning conjugate gradient method, which can save more memories and have fast calculating speed, lastly, an example is given.

1. INTRODUCTION

Nowadays, finite element method has been used for field calculation problems widely. But as the number of nodes and elements increasing, it needs much more memories to save the coefficient matrix, and abundant calculating time, sometimes it becomes impossible to achieve.

Topology finite element method (TFEM) represents the coefficient matrix of usual finite element method (FEM) with multiplication of several more simple matrixes, which need less memories to save. So if the algorithm in the next step of solving simultaneous equations only involves matrix multiplication, it can take the advantages of TFEM.

In this paper we show that by combining TFEM with a new preconditioning conjugate gradient method (PCGM), the calculating program needs much less memories than before while the computation is speeded up. It provides us a new approach for calculating large scale finite element problems on microcomputer. At last, An analysis example of brushless DC motor with surface-mounted NdFeB permanent magnet is presented.

2. TOPOLOGY FINITE ELEMENT METHOD

Take 2D triangle element mesh as shown in Fig. 1 to illustrate the TFEM. Each edge in the figure has been given a direction arbitrarily. In convenience, let the direction of each edge be from the node with smaller index number to the node with larger index number.

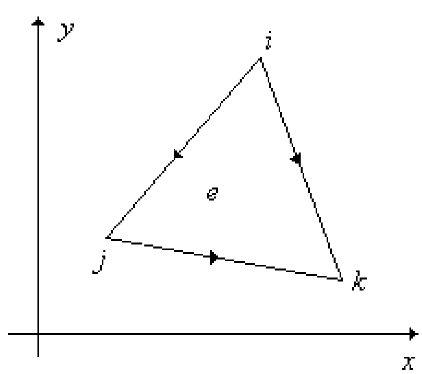

Figure 1: Triangle Element.

The potential function of the triangle element e can be written as:

$$\varphi_e(x,y) = N_i(x,y)\varphi_i + N_j(x,y)\varphi_j + N_k(x,y)\varphi_k \tag{1}$$

Here

$$N_i(x,y) = \frac{(x-x_k)(y_j-y_k)-(y-y_k)(x_j-x_k)}{(x_i-x_k)(y_j-y_k)-(y_i-y_k)(x_j-x_k)} = \frac{1}{2\Delta}(a_i+b_ix+c_iy)$$

$$N_j(x,y) = \frac{(x-x_k)(y_k-y_i)-(y-y_i)(x_k-x_i)}{(x_j-x_k)(y_k-y_i)-(y_j-y_i)(x_k-x_i)} = \frac{1}{2\Delta}(a_j+b_jx+c_jy)$$

$$N_k(x,y) = \frac{(x-x_j)(y_i-y_j)-(y-y_j)(x_i-x_j)}{(x_k-x_j)(y_i-y_j)-(y_k-y_j)(x_i-x_j)} = \frac{1}{2\Delta}(a_k+b_kx+c_ky)$$

Then the element energy is:

$$\iint_{S_e} \frac{\varepsilon}{2}\left[(\frac{\partial\varphi_e}{\partial x})^2+(\frac{\partial\varphi_e}{\partial y})^2\right]dxdy = \frac{\varepsilon}{8\Delta}\left[\varphi_i \quad \varphi_j \quad \varphi_k\right]\begin{bmatrix} b_i^2+c_i^2 & b_ib_j+c_ic_j & b_ib_k+c_ic_k \\ b_ib_j+c_ic_j & b_j^2+c_j^2 & b_jb_k+c_jc_k \\ b_ib_k+c_ic_k & b_jb_k+c_jc_k & b_k^2+c_k^2 \end{bmatrix}\begin{bmatrix}\varphi_i\\ \varphi_j\\ \varphi_k\end{bmatrix} \tag{2}$$

Because we have $b_i+b_j+b_k=0$ and $c_i+c_j+c_k=0$, it is easy to verify following equation.

$$\begin{aligned} W_eH_eW_e^T &= \frac{\varepsilon}{8\Delta}\begin{bmatrix} 1 & 1 & 0 \\ -1 & 0 & 1 \\ 0 & -1 & -1 \end{bmatrix}\begin{bmatrix} b_ib_j+c_ic_j & 0 & 0 \\ 0 & b_ib_k+c_ic_k & 0 \\ 0 & 0 & b_jb_k+c_jc_k \end{bmatrix}\begin{bmatrix} 1 & 1 & 0 \\ -1 & 0 & 1 \\ 0 & -1 & -1 \end{bmatrix}^T \\ &= \frac{\varepsilon}{8\Delta}\begin{bmatrix} b_ib_j+c_ic_j+b_ib_k+c_ic_k & -b_ib_j-c_ic_j & -b_ib_k-c_ic_k \\ -b_ib_j-c_ic_j & b_ib_j+c_ic_j+b_jb_k+c_jc_k & -b_jb_k-c_jc_k \\ -b_ib_k-c_ic_k & -b_jb_k-c_jc_k & b_ib_k+c_ic_k+b_jb_k+c_jc_k \end{bmatrix} \\ &= -\frac{\varepsilon}{8\Delta}\begin{bmatrix} b_i^2+c_i^2 & b_ib_j+c_ic_j & b_ib_k+c_ic_k \\ b_ib_j+c_ic_j & b_j^2+c_j^2 & b_jb_k+c_jc_k \\ b_ib_k+c_ic_k & b_jb_k+c_jc_k & b_k^2+c_k^2 \end{bmatrix} = -M_e \end{aligned} \tag{3}$$

Extend this equation to all elements and add them up, we can get the relation of the coefficient matrix of TFEM with the one of usual FEM as:

$$WHW^T = -M \tag{4}$$

Here M is the coefficient matrix of usual FEM, W is the node-edge incident matrix reflecting the relation between nodes and edges, W^T is the rotate matrix of W, H is the effect degree matrix. So the model of the field problem with TFEM can be derived as follows:

$$WHW^T\varphi = -M\varphi = P \tag{5}$$

P is a known matrix.

TFEM have a lot of advantages as bellow:

1. H is a diagonal matrix, and can be saved with a one-dimension array.

2. Each column of W has only two entries that equal to 1 and -1 respectively, while the others equal to zero. This can be saved with two one-dimension integer arrays whose length is equal to the number of edges, the first array saves the numbers of the starting nodes of directed edges, and the second array saves the numbers of the ending nodes of directed edges.

3. It needs much less memories than bandwidth-saving technique of usual FEM, and it need not optimize the node numbers, and can save much CPU time.

4. It needs fewer memories than nonzero-entry-saving technique, and it can save the addressing time of non-zero entries in the next step of solving simultaneous equations.

It needs to point out that the Equation (4) is correct in 3D problem yet.

3. COMBINING TFEM WITH A NEW PCGM

In this paper, a new preconditioning conjugate gradient method is applied to take full advantages of TFEM.

Introduce a diagonal matrix Q:

$$q_{ii} = \frac{1}{\sqrt{m_{ii}}} \tag{6}$$

m_{ii} is the ith diagonal entry of coefficient matrix M in usual FEM. Multiply Equation (5) by Q, so

$$QWHW^T\varphi = QWHW^TQQ^{-1}\varphi = QP \tag{7}$$

Rewrite this equation as:

$$\begin{aligned} A\varphi' &= P' \\ A &= QWHW^TQ \qquad \varphi' = Q^{-1}\varphi \qquad P' = QP \end{aligned} \tag{8}$$

Substituting this equation in conjugate gradient method, a new PCGM iterative form is developed:

1. $\gamma^{(0)} = Q\left(P - WHW^T\varphi^{(0)}\right)$
2. $\xi^{(0)} = \gamma^{(0)}$
3. i=0
4. $\zeta^{(i)} = QWHW^TQ\xi^{(i)}$
5. $a = \gamma^{(i)T}\gamma^{(i)}/\xi^{(i)T}\zeta^{(i)}$
6. $\varphi^{(i+1)} = \varphi^{(i)} + aQ\xi^{(i)}$
7. $\gamma^{(i+1)} = \gamma^{(i)} - a\zeta^{(i)}$
8. Let $\delta = Max(\gamma^{(i+1)})$

If $\delta \leq \varepsilon$, iteration terminates, otherwise continues.

9. $b = \gamma^{(i+1)T}\gamma^{(i+1)}/\gamma^{(i)T}\gamma^{(i)}$
10. $\xi^{(i+1)} = \gamma^{(i+1)} + b\xi^{(i)}$
11. Let $i = i$+1 turn to 4th step.

From these calculating step, it is obvious that the 4th step needs more calculations than other steps. Assuming that the mesh graph has N nodes and K edges, the calculating amount of 4th step is:

$Y_1 = Q\xi^{(i)}$ N multiplications
$Y_2 = W^TY_1$ K subtractions
$Y_3 = HY_2$ K multiplications
$Y_4 = WY_3$ $2K$ additions or subtractions
$\xi^{(i)} = QY_4$ N multiplications

The calculating amount of other step are:

5th step $2N$ multiplications and $2N$ additions
6th step $2N$ multiplications and N additions
7th step N multiplications and N subtractions
9th step $2N$ multiplications and $2N$ additions
10th step N multiplications and N additions

The calculating amount for one iteration is: $10N + K$ multiplications or divisions and $7N + 3K$ additions or subtractions. So total calculating amount $T(N)$ of this method is:

$$T(N) \sim \mathrm{O}(N) \tag{9}$$

This is much less than the $\mathrm{O}(N \cdot \log N)$ of ICCG.

The total memories required is $7N + 2K$ real number memory units and $2K$ integer number memory units.

Obviously, after combining this new PCGM with TFEM, because of no need for doing incomplete CHOLESKY factorization and addressing, not only can be simplified the calculating program, saved the memories and reduced the matrix calculating amount in each iteration, but also the fault that conjugate gradient method is difficult to converge can be overcome.

4. EXAMPLE

Brushless DC motor with surface-mounted NdFeB permanent magnet has been calculated with the preceding method. Variational presentation of this boundary value problem is:

$$\begin{aligned} F(A) \;=\; & \int_{S_1} \frac{1}{2\mu}(\nabla \times A)^2 dxdy + \int_{S_2} \frac{1}{2\mu}(\nabla \times A - \mu H_C)^2 dxdy - \int_{S_1} J_C A dxdy \\ =\; & \int_{S_1+S_2} \frac{1}{2\mu}\left[\left(\frac{\partial A}{\partial x}\right)^2 + \left(\frac{\partial A}{\partial y}\right)^2\right] dxdy - \int_{S_2} H_C \cos(\theta)\frac{\partial A}{\partial y} dxdy + \int_{S_2} H_C \sin(\theta)\frac{\partial A}{\partial x} dxdy \\ & -\int_{S_1} J_C A dxdy = \min \end{aligned} \tag{10}$$

Here, domain S_1 includes iron, slot and gap of motor, while domain S_2 includes the NdFeB permanent magnet. H_C is the coercivity of the NdFEB permanent magnet, and θ is the angle between the magnetized direction of the permanent magnet and X axis.

The mesh graph has 2569 nodes and 4920 edges as shown in Fig. 2, and the flux distribution is given in Fig. 3.

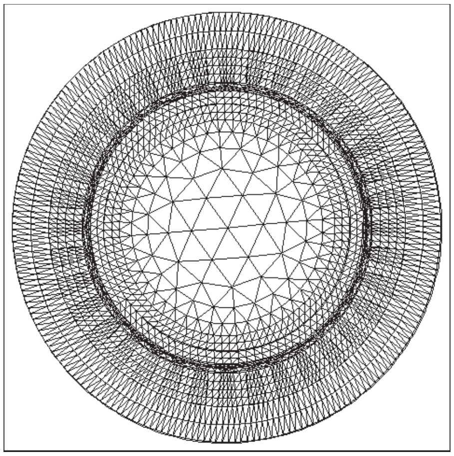

Figure 2: The mesh graph.

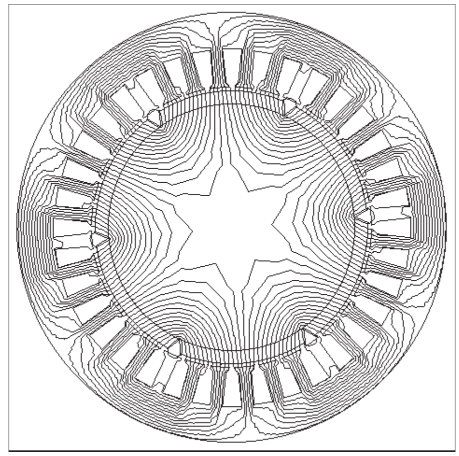

Figure 3: The flux distribution.

5. CONCLUSION

In this paper, the advantages of combination of topology finite element method and a new preconditioning conjugate gradient algorithm have been shown. Undoubtedly this combination is a simple and systematic approach that leads to a substantial gain in memory volume and computational cost, especially in the situation with node number increasing.

REFERENCES

1. Song, G. and H. Shi, "Topology finite element method for solving electromagnetic field problem," *Electronics Letters (IEE)*, Vol. 19, No. 15, 529–551, July 1983.
2. Henneberger, G., "An accelerated N-R method associated with the ICCG algorithms," *IEEE Trans. on Mag.*, Vol. 26, No. 2, 709–711, 1990.
3. Cui, X., "An new preconditioning conjugate gradient algorithm," *Trans. of North China Electric Power University*, No. 2, 1–7, 1989.

Design of Conformal Tapered Leaky Wave Antenna

O. Losito

Department of Innovation Engineering, University of Salento
Via per Monteroni, Lecce 73100, Italy

Abstract— The bend structure of leaky-wave antennas based on curve tapered design has been proposed and investigated. The new leaky-wave antenna (LWA) was designed running a simple procedure which use an FDTD code, and using a physical grounding structure along the length of the antenna, which allows to use only half of the structure, the adoption of a simple feeding, and the reduction of sidelobes. The good performance of this new tapered microstrip LWA are mainly wider band, higher gain, and higher efficiency whit reference to conventional uniform microstrip LWAs. Bending the curve tapered LWA, the major performance noticed of this antenna were the wider beam of radiation pattern and a further reduction of back lobes. Moreover since the tapering of linear LWA involves the variation of both phase and leakage constant, all the emitted rays are focused in a corresponding angular interval, allowing to obtain from the ray optical model a closed formula to predict the main beam angle of linear and curve taper LWA. Finally from theoretical analysis it should be appreciated that, as the relative dielectric constant of the substrate approaches 1, the leaky wave antenna bandwidth becomes much wider, improving its performance.

1. INTRODUCTION

Since the first microstrip leaky wave antenna (LWA) introduced by Menzel much progress has been made regarding the development of leaky wave antennas based on the higher order mode of microstip [1, 2]. The LWAs possess the advantages of low-profile, easy matching, fabrication simplicity, and frequency/electrically scanning capability. Nevertheless, in some applications especially with regard to communication applications, the main beam variation of LWA should be as low as possible.

A tapered steps microstrip LWA in which each step can irradiate in subsequent ranges of frequency, is a possible first solution studied to obtain a broadband and fixed mainbeam LWA. But the impedance mismatch between subsequent steps, reduces the bandwidth. Furthermore the excitation of a higher order mode without dominant mode perturbation, requires a more elaborate feeding scheme.

Subsequently, we studied a curved design of tapered antennas, from 8 to 11 GHz with a physical grounding structure along the length of antenna which allows a reduction of the impedance mismatch and a suppression of the dominant mode (the bound mode). Moreover, this solution allows the adoption of a simple feeding, the reduction of sidelobes, and due to the image theory it is also possible to design only half of an antenna with the same property of one in its entirety, reducing up to 60% the antenna's dimensions. This layout, improves the band, the gain and the efficiency compared with the conventional uniform microstrip LWAs. Nevertheless, we note that a tapered LWA for a fixed frequency, changes the main beam radiation angle and involves a focusing phenomena. This focusing phenomena determine a wide-beam radiation pattern of a tapered LWA allowing to predict the angle of main beam radiation pattern, using a simple geometrical-optical approach. Moreover, bending a tapered curve LWA allow the electromagnetic waves to diverge. This increases the beam, noticing a substantial reduction of the back lobes. The performance of the efficiency and the band of this LWA, can be improved further, if we use a substrate with relative dielectric constant that approached 1. In this paper we proposed such new conformal LWA, as discussed in the following sections.

2. CHARACTERISTICS OF MICROSTRIP LWA

The radiation mechanism of higher order modes on microstrip LWA is attributed to a traveling wave instead of the standing wave as in patch antennas, and is characterized by a complex propagation constant $k = \beta - j\alpha$, where β is the phase constant of the first higher mode, and α is the leakage constant. Above the cutoff frequency, where the phase constant equals the attenuation constant ($\alpha_c = \beta_c$), it is possible to observe three different ranges of propagation: leaky wave, surface wave and bound wave. Instead, at low frequency, below the cutoff frequency, we have the reactive region (without radiation) due to evanescent property of LWA. When the frequency is such that the phase constant of complex propagation constant, is higher than the free space wave number, we have the bound mode region.

The main-beam radiation angle of LWA can be approximated by:

$$\theta = \cos^{-1}\left(\frac{\beta}{K_0}\right) \tag{1}$$

where θ is the angle measured from the endfire direction, and K_0 is the free space wavenumber. From (1) we can observe that the leaky mode leaks away in the form of space wave when $\beta < K_0$.

3. DESIGN OF BROAD-BAND AND BROAD-BEAM LWA

Solving the dispersion equation, we can determine the range of the leakage propagation of the antenna. Generally the solution of such equation can be obtained through a full-wave analysis such as spectral domain analysis (SDA) [3], or through a transverse resonance approximation according to [4]. The complexity of full wave analysis suggest to use an easy FDTD algorithm that use PML boundary condition, as proposed in [5], to obtain the propagation characteristics of the normalized phase constant and attenuation constant.

From these characteristics curves we know the frequency range of the leaky-mode radiation indicated in the more useful way for the design of our antenna [6]:

$$\frac{c}{2w_{\mathit{eff}}\sqrt{\varepsilon_r}} = f_c < f < \frac{f_c\sqrt{\varepsilon_r}}{\sqrt{\varepsilon_r - 1}} \tag{2}$$

According to (2) we note, as the width of the antenna decreases, whereas the cutoff frequency increases shift toward high frequency. This behaviour allows to design, by running a simple procedure which uses an FDTD code, a broadband LWA in agreement with [6]. This multisections microstrip LWA, obtained overlapping different section, can irradiate in subsequent ranges of frequency because each section should be into bound region, radiation region or reactive region, permitting the power, to uniformly radiated at different frequencies.

Unfortunately this multisections LWA (layout Type I in Fig. 1), shows ripples in return loss curve, spurious sidelobes and impedance mismatch.

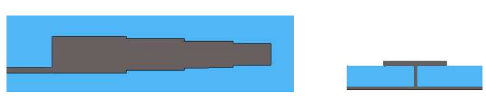

Figure 1: Layout Type I of multisections tapered LWA.

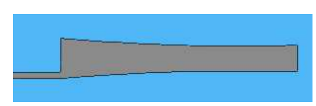

Figure 2: Layout Type II of curve tapered LWA.

A simple way to reduce these effects is to design a tapered antenna with linear profile, nevertheless better performance has been obtained design a smooth antenna profile using the same slope of the cutoff phase constant (or attenuation constant) curve ($\alpha_c = \beta_c$), as described in [7] and shown in Fig. 2. A suitable metal walls down the centerline connecting the conductor strip and the ground plane, was used in all Type of LWAs, allows to suppress the fundamental mode, the adoption of a simple feeding planar line and forcing the energy to propagate at the next higher mode. Moreover due to the image theory is possible to use only half of the curve tapered LWA, characterized by the same property of one in its entirety, but with the dimensions reduced of the 60%, as shown in Fig. 3. From (2) we note also, that, using a substrate material with relative dielectric constant approached 1, the leaky wave antenna bandwidth becomes much wider, increased drastically.

Figure 3: Layout Type III of half curve LWA.

Finally as was described in the alternative geometrical optics approach proposed in [8] the tapering of the LWA, for a fixed frequency, involves the variation of the phase constant β and the attenuation constant α changing the main beam radiation angle along the length of the antenna, as deduced from (1–2) and shown in Fig. 4. This variation with the cross section of the antenna, allowing a non-parallel emitted rays, such as happens in a uniform LWA and a corresponding beam radiation interval [$\theta_{\min}$, $\theta_{\max}$], obtained from (1).

Using the geometrical optics we note that all the emitted rays intersect the real focus F and the virtual focus F', therefore the main beam radiation angle is obtained from the intersection between the longitudinal dimension of the antenna and the straight which connects the real and the virtual focus (point M). Through simple passage, the main beam angle θ_m is related by the follows formula:

$$\theta_m = \sin^{-1}\left(\frac{A\sin\theta_{\min}}{\frac{1}{2}\sqrt{(2A\sin\theta_{\min})^2 + (L + 2C\cos\theta_{\max})^2}}\right) \tag{3}$$

where A and C are respectively the distance between real focus F and the beginning and the end of the length of the antenna, L. According to the simulation results, for the curve tapered LWA, the intersection point M is moved towards the centre of the antenna E , so that the angle is moved towards. This occurs because the curve tapering reduce more quickly than linear tapering, the cross section of the antenna. Furthermore this focusing phenomena of a tapered LWA can determine a wide-beam pattern in a beam radiation range which is evident when the antenna length is increased ($L \cong 50\lambda_0$) [8]. To obtain a broad beam pattern without the use of a longer LWA, we can bend a tapered curve LWA as shown in Fig. 5, allowing the electromagnetic waves to diverge. This increases the beam of the radiation pattern noticing a substantial reduction of the back lobes.

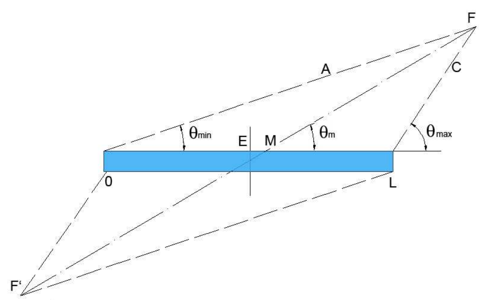

Figure 4: Ray optical model for a tapered LWA.

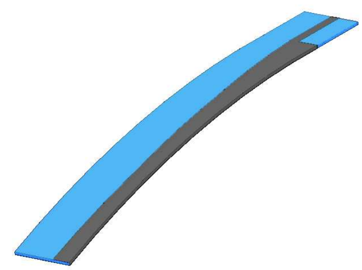

Figure 5: Layout of bend curve tapered LWA.

4. SIMULATION RESULTS

The ours LWAs were exited simply with an asymmetrical planar feed line of $50\,\Omega$, because the metal wall down the centerline connecting the conductor strip and the ground plane, used to suppress the dominant mode, allows to travel only the higher order mode. The length of the curve tapered LWA was chosen to be 120 mm to allow 90% radiation at an upper frequency of 9.5 GHz. All tapered LWAs were an open circuit, with a 15 mm start width, and 8.9 mm of final width, with a substrate of thickness of 0.787 mm and $\varepsilon_r = 2.32$. From the return loss (S11) of Type I, we noted that it was below -10 dB only in three short-range frequencies (see Fig. 6), while S11 of Type II and Type III were practically the same, below -10 dB from 8 to 11.17 GHz (VSWR< 2 between 8.01 and

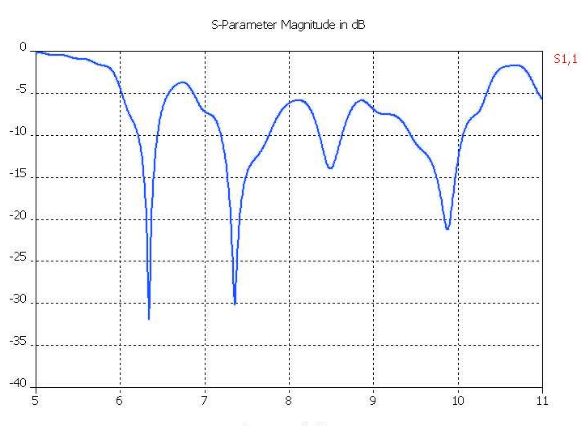

Figure 6: Simulated S11 of LWA Type I.

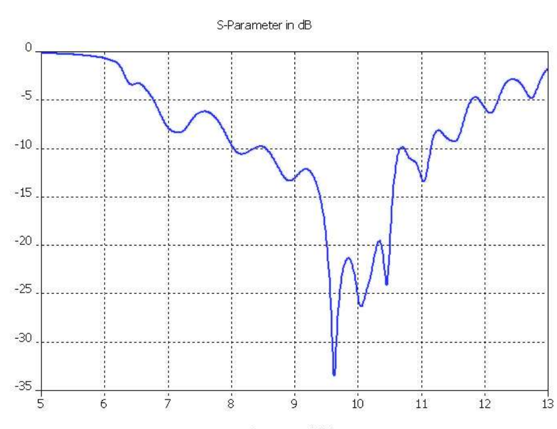

Figure 7: Simulated S11 of LWA Type II.

11.17 GHz) as shown in Fig. 7 and Fig. 8. In Fig. 9 is shown the return loss (S11) of Type III, whit a $\varepsilon_r = 1.1$ of substrate. It is clear that the leaky wave antenna bandwidth Type III, becomes much wider, increased drastically. The main lobe pattern of LWA Type III in Fig. 10, shown a reduction of sidelobe, and a peak of gain up to 12 dBi.

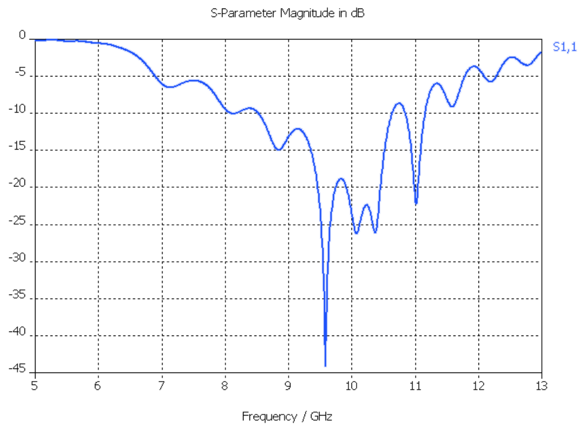

Figure 8: Simulated S11 of LWA Type III.

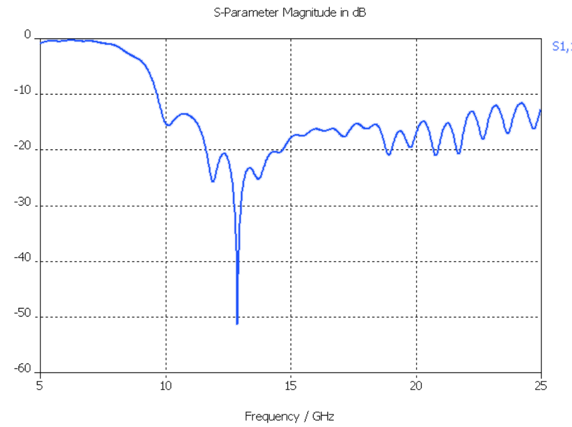

Figure 9: Simulated S11 of LWA Type III whit $\varepsilon_r = 1.1$.

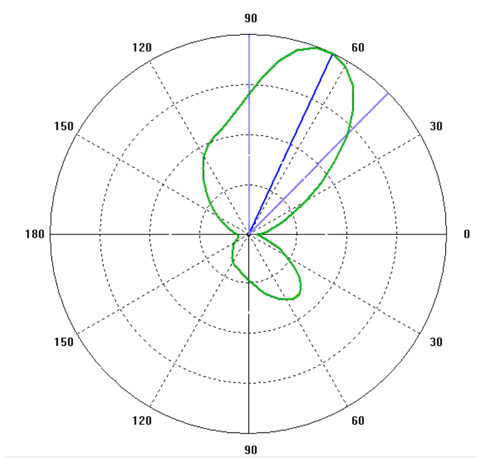

Figure 10: Radiation pattern of E field LWA Type III at 8 GHz.

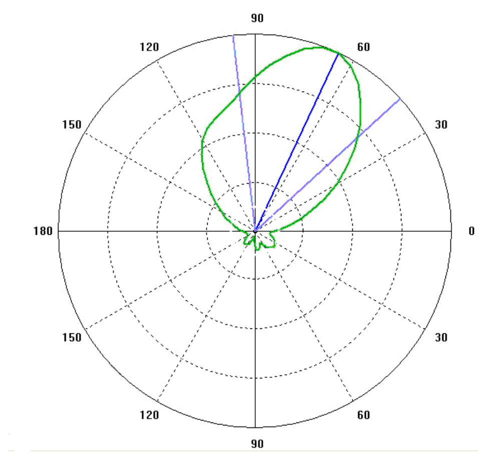

Figure 11: Radiation pattern of E field bend LWA Type III at 8 GHz.

This results indicate a high performance of antenna Type III (33% for VSWR< 2, high antenna efficiency and high power gain) compared with uniforms LWAs (20% for VSWR, peck power gain up to 10 dBi) as mentioned in [9]. Finally Fig. 11 shown the radiation pattern of a $-20°$ bend LWA for a frequency of 8 GHz. We note a major reduction of back lobe and an increases of beam pattern with reference to the LWA Type III pattern at 8 GHz.

5. CONCLUSION

In this study, a new design of broadband microstrip leakywave antenna from 8 to 11 GHz, was proposed with high added value. An FDTD code was used to determinate the propagation constant of LWA, necessary to design a smooth contour of LWA, whit the same shape of cutoff point curve of a multisection broadband microstrip LWA. The simulation results demonstrate the good performance, compared to conventional uniform microstrip LWAs (wider band and higher gain). Furthermore, bending a tapered curve LWA, we can obtain a broad beam microstrip LWA with a substantial reduction of the back lobes, and using a closed formula obtained with a geometrical-optical approach, we can know the main beam angle of tapered LWA. The performance of the efficiency and the band of this LWA can be improved further, if we use a substrate with relative dielectric constant that approached 1, highlighting that this structure is attractive for the design of high performance microstrip leaky-wave antennas for microwave and millimetre wave applications.

REFERENCES

1. Menzel, W., "A new traveling-wave antenna in microstrip," *Arch. Elek. Uhertragung.*, Vol. 33, 137–140, 1979.
2. Oliner, A., "Leakage from higher modes on microstrip line with application to antennas," *Radio Scienze*, Vol. 22, 907–912, 1987.
3. Itoh, T. and R. Mittra, "Spectral domain approach for calculating the dispersion characteristics of microstrip lines," *IEEE Trans. Microwave Theory Techn.*, Vol. MTT-21, 496–499, 1973.
4. Kuester, E. F., R. T. Johnk, and D. C. Chang, "The thin-substrate approximation for reflection from the end of a slab-loaded parallel-plate waveguide with application to microstrip patch antennas," *IEEE Trans. Antennas and Propagation*, Vol. AP-30, No. 5, Sep. 1982.
5. Zelinski, G. M., M. L. Hastriter, M. J. Havrilla, J. S. Radcliffe, A. J. Terzuoli, and G. A. Thiele, "FDTD analysis of a new leaky traveling wave antenna," *Wireless Communications and Applied Computational IEEE/ACES 2005 Intl. Conf.*, 152–155, Apr. 2005.
6. Hong, W., T. L. Chen, C. Y. Chang, J. W. Sheen, and Y. D. Lin, "Broadband tapered microstrip leaky-wave antenna," *IEEE Trans. Antennas and Propagation*, Vol. 51, 1922–1928, 2003.
7. Losito, O., "A new design of broadband microstrip leaky-wave antenna," *Proceeding of 23rd Applied Computational Electromagnetics, ACES 2007 Int. Conf.*, Verona, Italy, 19–23 March, 2007.
8. Burghignoli, P., F. Frezza, A. Galli, and G. Schettini "Synthesis of broad-beam patterns through leaky-wave antennas with rectilinear geometry," *IEEE Antennas and Wireless Propagation Letters*, Vol. 2, 136–139, 2003.
9. Qian, Y., B. C. C. Chang, T. Itoh, K. C. Chen, and C. K. C. Tzuang, "High efficiency and broadband excitation of leaky mode in microstrip structures," *IEEE MTT-S Microwave Symposium Digest*, Vol. 4, 1419–1422, 1999.

Design of an Internal Wideband Antenna for DTV Laptop Application

S. G. Jeon, D. H. Seo, and J. H. Choi

Department of Electrical & Computer Engineering, Hanyang University
17 Haengdang-Dong, Seongdong-Gu, Seoul 133-791, Republic of Korea

Abstract— A novel low profile folded asymmetric planar dipole antenna structure for laptop application is proposed. The antenna covers DTV (470∼740 MHz) frequency band and can be easily constructed by folding the metal plate dipole antenna with meandered pattern and occupies a small volume of 58 mm×20.125 mm×10 mm. The measured return losses are less than −7.5 dB over the DTV frequency band. The proposed antenna shows nearly omni-directional or monopole-like radiation patterns and has good antenna gain over the frequency band of interest.

1. INTRODUCTION

The advent and fast development of digital broadcasting technologies enables portable devices such as laptop to receive TV broadcasting signals. In order to receive TV signal on laptop, an antenna with good performance is required. However, due to the aesthetic and safety view points, the use of an internal antenna is preferred rather than using conventional external antenna for portable devices [1]. It also requires that an internal antenna should be less profile and compact. Therefore, the key design goal of an internal antenna is size reduction while maintaining the antenna performance the same as that of an external antenna. A low profile planar metal plate monopole antenna for DTV signal reception in the UHF band for laptops has been reported recently [2, 3].

In this paper, an embedded DTV antenna for laptop application is proposed. The designed antenna has a narrow width of 10 mm and is very promising to be embedded within the narrow space between the display and case unit of laptop. In addition, the antenna can provide wide bandwidth (about 50% centered at 625 MHz) for operating in UHF DTV services. (470 MHz∼740 MHz)

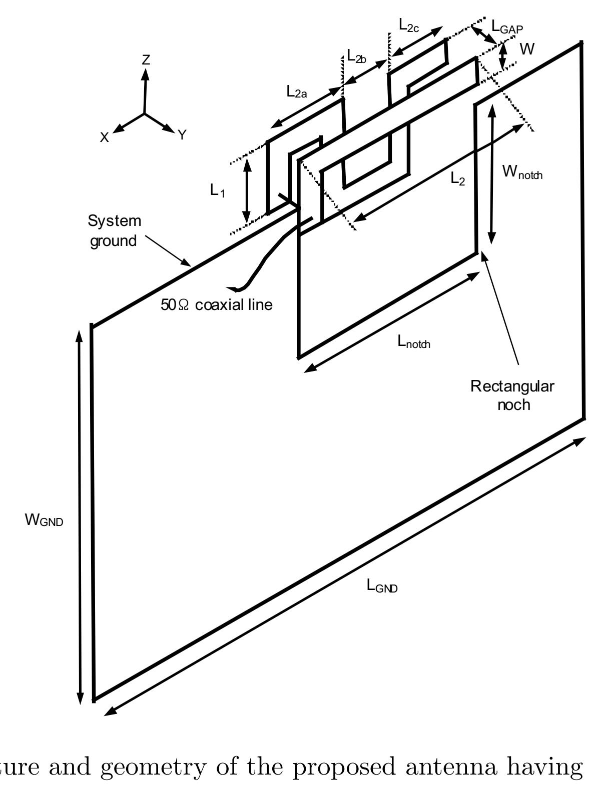

Figure 1: The structure and geometry of the proposed antenna having asymmetric structure.

2. ANTENNA DESIGN

Figure 1 shows the geometry of the proposed antenna. The antenna is placed on the metal plate has a dimension of 195 mm×70 mm. The proposed antenna is a folded planar dipole with asymmetric branches. The folded dipole and the system ground plane were fabricated using 0.2 mm thick brass sheet. There is a gap of 10 mm between the two metal plates of folded dipole structure and ground plane, and the feeding point is located at the end of the dipole structure. 50 Ω coaxial line is connected to the feed point to excite the folded dipole antenna and its sheath connected to the antenna ground plane. The folded dipole antenna consists of L-shaped metal plate and meandered metal plate. The asymmetric structure of folded antenna is a key element to determine the radiation characteristics of a proposed antenna.

To investigate the effect of meandered branch of folded dipole on the bandwidth characteristic, return losses of symmetric and asymmetric dipole antennas are calculated and compared in Figure 2(b). It is observed that the meandered structure of asymmetric dipole improves the bandwidth characteristics significantly.

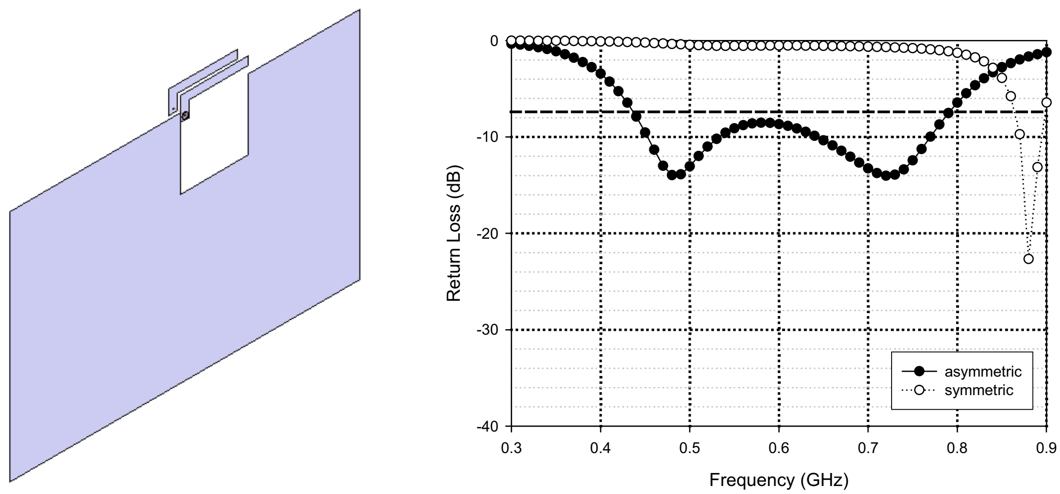

(a) (b)

Figure 2: Comparison about simulated return loss's with asymmetric radiation structure, (a) dipole antenna with symmetric structure, (b) comparison of return loss characteristics between Figure 1 and Figure 2(a).

3. SIMULATION AND MEASUREMENT

The performance of folded asymmetric planar dipole antenna with various parameters (L_{GAP}, W_{notch}, and L_2) was analyzed to demonstrate the proposed wide bandwidth technique. The simulated results were obtained using the Ansoft simulation software, high-frequency structure simulator

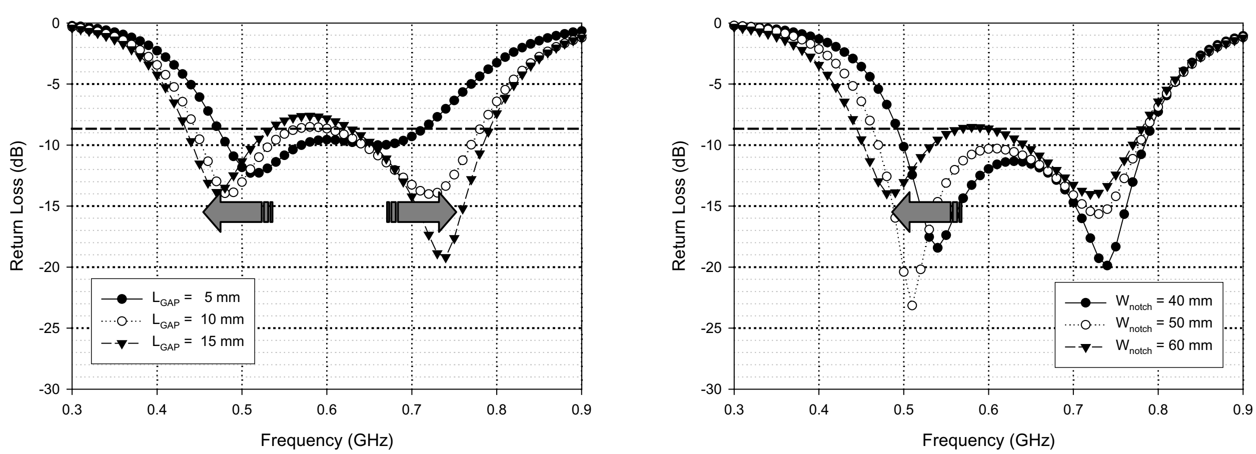

(a) (b)

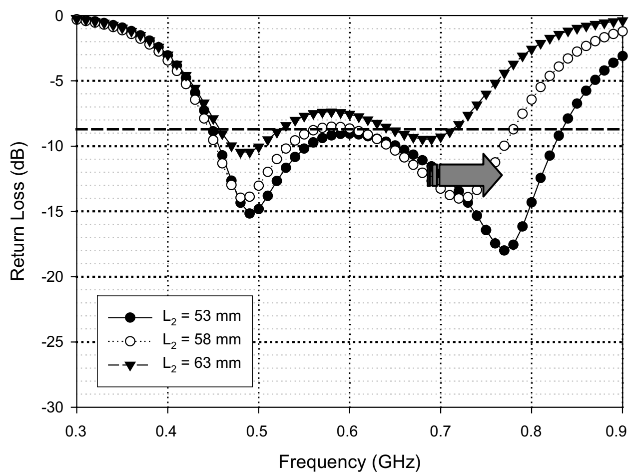

(c)

Figure 3: Simulated return loss characteristics for various values of L_{GAP}, W_{notch} and L_2, (a) L_{GAP}, (b) W_{notch} and (c) L_2.

(HFSS) [4]. Figure 3(a) shows the simulated return loss characteristics for various gap distances between branches. As the gap distances changes from 5 to 15 mm, the impedance bandwidth becomes wider. The simulated return loss characteristics with different values of W_{notch} are plotted in Figure 3(b). From the simulation results in Figure 3(b), it is found that the 7.5 dB impedance bandwidth increases as the notch length increases. It is also observed that the lower resonance frequency is significantly affected by the variation in the length of W_{notch}. The simulated return loss characteristics with different values of L_2 are plotted in Figure 3(c). The 7.5 dB impedance bandwidth increases as the notch length decreases. It is also observed that the upper resonance frequency is significantly affected by the variation in the length of L_2. On the other hand, the lower frequency is insensitive to the change in L_2.

Figure 4 shows measured and simulated return loss characteristics of the proposed antenna. Measured impedance bandwidth is wider than simulated one. The fabricated antenna satisfies the 7.5 dB return loss requirement from 451 to 817 MHz. The design parameters of the fabricated antenna are listed in Table 1. Figure 5 shows the simulated radiation patterns in the x-y plane, y-z plane and z-x plane at 480 MHz and 720 MHz. In Figure 6, shows measured antenna gain from 480 to 720 MHz for the proposed antenna is given. The antenna gain varies from 1.4 dBi to 2.6 dBi.

Parameter	Value (mm)	Parameter	Value (mm)
L_1	20.125	W	7
L_2	58	L_{GND}	300
L_{2a}	24	L_{notch}	58
L_{2b}	15	W_{GND}	200
L_{2c}	19	W_{notch}	60
L_{GAP}	10	-	-

Table 1: The design parameters.

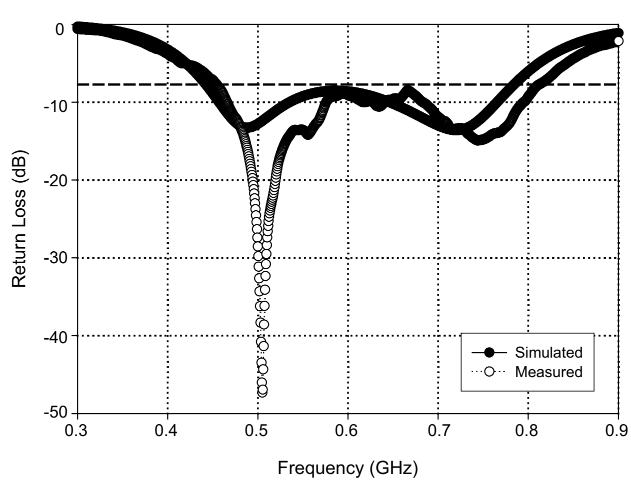

Figure 4: Simulated and measured return loss characteristics.

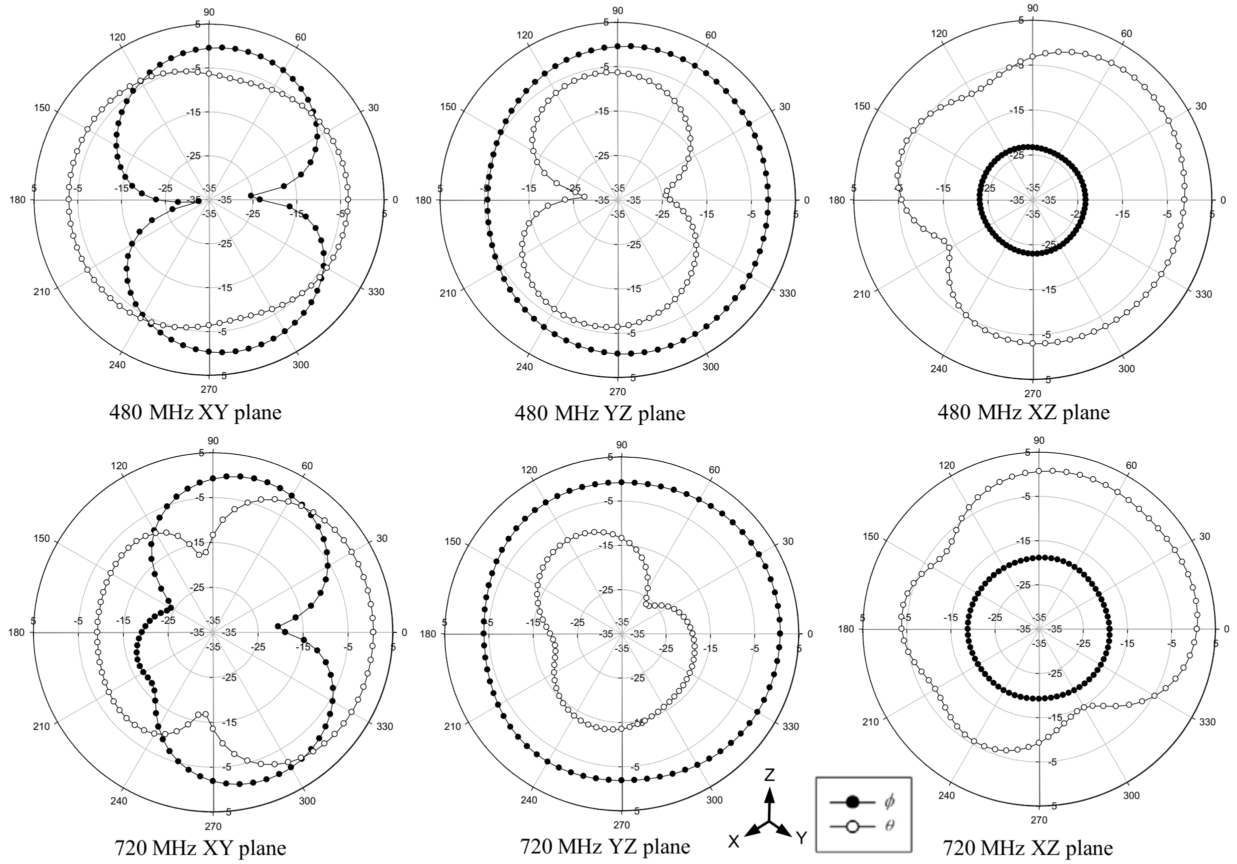

Figure 5: Simulated radiation patterns.

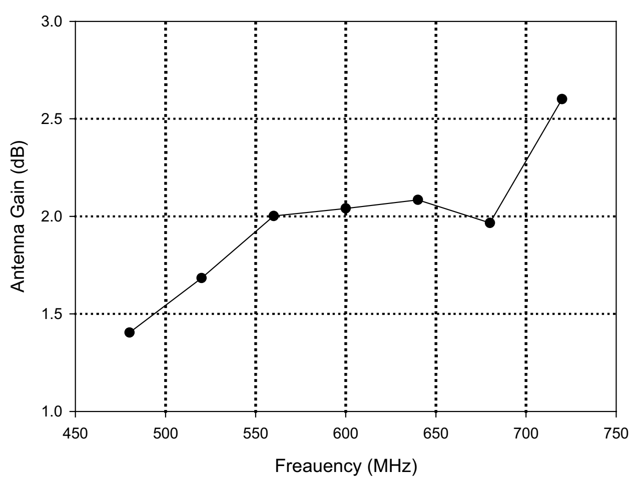

Figure 6: Simulated antenna gain.

4. CONCLUSION

A novel low profile folded asymmetric planar dipole antenna with wideband characteristic has been proposed and implemented for DTV application. The proposed antenna has asymmetric structure and wide bandwidth characteristic. The dimensions of folded dipole are optimized by the parametric analysis. The wide bandwidth performance from 451 MHz to 817 MHz is obtained. The measured radiation patterns and return loss characteristics of the proposed antenna are good enough for DTV application. This antenna can be a good candidate for mobile DTV handset due to its low profile, small size and wideband characteristics.

ACKNOWLEDGMENT

This work was supported by the HY-SDR Research Center at Hanyang University, Seoul, Korea, under the ITRC Program of IITA, Korea.

REFERENCES

1. Ang, I., Y. X. Guo, and Y. W. Chia, "Compact internal quad-band antenna for mobile phones," *Micro. Opt. Technol. Lett.,* Vol. 38, No. 3, 217–223, 2003.
2. Su, C. M., L. C. Chou, C. I. Lin, and K. I. Wong, "Embaded DTV antenna for laptop application," *2005 IEEE Antennas and Propagation Society International Symposium*, Vol. 4B, 68–71, 3–8 Jul., 2005.
3. Su, C. M., L. C. Chou, C. I. Lin, and K. I. Wong, "Internal DTV receiving antenna for laptop application," *Micro. Opt. Technol. Lett.*, Vol. 44, No. 1, 4–6 Jan., 2005.
4. Ansoft High-Frequency Structure Simulator (HFSS), Ver. 10, Ansoft Corporation.

Compact Representation of the Inductance Coefficients in Presence of Uncertain Parameters

B. De Vivo, L. Egiziano, P. Lamberti, and V. Tucci
Department of Electrical and Information Engineering, University of Salerno, Italy

Abstract— This paper presents an effective and reliable tool for evaluating inductance coefficients in presence of uncertain parameters in a simple and compact form. The inductance coefficients in some interesting applications are obtained by applying the Interval Arithmetic to the Hopkinson's law. The proposed approach allows to efficiently take into account the presence of the geometric tolerances and the non linearity of the ferromagnetic materials. It is shown that the resultant intervals include the actual values of the coefficients thus improving the reliability of the components design.

1. INTRODUCTION

The realization of power electronic circuits employed for the energy conversion process in a great number of applications involves the design of inductors and transformers [1]. This task assumes an increasing relevance when the miniaturization of the components is an essential requirement of the design [1–3]. However, the relevant parameters of such electromagnetic components obtained by performing a nominal value design are rarely correspondent to those available from market devices. Therefore an appropriate realization of such components may be required for each application which is usually performed by adopting the lumped parameters circuit approach [2, 3]. As an example, in the case of the nominal design of the simple inductor wound on a ferromagnetic core of Figure 1, we know that the inductance can be expressed as

$$L = \frac{N^2 i}{\Re i} = \frac{N^2}{\Re} \tag{1}$$

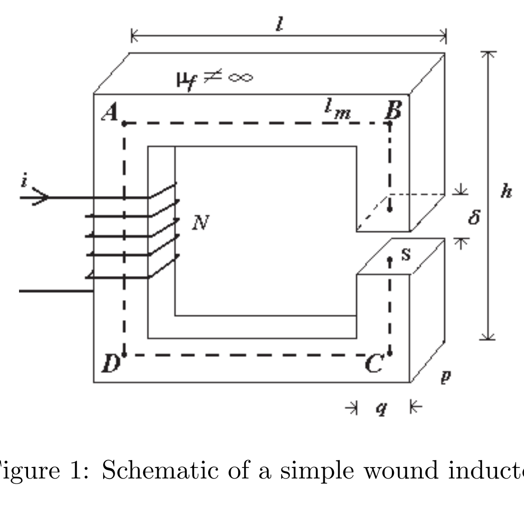

Figure 1: Schematic of a simple wound inductor.

The reluctance of the magnetic structure is:

$$\Re = \Re_{fe} + \Re_{\delta} = \frac{l_m - \delta}{\mu S} + \frac{\delta}{\mu_0 S} \tag{2}$$

where S is the (uniform) cross section of the core, l_m is its axial length, δ is the eventual gap length, μ_0 and μ are the permeability of the air and the ferromagnetic material respectively. Still for some production units, due to the mechanical tolerances affecting the geometric parameters and the uncertainty on the real value of μ which on the producer's data sheet is given in a band, the obtained inductance may be substantially different from the nominal value and hence out of an acceptable range. This drawback sensibly affects the performances of the overall system, especially in terms of power consumption and dimensions [1].

For this reason the availability of a compact and efficient model of the electromagnetic component able to keep into account the inevitable uncertainty associated to its physical and geometric parameters seems indeed useful to guarantee an appropriate design of the circuit.

In order to pursue this objective in this paper the representation of the inductance coefficients in presence of uncertain parameters is presented in a simple and compact form. In particular, the self inductance coefficients are obtained by applying the Interval Arithmetic to the so called Hopkinson's law [4]. This approach leads to the determination of inductance coefficients which are not expressed as point-values but as sets of *intervals*. Such intervals certainly include all the possible values that the coefficients can assume in presence of tolerances on physical and/or geometric parameters. In order to put in evidence the validity of the proposed method the procedure is exemplified with reference to simple wound components in presence of tolerances on the geometric parameters. The influence of the characteristics of the ferromagnetic material is considered by two approaches. Firstly, a linear behaviour is assumed where the permeability is an uncertain but bounded parameter. Then, a non linear B-H characteristics given in analytical form is considered. The materials are those adopted in realistic applications, whereas the values of the adopted geometrical parameters are derived from the data sheets of IEC standard magnetic configurations. The correctness of the proposed approach is ascertained by verifying that the resultant intervals, as obtained from experimental measurements or numerical tests by using a commercial software based on the Finite Element Method (FEM), include the actual values of the inductance coefficients.

2. INTERVAL ARITHMETIC

The Interval Arithmetic (IA) is an arithmetic that furnishes a reliable inclusion of the true range of a function for a given interval of values of the variables [5]. In fact, IA is defined on sets of intervals rather then sets of real numbers. An interval X is an ordered pair of real numbers $X = [a, b]$ such that $X = [a, b] = \{x|a < x < b$, with a, x, $b \in \Re\}$, and all the values in X are equally probable. The sets of intervals on $\Re$ is denoted as $I\Re$. All the operations defined on $\Re$ can be extended to $I\Re$. Moreover, the IA is characterised by a very interesting property, namely the "inclusion property" [4], which makes such a mathematical environment particularly useful in dealing with uncertain quantities. In fact, if $f : \Re \to \Re$ and $f : I\Re \to I\Re$ is the associated function having the same analytical expression and operating on interval rather than on "point" coefficients it results that $\forall x \in X = [a, b] f(x) \in F(X)$.

Thus the function $F(X)$ includes the true values assumed by $f(x)$ when the variable x spans the whole interval X and coincides with its true range in absence of wrapping or dependency effects [4].

Therefore, given a function of n variables $f(p_1, p_2, \ldots, p_n)$, as it is the case of the inductance coefficient (1), whose values, due to tolerances and uncertainties, can vary in the intervals $P_i = [p_{i\,\min}, p_{i\,\max}]$ $\forall i = 1, \ldots, n$, the IA allows to easily obtain an interval where the true value of the inductance is certainly included.

Moreover, if we consider the so called Hopkinson's law:

$$\Re\phi = Ni \tag{3}$$

where the reluctance is taken as an interval, we can evaluate the range of all the possible values assumed by the flux. The same approach can be adopted in order to take into account the uncertainties on the permeability. The interval associated to this parameter can be directly evinced from the material's data sheet or computed from a non linear expression linking the induction B to the magnetic field H. Similar reasoning can be applied in the case of multiple windings, thus allowing to achieve the intervals including the mutual induction coefficients.

3. APPLICATION OF IA AND RESULTS

As stated in the introduction, the uncertainty on the induction coefficient due to tolerances on the geometrical parameters will be examined. The influence of the characteristics of the ferromagnetic material is considered by two approaches. Firstly, the characteristics of the ferromagnetic material is assumed to be linear but uncertain in a bounded interval and secondly, a non linear B-H characteristics given in analytical form is considered.

a) linear magnetic permeability given in a bounded interval

Let us suppose that we have to design an inductor for keeping the output current in a boost converter whose switching frequency is 150 kHz in the range 125 mA ±10%. The design constraints

[1] lead to a nominal value of the inductance equal to 3.2 mH. A soft ferrite core is chosen in order to minimize the losses. We select a F44 ferromagnetic core of manganese zinc, type ETD 39, whose geometric dimensions, according to IEC standard 1185, are defined as described in Figure 2. The ranges of such dimensions, due to tolerances, are reported in Table 1.

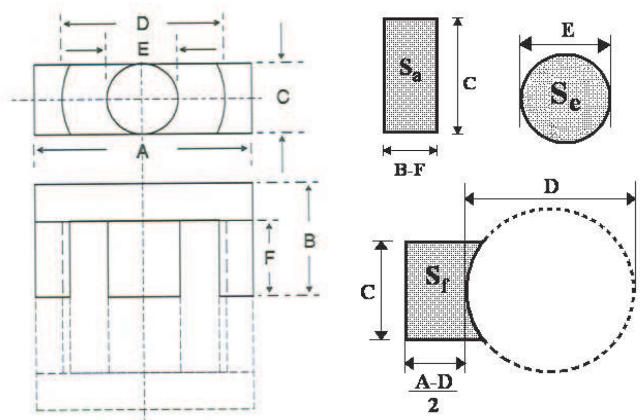

Figure 2: ETD 39 core structure and relevant geometric parameters.

For the design purposes the per unit turn inductance A_L is furnished in the materials data sheets and hence:

$$L = \frac{N\phi}{i} = \frac{N^2}{\Re_{eq}} = N^2 A_L \tag{4}$$

Table 1: ETD 39 core dimensions.

A [mm]	B [mm]	C [mm]	D [mm]	E [mm]	F [mm]
[38.2, 40.0]	[19.6, 20.0]	[12.2, 12.8]	[29.3, 30.9]	[12.2, 12.8]	[14.2, 15.0]

Therefore, the winding's number of turns is the integer r closest to $N = \sqrt{L/A_L}$. For the specific core shape considered in our case it results $A_L = 2470\,\text{nH} - 20/+30\%$. A total of $N = 36$ turns is thus required. By considering the possible variation of AL the realization of the component may lead to an inductance in the range [2.561, 4.161] mH. In order to check the validity of the design we have performed an experimental characterization of a prototype in the range 100–300 kHz by means of a Quadtech 7600 LCR meter (Figure 3).

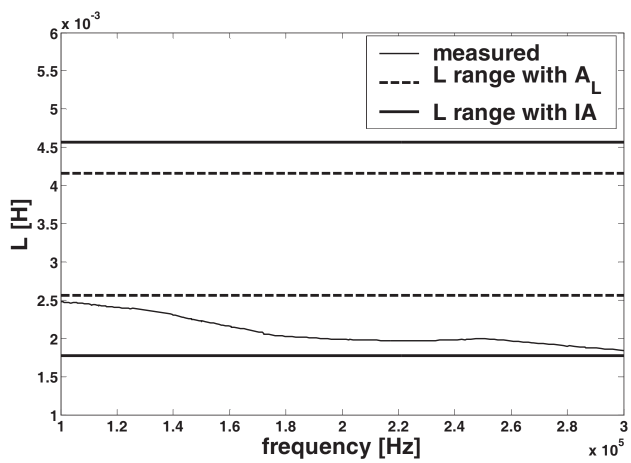

Figure 3: Measured inductance of the prototype and corresponding estimated ranges.

The results shown in Figure 3 imply that if we adopt a design approach based on the value of A_L given in the data-sheet we are not always guaranteed that the components actually belong to the estimated range. On the other side, if we perform an IA based analysis, taking into account the ranges on the geometric parameters in Table 1, we can achieve an interval which certainly includes the real value of the inductance. Moreover, with this approach we can consider also the uncertainty on the magnetic permeability of the selected material which, according to the manufacturer's data sheet, is $\mu_f = 1900 \pm 20\%$ @10 kHz for an induction $B < 0.1\,\mathrm{mT}$. In order to perform the IA based approach we refer to the simple associated lumped parameters circuit depicted in Figure 4, where:

$$\mathfrak{R}_a = \frac{A}{\mu_f S_a}, \quad \mathfrak{R}_e = \frac{F}{\mu_f S_e}, \quad \mathfrak{R}_f = \frac{F}{\mu_f S_f}$$

S_a, S_e and S_f are the different cross sections shown in Figure 2 and given by:

$$S_a = (B - F)C, \quad S_e = \pi \left(\frac{E}{2}\right)^2, \quad S_f = \int_0^{C/2} f(x)dx$$

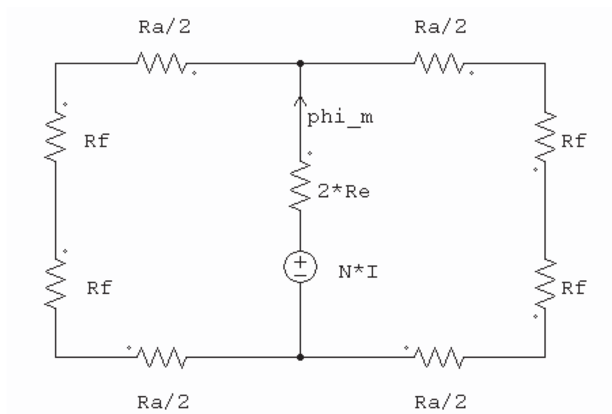

Figure 4: Electrical circuit associated to ETD magnetic structure.

In particular S_f is the area under the curve $f(x) = A/2 - \sqrt{(D^2 - 4) - x^2}$. Thus we have:

$$S_f = \int_0^{C/2} \left(\frac{A}{2} - \sqrt{\frac{D^2}{4} - x^2}\right) dx = \frac{1}{2}\left[\frac{AC}{2} - \left(\frac{D^2}{4}\arcsin\frac{C}{D} + \frac{C}{2}\sqrt{\frac{D^2}{4} - \frac{C^2}{4}}\right)\right] \tag{5}$$

The equivalent reluctance of the circuit of Figure 4 by using the expressions in terms of the geometric parameters is:

$$\mathfrak{R}_{eq} = \frac{1}{\mu_f}\left[\frac{8F}{C\left(2A - \sqrt{D^2 - C^2}\right) - D^2 \arcsin\frac{C}{D}} + \frac{A}{2(B-F)C} + \frac{8F}{\pi E^2}\right] \tag{6}$$

Therefore the reluctance is a function of the magnetic permeability and the 6 geometric parameters. If we consider for each one of such parameters p_i the uncertainty interval $P_i = [p_{i\,\min}, p_{i\,\max}]$ and apply the IA we obtain an inclusion interval for the equivalent reluctance. In particular, we have $\mathfrak{R}_{eq} \in [284.06, 728.74]\,\mathrm{mH}^{-1}$ and hence $L \in I_L = [1.778, 4.562]\,\mathrm{mH} = 3.17\,\mathrm{mH} \pm 44\%$. Such an interval, which contains all the results obtained experimentally as evidenced in Figure 3, is actually more reliable than that achieved by using the per unit turn inductance AL. Moreover, the interval which can be calculated for A_L from the values indicated on the producer's data sheet is included in that one obtainable through the equivalent reluctance:

$$A_L = [1.976, 3.211]\,\mathrm{mH} = \frac{1}{\mathfrak{R}_{eq}} \in [1.372, 3.520]\,\mathrm{mH}$$

b) non linear magnetic permeability

Let us now consider the C-shaped magnetic core of Figure 1 in which the ferromagnetic material is characterised by a non linear B-H relation given by [6]:

$$H(B) = 129.5B + 76.1Be^{1.26B^2} \tag{7}$$

We want to evaluate the inductance $L = f(N, \delta, h, l, \mu, p, q)$ corresponding to $N = 80$ turns in the hypothesis that the geometric parameters are characterised by uncertain values as reported in Table 2.

Table 2: Geometric parameters of the example b.

	$\boldsymbol{\delta}$ [mm]	**h** [mm]	**l** [mm]	**p** [mm]	**q** [mm]
nominal value and tolerance	2 ±15%	40±5%	30±5%	15±10%	10±10%
equivalent interval	[1.7, 2.3]	[38, 42]	[28.5, 31.5]	[13.5, 16.5]	[9.0, 11.0]

By applying with the typical simplifying hypothesis the Ampère equation to the curve $l_m \cup \delta$ in Figure 1 and using the continuity condition of the normal component of $\mathbf{B}$ in the gap we have:

$$Ni = \oint \underline{H} \cdot \underline{dl} = \int_{l_n} \left(129.5B + 76.1Be^{1.26B^2}\right) dl + \frac{1}{\mu_0}\int_{\delta} B_0 dl \cong \left[\left(129.5 + 76.1e^{1.26<B>^2}\right)\frac{l_m}{pq} + \frac{\delta}{pq\mu_0}\right]\phi \tag{8}$$

where $< B > pq = \varphi$, B_0 is the induction in the gap and $< B >$ is a mean value. Thus

$$Ni \cong [\Re(B) + \Re_0]\phi \tag{9}$$

where

$$\Re(B) = \left(129.5 + 76.1e^{1.26<B>^2}\right)\frac{l_m}{pq} \tag{10}$$

Now instead of considering the non linear behaviour, we can employ the inclusion property of the IA in order to furnish a linear relationship, given by an interval coefficient which, for all the values of $< B >$, includes the (10). We assume as the interval containing $< B >$ the interval obtainable from the material's data sheet $[0, B_{\max}] \in I\Re$. We get:

$$\Re(B) \in \left(129.5 + 76.1e^{1.26[0,B_{\max}]^2}\right)\frac{l_m}{pq} = \left[205.6, 129.5 + 76.1e^{1.26B_{\max}^2}\right]\frac{l_m}{pq} \tag{11}$$

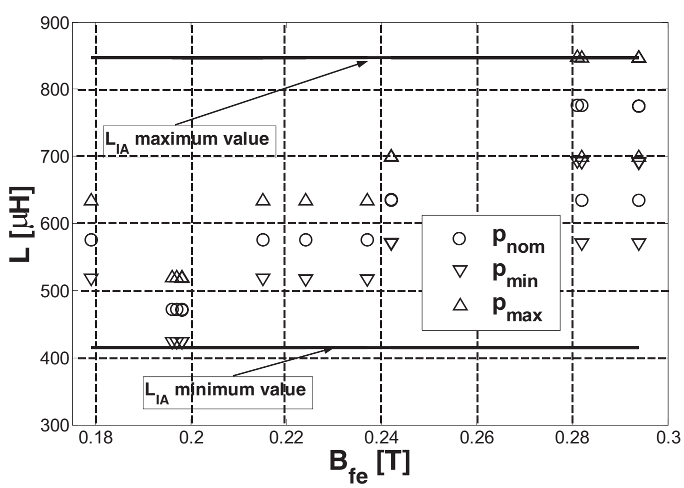

Figure 5: Inclusion of L in the case of a non linear B-H characteristics.

where $[205.6, 129.5 + 76.1e^{1.26B_{\max}^2}]$ is a constant and known interval. If for example $B_{\max} = 1$, from (11) we have $\Re(B) \in [205.6, 397.8]\frac{l_m}{pq}$ and the related inductance of the component of Figure 1 is thus enclosed in $I_L \in I\Re$:

$$I_L = \frac{N^2}{[205.6, 397.8]\frac{2[l_{\min},l_{\max}]+2[h_{\min},h_{\max}]-4[q_{\min},q_{\max}]-[\delta_{\min},\delta_{\max}]}{[p_{\min},p_{\max}][q_{\min},q_{\max}]}\frac{[\delta_{\min},\delta_{\max}]}{\mu_0[p_{\min},p_{\max}][q_{\min},q_{\max}]}} \tag{12}$$

where the min and max values for the parameters are obtained from the tolerances. The inductance of all possible realizations will be contained in the interval $I_L = [414.99, 847.49]$ µH= 631.24 µH $\pm$ 34.3%, as also confirmed by the results of a FEM based numerical Vertex Analysis [7] considering 2^5 different structures resultant to each possible combination of the 5 parameters. Such results are summarised in Figure 5.

4. CONCLUSION

In this paper an effective and reliable tool for evaluating inductance coefficients in presence of uncertain parameters in a straightforward form has been presented. The proposed approach allows to simply take into account the geometric tolerances and efficiently deal with the non linearity of the ferromagnetic materials. The effectiveness of the proposed approach has been tested in realistic cases for power electronics applications. The results can be easily extended to problems where also mutual inductance coefficients or derived quantities, such as the force in electromechanical actuators have to be evaluated.

ACKNOWLEDGMENT

This work has been carried out with the financial support of ex MURST 60% funds of the University of Salerno.

REFERENCES

1. Erickson, R. W. and D. Maksimovic, *Fundamentals of Power Electronics*, Kluwer, Norwell, MA, 2001.
2. McLyman, Wm. T., *Magnetic Core Selection for Transformers and Inductors: A user's guide to pratice and specification*, Kg Magnetics Inc., Idyllwild, California, USA, 1997.
3. McLyman, Wm. T., *Transformer and Inductor Design Handbook*, Third Edition, Kg Magnetics Inc., Idyllwild, California, USA, 2004.
4. Moore, R. E., *Interval Analysis*, Prentice Hall, Englewood Cliffs, NJ, 1969.
5. http://www.cs.utep.edu/interval-comp/
6. Spagnuolo, G., "Worst case tolerance design of magnetic devices by evolutionary algorithms," *IEEE Trans. on Magn.*, Vol. 39, No. 5, 2170–2178, Sep. 2003.
7. Femia, N., P. Lamberti, V. Mainardi, and G. Spagnuolo, "Selection criteria of closed-loop controllers for dc-dc voltage regulators based on nominal and tolerance design: Genetic algorithms and vertex analysis based optimization" *Proc. of IEEE ISIE'02*, Vol. 3, 1015–1020, L'Aquila, Italy, April 2002.

Balancing the Interference Probability between Systems for Sharing Frequency Spectrum

Taekjin Hwang[1], **Sanggee Kang**[2], **and Heonjin Hong**[1]

[1]ETRI, Korea
[2]Kunsan National University, Korea

Abstract— In order to share frequency spectrum, balancing the transmitting parameters, such as power, bandwidth, duty factors etc., is necessary for using the limited frequency resources efficiently. In this paper we study how to adjust transmitting parameters for sharing frequency bands in two cases. First we consider that a frequency band is already allocated to the specific communications. The second is the case of allocating new frequency bands to communication systems having interference mitigation techniques. For each case we investigate the conditions for sharing frequency bands and suggest a balancing factor for adjusting the interference effects between systems using different interference mitigation techniques.

1. INTRODUCTION

Many methods have been studied in order to use the limited frequency resources efficiently by means of improving the rate of data transmission and increasing the purity of the output spectrum of communication systems [1]. Recently how to advance the spectrum policy for the efficient use of frequency resources in the future was studied. According to the results of the study, we can improve the efficiency of using frequency resources though the competition rather than the regulation of using them [2].

Mobile communications was began with a long distance service such as WMAN, and now WPANs providing high or low rate data communication services according to its applications have been investigated. The trends in developing and researching WPANs will promote the appearance of many low power communication systems in the market for the time being. To realize ubiquitous sensor networks, we must use low power transceivers inevitably. Communication systems sharing frequency resources are necessary for using them efficiently. The techniques avoiding the interference between communication systems would be required as a basic function for sharing frequency bands in the future.

There are two methods for allocating frequency bands with considering a means of sharing frequency. One is to reallocate the assigned frequency for the specific communication system to a system having the interference avoiding techniques as a prerequisite condition. The other is to assign new frequency bands for several communication systems. There are many frequency sharing techniques, such as underlay, LBT (Listen before talk), and DAA (Detect and avoid), etc. Underlay technique uses the limited output power for reducing the interference effects to other systems. LBT and DAA can share frequency bands which are not used by other communication systems. Therefore LBT and DAA must be able to monitor the frequency bands in order to check whether other systems are occupying them or not.

The interference between transceivers can not avoid even though interference mitigation techniques are used in the transceivers. Therefore the amount of interference caused by a communication system must be investigated before the system will start a new service and the results of studying the interference effects will be reflected for making the specification of the system for sharing frequency bands. In this paper we study the condition for sharing frequency bands. First the method of sharing the frequency spectrum is studied when the frequency band is already allocated to the specific communication systems. Second we investigate the sharing condition of frequency bands when new frequency bands are allocated to communication systems having interference mitigation techniques.

2. FREQUENCY SHARING CONDITION

2.1. Sharing the Allocated Frequency Spectrum

In order to minimize the interference between systems, underlay, LBT or DAA technique must be used for sharing the frequency spectrum used by other systems. FH (Frequency Hopping) system and DS (Direct Spreading) system can be used for reducing the interference. The interference between systems can not avoid even though the interference mitigation techniques are used. Therefore the amount of interference caused by a communication system must be studied before the communication system is serviced. And the results of the interference study must be considered in making the specification of the system for sharing the frequency band occupied already by other systems. Even if the changing PHY will be required for sharing the frequency bands, the minimization of changing PHY is recommended.

Interference always exits among communication systems. In case of sharing the allocated frequency spectrum, the interference will be occurred among the previously existing systems and the interference between a new service and the previous one will be generated also. The amount of interference caused by communication systems is different. Therefore we can use the amount of interference generated by the system as a reference for considering whether the frequency bands can be shared or not. If the amount of interference generated by the new service is less than that by the previous system, then the new service can share the frequency bands with the previous one.

2.2. Sharing the New Frequency Spectrum

ISM bands are non-specified frequency bands. Therefore the frequency bands can be easily accessed by new communication systems. FCC part 15.247 describes FH and DS system as the frequency sharing techniques for minimizing interference [3]. In Europe, 860∼868 MHz and 2.4 GHz frequency bands are used for non-specified frequency bands and the frequency bands are specified for the required frequency sharing techniques in detail. ERC-REC 70-03 describes FH, LBT and DS system as interference avoiding techniques [4]. When comparing the specification of systems operated in non-specified frequency bands in the united state to that of in Europe, FCC's specification is rough than Europe. If we can make the sharing condition and the technical specification for sharing frequency bands then new systems easily use the frequency bands.

A transmitter should not emit the power if the transmitter does not generate interference. Communication systems using the same interference avoiding technique can easily share frequency bands because the transmitting condition, such as an output power, out-of band emission etc., can be fairly maintained between the systems. However we must find the balancing factor between communication systems using the different interference avoiding technique, for example between LBT and FH, FH and DS, etc. In this paper we consider LBT, FH and DS as an interference mitigation technique and we investigate how to balancing the interference between the above interference mitigation techniques.

3. SIMULATION OF INTERFERENCE EFFECTS

3.1. The Method of Simulation

We investigate the interference probability caused by a system to decide whether the system can share the frequency bands or not. In analyzing the interference, the system parameters of an interference transmitter, such as an output power, out of band emission, channel bandwidth and duty factor and etc. are considered and a receiver bandwidth, intermodulation response attenuation and single tone desensitization of a victim receiver are also included into the analysis. The channel characteristics of the environment surrounding the system and the proper scenarios are needed also. If C/(N+I),the ration of the carrier power to noise and interference power, of a victim receiver is lower than the required C/(N+I) then the victim receiver can not communicate because of the interference signal. The following is the simplified simulation procedure,

- Select the location of an interference transmitter and receiver
- Select the location of an victim transmitter and receiver
- Calculate the propagation loss between the interference transmitter and the victim receiver
- Calculate the interference power induced into the victim receiver including the interference power caused by an intermodulation response attenuation, single tone desensitization etc.
- Calculate C/(N+I) of the victim receiver.

3.2. Interference Simulation for Sharing the Alloca Ted Frequency Spectrum

Table 1 shows the interference simulation results between systems, and the system parameters for the simulation are listed in Table 2. When comparing the interference probability between RFID (Radio Frequency Identification) and Bluetooth, Bluetooth's interfering effects are high than that of RFID system itself. Therefore Bluetooth's transmitting parameters must be changed for sharing the frequency bands. And the interfering effects of RFID and DCP(Digital Cordless Phone) to Bluetooth are high than the interference effects of Bluetooth itself, so the transmitting parameters of RFID and DCP must be changed for sharing the frequency bands.

Table 1: Interference probability between systems.

		Victim transceiver							
		ZigBee(total)		RFID(total)		Bluetooth(total)		DCP(total)	
		Spur	Block	Spur	Block	Spur	Block	Spur	Block
Interferer	ZigBee	0.084		0.0001		0.02		0.057	
		0.078	0.069	0	0.0001	0.02	0	0.057	0
	RFID	0.051		0.02		0.018		0.046	
		0.016	0.044	0.0035	0.02	0.007	0.014	0.025	0.04
	Bluetooth	0.022		0.025		0.014		0.028	
		0.0092	0.02	0.011	0.022	0.008	0.007	0.02	0.023
	DCP	0.08		0.11		0.04		0.175	
		0.074	0.066	0.063	0.058	0.038	0.008	0.153	0.089

Table 2: System parameters for interference probability simulation.

Parameters	RFID		Zig Bee	DCP	Bluetooth
	Reader	Tag			
Channel spacing	200 kHz	200 kHz	600 kHz	2 MHz	1 MHz
Transmit power	1W	-10dBm	0 dBm	24 dBm(250mW)	10 dBm
Receiver bandwidth	200 kHz	200 kHz	600 kHz	1.78 MHz	1 MHz
Cell Radius	10 m	10 m	10 m	50 m	0.01 km
Antenna height	1.5 m	1.5 m	1.5 m	1.5 m	1.5 m
Antenna gain	6 dBi	2 dBi	0 dBi	0 dBi	0 dBi
Sensitivity	- 70 dBm	-	- 92 dBm	- 83 dBm	- 70 dBm
Receiver protection ratio (C/I)	9 dB	9 dB	15.2 dB	10 dB	11 dB
Receiver blocking	-35dBm @1MHz	-	adjacent : 0 dB alternative:30 dB	Refer to [5]	Refer to [6]
Intermodulation rejection	-	-	-	-	Refer to [6]

3.3. Interference Simulation for Sharing the New FR Equency Spectrum

The characteristics of an interfering transceiver and a victim transceiver are listed in Table 3. To find the balancing factor between the different interference avoiding techniques, we must simulate interference effects between systems which use the different frequency sharing techniques. Table 4 gives for system variety, the system bandwidth is listed in Table 4. The total bandwidth of 25 MHz is used for simulation. Table 4 shows that the bandwidths of 250 kHz and 500 kHz for FH and 500 kHz for LBT and DS are mainly considered.

The interference simulation of (FH, FH), (FH, LBT), (FH, DS), (LBT, FH), (LBT, LBT), (LBT, DS), (DS, FH), (DS, LBT), (DS, DS) are performed, where A is the interference system and B is the victim system. The simulation condition between (FH, LBT) and (FH, DS) is the same because of the same interfering mechanism. And the simulation condition of (LBT, LBT) equals (LBT, DS) and (DS, LBT) equals (DS, DS).

Figure 1 is the simulation results of (FH, FH) and (LBT, FH). Fig. 1 shows that the interference probability of FH1 (BW = 250 kHz) is lower than that of FH2 (BW = 500 kHz). The interference probability of LBT system having the BW of above 500 kHz is lower than that of FH. In Fig. 1, if we apply a balancing factor to LBT system rather than to FH, LBT applied a balancing factor has a little negative effect for communication because the interference probability of LBT without a balancing factor is not high than FH. However LBT could be more difficult in implementation when the number of systems operated in the same frequency band is increased. And FH system can be easily implemented than LBT system. Therefore the applying the balancing factor to LBT system is reasonable. Fig. 2 show that the simulation results of interference effects of FH, LBT and DS to FH. In Fig. 2 we can see that LBT and DS being applied by a balancing factor have low interference probability than FH. In this case we use the duty factor for balancing the transmitting condition.

Table 3: The interfering transceiver and victim transceiver's characteristics.

Parameters	Tx	Rx
Channel spacing	<Table 4>	<Table 4>
Transmit power	10 dBm	-
Receiver bandwidth	-	<Table 4>
Cell Radius	10 m	10 m
Antenna height	1.5 m	1.5 m
Antenna gain	0 dBi	0 dBi
Active interferer number	1	-
Sensitivity	-	- 83 dBm
Out of band emission	-36 dBm/1MHz	-
Receiver protection ratio(C/I)	-	25 dB

Table 4: System bandwidth for calculation the balancing factor.

		Case1	Case2	Case3	Case4	Case5	Case6
F	250kHz	25kHz	125kHz	250kHz	2.5MHz	6.25MHz	25MHz
H	500kHz	50kHz	250kHz	500kHz	5MHz	12.5MHz	-
LBT(500kHz)		50kHz	250kHz	500kHz	5MHz	12.5MHz	-
DS(500kHz)		50kHz	250kHz	500kHz	5MHz	12.5MHz	-

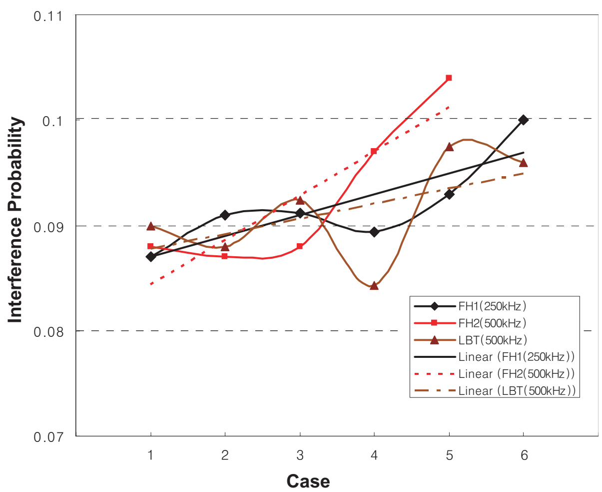

Figure 1: Simulation results of interference probability of (FH, FH) and (LBT, FH).

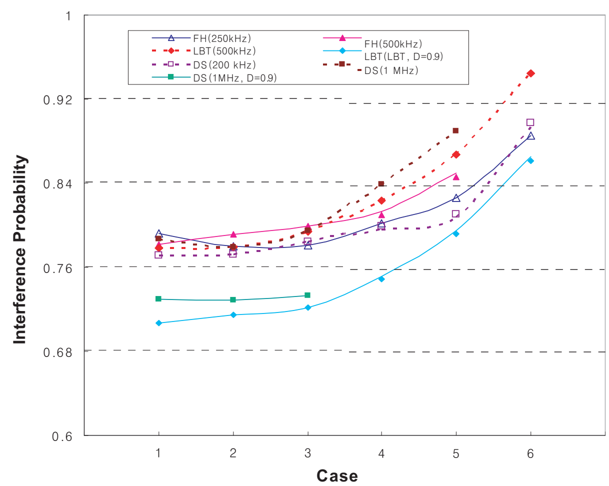

Figure 2: Simulation results of interference effects of FH, LBT and DS to FH systems including balancing factor.

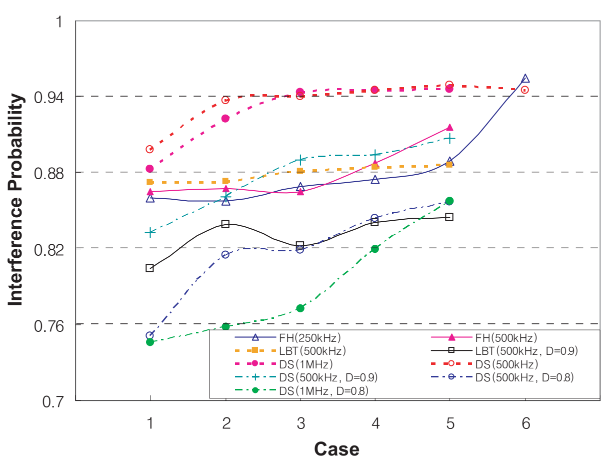

Figure 3: Simulation results of interference effects of FH, LBT and DS to LBT systems including balancing factor.

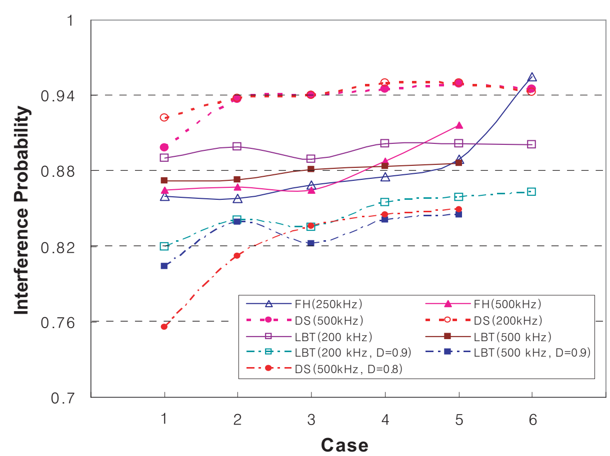

Figure 4: Simulation results of interference effects of FH, LBT and DS to DS systems including balancing factor.

And the duty factor of 0.9 is used. Fig. 3 shows that the simulation results of interference effects of FH, LBT and DS to LBT. And the bandwidths of 500 kHz and 1 MHz are considered. From Fig. 3 we know that if the victim receiver's bandwidth is the same or larger than the interferer's bandwidth then the interference effects are saturated. In Fig. 3 we use duty factor of 0.9 for LBT and 0.8 for DS for balancing the transmitting condition. Fig. 4 shows that the simulation results of interference effects of FH, LBT and DS to DS. As in the case of Fig. 3 we use the duty factor of

0.9 for LBT and 0.8 for DS in Fig. 4.

4. CONCLUSION

In this paper we study the condition for sharing frequency bands in two cases. One is the case that the frequency band is already allocated to the specific communication. The other is the case of allocating the new frequency bands to communication systems having interference avoiding techniques. From the simulation results we know that the balancing factor of 0.9 of FH system's duty factor for LBT systems and 0.8 for DS systems is needed for balancing the transmission characteristics.

REFERENCES

1. Haykin, S., *Communication Systems*, 3rd ed., 1994.
2. Spectrum Policy Task Force report, ET Docket No. 02-135, Nov. 2002.
3. IEEE Std 802.15.4, "IEEE standard for information technology — Telecommunications and information exchange between systems — Local and metropolitan area networks — Specification requirements — Part 15.4 : Wireless Medium Access Control (MAC) and Physical Layer (PHY) specifications for low-rate Wireless Personal Area Networks (WPANs)," 2003.
4. ETSI EN 302 208-1 V1.1.1, "Electromagnetic compatibility and Radio spectrum Matters(ERM); Radio frequency identification equipment operating in the band 865 MHz to 868 MHz with power levels up to 2 W; Part 1: Technical requirements and methods of measurement," Sep. 2004.
5. IEEE Std 802.15.1, "IEEE Standard for information technology — Telecommunications and information exchange between systems — Local and metropolitan area networks — Specification requirements — Part 15.1: Wireless Medium Access Control(MAC) and Physical Layer(PHY) specifications for low-rate Wireless Personal Area Networks(WPANs)," June 2002.

Impulse Response of Seafloor Hydrocarbon Reservoir Model

Jingtian Tang and Weibin Luo
School of Info-physics and Geomatics Engineering, Central South University, China

Abstract— The step response and impulse response to horizontal electric dipole (HED) source in three typical models such as uniform earth half space, marine double half space and four-layer reservoir-bearing seafloor models were computed, through the use of Gaver-Stehfest inverse Laplace transforms and numerical integration Hankel transforms. And concept of transient impulse time was proposed. It was confirmed that the transient impulse time of the conductive medium to HED can directly indicate the conductivity of the earth. Inline dipole-dipole transient EM sounds with geometry, and it is suitable for surveying with multi offsets. For the high resolution to thin resistive subsurface formations, this method can be applied for hydrocarbons explorations on land, also in marine.

1. INTRODUCTION

Although marine or land 3-D seismic has highest resolution for identifying the possible structure of hydrocarbon reservoir, it cannot make sure whether the structure is filled with conductive water or economic resistive hydrocarbon. Using electromagnetic (EM) method to explore the hydrocarbon reservoir has the good preconditions of physical property, because the electrical resistivity of the subsurface formations is known strongly related to the pore fluids and saturation. The electrical resistivity variation can be detected when the fluids contained in the reservoirs changed from water to hydrocarbon. The method of marine controlled source electromagnetic (mCSEM) has a high ability to indicate the resistive hydrocarbon reservoir [2–4, 1]. At present there are several methods have been developed maturely for hydrocarbon exploration such as seabed logging (SBL) and multi-channel transient electromagnetic (MTEM). The former works in frequency domain with the latter in time domain [3, 4] (Hobbs and Wright, et al., 2005).

Studies in many literature have shown that the EM field travels in conductive mediums obeyed the diffusion equations [4, 8, 1]. The EM field excited by a horizontal electric dipole (HED) or a horizontal magnetic dipole (HMD) travels in sea water and seafloor strata at different velocities. The HED can generate both galvanic effects currents and inductive effects currents, so it is sensitive to thin resistive layers, and inline dipole-dipole configuration is the main surveying system, and works with multi offsets. The electromagnetic response of resistive hydrocarbon reservoirs measured at seafloor is a frequency dependent function of source-receiver offsets and seafloor conductivity [5, 6, 4, 1]. Multi receiver dipoles and transmitter dipoles can be laid in line with different offsets, and source signal can be a wideband low frequency due to electromagnetic (EM) attenuation in conductive sea water. According to the different diffusion velocity of the EM energy in the sea water and in the seafloor strata, the impulse response of electric field or magnetic field measured at some offsets would have two separated arrive peak time. In marine, the first peak time can be used to map the seafloor strata electricity property distribution.

In this paper we computed the impulse response of uniform half space, marine double half space and four-layer reservoir-bearing seafloor earth models to horizontal electric dipole source, so that it is helpful to choose the measure methods, measure parameters and explaining methods to the high resolution exploring hydrocarbon reservoir.

2. METHOD

The step response and impulse response to the horizontal electric dipole source in the uniform half space, marine double half space and reservoir-bearing seafloor models have analytic expressions in frequency domain [5, 4, 9]. Firstly to get time domain step response from the frequency analytical form or numerical solution through the use of Gaver-Stehfest inverse Laplace transforms and numerical Hankel transform, and then to get the earth impulse response through differential of step response. The inline electrical dipole-dipole configuration is selected.

3. NUMERICAL RESULTS

3.1. Transient Response of the Homogeneous Earth Model

In the inline electrical dipole-dipole configuration, the electric field radial horizontal component of frequency domain on homogeneous half space earth model is listed:

$$E(\omega)\,|_{\varphi=0^\circ} = \frac{P_E}{2\pi\sigma_1 r^3}\left[1+(1+k_1 r)\,e^{-k_1 r}\right] \tag{1}$$

To the later field (frequency equals to 0), it is:

$$E(0)\,|_{\varphi=0^\circ} = \frac{P_E}{\pi\sigma_1 r^3} \tag{2}$$

where $P_E = P_{E0}e^{-i\omega t}$ is electric dipole polar moment, r is transmitter-receiver (T-R) separation, σ_1 is the homogeneous earth conductivity, and k_1 is the homogeneous earth wave number with $k_1^2 = i\omega\mu_0\sigma_1$. The normalization of later electric field is as following:

$$\frac{E(\omega)}{E(0)}\,|_{\varphi=0^\circ} = \frac{1}{2}\left[1+(1+k_1 r)\,e^{-k_1 r}\right] \tag{3}$$

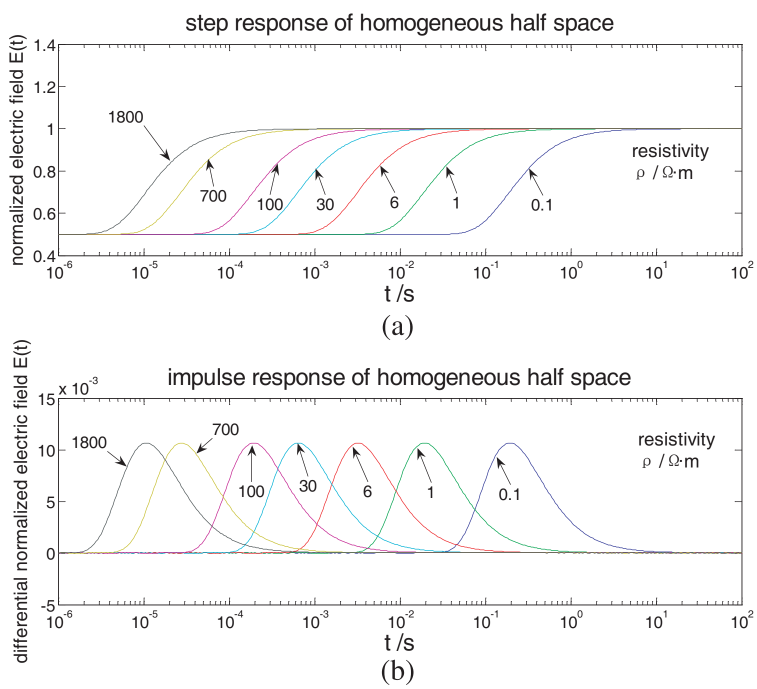

Figure 1: Step response (a) and impulse response (b) of homogenous half space with different resistivity.

With the Equation (3) divided by Laplace variation $s = i\omega$, and then by Gaver-Stehfest inverse Laplace transforms, we can get the step response of homogeneous earth as following:

$$e(t) = \frac{\ln 2}{t}\sum_{i=1}^{N} K_i \frac{E(\rho_n, h_n, s_i)}{s_i} \tag{4}$$

The parameter K_i is the N number G-S inverse conversion coefficient during the computation $N = 14$, with $s_i = \frac{\ln 2}{t}i, (i = 1, 2, \ldots, N)$ to replace $s = i\omega$ and $E(\rho_n, h_n, s_i)$ is electrical field response in frequency domain, ρ_n, h_n is the layer coefficient. Fig. 1 is the result of step response in (a) and impulse response in (b) of homogeneous earth with different resistivity, the T-R space $r = 300$ m, earth resistivity is 0.1 Ω·m, 1 Ω·m, 6 Ω·m, 30 Ω·m, 100 Ω·m, 700 Ω·m, 1800 Ω·m, respectively. In the computation, there is no consideration of EM energy of the air transmission. It is shown that the impulse response peak value will appear ahead of time with the resistivity increasing, we give the reach time of the impulse response peak a name as transient impulse time which changes with the resistivity of earth.

3.2. Transient Response of Double Half Space Model

When the conductivity of sea water is much larger than the conductivity of the seafloor strata, the analytical form of radial electric field response to homogeneous double half space model in frequency domain in inline configure is as following [5]:

$$E(s)\Big|_{\varphi=0^\circ} = \frac{j(s)}{2\pi\sigma_0 r^3}\left[(\sqrt{\tau_0 s}+1)e^{-\sqrt{\tau_0 s}} + (\tau_1 s + \sqrt{\tau_0 s}+1)e^{-\sqrt{\tau_0 s}}\right] \tag{5}$$

where parameter $\tau_i = r^2\mu_0\sigma_i$ is the EM energy diffusion time coefficient of the sea water or seafloor strata, $s = i\omega$ is the Laplace variable, r is T-R space, σ_0 is the conductivity of sea water and $j(s) = P_{\mathrm{E}0}e^{-st}$ is the electric dipole polar moment. The normalization of the later electric field is as following:

$$\frac{E(s)}{E(0)}\,|_{\varphi=0^\circ} = \frac{1}{2}\left[(\sqrt{\tau_0 s}+1)e^{-\sqrt{\tau_0 s}} + (\tau_1 s + \sqrt{\tau_0 s}+1)e^{-\sqrt{\tau_1 s}}\right] \tag{6}$$

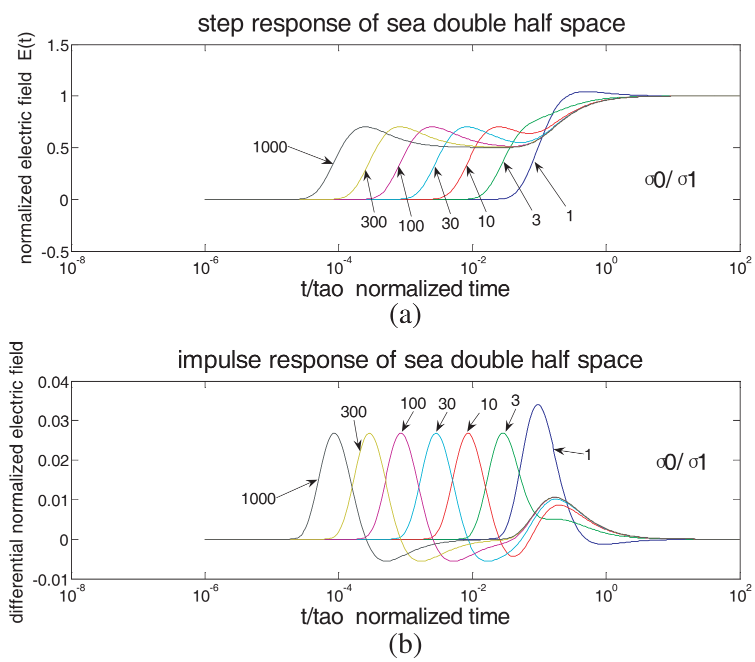

Figure 2: Transient response of double half space with different conductivity ($\sigma_0/\sigma_1 \geq 1$).

In Fig. 2 we have computed the step response (a) and impulse response (b) with offset $r = 500\,\mathrm{m}$, when the ratio of σ_0/σ_1 is 1, 3, 10, 30, 100, 300, 1000, respectively. The impulse response has two peak reach time, the first peak indicates the EM energy travel through the resistive seafloor reaches receiver firstly, which is related to the seafloor conductivity. The two distinct impulse peak separation in time is increased with the conductivity contrast between sea water and seafloor crust.

In Fig. 3 we have computed the EM transient response of homogeneous double half space model when the seawater conductivity is $3.2\,\mathrm{S/m}$, and the seafloor strata conductivity is less 300 times than seawater conductivity. The first peak value in the figure designates the transient impulse time when the EM energy travels through the seafloor strata; the second smaller peak value designates the transient impulse time when the EM energy travels through the seawater with high conductivity. This fact explains that the transient impulse time is the function of offsets, and it will be increasing with the offsets increasing.

3.3. Transient Response of the Marine Bedded Formation Model

Suppose the thickness of layers is $d1, d2, d3, \ldots, dN-1$, respectively and the conductivity of layers is $\sigma_1, \sigma_2, \ldots, \sigma_N$, respectively, $d0$, $\sigma 0$ is the depth and conductivity of seawater, $\mu 0$ is the magnetic permeability, and r is the transmitter-receiver separation. Edwards (2005) has given the radial EM response of horizontal electric dipole source as follows:

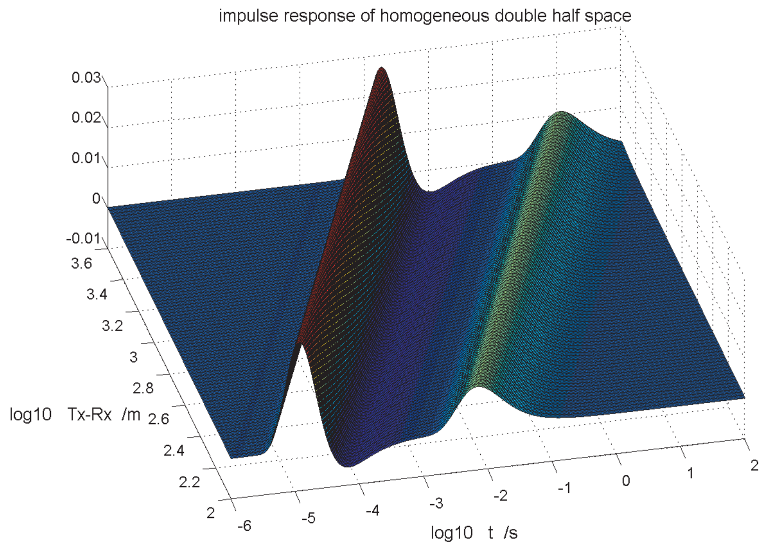

Figure 3: Transient response of two half space with different offsets ($\sigma_0/\sigma_1 = 300$).

When the initial condition is zero, the Laplace transforms ($s = i\omega$) of the receiver measured electric field is as following:

$$E(s) = \frac{j(s)}{2\pi}\left[F(s) + G(s)\right] \tag{7}$$

where $j(s)$ is electric dipole polar moment of electric dipole length ΔL, the current step on with current is I (Ampere) at $t = 0$, and the Laplace transforms of the dipole moment as follows:

$$j(s) = \frac{I\Delta L}{s} \tag{8}$$

To axial dipole, $F(s)$ and $G(s)$ are Hankel transforms:

$$F(s) = -\int_0^\infty \frac{Y_0 Y_1}{Y_0 + Y_1}\lambda J_1'(\lambda r)d\lambda \tag{9}$$

And

$$G(s) = -(s/r)\int_0^\infty \frac{Q_0 Q_1}{Q_0 + Q_1}J_1(\lambda r)d\lambda \tag{10}$$

where J_1 is the first order Bessel function in first class, and λ is the Hankel integration variable, and in the equations:

$$Y_0 = \frac{\theta_0}{\sigma_0}\left[\frac{\sigma_0 u_a + s\varepsilon_0\theta_0 tanh(\theta_0 d_0)}{s\varepsilon_0\theta_0 + \sigma_0 u_a tanh(\theta_0 d_0)}\right] \tag{11}$$

And

$$Q_0 = \frac{\mu_0}{\theta_0}\left[\frac{\theta_0 + u_a tanh(\theta_0 d_0)}{u_a + \theta_0 tanh(\theta_0 d_0)}\right] \tag{12}$$

where $\theta_0^2 = \lambda^2 + s\mu\sigma_0$ is the wave number of seawater, $u_a^2 \approx \lambda^2$ is the wave number of air, and Y_1, Q_1 are layers' parameters of seafloor, respectively. Recursion according to following equation:

$$Y_i = \frac{\theta_i}{\sigma_i}\left[\frac{\sigma_i Y_{i+1} + \theta_i \tanh(\theta_i d_i)}{\theta_i + \sigma_i Y_{i+1}\tanh(\theta_i d_i)}\right] \tag{13}$$

And

$$Q_i = \frac{\mu_0}{\theta_i}\left[\frac{\theta_i Q_{i+1} + \mu_0 \tanh(\theta_i d_i)}{\mu_0 + \theta_i Q_{i+1}\tanh(\theta_i d_i)}\right] \tag{14}$$

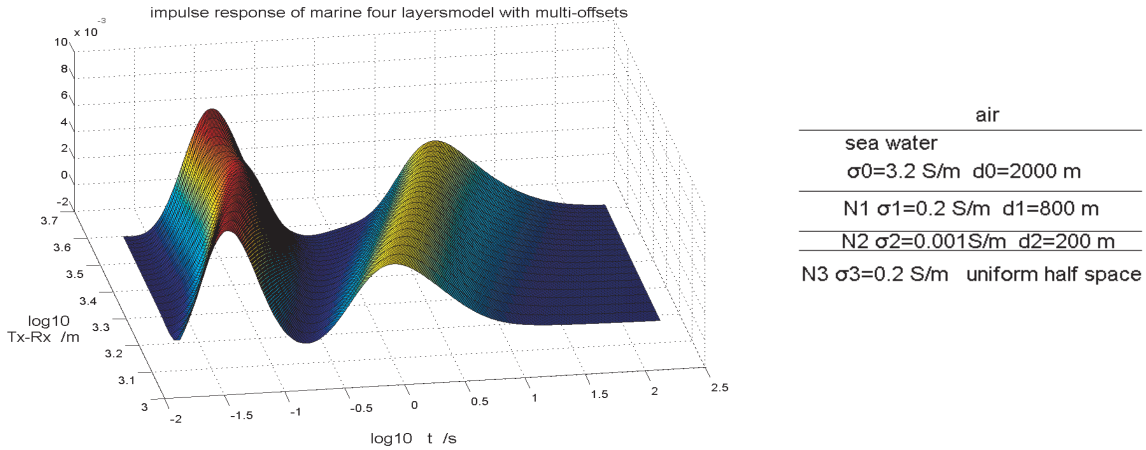

(a) (b)

Figure 4: Transient response in (a) of four-layer model in (b) with different T-R space (T-R space r is range from 1200 m to 3200 m).

where $\theta_i^2 = \lambda^2 + s\mu\sigma_i$, $Y_N = \theta_N/\sigma_N$ and $Q_N = \mu_0/\theta_N$. If the depth of seawater is more than the T-R space of r, it is simplified as $Y_0 = \theta_0/\sigma_0$ and $Q_0 = \mu_0/\theta_0$; and if the seafloor strata is homogeneous within the T-R space r, it is simplified as $Y_1 = \theta_1/\sigma_1$ and $Q_1 = \mu_0/\theta_1$.

To get the impulse response of layered reservoir-bearing seafloor model, we need to compute the Hankel transforms in Equations (9) and (10) like form in Equation (15). This paper adopts the direct computation numerical integration method to compute the Hankel transform, and the kernel function is dealed with subtracting the homogeneous double half space kernel function, and then use the integration result plus the homogeneous double half space analytical solution.

$$f(r, P) = \int_0^\infty K(\lambda, P) J_n(\lambda r) d\lambda \tag{15}$$

In Fig. 4(a) we have shown the impulse response computation results of multi T-R space of the model in Fig. 4(b) with the depth of seawater is $d0 = 2000$ m, and resistive N2 layer is interbedded between more conductive layers N1 and N3, the T-R space r changes from 1200 m to 3200 m, interval is 100 m. During the computation we use the logarithm of both time and T-R space. It is clearly to find that the first impulse peak time changed at appropriated offsets with resistive hydrocarbon present. The existence of resistive structure largely influence the first transient impulse peak time which travels through the seafloor. It is also suggested that surveying with multi-offsets can detect thin resistive layer.

4. CONCLUSION

The numerical computation results showed that impulse response transient time of earth system can indicates the electrical property of the earth. Electromagnetic attenuation in seawater is the function of both frequency and T-R space, and we should adopt the multi offsets electric dipole-dipole survey system and choose the wide frequency band signal source which we can measure the biggest impulse response of resistive hydrocarbon in both appropriated frequency and offsets. Moving the set array can complete the profile measurement and sounding measurement. And it has high resolution to the thin resistive subsurface formations, therefore this method can be applied for hydrocarbons explorations on land, also in marine.

REFERENCES

1. Um, E. S. and D. L. Alumbaugh, "On the physics of the marine controlled-source electromagnetic method," *Geophysics*, Vol. 72, No. 2, WA13–WA26, 2007.
2. Constable, S. and C. J. Weiss, "Mapping thin resistors and hydrocarbons with marine EM methods: Insights from 1D modeling," *Geophysics*, Vol. 72, No. 2, G43–G51, 2006.
3. Constable, S. and L. J. Srnka, "An introduction to marine controlled-source electromagnetic methods for hydrocarbon exploration," *Geophysics*, Vol. 72, No. 2, WA3–WA12, 2007.

4. Edwards, N., "Marine controlled source electromagnetics: Principles, methodologies, future commercial applications," *Surveys in Geophysics*, No. 26, 675–700, 2005.
5. Edwards, R. N. and A. D. Chave, "A transient electric dipole-dipole method for mapping the conductivity of the sea floor," *Geophysics*, Vol. 51, No. 4, 984–987,1986.
6. Edwards, R. N., "On the resource evaluation of marine gas hydrate deposits using sea-floor transient electric dipole-dipole methods," *Geophysics*, Vol. 62, No. 1, 63–74, 1997.
7. Cheesman, S. J., R. N. Edwards, and A. D. Chave, "On the theory of sea-floor conductivity mapping using transient electromagnetic systems," *Geophysics*, Vol. 52, No. 2, 204–217, 1987.
8. MacGregor, L. and M. Sinha, "Use of marine controlled-source electromagnetic sounding for sub-basalt exploration," *Geophysical Prospecting*, No. 48, 1091–1106, 2000.
9. Kaufman, A. A. and G. V. Keller, *Electromagnetic Sounding in Frequency Domain and Time Domain*, Geology Press, Beijing, 1987 (in Chinese).

Generalized Approach for Phase Interferometric Measurements of Electromagnetic Field

Jan Zela, Karel Hoffmann, and Premysl Hudec
Department of Electromagnetic Field, Czech Technical University
Technicka 2, 166 27 Prague 6, Czech Republic

Abstract— A new generalized approach for microwave phase interferometric measurement of electromagnetic field using an antenna matrix (AM) was developed. The approach allows correction of most significant measurement errors caused by mutual couplings of closely spaced antenna elements. It is based on vector measurements of the AM designed for the frequency 2.60 GHz and Matlab simulations.

1. INTRODUCTION

Microwave phase interferometry has a long history since 1950, when the first microwave hologram was created at the Bell laboratories. Now, it is being used in a number of applications in industrial and medical areas like antenna testing, [1], testing of large civil mechanical and aerospace structures, [2], medical applications, [3], location systems, [4], etc. Different systems were designed in frequency ranges from units of GHz up to mm wavelengths, [5]. From the measurement point of view, all these applications need to determine either only amplitude, or amplitude and phase of electrical intensity of an electromagnetic field distribution in a certain plane, area or even space. The measurements can be realized using some form of a single probe mechanically scanning system, [2, 5], using a number of switched transmitting and receiving antennas in tomography applications, [3], or using some form of AMs, sometimes called microwave cameras, [6]. The last solution has a great advantage in a possibility of fast real time measurements.

A great effort has been devoted to development of reconstruction algorithms for imaging of measured objects. Surprisingly, measurement errors and proper calibration attracted only a minor if any attention. This problem is important namely in the case of measurement systems using multiple antennas. In order to obtain a good resolution of the measured field, small distances between individual antennas compared to wavelength are required. However, these small distances cause mutual coupling between antennas, which results in systematic measurement errors and smaller attainable dynamics in measured data. Some recommendation can be found in [7]. For dipoles shorter than $0.1\lambda_0$ and spacing between dipoles greater than three times the dipole length, the mutual coupling between dipoles can be neglected. If these conditions are not satisfied, some form of mutual couplings occurs. For scalar interferometric measurement systems there is probably no better solution than that proposed in [7]. Vector measurements, however, offer other possibilities.

The purpose of this paper is to analyze the problem, to develop an error model and to suggest a new calibration and correction method for vector measurements using AMs with a non negligible coupling between individual antennas.

2. ERROR MODEL

An experimental arrangement for an interferometric measurement consists of one or more transmitting antennas and receiving antennas placed in a certain plane, area or space. The electromagnetic wave from at least one transmitting antenna illuminates the measured object (MO). The transmitted wave is generally reflected, scattered, diffracted or passes through the MO dragging along some information about properties of the MO. Consequently, it interferes with a reference wave not affected by the MO or it interferes with itself creating in both cases a space standing electromagnetic wave. This standing wave is sampled by the AM. Fig. 1 shows an example of an arrangement for measurement of deformations in civil engineering.

In an ideal case, the receiving antennas measure the interfering field only. In case of a real AM some mutual coupling between neighbouring antennas spaced a fraction of the wavelength occurs. The coupling can significantly influence measured data namely in the vicinity of a minimum of the standing wave which may result in high measurement errors. It is the case of interferometric measurements namely.

A level of mutual coupling in a AM was studied experimentally. An AM composed of SMD antennas for WiFi applications was designed and realized, see Fig. 2. Individual dipole antennas

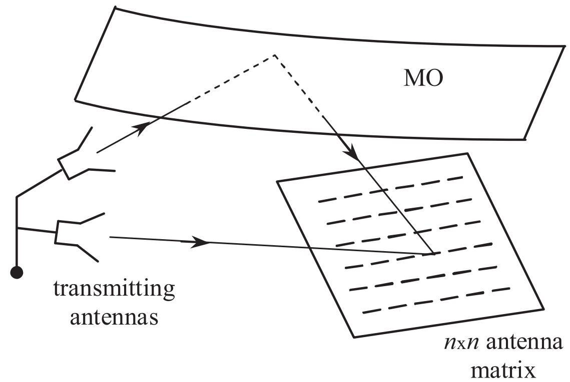

Figure 1: The arrangement for deformation measurements.

were mechanically short but electrically half wavelength long working on frequency 2.6 GHz. The antennas were spaced 27 mm apart, which corresponds to 0.23 times the wavelength. Fig. 2 shows also the coupling factor between individual closest adjacent antennas measured by Agilent PNA E8364A vector network analyser (VNA). The coupling between more spaced antennas was not significant.

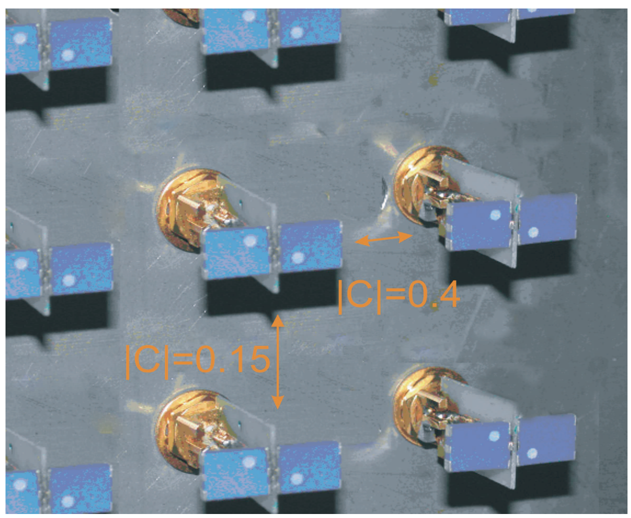

Figure 2: A part of the realized antenna matrix with measured coupling coefficients between two adjacent antennas.

The measured values of coupling factors were used for further simulation of a measurement arrangement. Let us study a case of an AM with 8 rows and 8 columns with 64 antennas. The flow-graph corresponding to 5 neighbouring antennas inside the matrix is shown in Fig. 3. Fig. 4 explains numbering of ports. Port number 65 is a transmitting antenna. $S_{i,65}$ represents a transmission scattering parameter giving information about the intensity of electromagnetic field in the place of the i-th antenna. $S_{i,i}$ represents a reflection of the antenna. 64 antennas are supposed to be step by step switched to a measurement port of a VNA by means of electronic switches. Γ_i correspond to reflection coefficients of individual switches. It can be expected approximately $|\Gamma_i| \leq 0.25$ for Hittite HMC321 switches for example. Further s-parameters such as $S_{i-1,i}$ represent mutual coupling of neighbouring antennas. Mutual coupling influences measured scattering parameters. $S^M_{i,65}$ instead of $S_{i,65}$ is measured then.

For the measured $S^M_{i,65}$ it can be derived

$$S^M_{i,65} = S_{i,65} + \frac{S_{i-1,i}S_{i-1,65}\Gamma_{i-1}}{1 - S_{i-1,i-1}\Gamma_{i-1}} + \frac{S_{i+1,i}S_{i+1,65}\Gamma_{i+1}}{1 - S_{i+1,i+1}\Gamma_{i+1}} + \frac{S_{i-8,i}S_{i-8,65}\Gamma_{i-8}}{1 - S_{i-8,i-8}\Gamma_{i-8}} + \frac{S_{i+8,i}S_{i+8,65}\Gamma_{i+8}}{1 - S_{i+8,i+8}\Gamma_{i+8}} \quad (1)$$

Simple $S_{i,65}$ measurement error simulations in Matlab environment were made. Two interfering electromagnetic plane waves were supposed in simulations. Mutual angle of interfering plane waves

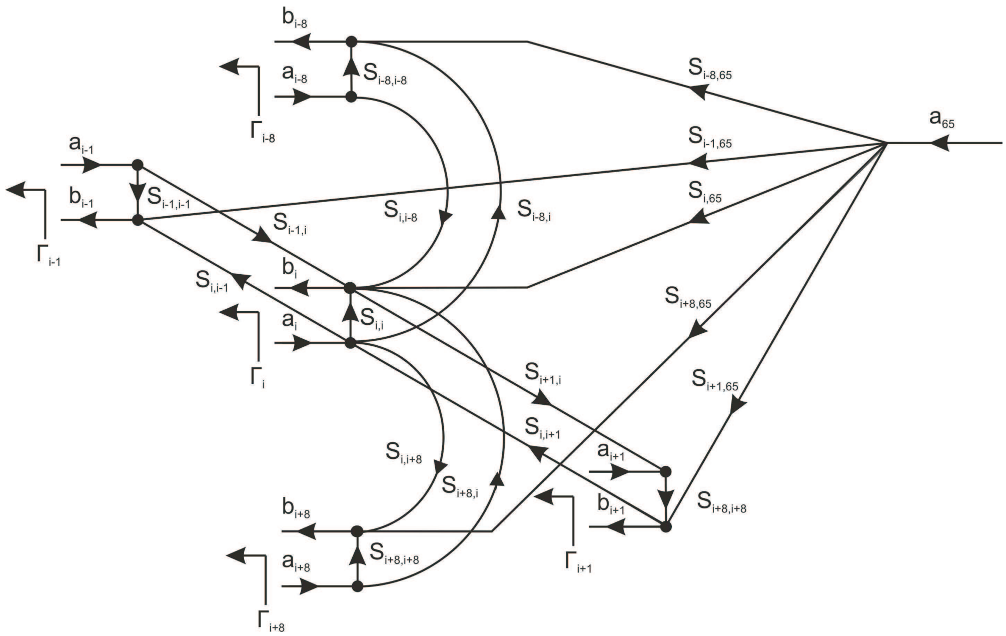

Figure 3: Flow-graph-coupling effect between adjacent antennas.

was 45 degrees. Measurements of corresponding space standing wave distribution by means of studied AM were simulated. Main parameters of simulations are in Tab. 1. Let us assume for simplicity that angles of reflection coefficients Γ of all 64 switch are identical and equal to zero. Then measurement errors as differences between $S^M_{i,65}$ and $S_{i,65}$ can be simulated. Fig. 5 shows amplitude errors and Fig. 6 shows phase errors.

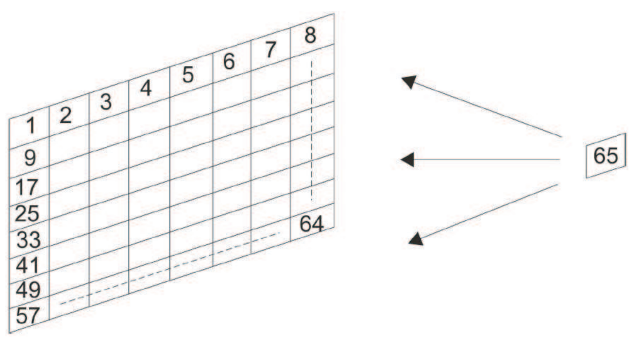

Figure 4: Antenna matrix 8 × 8-port numbering.

Table 1: Simulation Parameters.

Amplitude of coupling coefficient between adjacent antennas in an axial directions	0.4
Amplitude of coupling coefficient between adjacent antennas in a transversal directions	0.15
Amplitude of reflection coefficient of antennas	0.1
Amplitude of reflection coefficient of switches	0.25
Span between centers of adjacent antennas	29 mm
Frequency	2.60 GHz
Mutual angle of interfering plane waves	45 deg

A simulation of space standing wave distribution of intensity of electromagnetic field along rows of the AM described by $|S_{i,65}|$ can be seen on Fig. 7. While in an ideal case of an AM with no coupling between adjacent antennas $|S_{i,\,65}|$ distribution is sampled exactly mutual couplings result in significant discrepancy between measured $|S^M_{i,\,65}|$ and correct distribution.

In general phases of reflection coefficient of individual switches can be various. Therefore random phases in simulations were studied too. Fig. 8 shows significant increase of $S_{i,\,65}$ measurement errors in this case.

These simulations show that mutual coupling between adjacent antennas in an AM can have dramatic influence on accuracy of measurements. Therefore a new general approach to measurements of electromagnetic field space distribution by means of AM was designed. A proper calibration and correction measurement method can be applied.

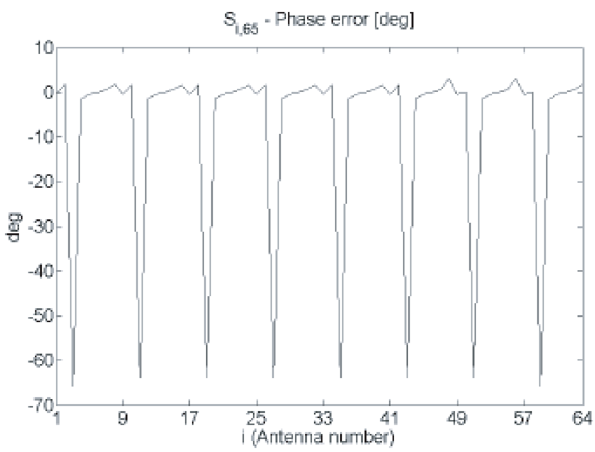

Figure 5: Simulated $S_{i,65}$ phase errors-angles of the reflection coefficients of each channel of the 1 to 64 switch are identical and are equal to zero.

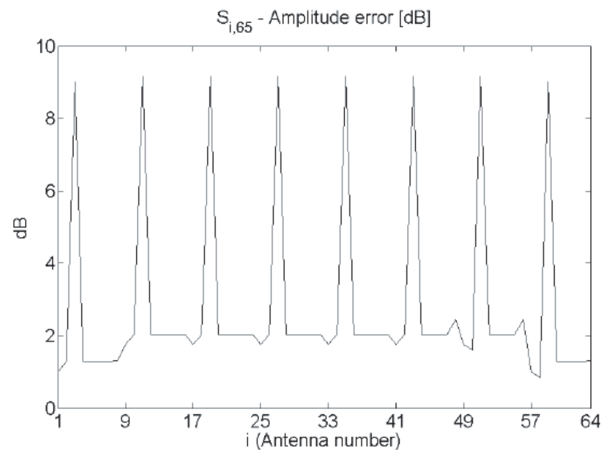

Figure 6: Simulated $S_{i,65}$ amplitude errors-angles of the reflection coefficients of each channel of the 1 to 64 switch are identical and are equal to zero.

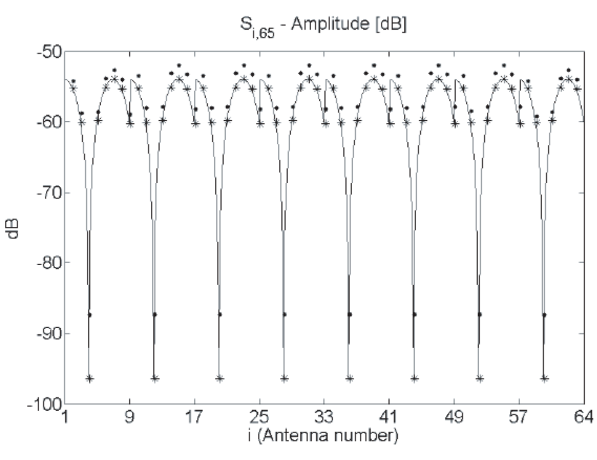

Figure 7: Ideal distribution of $|S_{i,65}|$ solid line, $|S_{i,65}|$ sampled by the AM with no coupling between adjacent antennas (stars), $|S_{i,65}|$ sampled by the AM with coupling between adjacent antennas (circles).

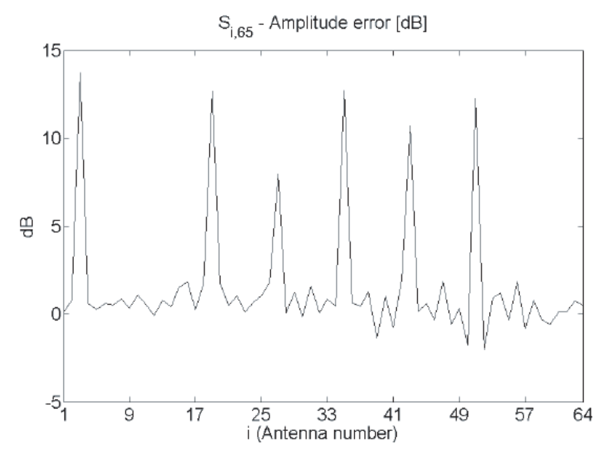

Figure 8: Simulated $|S_{i,65}|$ measurement errors-angles of reflection coefficients of individual switches are different (randomly generated).

3. GENERALIZED APPROACH

No matter how the arrangement for an interferometric vector measurement looks like, in can be considered as an n-port, see Fig. 9. $n-1$ ports belong to AM connectors, the nth port corresponds to the illuminating antenna or antennas.

The situation can be described by an s-parameter matrix (2). In case of an ideal AM with no coupling between antennas $S_{i,j} = 0$ for $i = 1, \ldots, n-1$ and $j = 1, \ldots, n-1$. The s-parameters $S_{i,j}$ for $i = 1, \ldots, n-1$ and $j = n$ can be simply determined by a calibration with a planar or

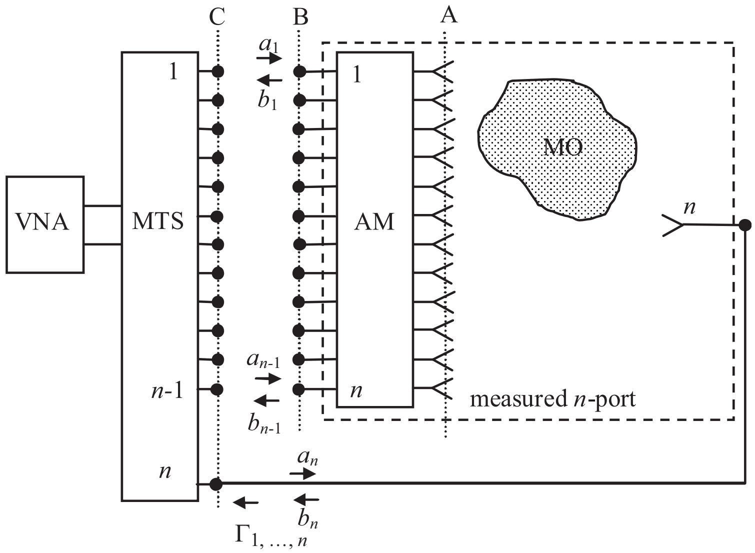

Figure 9: Generalized scheme of the interferometric problem.

semi-planar

$$\begin{bmatrix} b_1 \\ b_2 \\ \cdot \\ \cdot \\ \cdot \\ \cdot \\ b_{n-1} \\ b_n \end{bmatrix} = \begin{bmatrix} S_{11} & S_{12} & \cdot & \cdot & \cdot & \cdot & S_{1,n-1} & S_{1,n} \\ S_{21} & \cdot & \cdot & \cdot & \cdot & \cdot & \cdot & \cdot \\ \cdot & \cdot & \cdot & \cdot & \cdot & \cdot & \cdot & \cdot \\ \cdot & \cdot & \cdot & \cdot & \cdot & \cdot & \cdot & \cdot \\ \cdot & \cdot & \cdot & \cdot & \cdot & \cdot & \cdot & \cdot \\ \cdot & \cdot & \cdot & \cdot & \cdot & \cdot & \cdot & \cdot \\ S_{n-1,1} & \cdot & \cdot & \cdot & \cdot & \cdot & S_{n-1,n-1} & S_{n-1,n} \\ S_{n,1} & \cdot & \cdot & \cdot & \cdot & \cdot & \cdot & S_{n,n} \end{bmatrix} \cdot \begin{bmatrix} a_1 \\ a_2 \\ \cdot \\ \cdot \\ \cdot \\ \cdot \\ a_{n-1} \\ a_n \end{bmatrix} \tag{2}$$

wave known and with the MO removed. Let us mark these S parameters as S_{ij}^C. Next measurements with MO inserted in, provide parameters $S_{i,j}^M$ for $i = 1, \ldots, n-1$ and $j = n$. The intensity of electromagnetic field in the i, j position of the AM, normalized to the intensity of the planar calibrating wave is then

$$E_{i,j} = \frac{S_{i,j}^M}{S_{ij}^C} \tag{3}$$

There are no differences between actual data in the A plane and measured data in the B plane in this ideal case.

The situation in a real AM with existing internal couplings is more complicated. Data in the planes A and B differ due to these couplings in the AM.

Firstly, it is necessary to describe a calibration of the VNA itself. From a practical point of view, a manual switching of antennas during the measurement is not acceptable and electronic switching and usage of a multiport test set (MTS) using electronic switches is necessary. In principle, it can be designed similarly as for example the Agilent 87050E Multi-port Test Set but for n measurement ports. In a certain moment, the "selected" couple of measurement ports in the C plane are connected to the measurement ports of the two-port VNA, other unselected ports are connected to internal loads. A calibration of the MTS can be performed by the same way as it is described in the instruction manual for the Agilent 8714ES VNA. If insignificant internal cross-talks between measurement ports can be supposed, a simplified procedure calibrating only pairs of measurement ports is applicable. However, in our case this known calibration procedure must be extended. As will be explained below, measurements of reflection coefficients $\Gamma_{1,\ldots,n}$ of the "unselected" ports of the MTS must be performed. It can be simply done using a piece of a known transmission line connected between "selected" and "unselected" ports.

Systematic errors of the calibrated VNA plus MTS in the C plane are removed only on the "selected" pair of ports. The other "unselected" ports of the MTS are not corrected as they are connected to the internal loads of the MTS. Hence, the reflection coefficients $\Gamma_{1,\ldots,n}$ of the "unselected" ports of the MTS are connected to currently not being measured ports of the AM. It means that the twoport S parameters of the currently measured ports of the AM are measured with some systematic errors due to imperfect matching at the other ports. Elimination of systematic errors under these conditions was proposed by Rautio, [8]. Using his method with the Gamma-R parameters enables determination of $S^C_{i,j}$ during the calibration of AM and also determination of $S^M_{i,j}$ during the measurement with the MO included. Corrected results of the measured normalized $E_{i,j}$ in the A plane can be determined by the equation (3).

The procedure described above can be simplified. Mutual couplings between individual antennas of the AM are the most significant in case of adjacent antennas. Couplings between far spaced antennas can be neglected. It results in a number of zeros in the matrix (2). Corresponding measurements are not necessary, therefore.

4. CONCLUSIONS

A study of systematic errors in electromagnetic field space distribution measurements using antenna matrix was performed. The study was based on vector measurements of mutual couplings between adjacent antennas of the antenna matrix and Matlab simulations of measurements. Significant influence of mutual couplings between adjacent antennas on measurement accuracy was discovered.

A general n-port approach not used up to now in electromagnetic field space distribution measurements was proposed. The approach makes possible to use an error model based on the n-port characterization of the measurement problem and to apply a corresponding correction method for elimination of mutual couplings between individual antennas. The method is applicable for vector electromagnetic field measurements only. It permits to correct measurements even with antennas in the matrix spaced less than a quarter wavelength. The method is suitable in electromagnetic field space distribution measurements. It is advantages namely in such measurements where sharp local space minima it the field distribution can be expected such as in the case of microwave phase interferometry.

ACKNOWLEDGMENT

This work has been conducted at the Department of Electromagnetic Field of Czech Technical University in Prague and supported by the research program MSMT6840770015 "Research of Methods and Systems for Measurement of Physical Quantities and Measured Data Processing" of CTU in Prague sponsored by the Ministry of Education and Sports of the Czech Republic and by the program No. GA102/04/0898 "Microwave Phase Interferometry" of Czech Grant Agency.

REFERENCES

1. Rochblatt, D. J. and B. L. Seidel, "Microwave antenna holography," *IEEE Trans. Microwave Theory Tech.*, Vol. MTT-40, 1294–1300, June 1992.
2. Pieraccini, M., G. Luzi, D. Mecatti, L. Noferini, and C. Atzeni, "A microwave radar technique for dynamic testing of large structures," *IEEE Trans. Microwave Theory Tech.*, Vol. MTT-51, 1603–1609, May 2003.
3. Semenov, S. Y., et al., "Spatial resolution of microwave tomography for detection of myocardial ischemia and infarction-experimental study on two-dimensional models," *IEEE Trans. Microwave Theory Tech.*, Vol. MTT-48, 538–544, April 2000.
4. Delai, A. B. and J. C. Cousin, "3D indoor micro location using a stereoscopic microwave phase sensitive device," *IEEE MTT-S Int. Microwave Symp. Dig.*, 623–626, 2003.
5. Mohon, R. J., J. A. Murphy, and W. Lanigan, "Digital holography at millimetre wavelengths," *Optical Communications*, Vol. 260, 469–473, 2006.
6. Bolomey, J. C., "Recent european developments in active microwave imaging in for industrial, scientific, and medical applications," *IEEE Trans. Microwave Theory Tech.*, Vol. MTT-37, 2109–2117, Dec. 1989.
7. Alden, A., P. Bouliane, and M. Zhang, US Patent No. US 6,762,726 B2, Jul. 13, 2004.
8. Rautio, J. C., "Techniques for correction scattering parameter data of an imperfectly terminated multiport when measured with a two-port network analyzer," *IEEE Trans. Microwave Theory Tech.*, Vol. MTT-31, 407–412, May 1983.

Artificial Neural Network Employment in the Design of Multilayered Microstrip Antenna with Specified Frequency Operation

K. Siakavara

Radiocommunications Lab., Department of Physics, Aristotle University of Thessaloniki
Thessaloniki 54124, Greece

Abstract— This paper deals with the utilization of Artificial Neural Networks (ANN) methodology in the design of microstrip antennas with prespecified operational features. A printed annular ring antenna, textured by slits, was designed in a multilayered dielectric substrate. The operational features of the antenna depend on the width and the position of the slits, the values of the structural parameters and the feed position. In this work a solution of the inverse problem, namely to find out the proper combination of all these parameter values which would yield the desired frequency response, was given via a Multiple Layer Perceptron (MLP) Neural Network.

1. INTRODUCTION

Microstrip antennas are used in a wide range of mobile communication applications which demand multi-band and/or wide band frequency operation, high power gain, omnidirectional radiation patterns etc.. Therefore the design of printed antennas suitable to meet the requirements of multiple operational services becomes a difficult task. Multiband microstrip antennas have been developed in the past using various techniques [1–4]. Recent works have shown that printed antennas e.g., fabricated in multilayered substrates or/and shape configured, [5, 6], provide the ability to achieve multifrequency operational characteristics. The difficulty in designing these antennas is due to the high number of physical parameters which they have. Therefore the number of the appropriate values that they must have, in order the antenna to exhibit the desired response, is also large. Artificial Neural Networks (ANN) were proved to be a useful tool for the design of printed antennas. The resonate frequency the radiation pattern as well the input impedance of the radiating element have been accurately calculated [7, 8] via Neural Network algorithms.

In the work at hand a printed ring antenna was designed in a three layered substrate (Figure 1). The inherent advantage of a ring antenna is its property to resonate for a diameter less than $\lambda g/2$ (λg is the guiding wavelength of the equivalent linear microstrip line having width equal to that of the ring). This attribute means a physical size smaller than the size of the respective circular disc resonating at the same frequency. The basic problem of a probe fed ring on a single dielectric layer was initially solved. To approximate the associate resonate frequencies of the three layer antenna, the effective dielectric constant of the structure was used. The modification of the ring shape, via slits, would increase the frequency bandwidth if the slits were notched on proper positions and had suitable dimensions. The frequency performance is also affected by the dielectric constant values and the heights of the substrates. The inverse problem that is to find the proper values of the antenna parameters in order to have a desired frequency response was solved via an MLP artificial neural network.

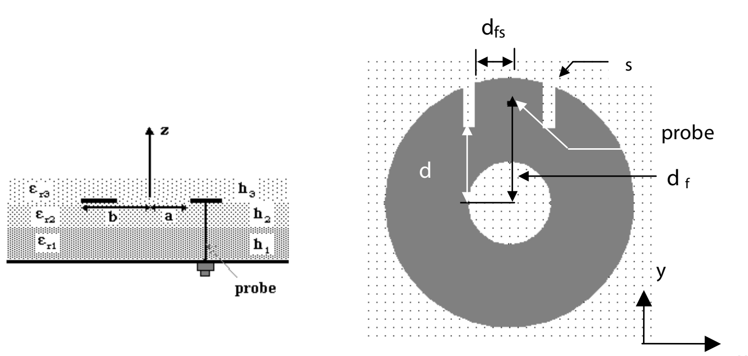

(a) (b)

Figure 1: The three layer annular microstrip ring.

2. FORMULATION

2.1. Printed Ring Solution

The spatial domain electromagnetic problem of a probe fed annular ring antenna, printed on a single dielectric layer substrate, was solved via the Green's Function technique [9]. The Green's Function, $G(\rho, \varphi|\rho', \varphi')$, was expanded in series of the eigenfunctions of the associate differential equation in the cylindrical coordinate system and it was found that it takes the form

$$\begin{aligned} G(\rho, \varphi|\rho', \varphi') = & \sum_n \sum_m \left[\sqrt{\frac{1}{\pi C_{Jn}}} J_n\left(\sqrt{\lambda_{mn}}\rho\right) + \sqrt{\frac{1}{\pi C_{Yn}}} Y_n\left(\sqrt{\lambda_{mn}}\rho\right) \right] \cdot \\ & \left[\sqrt{\frac{1}{\pi C_{Jn}}} J_n\left(\sqrt{\lambda_{mn}}\rho'\right) + \sqrt{\frac{1}{\pi C_{Yn}}} Y_n\left(\sqrt{\lambda_{mn}}\rho'\right) \right] \cdot \frac{\cos(n\varphi)\cos(n\varphi')}{\lambda - \lambda_{mn}} \end{aligned} \tag{1}$$

where C_{Jn} and C_{Yn} are constants produced via the ortho-normalization process of the eigenfunctions. In order the orthonormal eigenfunctions to satisfy the boundary conditions, the following equation must be satisfied

$$J_n{}'\left(\sqrt{\lambda_{mn}}a\right) Y_n{}'\left(\sqrt{\lambda_{mn}}b\right) + Y_n{}'\left(\sqrt{\lambda_{mn}}a\right) J_n{}'\left(\sqrt{\lambda_{mn}}b\right) = 0 \tag{2}$$

where m indicates the mth zero of the equation. Equation (2) is the characteristic equation of the problem and its solution gives the frequencies at which the ring resonates, that is

$$f_{mn} = \frac{\sqrt{\lambda_{mn}}}{2\pi\sqrt{\mu\varepsilon}} \tag{3}$$

In the above equation, ε is the dielectric constant of the substrate. In the problem at hand an approximate calculation of the resonate frequency can be done, via Equation (3), if the effective dielectric constant of the three layer substrate is used for ε. This effective dielectric constant is calculated considering a microstrip line that has width equal to the width of the ring and is embedded in the same multiple layer substrate.

2.2. The Neural Network Solution

The determination of the frequency performance, e.g., the scattering coefficient at the input of the antenna versus frequency, if its structural characteristics are given, is a 'direct' procedure. Various techniques exist and accurate results can be derived. However the determination of the structural parameter values for a pre-specified operation, is a problem for which analytical expressions do not exist. This inverse procedure is complicated and non linear. Therefore the utilization of a Neural Network technique would be advisable for its solution.

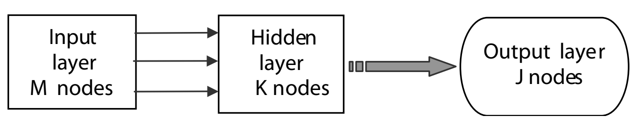

Figure 2: The MLP architecture, $M = 144$, $K = 144$ and $J = 12$.

In the present work the MLP architecture is used (Figure 2). The input of the NN can receive patterns of the antenna input reflection coefficient, versus frequency, and its output responds giving the associate structural parameters. The MLP-NN is trained via a backpropagation algorithm [10] and consists of three layers: the input layer, the hidden one and the output layer containing M, K and J nodes respectively. A supervised learning strategy is applied. So, for each input pattern $x(p)$ containing the reflection coefficient values, an output pattern of the values of the respective structural antenna parameters, by which the input values were calculated, is presented to the network. The target of the learning procedure is, when the pth input pattern is presented to the network, the output values $y_j^o(p)$, $j = 1 \ldots J$, to be equal to the respective pth output pattern values. The criterion for this convergence are the values of the error function defined as

$$E_p(w) = \frac{1}{2}\sum_{i=1}^{J}\left[d_j(p) - y_j^o(p)\right]^2 = \frac{1}{2}\sum_{i=1}^{J}\left[d_j(p) - F_2^h\left(\sum_{j=1}^{ml} w_1^{jk}\left(F_1^h \sum_{i=1}^{I} w_{in}^{ij} x_i^p\right)\right)\right]^2 \tag{4}$$

where $d_j(p)$ is the pth output pattern, w_q^{nt} represents the synaptic weight from nth neuron of the qth layer towards the tth neuron of the next layer x_i^p represents the ith element of the pth input pattern and F_m^h is the activation function of the mth layer. During the training phase the network changes its weights so that the above function is minimized. It is realized by the gradient descent procedure [10, 11] via which the weights change by an amount proportional to the negative gradient of the error function, that is $\Delta w(p) = -\eta \nabla E_p(w) + \alpha \Delta w(p-1)$. The constant of proportionality, η, is the learning rate and α is the momentum constant.

Table 1: Ranges of the structural parameter values of the antennas by which the NN was trained. Structural parameter values of the first antenna, received by the NN when the NN's input accepted the desired reflection coefficient pattern. Structural parameter values of the second antenna, received by the NN, when the simulated reflection coefficient pattern of the first antenna was presented at the NN's input.

Parameters	Range of values for training	Figure 3		Figure 4	
		ANN	ANN (from ANN results)	ANN	ANN (from ANN results)
a	10 mm–15 mm	12.05 mm	12.02 mm	9.9 mm	10.1 mm
b	30 mm–42 mm	36.1 mm	36.08 mm	30.1 mm	30 mm
s	1 mm–4 mm	3 mm	2.95 mm	3 mm	1.98 mm
d_f	0.75b–0.85b	27.6 mm	27.7 mm	25.7 mm	26.2 mm
d_{fs}	4 mm–8 mm	8.1 mm	8.0 mm	8.32 mm	7.93 mm
d	0.6b–0.8b	22 mm	22.06 mm	17.9 mm	18 mm
ε_{r1}	1–2.5	1.03	1.01	1.02	1.0
ε_{r2}	3.2–3.5	3.5	3.49	3.5	3.52
ε_{r3}	1–2.2	1.04	1.6	1.5	1.07
h_1	3 mm–10 mm	6.1 mm	5.92 mm	5.9 mm	6 mm
h_2	3 mm–10 mm	6.05 mm	6.02 mm	6.05 mm	6.1 mm
h_3	1 mm–2 mm	1.1 mm	1.45 mm	2 mm	1.08 mm

3. RESULTS

The ANN that was used for the design of the ring antenna contains $M = 144$ input nodes, $K = 144$ nodes in the hidden layer and $J = 12$ output nodes. The output nodes correspond to the parameters:

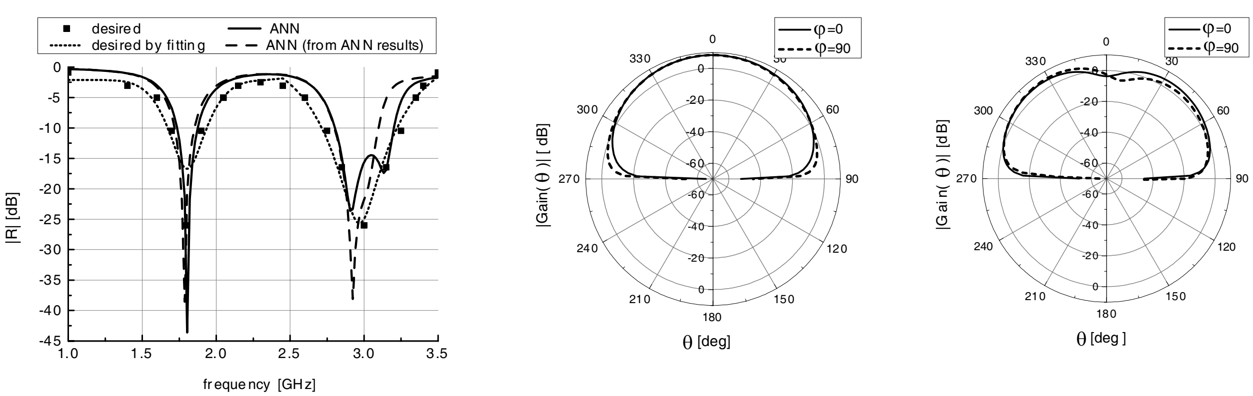

(a) (b) (c)

Figure 3: (a) The desired reflection coefficient pattern, the respective one composed by curve-fitting, the pattern of the first antenna constructed via the results of the NN and the pattern of the second antenna composed by the results given by the NN, when it accepted at its input the values of the reflection coefficient pattern of the first antenna. (b), (c) The gain patterns of the first antenna at 1.572 GHz, and 2.5 GHz respectively.

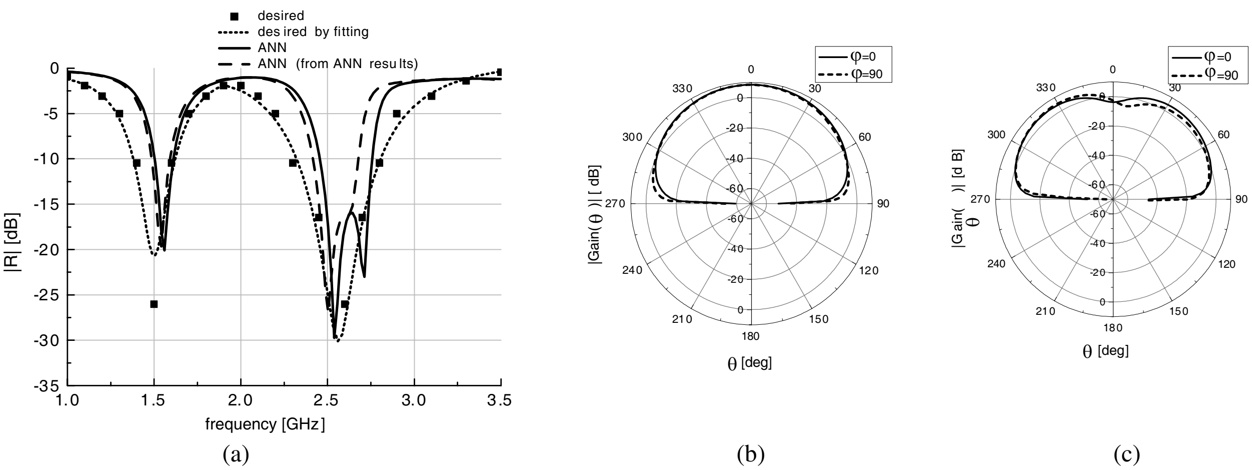

Figure 4: (a) The desired reflection coefficient pattern, the respective one composed by curve-fitting, the pattern of the first antenna constructed via the results of the NN and the pattern of the second antenna composed by the results given by the NN, when it accepted at its input the values of the reflection coefficient pattern of the first antenna. (b), (c) Gain patterns at 1.8 GHz and 3 GHz respectively.

$a, b, s, d_f, d_{fs}, d, \varepsilon_{r1}, \varepsilon_{r2}, \varepsilon_{r3}, h_1, h_2$ and h_3 of the antenna (see Figure 1).

For the training of the network, a collection of 144 input patterns was created. The values of each input set were the reflection coefficient values at the input of the antenna, calculated via simulation at 144 different frequencies between 1 GHz and 3.5 GHz. The parameter values of the antenna were properly chosen in order the resonate frequencies to be inside this frequency range. To ensure this fact, a theoretical assessment of the resonate frequency via Equation (3) was made a priori for each set. The effective dielectric constant contained in the equation was computed using a quasi-static technique. The ring was fed by a 50 Ohms probe and the simulation was made via a software based on the Method of Moments. It is noticed that the creation of slots on the surface of the patch causes a shifting of the resonate frequencies. This is not so important because the exact frequency response was received via simulation.

Initially, training sets with few pairs of input-output patterns were used. The number of pairs was gradually increased, by six patterns, with intense to minimize the Root Mean Square (RMS) of the error function of Equation (4).

Via 144 training pairs an RMS value of 1% was obtained. More increase of the number of patterns did not reduce the above RMS value. The values of the parameters used in the training collection, range as shown in Table 1. In all training sets the total substrate height, namely (h_1+h_2), was high, larger than 10 mm, and the values of dielectric constants less or equal to 3.5 that is the NN was trained with wideband frequency antennas.

During the aforementioned procedure the smallest RMS values were obtained using a) as activation function the hyperbolic tangent type, $g(x) = \left(1 - e^{-2x}\right) / \left(1 - e^{2x}\right)$ b) learning rates $\eta = 0.1$ for the weights from the input to the hidden layer, $\eta = 0.05$ from the hidden to the output layer c) momentum $\alpha = 0.05$ and d) an epoch size equal to 32.

Indicative results received by the network are presented in Figures 3 and 4. In both cases desired reflection coefficient patterns with dual frequency band operation (e.g., at frequencies of GPS or in bands of WLAN applications) were presented to the trained network. For each frequency band the desired reflection patterns were composed by curve fitting and under the constraints of specified frequency bandwidths at -10 dB, at -5 dB and at -3 db and also the minimum values of the pattern. Then each one of the patterns was sampled at 144 distinct frequencies and the set of samples was presented to the NN as input pattern. The output of the NN gave the structural parameter values by which the desired performance could be obtained. For the verification of these results, printed antennas were composed by these values and were simulated. The results are presented in Figures 3 and 4. In the last step of the procedure the above simulated reflection coefficient patterns were presented to the input of the NN. The new structural parameter values, received at the NN output, were used for the construction of new antennas, the frequency response of which is depicted in the associate figures. It is observed that both solutions, received by the NN, converge giving resonances inside the desired frequency region.

In Figures 3 and 4 the gain patterns of the antennas constructed via the first solution of the network are illustrated. The gain patterns of the second antennas are almost similar to those of the respective first ones. The structural parameters of the first and second antennas are included in Table 1.

It was ascertained that the NN can not find a solution for any pattern presented at its input e.g., a) for a dual-band frequency operation, the separation of frequency bands must be greater than 1GHz b) at the lower frequency band, bandwidth less than 7% can be achieved and at the higher one it can not exceed the 16% (nevertheless it is greater than that obtained for a single dielectric layer printed antenna [12]. Concerning to the gain patterns all three antennas appear similar distribution of the radiated power on both main planes. At frequencies up to 2 GHz the radiation is broadside, the maximum gain values are about 9 dB and the half power beam-widths (HPBW) large. At larger frequencies the directions of maxima appear at thirty or more degrees far from the broadside, the maximum gain values are up to 6 dB and gain values greater than 0 dB exist at small elevation angels above the plane of the antenna.

4. CONCLUSION

In the paper the Artificial Neural Network methodology was employed for the design of microstrip antennas with pre-specified operational features and it was proved that it can efficiently give solutions for this inverse problem. In all cases the ANN gave correct answer when, in the desired reflection coefficient pattern, the frequency separation between the resonate regions was at least 1 GHz. This fact and also the upper limit values of the obtained bandwidths depend mainly on the shape of the printed elements and a few on the regions of the antenna's parameter values by which the ANN was trained.

REFERENCES

1. Shynu, S. V., G. Augustin, C. K. Aanadan, P. Mohanan, and K. Vasudevan, "Development of a varactor-controlled dual frequency reconfigurable microstrip antenna," *Microwave Opt. Technol. Lett.*, Vol. 46, 375–377, 2005.
2. Siakavara, K. and F. Tsaldaris, "A multi-wideband microstrip antenna designed by the square-curve fractal technique," *Microwave Opt. Technol. Lett.*, Vol. 41, 180–185, 2004.
3. Yeo, J. and R. Mittra, "Design of conformal multiband antennas based on fractal concepts," *Microwave Opt. Technol. Lett.*, Vol. 36, 333–338, 2003.
4. Ganatsos, T. and K. Siakavara, "Improved microstrip antenna polarization by using electromagnetic band-gap substrates," *Proc. of International Conference on Antenna Technologies (ICAT 2005)*, 539–543, Ahmedabad, India, February 2005.
5. Chen, Z. Z., A. D. Ganjara, and X. M. Chen, "A dual-L antenna with a novel tuning technique for dual frequency applications," *IEEE Trans. Antennas Propag.*, Vol. 50, 402–403, 2002.
6. Guo, Y. X., K. M. Luke, K. F. Lee, et al., "A quarter wave U-shaped patch antenna with two unequal arms for wideband and dual frequency operation," *IEEE Trans. Antennas Propagation*, Vol. 50, 1082–1087, 2002.
7. Mishra, R. K. and A. Patnaik, "Neural network-based CAD model for the design of a square-patch antennas," *IEEE Trans. Antennas Propag.*, Vol. 46, 1890–1891, 1998.
8. Neog, D. K., S. S. Pattnaik, D. C. Panda, S. Devi, B. Khuntia, and M. Dutta, "Design of wideband microstrip antenna and the use of artificial neural networks in parameter calculation," *IEEE Trans. Antennas Propag. Magazine*, Vol. 47, 60–65, 2005.
9. Balanis, C. A., *Advanced Engineering Electromagnetics*, John Wiley & Sons, New York, 1989.
10. Christodoulou, C. and M. Georgiopoulos, *Applications of Neural Networks in Electromagnetics*, Artech House, Boston, 2001.
11. Haykin, S., *Neural Networks — A Comprehensive Foundation*, Second edition, Prentice-Hall Inc., Boston, 1999.
12. Kanaujia, B. K. and B. R. Vishvakarma, "Design considerations for the development of the annular ring microstrip antenna," *Int. J. Electronics*, Vol. 81, 665–677, 2002.

Electrical Vibrations of Yeast Cell Membrane

M. Cifra[1,2], **J. Vaniš**[2], **O. Kučera**[1,2], **J. Hašek**[3], **I. Frýdlová**[3], **F. Jelínek**[2]
J. Šaroch[2], **and J. Pokorný**[2]
[1]Department of Electromagnetic Field, Czech Technical University
Technická 2, 166 27 Prague, Czech Republic
[2]Institute of Photonics and Electronics, Academy of Sciences of the Czech Republic
Chaberská 57, 182 51, Prague 8, Czech Republic
[3]Institute of Microbiology, Academy of Sciences of the Czech Republic
Vídeňská 1083, 142 20 Prague 4-Krč, Czech Republic

Abstract— Cytoskeleton with microtubules is the main organization structure of the eukaryotic cell. Possible sources of vibrational excitations of electrically polar cytoskeleton components are enumerated. Temperature stabilized, triple screened box (electrically and electromagnetically by mumetal) with point sensor and preamplifiers was used for measurement of electrical oscillations of yeast cell. Preliminary findings of the electrical measurement and local nanomechanical AFM measurements are presented. Findings correspond to the Frölich's postulate of coherent electrically polar longitudinal vibrations in biological systems.

1. INTRODUCTION

Fröhlich postulated electrically polar longitudinal vibrations in biological systems [1–4]. The vibrations generate endogenous electromagnetic field. The electromagnetic field is generated in a broad frequency spectrum. The oscillations in megahertz [5], gigahertz [6, 7], far infra red [8], visible and UV [9, 10] range are detected. Sources of the electromagnetic fields vary over the spectrum.

Pohl observed attraction of small dielectric particles to cells [11, 12]. He explained this effect as a result of dielectrophoresis, what is attraction of polarized particles in a non-uniform electric field. This effect was greatest during the M-phase of the cells, when the rate of polymerization and depolymerization (treadmilling) of microtubules in the mitotic spindle is enhanced compared with the rate in the interphase (dynamic instability).

Local nanomechanical motion of yeast cell (*Saccharomyces cerevisiae*) membrane was measured by Pelling et al. [13, 14] with atomic force microscope (AFM). By means of the Fourier transform of the measured signal they found oscillations with amplitude of a few tenths of nm to a few nm's in the frequency range below 2 kHz. Frequency of these oscillations was temperature dependent. Background noise of the AFM was of the order of magnitude of 10^{-2} nm. Oscillations at a single frequency have been detected on the normal yeast cell wall and those at multiple frequencies different from the frequency on the normal cell wall have been detected on the bud scar. Oscillations of the yeast cell wall and of the bud scar ceased after addition of metabolic inhibitor, which suggests cellular metabolism is involved in the generation of motion.

This paper describes possible sources of vibrational excitations of polar cellular membrane through the cytoskeleton and refers about the electrical and AFM measurements of vibrations of yeast cell membrane.

2. CYTOSKELETON AND ITS EXCITATION BY CELLULAR METABOLISM

Cytoskeleton is organizing network of the eukaryotic cell, which helps the cell to move, to maintain its shape and to transport molecules and cellular organelles. Cytoskeleton is comprised of three types of protein filaments: actin filaments (microfilaments), intermediate filaments and microtubules [15].

Microtubules are highly polar, deformable and dynamic structures. They resemble hollow tubes with inner and outer diameter of 17 nm and 25 nm, respectively (Fig. 1(a)). Microtubule consists of 13 protofilaments. The building subunits are tubulin heterodimers composed of α-tubulin and β-tubulin (Fig. 1(b)). These heterodimers have high electrical dipole moment of over 1000 Debye (10^{-26} C.m); they are responsible for the high electrical polarity of microtubules. In the interphase of the cell cycle, microtubules are radially organized with their minus ends embedded in a centrosome, which is located in the center of the cell near the cell nucleus. There are approximately 400 microtubules in a cell, depending on the organism and the cell type. In the interphase microtubules undergo dynamic growth (polymerization) and shrinkage (depolymerization), so-called "dynamic instability" (Fig. 1(c)). In the M phase microtubules are subject to treadmilling, i.e., polymerize at the plus end and depolymerize at the minus end (chemical plus and minus).

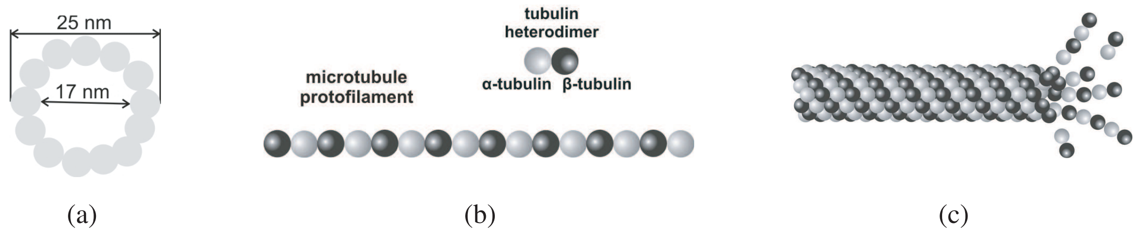

Figure 1: (a) Dimensions of microtubule, (b) Structural subunits of microtubules: protofilaments composed of tubulin heterodimers, (c) Detail of plus end of a microtubule undergoing dynamic instability.

There are three possibilities how the vibrations of microtubules can be excited:

1. **release of energy stored in microtubules by hydrolysis of guanosine triphosphate (GTP) to guanosine diphosphate (GDP)** [17–19]
2. **microtubule motor proteins (dyneins and kinesins) "crawling" along the microtubule** [13, 14, 16]
3. **vibrational energy released from mitochondria during the production of ATP by oxidative phosphorilation in the Kreb's cycle (citric acid cycle)**

Microtubules can be considered as a longitudinally vibrating chain of dipoles which are source of oscillating electric field. Effect of electromagnetic field of microtubules on transfer of mass particles and electrons has been analyzed in [20, 21].

Actin filaments are polar structures too, and undergo hydrolysis of ATP (built in the actin molecules) shortly after polymerization. This process is similar to hydrolysis of GTP in microtubules, however in much smaller rate than in microtubules [15]. Actin filaments may be sources of electric vibrations as well.

3. VIBRATIONS OF THE CELL MEMBRANE

Possibilities of the excitation of vibration in the microtubules have been discussed. If the vibrations are excited in the cytoskeleton, they may cause vibration of the cell membrane because of the bonding of cytoskeleton to the cell membrane. If the measured mechanical vibrations of the cell membrane are caused by the vibrations of microtubules, it is likely that electromagnetic oscillations of microtubules at the membrane are detectable. At the frequency measured by Pelling et al. [13, 14] (~ 1 kHz) the electric field would be screened in a close distance by activity of ions in the extracellular medium (mostly Na^+ and Cl^-). Therefore, to measure this electric field the sensor must be in the vincinity of a cell membrane [5]. Furthermore, the large number of vibrational and electric sources may create high order spherical harmonics structure (of zonal type) of the vibrational and electrical field on the membrane. The measurement of both types of oscillations requires "point" detector with the size smaller than the half of the wavelength of the surface wave, otherwise the effective amplitude would be zero, since the negative and positive peak of the surface wave would cancel out.

4. MATERIALS AND METHODS

4.1. Yeast Cells

Cold sensitive β-tubulin mutant *tub2-401* of yeast cells *Saccharomyces cerevisiae* (strain CUY67 Mata *tub2-401 ura3-52 ade2-101*) was used. Evolution of the cells in the cell cycle can be synchronized by cultivation at the restrictive temperature (14°C) when the microtubules cannot be formed. The mutant cells at the restrictive temperature continue in their pathway along the cell cycle up to the point before entering the M phase, whose processes depend on the microtubules. Thus after certain time period all the mutant cells are stopped at the same point of the cell cycle. When the temperature increases to the permissive temperature (≥ 25°C) microtubules are reassembled and the mitotic spindle is formed. Therefore, start of the M phase in the cells cultivated under the restrictive temperature is triggered by the temperature increase above 25°C. Thus the cells are synchronized. Evolution of the M phase after the warm-up above the permissive temperature is described in detail in [5].

We measured synchronized and non-synchronized cells in suspension. The cells were suspended in the aqueous sucrose solution. After warming to the permissive temperature, synchronized cells synchronously enter the M-phase, in which they are more active in generating the electric field in their vincinity than in the interphase.

4.2. Measurement System

A schematic diagram of the measurement system is shown in the Fig. 2. The crucial parts are the sensor (schematically in Fig. 3.) and the preamplifiers, which are located in the temperature stabilized and triple shielded box (electrically and electromagnetically by mumetal box). The effectiveness of the screening was verified in [5]. The batteries for the power supply of the amplifier are located inside the screened box, too. At the bottom of a small cuvette there is an evaporated Pt layer forming one electrode. Detecting wire electrode cut at an angle to obtain a point end (about 50 nm) is at a distance of 8 μm above the bottom of the cuvette. Dimension of 8 μm corresponds approximately to the diameter of a cell.

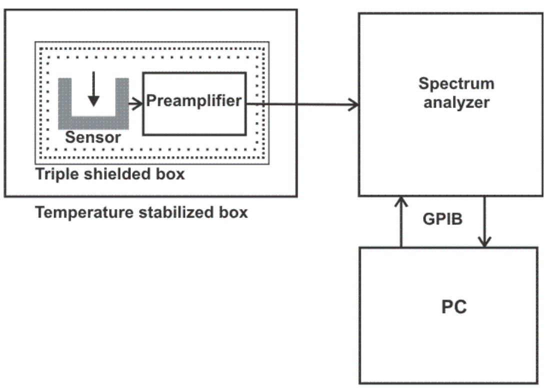

Figure 2: Schematic depiction of the used measurement system.

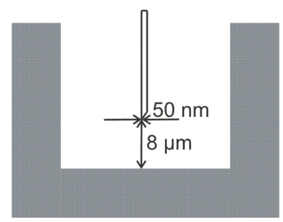

Figure 3: Dimensions of the used sensor.

The sensor with the preamplifier is connected to spectrum analyzer through semirigid coaxial cable. Control of the spectrum analyzer is provided by a PC program via GPIB interface. Spectrum analyzer used is R&S FSEA 30 (20 Hz–3.5 GHz). Detected cellular signal is amplified by two preamplifiers; the first one provides transition of "nano" to macroscopic signals. We performed measurements in the frequency range 0.5–2.5 kHz.

4.3. Measurement Protocol

Suspension with synchronous cells was cultivated at the temperature of 14°C. Suspension with non-synchronous cells was cultivated at the temperature of about 30°C. Before measurement the test tubes with the suspension were warmed in water bath of 28°C for 3 minutes. Optical density (OD 600) of the suspension was 4.5 [5], which corresponds to concentration of about 2×10^8 cells per milliliter. Afterwards, the cuvette was filled with the 60 μl of suspension. Measurement was started immediately after filling the cuvette. Cells sediment at the bottom of cuvette. Similar measurements of non-synchronous cells were performed, too.

4.4. AFM Measurements

We realized the measurements with AFM device similar to those published by Pelling et al. [13, 14]. Noise was on the level of 10^{-1} nm.

5. RESULTS

Results of preliminary measurement of electrical oscillations of yeast cells are presented. Fig. 4 shows measured spectrum in the frequency bandwidth from 1280 to 1400 Hz.

When a high amplitude spectral line was observed the frequency of the line was evaluated (1315.5 Hz) and the spectrum analyzer was switched to a 2.5 Hz bandwidth. Fig. 4(b) shows shifted 2.5 Hz bandwidth spectra with selected spectral line in time $t_1 = 0$, $t_2 = 33$ s, $t_3 = 53$ s, $t_{43} = 73$ s. Temperature in the box with yeast cell suspension was 27.6–28°C. Preliminary result from AFM is presented in Fig. 5.

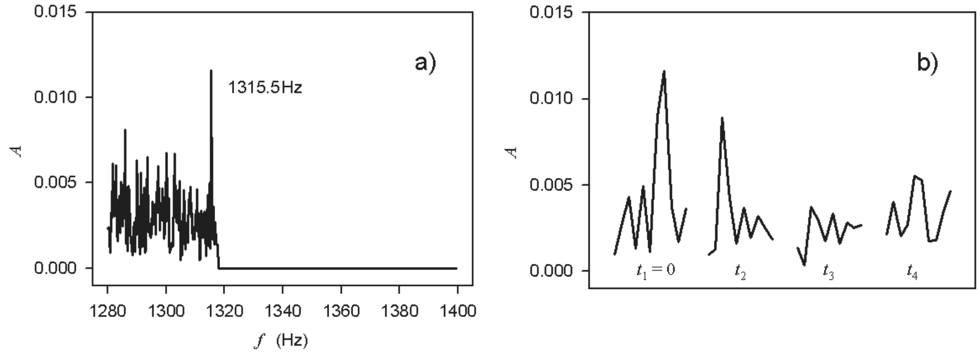

Figure 4: Frequency of electrical oscillations of yeast cells in the range 1280–1400 Hz. RBW and VBW of the spectrum analyzer was 1 Hz. The sweep time was 600 s. (a) Frequency spectrum before detailed examination. (b) The successively measured 2.5 Hz bandwidth spectra shifted according to the time of measurement.

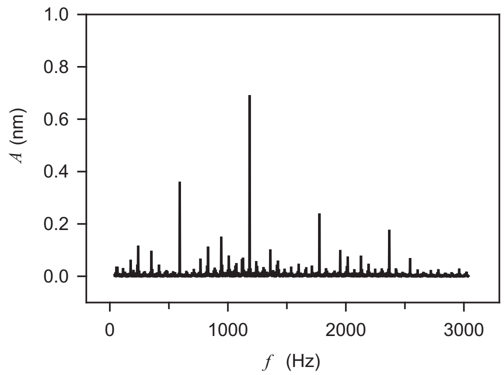

Figure 5: Frequency of local nanomechanical oscillations of synchronized yeast cell in the range 0–3 kHz as measured with AFM.

6. DISCUSSION & CONCLUSIONS

Our findings correspond to the Fröhlich's postulate of coherent electrically polar longitudinal vibrations in biological systems.

The electrical measurement system used does not enable precise spatial localization of the tip of electrode. Since the cells exhibit a movement, we cannot assure that cell is under the sensor when the spectrum analyzer sweeps through the frequency of cell oscillations.

The electrical measurements were performed in temperature stabilized box, but the character of the measurement setup and protocol (opening of the box in order to change of the measured cell samples) introduced slight temperature changes in the environment of cells. Temperature changes cause shift in spectra of a signal, according to [14, 15], the shift is about 135.5 Hz/1°C.

Implications of existence of endogenous electromagnetic field in biological systems are far-reaching in terms of structural organization in organisms and possible mutual electromagnetic interactions of organisms.

REFERENCES

1. Fröhlich, H., "Bose condensation of strongly excited longitudinal electric modes," *Phys. Letters Ser. A*, Vol. 26, 402–403, 1968.
2. Fröhlich, H., "Long-range coherence and energy storage in biological systems," *Intern. J. Quantum Chem.*, Vol. 2., 641–649, 1968.
3. Fröhlich, H., "Quantum mechanical concepts in biology," *In. theoretical physics and biology (ed. M. Marois), Proceedings of 1st International Conference on Theoretical physics and biology 1967*, 13–22, Versailles, France, 1969.
4. Fröhlich, H., "The biological effects of microwaves and related questions," *Adv. Electronics Electron Physics*, Vol. 53, 85–152, 1980.
5. Pokorný, J., J. Hašek, F. Jelínek, J. Šaroch, and B. Palán, "Electromagnetic activity of yeast cells in the M phase," *Electro-Magnetobiol.*, Vol. 20, 371–396, 2001.

6. Jelínek, F., J. Pokorný, J. Šaroch, and J. Hašek, "Experimental investigation of electromagnetic activity of yeast cells at millimeter waves," *Electromagn. Biol. Med.*, Vol. 24, No. 3, 301–307, 2005.
7. Jelínek, F., J. Šaroch, O. Kučera, J. Hašek, J. Pokorný, N. Jaffrezic-Renault, and L. Ponsonnet, "Measurement of electromagnetic activity of yeast cells at 42 GHz," *Radioengineering*, Vol. 16. No. 1, 36–39, 2007.
8. Vos, M. H., F. Rappaport, J.-C. Lambry, J. Breton, and J.-L. Martin, "Visualisation of coherent nuclear motion in membrane protein by femtosecond spectroscopy", *Nature*, Vol. 363, 320–325, 1993.
9. Beloussov, L., F. A. Popp, V. Voiekov, and R. Van Wijk,, *Biophotonics and Coherent Systems*, Moscow University Press, 2000.
10. Shen, X. and R. Van Wijk, *Biophotonics — Optical Science and Engineering of 21st Century*, Springer, 2005.
11. Pohl, H. A., "Oscillating fields about growing cells," *Int. J. Quant. Chem, Quant. Biol. Symp.*, Vol. 7, 411–431, 1980.
12. Pohl, H. A., T. Braden, S. Robinson, J. Piclardi, and D. G. Pohl, "Life cycle alterations of the micro-dielectrophoretic effects of cells," *J. Biol. Physics*, Vol. 9, No. 3, 133–134, 1981.
13. Pelling, A. E., S. Sehati, E. B. Gralla, J. S. Valentine, and J. K. Gimzewski, "Local nanomechanical motion of the cell wall of Saccharomyces cerevisiae," *Science*, Vol. 305, 1147–1150, 2004.
14. Pelling, A. E., S. Sehati, E. B. Gralla, and J. S. Gimzewski, "Time dependence of the frequency and amplitude of the local nanomechanical motion of yeast," *Nanomedicine*, Vol. 1, 178–183, 2005.
15. Alberts, B., et al., *Molecular Biology of the Cell*, 3rd version, Garland Publishing, 1994.
16. Kawaguchi, K. and S. Ishiwata, "Thermal activation of single kinesin molecules with temperature pulse microscopy," *Cell Motility and the Cytoskeleton*, Vol. 49, 41–47, 2001.
17. Pokorný, J., "Viscous efects on polar vibrations in microtubules," *Electromagn. Biol. Med.*, Vol. 22, No. 1, 15–29, 2003.
18. Pokorný, J., "Excitation of vibrations in microtubules in living cells," *Bioelectrochemistry*, Vol. 63, 321–326, 2004.
19. Pokorný, J. and T.-M. Wu, *Biophysical Aspects of Coherence*, Academia, Prague, 1998.
20. Pokorný, J., J. Hašek, and F. Jelínek, "Endogenous electric field and organization of living matter," *Electromagn. Biol. Med.*, Vol. 24, 185–197, 2005.
21. Pokorný, J., J. Hašek, and F. Jelínek, "Electromagnetic field of microtubules: Effect on transfer of mass particles and electrons," *J. Biol. Physics*, Vol. 31, 501–514, 2005.

A New Spectral Method for Scattering by Impedance Polygons

J. M. L. Bernard
CEA-DIF, Département de Physique Théorique et Appliquée
91680, Bruyères le Châtel, France

Abstract— A new spectral approach for scattering by two-dimensional polygonal objects with arbitrary surface impedance conditions is studied. In this problem, the Wiener-Hopf method cannot be applied, while asymptotic methods can only be used if corners are widely spaced compared to wavelength. We present here a general method to handle in a global manner the problem of n-part polygonal objects using the Sommerfeld-Maliuzhinets representation of the field. Some of our recent developments permit us to consider a new integral expression of the spectral function, in some domain of complex angles, where it becomes possible to take globally account of boundary conditions on a complex geometry. This generalization of Maliuzhinets methods enables us to derive, for the first time, the functional equations for the spectral functions for scattering by a general impedance polygon with finite or infinite surface, and to reduce generally the problem to a system of Fredholm integral equations of the second kind with non-singular kernels, allowing approximations. We apply in particular this approach to the important class of three-part impedance polygons composed of a finite segment attached to two semi-infinite planes, and show how to decouple the set of integral equations in some particular cases, then we study particular properties of kernels permitting approximations when the wave number k is large or small.

We study a new spectral approach for scattering by two-dimensional polygonal objects with arbitrary surface impedance conditions. In this delicate exterior problem, the Wiener-Hopf method cannot be applied, while asymptotic methods can only be used if corners are widely spaced compared to wavelength, and the presence of imperfectly reflective surfaces particularly complicates the problem.

We present here a general method to handle in a global manner the problem of n-part polygonal objects using the Sommerfeld-Maliuzhinets representation of the field,

$$u(\rho,\varphi)=\frac{1}{2\pi i}\int_{\gamma}f(\alpha+\varphi)e^{ik\rho\cos\alpha}d\alpha, \tag{1}$$

which satisfies the Helmholtz equation $(\Delta+k^2)u(\rho,\varphi)=0$, in free space sector $-\Phi\leq\varphi\leq\Phi$. In this representation, f is an analytic function and the path γ (Figure 2) consists of two branches: one, named γ_+, going from $\left(i\infty+\arg(ik)+\left(a_1+\frac{\pi}{2}\right)\right)$ to $\left(i\infty+\arg(ik)-\left(a_2+\frac{\pi}{2}\right)\right)$ with $0<a_{1,2}<\pi$, as $\mathrm{Im}\alpha\geq d$, above all the singularities of the integrand, and the other, named γ_-, obtained by inversion of γ_+ with respect to $\alpha=0$.

This representation has long been devoted to the rigorous analysis of isolated wedges. However, some of our recent developments permit us to consider a new integral expression of the spectral function, in some domain of complex angles, where it becomes possible to take globally account of boundary conditions on a complex geometry [1, 2].

For this, we show first that

$$f(\pm\pi+\varphi)=\frac{1}{2}\int_0^{\infty}(iku(\rho',\pm\Phi)\sin(\varphi\mp\Phi)\pm\frac{\partial u}{\partial n}(\rho',\pm\Phi))e^{ik\rho'\cos(\varphi\mp\Phi)}d\rho', \tag{2}$$

as $\frac{\pi}{2}<\Phi\mp\varphi_o<\frac{3\pi}{2}$ and $\frac{\pi}{2}<\Phi\mp\varphi<\frac{3\pi}{2}$, $|\arg(ik)|<\frac{\pi}{2}$, where φ_o is the incident plane wave direction, considering some general properties of the field permitting the convergence of the integral.

Using Green's theorem, we note that the contour of integration along $\varphi=\pm\Phi$ can be deformed into any path $L^{\pm}_{0,\infty}$, provided that the integral remains bounded and no source passes through the path during the deformation.

So, if we divide the semi-infinite paths $L^{\pm}_{0,\infty}$ (deriving from a deformation of the faces $\varphi=\pm\Phi$ enclosing the scatterer, described above) into $L^{\pm}_{0,\Delta^{\pm}}$ (i.e., $0<l'<\Delta^{\pm}$) and $L^{\pm}_{\Delta,\infty}$ (i.e., $l'>\Delta^{\pm}$), we have

$$f(\pm\pi+\varphi) = \frac{1}{2}\int_{L^{\pm}_{0,\Delta^\pm}} (iku(\rho',\varphi')\sin(\varphi-\varphi'_t)\pm\frac{\partial u}{\partial n}(\rho',\varphi'))e^{ik\rho'\cos(\varphi-\varphi')}dl'(\rho',\varphi')+f_{L^{\pm}_{\Delta^\pm,\infty}}(\pm\pi+\varphi), \quad (3)$$

where $f_{L^{\pm}_{\Delta^\pm,\infty}}(\alpha) = e^{-ik\rho_{\Delta^\pm}\cos(\alpha-\varphi_{\Delta^\pm})}f^{\pm}_{e}(\alpha)$, $f^{\pm}_{e}(\alpha)$ is the spectral function related to the Sommerfeld-Maliuzhinets representation of the field in coordinates with origin at $l' = \Delta^{\pm}$.

We can then write, by analytic continuation,

$$f(\alpha) = \frac{1}{2}\int_{L^{\pm}_{0,\Delta^\pm}} (-iku(\rho',\varphi')\sin(\alpha-\varphi'_t)\pm\frac{\partial u}{\partial n}(\rho',\varphi'))e^{-ik\rho'\cos(\alpha-\varphi')}dl'(\rho',\varphi')+f_{L^{\pm}_{\Delta^\pm,\infty}}(\alpha), \quad (4)$$

that is called henceforth the single-face expressions of f.

Let us consider a polygonal surface located inside the domain $|\varphi| > \Phi$ enclosing a scatterer (Figure 1). This surface is composed of two joined semi-infinite polygonal faces, denoted + and $-$, respectively with $m^{\pm}$ segments of lengths $d^{\pm}_{j}$ with tangent angles $\pm\Phi^{\pm}_{j}$, $j = 1, 2, \ldots,\ m^{\pm}$ and a semi-infinite plane with tangent angles $\pm\Phi^{\pm}_{e}$. Then, the single face expression of the spectral function f becomes [2]

$$\begin{aligned} f(\alpha) \ =\ & \frac{1}{2}\sum_{1\le j\le m^\pm} e^{-ik\sum\limits_{1\le i<j} d^{\pm}_{i}\cos(\alpha\mp\Phi^{\pm}_{i})} \int_0^{d^{\pm}_{j}} (-iku(\rho'_j,\pm\Phi^{\pm}_{j})\sin(\alpha\mp\Phi^{\pm}_{j}) \\ & \pm\frac{\partial u}{\partial n}(\rho'_j,\pm\Phi^{\pm}_{j}))e^{-ik\rho'_j\cos(\alpha\mp\Phi^{\pm}_{j})})d\rho'_j + e^{-ik\sum\limits_{1\le i\le m^\pm} d^{\pm}_{i}\cos(\alpha\mp\Phi^{\pm}_{i})} f^{\pm}_{e,m^\pm}(\alpha), \end{aligned} \quad (5)$$

where $f^{\pm}_{e,m^\pm}(\alpha)$ is the analytic continuation of the integral expression

$$f^{\pm}_{e,m^\pm}(\alpha'\pm\Phi^{\pm}_{e}) = \frac{1}{2}\int_0^{\infty}(-iku(\rho'_e,\pm\Phi^{\pm}_{e})\sin\alpha'\pm\frac{\partial u}{\partial n}(\rho'_e,\pm\Phi^{\pm}_{e}))e^{-ik\rho'_e\cos\alpha'}d\rho'_e, \quad (6)$$

valid as $\mathrm{Re}(ik(\cos\alpha' - \cos(\Phi^{\pm}_{e}\mp\varphi_o))) > 0,\ |\mathrm{Re}\alpha'| < \pi,\ |\arg(ik)| < \frac{\pi}{2}$.

This original expression of the spectral function and its properties enable us to derive, for the first time, the functional equations for the spectral functions for scattering by a general impedance polygon with finite or infinite surface [2], and to reduce generally the problem to a system of Fredholm integral equations of the second kind with non-singular kernels, allowing approximations.

We apply in particular this approach to the important class of three-part impedance polygons composed of a finite segment attached to two semi-infinite planes, and show how to decouple the set of integral equations in some particular cases, then we study particular properties of kernels permitting approximations when the wave number k is large or small.

REFERENCES

1. Bernard, J. M. L., "Scattering by a three-part impedance plane: a new spectral approach," *Quarterly J. of Mech. and Appl. Mathematics*, Vol. 58, No. 3, 383–418, 2005.
2. Bernard, J. M. L., "A spectral approach for scattering by impedance polygons," *Quarterly J. of Mech. and Appl. Math.*, Vol. 59, No. 4, 517–549, 2006.

A Finite Difference Frequency Domain Study of Curvature Lifted Modes Degeneration

C. S. Lavranos and G. A. Kyriacou

Microwaves Lab., Department of Electrical & Computer Engineering
Democritus University of Thrace, 12 Vas. Sofias St., Xanthi 67100, Greece

Abstract— The curvature induced degenerated modes separation in curved waveguides is studied in this paper. The analysis of curved waveguides is performed by using a two dimensional (2-D) Finite Difference Frequency Domain (FDFD) eigenvalue method employing orthogonal curvilinear coordinates. The eigenvalues frequency spectrum (propagation constants dispersion curves) of curved circular waveguides is considered. Curvature lifted modes degeneration is observed in these numerical results. The accuracy of the method is examined through comparisons with already published results.

1. INTRODUCTION

Curved waveguides have become a significant key in the design of several microwave circuits and systems. A variety of applications like moving airborne platforms or modern phased arrays carrying microwave transmit-receive systems require their antennas to be made conformal to the objects surface. The recent adoption of "smart skin" ideas asks for the whole RF front end to be made conformal to the host object's surface. This approach enforces printing or integrating microwave devices on curved surfaces. The curvature varies from canonical objects surfaces as cylinders, to almost arbitrary (usually aerodynamic) curvatures. In turn, a plethora of microwave devices can be considered as comprised of curved waveguiding sections. Therefore, the accurate design of conformal systems requires the knowledge of curved waveguides and particularly printed transmission lines characteristics. This paper contributes exactly to this specific research field.

Despite its apparent simplicity, the analysis of propagation in a curved waveguide continues to be a challenging electromagnetic problem. Since the publication of Lewin et al book in 1977, [1], an extensive research on curved waveguides has been carried out, e.g., [2–4]. However, these works were mainly restricted to the study of canonical geometries. In Particular, Lewin et al., [1], investigated E- and H- plane bends of rectangular or circular waveguides with a perturbation method. Besides, other perturbation methods were employed for the analysis of curved waveguides mainly in the optical spectrum, for example Xi Sheng Fang, [2]. Within this effort the "expansion of the bend modes into straight waveguide modes" was also employed by many researchers, e.g., [3]. Experiments with bends in nonradiative dielectric waveguides were also performed, [4].

Concerning the analysis of practical devices, numerical methods like the two dimensional Finite Element Method (FEM) or the Method of Moments (MoM) are in principle capable of handling curved geometries e.g., [5–6]. Yet, FEM is unable to handle waveguide curvatures in the propagation direction and MoM involves the Green's functions of the structure which are not usually available for arbitrary shaped curved geometries. Hence, these methods by no means can serve as a general tool for the analysis of arbitrary curved waveguides.

Our research effort is based on a two-dimensional Finite Difference Frequency Domain (2-D FDFD) eigenvalue method formulated in orthogonal curvilinear coordinates. The theoretical basics have been presented in our previous works, [7–8]. This analysis is formulated as an eigenvalue problem for the complex propagation constants. It is restricted to structures uniform along the propagation direction. The waveguiding structure can be curved in all directions and this constitutes its main advantage. Besides that, it retains the classical FDFD method capability of handling arbitrary shaped geometries loaded with either isotropic or anisotropic materials.

The present work mainly focuses on the degenerated modes separation. For instance, in straight circular waveguides the TE_{01} and TM_{11} modes are degenerative, namely they present the same dispersion curves. Besides that, all right and left hand circularly polarized modes are also degenerative. When the waveguide is curved - bend the degeneration is lifted and the dispersion curves are separated. This phenomenon must be distinguished from the "birefringence", where a new mode (not existed before) is generated due to some perturbation, for example a material anisotropy. In the following sections this phenomenon will be studied for a curved circular waveguide.

2. GEOMETRY OF A CURVED CIRCULAR WAVEGUIDE

The curved circular waveguide geometry shown in Fig. 1(a) will be studied, where the modified cylindrical coordinate system $(\hat{\rho}, \hat{\varphi}, \hat{s})$ introduced in [1] will be employed. This geometry is obtained by bending a straight circular waveguide, so that its symmetry axis-z forms an arc with radius R. The unit vector $\hat{s}$ is tangential to this arc, which also defines the propagation direction.

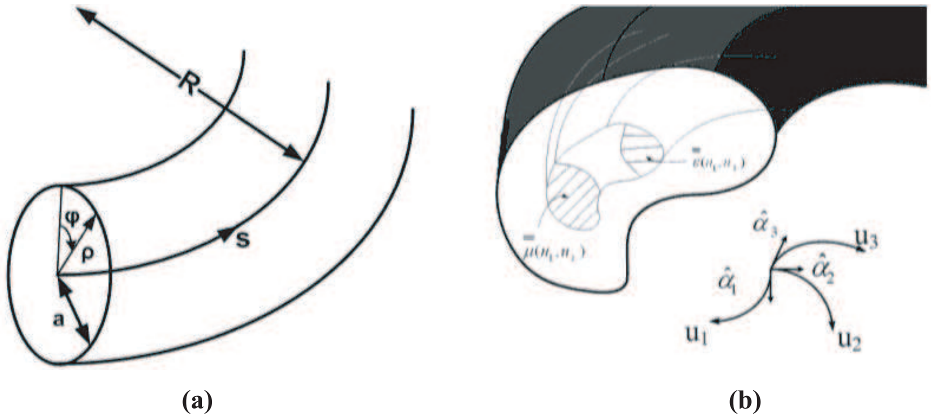

Figure 1: a) A curved circular waveguide. R is the curvature radius, b) An arbitrary curved waveguide.

Thus, the assumed propagation can be represented as, e.g., [1]:

$$E(\rho, \varphi, s) = E(\rho, \varphi) \cdot e^{-j\beta s} \quad \text{and} \quad H(\rho, \varphi, s) = H(\rho, \varphi) \cdot e^{-j\beta s} \tag{1}$$

3. THE 2-D FDFD EIGENVALUE METHOD FOR CURVED WAVEGUIDES

In order to analyze the specific geometry of Fig. 1(a), the general purpose 2-D FDFD method established in our previous works, [7–8] is employed. This approach considers an orthogonal curvilinear coordinate system $(\hat{u}_1, \hat{u}_2, \hat{u}_3)$ as shown in Fig. 1(b). The next paragraphs give a short description of the method.

Maxwell's curl equations for the electric and magnetic field are expressed in $(\hat{u}_1, \hat{u}_2, \hat{u}_3)$ coordinates system according to [9]. The wave is assumed to propagate along the $\hat{u}_3$-direction similar to equation (1), while the cross section $(\hat{u}_1, \hat{u}_2)$ of the waveguide structure can be of arbitrary geometry loaded with inhomogeneous and in general anisotropic materials. In order to ensure the problem's correct establishment the curvature of the guide axis is restricted to constant curvatures, [9]. A key point of the analysis is the separation of the field into axial and transverse components. In this manner the electric fields curl equation reads:

$$\overline{\nabla} \times \overline{E} = -j\omega\overline{\overline{\mu}}\overline{H} \rightarrow \begin{bmatrix} -(j\beta) \cdot (\frac{1}{h_3}) \cdot \hat{a}_3 \times (\cdot) & -\hat{a}_3 \times ((\frac{1}{h_3}) \cdot \overline{\nabla}_{tc}(\cdot)) \\ -\overline{\nabla}_{tc} \cdot \hat{a}_3 \times (\cdot) & 0 \end{bmatrix} \begin{bmatrix} \overline{E}_t \\ h_3 E_3 \end{bmatrix} = -j\omega \begin{bmatrix} \overline{\overline{\mu}}_{tt} & \overline{\mu}_{tl} \\ \overline{\mu}_{lt} & \mu_{ll} \end{bmatrix} \begin{bmatrix} \overline{H}_t \\ H_3 \end{bmatrix} \tag{2}$$

where $\overline{\nabla}_{tc} = \hat{a}_1(\frac{1}{h_1}) \cdot \frac{\partial}{\partial u_1} + \hat{a}_2(\frac{1}{h_2}) \cdot \frac{\partial}{\partial u_2}$ and h_1, h_2, h_3 are the scale (or metric) factors. These metric factors in the modified cylindrical coordinate system $(\hat{\rho}, \hat{\varphi}, \hat{s})$, according to [1], are:

$$h_\rho = 1, \quad h_\varphi = \rho, \quad h_s = 1 - \rho \cos\varphi / R \tag{3}$$

Likewise, its dyadic expression representing the curl of magnetic field is obtained. These two expressions are in turn discretized with the aid of a curvilinear grid over the whole solution domain, according to the basic principles of Yee's cell, [10]. The discretized form of (2) and its dyadic are then formulated in a non-deterministic eigenproblem of the form $[A][u] = \beta[u]$. Vector $[u]$ is the eigenvector and β the sought eigenvalue. Matrix $[A]$ consists of sub-matrices, which represent the discrete form of the basic operators, such as the gradient and the divergence. Every single operator is descretized with respect to the curvilinear mesh. The boundary conditions are incorporated into this system by direct modification of the matrices involved. Due to the sparcity of these matrices, the final eigenvalue problem is solved using the Arnoldi Algorithm, [11].

4. NUMERICAL RESULTS & DISCUSSIONS

Numerical tests are carried out for two curved circular geometries. First, an empty curved circular waveguide of radius 0.02 m as shown in Fig. 1(a) is simulated. Dispersion curves for two indicative curvature radiuses are given in Fig. 2. In this case, the TE_{01} and TM_{11} mode degeneration lifting is studied. In straight waveguides this degeneration becomes triple for the TE_{01} and TM_{11} modes. Namely, TE_{01}, left hand circularly polarized and right hand circularly polarized TM_{11} modes have the same dispersion curves. The waveguide curvature breaks this degeneracy and separates these three modes as shown in Fig. 2. However, these modes are not completely independent. Lewin et al., [1], studied this case and distinguished these three separated modes of the curved circular waveguide as one pure TM_{11} and two distinct modes similar to the sum and difference of TE_{01} and TM_{11} mode. These two modes seem to be resulting from a coupling between TE_{01} and TM_{11} modes of the straight waveguide. Lewin et al. spotted on these two mixed modes and gave the propagation constants correction formula for a curved circular waveguide with inner radius α and curvature radius R as, [1]:

$$\Delta\beta = jk\sqrt{2}/\Gamma_0 R \quad \text{where} \quad \Gamma_0 = j_{11}/\alpha,\ J_1(j_{11}) = 0 \tag{4}$$

As explained by Lewin and also noticed in Fig. 2, these two mixed modes dispersion curves are shifted symmetrically upwards and downwards with respect to those of the straight case. In addition, the curved TM_{11} mode's dispersion curve is slightly shifted downwards comparing also to that of the straight case. Our numerical results are mainly focused on the mixed modes; let's denote them as TE_{01a} and TE_{01b}. These are compared with the propagation constants correction formula (4). In Fig. 2(a) the curvature radius is 25 times the waveguide dimension while in Fig. 2(b) this ratio is 10. Fig. 2(a) shows that the propagation constants change for the two mixed modes is about to 1% upwards and downwards. On the other hand, for a smaller curvature radius as shown in Fig. 2(b), the propagation constants change rises to 3%. The deviation between our results and (4) in both cases is smaller than 0.07%, so a good agreement is observed. Moreover, the curved TM_{11} mode's dispersion curve shown in Fig. 2(a) is almost the same with that of TM_{11} mode in the straight waveguide, while in Fig. 2(b) a difference of about 1% is observed. However, propagation constants correction formula for curved TM11 mode is not given in [1], so comparison can not be done. It is important to note, that when the curvature radius becomes significantly small the agreement between our results and (4) breaks down. That's because Lewin's theory as well as our method are not accurate for significantly small curvature radiuses, due to the restrictions that are imposed.

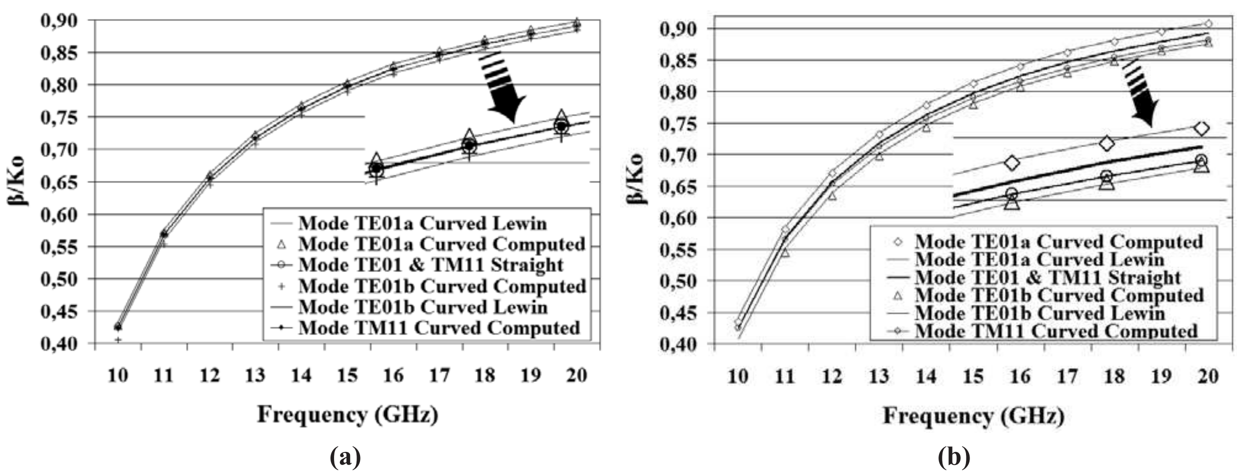

Figure 2: Dispersion curves of coupled TE_{01a} and TE_{01b} modes in a curved circular waveguide of radius 0.02 m for two curvature radiuses: a) 0.5 m, b) 0.2 m, compared with those given by Lewin, [1]. The dispersion curves of degenerated TM_{11}/TE_{01} mode in a straight circular waveguide with the same dimensions along with those of TM_{11} mode in the curved circular waveguide are depicted.

Since the method is validated in the first example, the second example refers to a partially loaded curved circular waveguide as shown in Fig. 3(a). In the corresponding straight waveguide all right and left hand circularly polarized modes are degenerative. On the other hand, in the curved waveguide all these degenerative modes are separated. As shown in Fig. 3(b) the first mode of the straight waveguide which was degenerative is spitted now to two distinct modes. In contrary to the first example, the two modes dispersion curves are both shifted upwards comparing to that of the straight waveguide after 7 GHz. But, at lower frequencies the dispersion curve of mode 1a was shifted downwards.

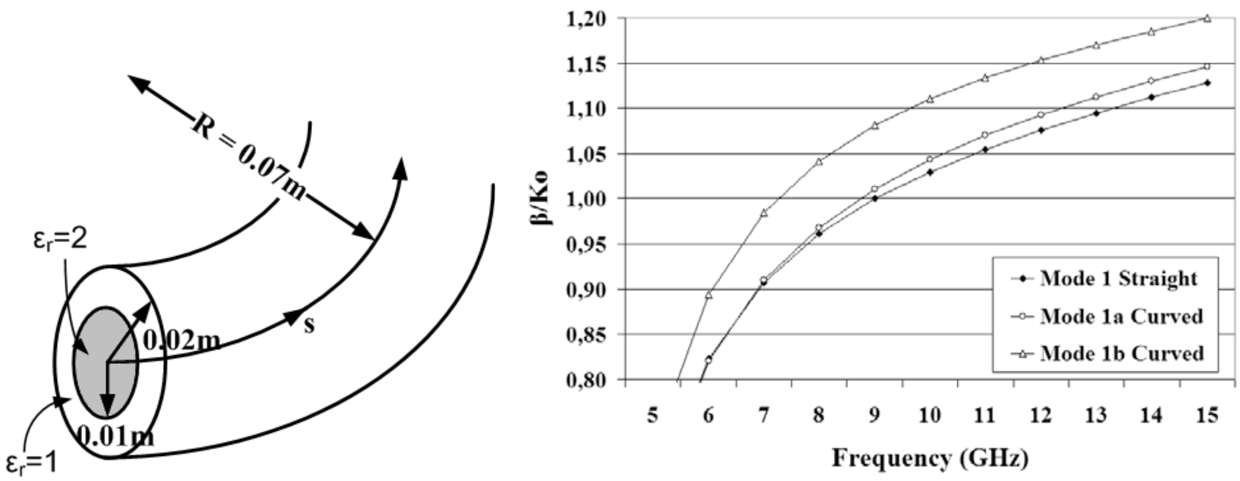

(a) (b)

Figure 3: a) A curved circular partially loaded waveguide, b) Dispersion Curves of mode 1a and mode 1b in the curved circular partially loaded waveguide compared with that of mode 1 in the corresponding straight waveguide.

5. CONCLUSIONS

Numerical results for the curvature induced degenerated modes separation in a curved circular waveguide were presented in this paper. The propagation constants dispersion curves for two curved circular geometries were computed with our already proposed two dimensional (2-D) Finite Difference Frequency Domain (FDFD) curvilinear eigenvalue method. The results were validated by comparison to already published ones. An important conclusion is that all these studied phenomena can not be characterized as birefringence phenomena, because all the "new" separated modes were existed as degenerative in the straight waveguide. A variety of simulations for different curved structures will be presented at the conference along with a discussion on a number of new subjects that need investigation.

ACKNOWLEDGMENT

This work is implemented in the framework of Measure 8.3 through the O.P. Competitiveness 3rd Community Support Programme and is co-funded by: 75% of the Public Expenditure from the European Union — European Social Fund, 25% of the Public Expenditure from the Hellenic State — Ministry of Development — General Secretariat for Research and Technology, and Private Sector (INTRACOM SA).

REFERENCES

1. Lewin, L., D. C. Chang, and E. F. Kuester, *Electromagnetic Waves And Curved Structures*, Peregrinus, London, U.K., 1977.
2. Fang, X.-S. and Z.-Q. Lin, "Birefringence in curved single-mode optical fibers due to waveguide geometry effect — Perturbation analysis," *Journal of Lightwave Technology*, Vol. LT-3, No. 3, 789–794, June 1985.
3. Melloni, A., F. Carniel, R. Costa, and M. Martinelli, "Determination of bend mode characteristics in dielectric waveguides," *Journal of Lightwave Technology*, Vol. 19, No. 4, 571–577, April 2001.
4. Yoneyama, T., M. Yamaguchi, and S. Nishida, "Bends in nonradiative dielectric waveguides," *IEEE Trans. Microwave Theory Tech.*, Vol. MTT-30, No. 12, 2146–2150, Dec. 1982.

5. Marais, N. and D. B. Davidson, "Numerical evaluation of hierarchical vector finite elements on curvilinear domains in 2-D," *IEEE Trans. Antennas Propagation*, Vol. 54, No. 2, 734–738, Feb. 2006.
6. Blas, A. A. S., B. Gimeno, V. E. Boria, H. Esteban, S. Cogollos, and A. Coves, "A rigorous and efficient full-wave analysis of uniform bends in rectangular waveguide under arbitrary incidence," *IEEE Trans. Microwave Theory Tech.*, Vol. 51, No. 2, 397–405, Feb. 2003.
7. Lavranos, C. S. and G. A. Kyriacou, "Eigenvalue analysis of curved open waveguides using a finite difference frequency domain method employing orthogonal curvilinear coordinates," *PIERS Online*, Vol. 1, No. 3, 271–275, 2005.
8. Lavranos, C. S. and G. A. Kyriacou, "Eigenvalue analysis of curved waveguides employing FDFD method in orthogonal curvilinear co-ordinates," *IEE Electronic Lett.*, Vol. 42, No. 12, 702–704, June 2006.
9. Lewin, L., "A decoupled formulation of the vector wave equations in orthogonal Curvilinear Coordinates, with application to ferrite- filled and curved waveguide of general cross section," *IEEE Trans. Microwave Theory Tech.*, Vol. MTT-20, 338–342, May 1972.
10. Yee, K. S., "Numerical solution of initial boundary value problems involving Maxwell's equation in isotropic media," *IEEE Trans. Antennas Propagation*, Vol. AP-14, 302–307, May 1966.
11. Sorensen, D. C., "Implicit application of polynomial filters in a K-step Arlondi method," *SIAM J. Matrix Analysis and Applications*, Vol. 13, No. 1, 357–385, Jan. 1992.

Optimization of a Microwave Amplifier Using Neural Performance Data Sheets with a Memetic Algorithm

Y. Cengiz[1], **F. Güneş**[2], **and U. Kılıç**[3]

[1]Department of Electronics and Communication Engineering
Süleyman Demirel University, Isparta, Turkey
[2]Department of Electronics and Communication Engineering
Yıldız Technical University, Beşiktaş, Istanbul, Turkey
[3]Akdeniz University, Antalya, Turkey

Abstract— In this work, the neural performance data sheets of the transistor are employed to determine the feasible design target space in the optimization of a microwave amplifier. In order to obtain these data sheets the ANN model of the active device is utilized to approximate the small-signal [S] and noise [N] parameter functions in the operation domain. Inputting of these characterization parameters into the performance characterization of the device results in the triplet of gain G_T, noise F, and input VSWR V_i and its source (Z_S) and load (Z_L) termination functions in the operation domain, from which the neural performance data sheets can be obtained. The memetic algorithm with the decimal mode is utilized in the multi-objective optimization process for the global minimum of the objective function which is expressed as a function only gain of a matching circuit, in the negative exponential form to ensure the rapid convergence. Here optimization of a microwave amplifier with the matching circuits is given as a worked example and its resulted performance ingredients are compared with the design targets.

1. INTRODUCTION

Characterization of active microwave devices and design of the wideband microwave amplifiers can still be considered as a state of art in microwave engineering. Especially, in designing microwave amplifiers, many sophisticated numerical methods are utilized to optimize the system performance. Generally, the optimization is focused on the transducer power gain (G_T) over the band of operation without being aware of the other performance criteria such as noise (F), the input VSWR (V_i) and the output VSWR (V_o). It should also be mentioned that the optimization process of the performance is highly non-linear in terms of descriptive parameters of the system. Certainly, within the optimization process, one can easily imbed the desired performance goals without knowing physical limits and/or compromise the performance merits among (F), VSWR and (G_T) appropriately. But unfortunately, this process often fails in hitting the desired goals. However the work presented in this paper overcomes all the above-mentioned handicaps.

Block diagram of the microwave amplifier considered in this work is given in the Figure 1, where the input (IMC) and output (OMC) matching circuits are lossless and reciprocal and designed by transmission line segments in Π- and T- configurations, respectively.

The stages of the work can be ordered as follows:

(i) First stage is to obtain the potential performance characteristics of the given transistor and to choose a compatible $F(\omega_i)$, $V_i(\omega_i)$, $G_T(\omega_i)$ triplet together with the termination functions $Z_L(\omega_i)$, $Z_S(\omega_i)$, for $i = 1, \dots, N$;
(ii) Second stage is to form $F(\omega)$, $V_i(\omega)$, $G_T(\omega)$ functions in term of circuit parameters for the given configuration;
(iii) Third stage is to determine the optimization vector and the objective function to be minimized in the optimization process;
(iv) Final stage is to apply chosen data processing techniques to calculate the optimization vector and to form the circuit and resulted characteristics.

Design potential characteristics and $F(\omega)$, $V_i(\omega)$, $G_T(\omega)$ function are given in the next section.

We present a method called Memetic Algorithm (MA) for solving the optimization problem. The term 'MA' was introduced by Moscato and Norman. Memetic algorithm is a kind of an improved type of the traditional genetic algorithm. By using local search procedure, it can avoid the shortcoming of the traditional genetic algorithm, whose termination criteria are set up by using the trial and error method. For many problems, there exists a well-developed, efficient search strategy for local improvement, e.g., hill-climber for optimization. These local search strategies make the searching convergence reasonable, yielding a more efficient overall search strategy. A search procedure based on the memetic algorithm is used to obtain the required perturbations for the designed patterns with null steering. This procedure for the proposed nulling techniques provides an iterative solution. The excellent nulling results are derived in this paper. For our paper, the proposed numerical method can be used in a real time signal processing and the wireless mobile communication [1].

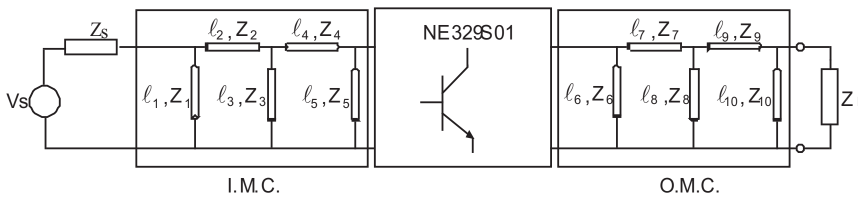

Figure 1: The Single Transistor Amplifier with the "Π" + "L" Type Matching Circuits.

2. POTENTIAL PERFORMANCE CHARACTERISTICS

Potential performance characteristics of a microwave transistor is obtained from the following three major stages:

(i) In the first stage, the signal and noise behaviors of the transistor is modeled by a multiple bias and configuration, signal-noise neural network or fuzzy logic. So the scattering (S) and the noise (N) parameters are resulted from the output of this neural network and fuzzy logic as the functions of the configuration type (CT), the bias condition (V_{DS}, I_{DS}) and the operation frequency (f).

This part of the work can be considered as the function approximation through neural network and fuzzy logic and include highly accurate approximations of the 8 scattering and 4 noise functions [2, 3].

(ii) Second stage consists of determining of the Compatible Performance (F_{req}, V_{ireq}, G_{Treq}) Triplets and their associated source (Z_{Sreq}) and load (Z_{Lreq}) terminations. In this part of the work, a Computer Program based upon the formulation of "Performance Characterization" theory for the transistor is employed [4, 5].

Input of the second block are the scattering and the noise parameters resulted from the signal-noise neutral network, and the free variables of $F_{req} > F_{\min}$, $V_{ireq} > 1$, $G_{T\min} < G_{Treq} < G_{T\max}$.

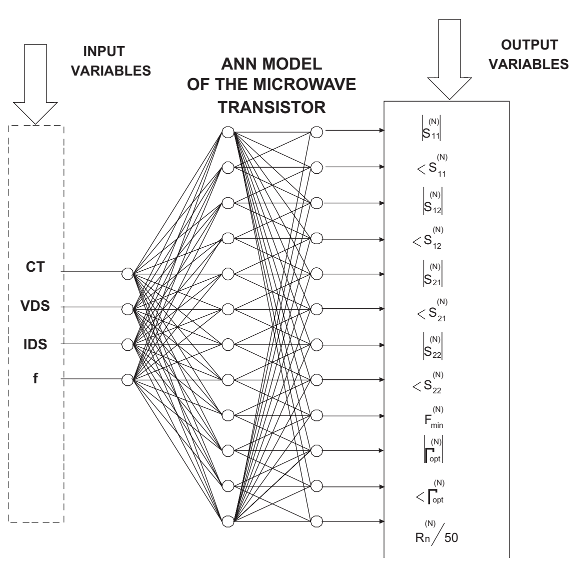

Figure 2: Neural network model for a microwave transistor.

The second block results in the following triplet and termination data in the operation domain of the device:

$$
\begin{array}{lcl}
(F_{req}, V_{ireq}, G_{T\max}) & \Leftrightarrow & Z_{S\max} = R_{S\max} + jX_{S\max}, \\
 & & Z_{L\max} = R_{L\max} + jX_{L\max}; \\
(F_{req}, V_{ireq}, G_{T\min}) & \Leftrightarrow & Z_{S\min} = R_{S\min} + jX_{S\min}, \\
 & & Z_{L\min} = R_{L\min} + jX_{L\min}; \\
(F_{req}, V_{ireq}, G_{Treq}) & \Leftrightarrow & Z_{Sreq} = R_{Sreq} + jX_{Sreq}, \\
 & & Z_{Lreq} = R_{Lreq} + jX_{Lreq}.
\end{array} \tag{1}
$$

(iii) Final stage of this part of the work is to obtain the potential performance characteristics of the transistor for the design of the broadband microwave amplifier. In fact, there may be numerous number of the performance characteristics [6]. It should be noted that the potential characteristics should let the designer know the amount of bias condition (V_{DS}, I_{DS}), input mismatching (V_{ireq}), noise F_{req}, gain G_{Treq} and the resulted operation bandwidth B.

Since the heart of the design is the compatible (F, V_i, G_T) triplets and their (Z_S, Z_L) terminations, so their properties are given in the next section without having the method utilized in the Performance Characterization. In the later sections worked examples of the design for the potential performance and computed results are given.

3. COMPUTED RESULTS

The aim of the optimization is to obtain a flat gain response subject to the constraint functions $V_{ireq}(\omega)$, $F_{req}(\omega)$ in the frequency band of interest. It should be pointed out that stability is not included to the optimization as a constraint since all gains values G_T between $G_{T\max}$ and $G_{T\min}$ take place in the "Unconditionally Stable Working Area" (USWA).

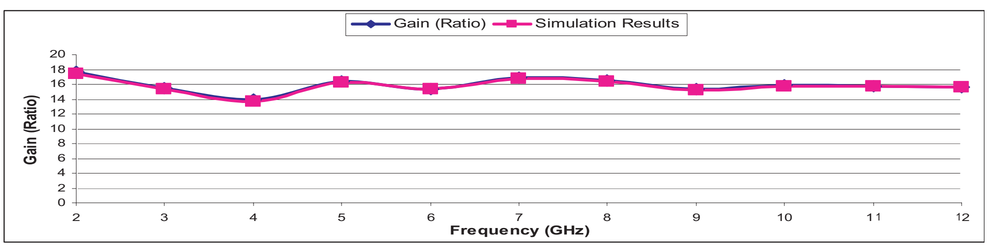

(a)

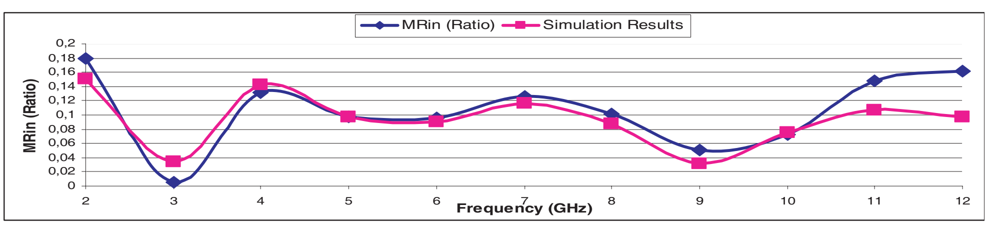

(b)

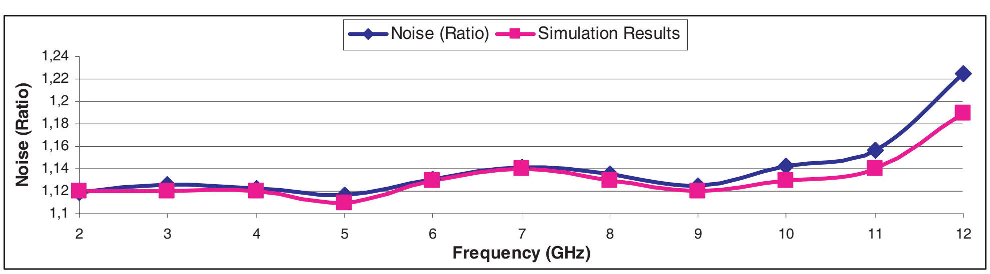

(c)

Figure 3: (a) G_T (ratio) variation of the microwave amplifier, (b) Noise (ratio) variation of the microwave amplifier, (c) Input reflection coefficient variation of the microwave amplifier $G_{Treq}(ratio) = 15.85$, $V_{ireq}(ratio) = 1.0$, $F_{req}(ratio) = 1.11$.

In this work, memetic data processing is worked out for the global minimum of the objective function. Input and output matching circuits are optimized separately using the required terminations. Figures 3(a), 3(b) and 3(c) give the overall Gain G_T (ratio), Noise F (ratio) and Input VSWR V_i variations over the operation band, compared with the results obtained by a professional microwave program. Bandwidth of amplifier is between 3 GHz and 11 GHz

NE329S01 is biased at $I_C = 5\,\mathrm{mA}$ and $V_{CE} = 10\,\mathrm{V}$, for which the potential performance characteristics are given $F_{req}(\omega_i) = 0.46\,\mathrm{dB}$, $V_{ireq}(\omega_i) = 1.0$, $G_{Treq}(\omega_i) = 12\,\mathrm{dB}$, $i = 2, \ldots, 12$ are supplied into the optimization process as the target values over the operation bandwidth. These reference values give the physically realizable $Z_S(\omega_i) = R_S(\omega_i) + jX_S(\omega_i)$; $Z_L(\omega_i) = R_L(\omega_i) + jX_L(\omega_i)$, $i = 2, \ldots, 12$ termination solutions to the simultaneous nonlinear equations of $F(R_S, X_S) = F_{req}$, $V_i(R_S, X_S, R_L, X_L) = V_{ireq}$, $G_T = (R_S, X_S, R_L, X_L) = G_{Treq}$. Since the optimization process also find out the approximately solutions to the same equations in terms of the predetermined variables, so the values will no longer be computed design equal to the reference values, but will be values nearly the reference values ruled by the objective function and the data processing method. "Π" + "L" type matching circuit of all kinds of optimization vector. Matching circuit parameters for NE329S01 transistor are found as follows:

Table 1: Computed results for the performance and design parameters of the microwave amplifier.

Frequency (GHz)	Gain (Ratio)	Simulation Results	MRin (Ratio)	Simulation Results	Noise (Ratio)	Simulation Results
2	17,65	17,4	0,18	0,15	1,12	1,12
3	15,52	15,3	0,01	0,03	1,13	1,12
4	13,91	13,7	0,13	0,14	1,12	1,12
5	16,44	16,3	0,10	0,10	1,12	1,11
6	15,42	15,3	0,10	0,09	1,13	1,13
7	16,88	16,8	0,13	0,12	1,14	1,14
8	16,50	16,4	0,10	0,09	1,14	1,13
9	15,33	15,2	0,05	0,03	1,12	1,12
10	15,91	15,7	0,07	0,08	1,14	1,13
11	15,59	15,8	0,15	0,11	1,16	1,14
12	15,76	15,6	0,16	0,10	1,22	1,19

$l_1 = 1.098\,\mathrm{cm}$, $l_2 = 15\,\mathrm{cm}$, $l_3 = 14.335\,\mathrm{cm}$,
$l_4 = 13.83\,\mathrm{cm}$, $l_5 = 0.688\,\mathrm{cm}$, $l_6 = 13.90\,\mathrm{cm}$,
$l_7 = 1.211\,\mathrm{cm}$, $l_8 = 0.877\,\mathrm{cm}$, $l_9 = 7.107\,\mathrm{cm}$,
$l_{10} = 0.979\,\mathrm{cm}$, $Z_1 = 117.91\,\Omega$, $Z_2 = 150\,\Omega$,
$Z_3 = 39.49\,\Omega$, $Z_4 = 51.64\,\Omega$, $Z_5 = 132.05\,\Omega$,
$Z_6 = 89.36\,\Omega$, $Z_7 = 103.21\,\Omega$, $Z_8 = 50.46\,\Omega$,
$Z_9 = 50.16\,\Omega$, $Z_{10} = 150\,\Omega$,

4. CONCLUSIONS

In this work, the major problems of optimization of a microwave amplifier are solved employing novel computation methods. Feasible design target space is determined by defining small-signal and noise behaviors of the active device throughout its operation domain employing ANN as a novel function approximator. At each operation point, "Performance Characterization" theory is utilized to determine the Compatible Triplets and their terminations. Two simple objective functions are used in terms of gain for the multi-objective optimization of the circuit. Memetic data processing is employed successfully for the global optimization of each objective function. Since system approach is used, the method is applicable to any amplifier in any configuration. Here a work example is also given with an amplifier "Π" + "L" type matching.

REFERENCES

1. Hsu, C, W. Shyr, and C. Chen, "Adaptive pattern nulling design of linear array antenna by perturbations using memetic algorithms," *Proceedings of the First International Conference on Innovative Computing, Information and Control (ICICIC'06)*, IEEE 2006.
2. Güneş, F., H. Torpi, and F. Gürgen, "A multidimensional signal-noise neural model for microwave transistors," *IEE Proc.-Circuit Devices and Systems*, Vol. 145, No. 2, 11–117, 1998.
3. Cengiz, Y., F. Güneş, and M. F. Çağlar, "Soft computing methods in microwave active device modeling," *Third International Conference on Electrical and Electronics Engineering ELECO'2003*, The Chamber of Electrical Engineers Bursa Section, Uludağ University Faculty of Engineering, İstanbul Technical University Electrical and Electronics Faculty, Bursa Türkiye, 3–7 December, 2003.

4. Güneş, F., M. Güneş, and M. Fidan, "Performance characterisation of a microwave transistor," *IEEE Proc. Circuits Devices System*, Vol. 141, No. 5, October 1994.
5. Güneş, F. and B. A. Çetiner, "Smith chart formulation of performance characterisation for a microwave transistor," *IEEE Proc. Circuits Devices Syst.*, Vol. 145, No. 6, December 1998.
6. Güneş, F. and C. Tepe, "Gain-bandwidth limitations for a microwave transistor," to be submitted into *RF and Microwave Computer Aided Engineering*, June 2001.

A Simple and Accurate Model for Wire Diagnosis Using Reflectometry

F. Auzanneau, **M. Olivas**, **and N. Ravot**
CEA LIST, France

Abstract— This paper proposes a new theoretical model allowing the numerical simulation of reflectometry signals for any kind of homogeneous wired network topology. Based on standard microwave propagation theory, this model provides simple explicit formulas for both Time Domain and Frequency Domain Reflectometry simulation, and helps to understand and explain reflectometry measurements results.

1. INTRODUCTION

Today's automotive electronic systems rely heavily on wired networks, and their near-future counterparts ("by wire" functions) will be based on high reliability wired interconnections. Aging wire has been identified as a major risk factor for aircrafts, this is true for many safety critical systems (systems whose failure may cause injury to human beings) such as cars, nuclear plant control systems, medical intensive care and life support systems.

To improve the reliability of wired networks or to help for maintenance purposes, the reflectometry method is the most promising approach. Based on the injection of probe signal(s) into the network and the analysis of the reflected signals, this method provides useful information for the diagnosis of electrical defects in wires.

Reflectometry can be divided into two main domains [1]: Time Domain Reflectometry (TDR) [2] and Frequency Domain Reflectometry (FDR) [3–4]. Both are based on the methodology described above. The main difference lies in the injection method and data processing. When the probe signal encounters an electrical discontinuity (defect, branch, impedance mismatch, etc) part of its energy is sent back to the injection port. In the time domain, the analysis of the reflected signal provides information about the topology of the network, in the frequency domain the analysis of the stationary waves also provides this information. Many different methods have been developed and sometimes implemented on real systems, for example to locate defects in aircraft wiring networks, in order to decrease maintenance duration and costs. Of course, data processing is an important phase for the accurate detection and localization of these defects [5], but a precise physical and numerical model is needed to improve their performances.

This paper proposes an accurate model of reflectometry signals for any wired network. Based on standard microwave propagation theory, this model provides simple explicit formulas for the simulation of both time domain and frequency domain reflectometry signals. Comparison with experimentation is good, and it can be applied to complex network topologies to provide a clear explanation of measured TDR or FDR signals.

This work is based on internal research at CEA LIST.

2. PHYSICAL MODEL AND APPLICATION TO Y-SHAPED STRUCTURE

High frequency propagation in a wire can be modeled with the so-called RLCG transmission line (TL) model. The analytical model has been developed in this paper [6].

Time domain reflectometry can be applied to complex wired networks, and this model can be adapted to such topologies. In the case of a "Y" shaped structure (Figure 1), several methods can provide the desired result. We use here the simplest one.

We consider in this paper a homogeneous network, i.e., all the branches are identical with characteristic impedance Z_c but the model can be easily extended to heterogeneous networks. In this example, the input port for the time domain reflectometry signal is port 0 ($x = 0$), and the other wires are loaded by reflection coefficients Γ'_2 and Γ'_3. These reflection coefficients can be used to simulate defects on TL 2 and 3. Then, the equivalent reflection coefficients Γ_2 and Γ_3 at the junction for lines 2 and 3 are given by :

$$\Gamma_{2,3} = \exp(-2\gamma\Gamma_{2,3}) \cdot \Gamma'_{2,3} \tag{1}$$

where Γ_2 and Γ_3 are the lengths of lines 2 and 3 respectively.

The equivalent impedances are given by:

$$Z_{2,3} = Z_c(1+\Gamma_{2,3})/(1-\Gamma_{2,3}) \tag{2}$$

We put these impedances in parallel and compute the associated reflection coefficient Γ_1: defining Z_1 as the equivalent impedance for Z_2 and Z_3 in parallel, we obtain

$$\Gamma_1 = (Z_1 - Z_c)/(Z_1 + Z_c) \tag{3}$$

Γ_1 is the reflection coefficient equivalent to the entire "Y" shaped structure, except for line 1; and is given by:

$$\Gamma_1 = \frac{-1+\Gamma_2+\Gamma_3+3\Gamma_2\Gamma_3}{3+\Gamma_2+\Gamma_3-\Gamma_2\Gamma_3} \tag{4}$$

Then, using (1), we get $\Gamma_0(\omega) = \Gamma(x=0,\omega)$, which is the equivalent reflection coefficient for the entire "Y" shaped structure:

$$\Gamma_0 = \exp(-2\gamma L_1)\cdot\Gamma_1 \tag{5}$$

where L_1 is the length of line 1.

Γ_0 is the frequency domain reflectometry signal. A "reflectometry impulse response" $h(t)$ for the "Y" shaped structure can also be deduced from these results. The output time domain reflectometry signal $s(t)$ is then obtained using inverse Fourier transform.

The function $h(t)$ is quite complex, due to the shape of Γ_1 given by (4). But, Γ_1 can be written in another form, which is more closely related to the physics of the signal propagation into the cables. Using simple polynomial division, (4) can be developed as:

$$\Gamma_1 = -1/3 + 4/9^*(\Gamma_2+\Gamma_3) - 4/27^*(\Gamma_2^2+\Gamma_3^2) + 16/27\Gamma_2\Gamma_3 - 4/81^*(\Gamma_2^3+\Gamma_3^3) - 8/27^*(\Gamma_2\Gamma_3^2+\Gamma_3\Gamma_2^2) + \dots \tag{6}$$

Equation (6) describes the interactions of the various signals propagating into the cables with the network itself.

The first term of (6) is $-1/3$: this term is the reflection coefficient of the input signal at the junction of line 1 with lines 2 and 3. It shows that 1/3 of the input signal's amplitude is reflected towards the input port, whatever the loads of lines 2 and 3. The minus sign accounts for an equivalent impedance lower than the characteristic impedance of the lines Z_c and will be seen on the reflectogram as a negative peak.

The second term is $4/9^*(\Gamma_2+\Gamma_3)$: this term corresponds to the part of the energy of the signals propagating through lines 2 and 3 coming back to the input port. 4/9 of the amplitudes of these signals, times the reflection coefficient of the load, arrive at the input port. Note that if $\Gamma_2 = -\Gamma_3$, this term vanishes: the two contributors cancel each other [7].

The rest of the energy of these signals propagates again into lines 2 and 3, and the third term of (6) describes these additional trips: $-4/27^*(\Gamma_2^2+\Gamma_3^2)+16/27\Gamma_2\Gamma_3$. The square terms are for the new round trips in lines 2 and 3, and the cross term is the energy exchange between the two lines. After these additional paths, part of the energy goes back to the input port, which is quantified by the numerical terms $-4/27$ and $16/27$. These results are confirmed by those of [7 — Figs. 3 and 5].

Going further in the polynomial division would lead to additional paths or interactions between line 2 and line 3. As each part of Equation (6) corresponds to outgoing signals, the energy stored in the network decreases. Then the numerical terms associated with the Γ_i^n become smaller as the polynomial degree n increases, thus the amplitudes of the corresponding peaks on the reflectogram also decrease.

Equations (5) and (6) provide a simplification of the impulse response $h(t)$:

$$h(t) = \frac{1}{2\pi}\left[-\frac{1}{3}\int_{-\infty}^{+\infty} e^{-2\gamma L_1+j\omega t}d\omega + \frac{4}{9}\int_{-\infty}^{+\infty}(\Gamma_2+\Gamma_3)\,e^{-2\gamma L_1+j\omega t}d\omega + \dots\right] \tag{7}$$

In the simple case of lossless line and frequency independent terminations (i.e., simple defects such as open or short circuits) $h(t)$ is a weighted sum of Dirac functions.

In (4) and (6), Γ_2 and Γ_3 play a symmetrical role, this means that if they have the same value ($\Gamma_2 = \Gamma_3$) they are indistinguishable. Then, if a defect causes TL 2 and 3 to be equivalent (same length, same load), there is ambiguity and the defect cannot be precisely located. This problem is treated in [8].

Figure 2 shows time domain reflectometry simulation results for a Y shaped network with $L_1 = 2\,\text{m}$, $L_2 = 1\,\text{m}$ and $L_3 = 2.3\,\text{m}$, ports 2 and 3 being loaded by either an open circuit ($\Gamma_{2,3} = 1$) or a short circuit ($\Gamma_{2,3} = -1$). The input signal corresponds on a Dirac pulse of unit amplitude.

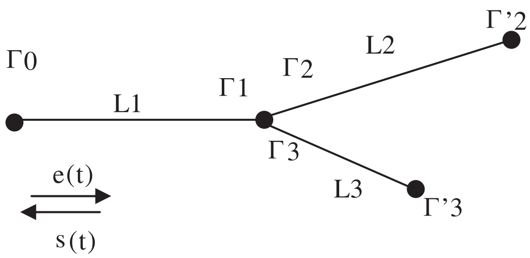

Figure 1: "Y" shaped structure.

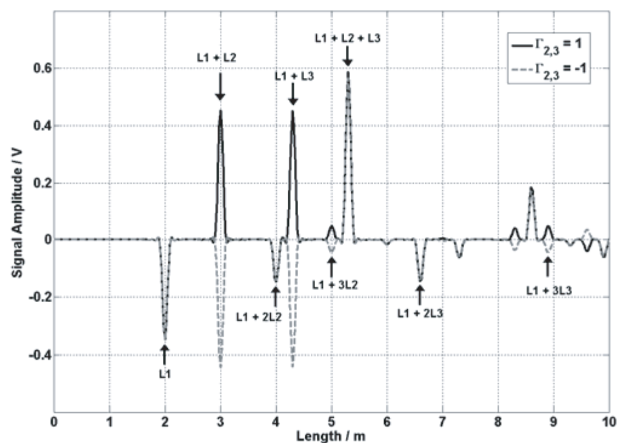

Figure 2: Time domain reflectometry simulation results for a Y shaped network with $L_1 = 2\,\text{m}$, $L_2 = 1\,\text{m}$ and $L_3 = 2.3\,\text{m}$, $\Gamma 2, 3 = 1$ — for simplicity, distances have been divided by two, to better show the line's lengths.

The first negative peak is the reflection at the junction (2 m); the amplitude is $-1/3$ as predicted. We can then see two peaks of equal amplitude, at distances 3 m and 4.3 m, corresponding to the round paths in TL 2 and 3. These two peaks are both negative when Γ_2 and Γ_3 are negative (short circuit). The amplitudes of these peaks (4/9) match the model. The negative peaks at distances 4 and 6.6 m are the additional round trips in lines 2 and 3. The positive peak at distance 5.3 m is the energy exchange between lines 2 and 3: its amplitude is higher than the previous positive peaks as predicted by the theory ($16/27 > 4/9$). The other peaks come from higher order paths.

3. TDR SIMULATION FOR A COMPLEX NETWORK TOPOLOGY

The results of section 2 can be generalized to more complex network structures, such as star shaped structures. A "star" is the junction of more than 3 lines. In this section the equivalent reflection coefficient has been derived for a star shaped junction and its lines.

This formalism can be used to simulate the time domain reflectometry signals for a much more complex network. The principle of the method is to divide the network topology into successive generic sub-networks of the shape shown on Figure 1. Then, one just needs to cascade the equivalent reflection coefficients to compute the Γ_0 reflection coefficient equivalent to the complete network. The generalized formulas have been developed in [6].

For example; we consider the network shown on Figure 3, made up of 3 simple topology sub-networks (A, B and C). We calculate the equivalent reflection coefficient of sub-network A with $n = 4$:

$$\Gamma_A = -\frac{1}{2} + \frac{\dfrac{\Gamma_2}{1+\Gamma_2} + \dfrac{\Gamma_3}{1+\Gamma_3} + \dfrac{\Gamma_4}{1+\Gamma_4}}{4 - 2\dfrac{\Gamma_2}{1+\Gamma_2} - 2\dfrac{\Gamma_3}{1+\Gamma_3} - 2\dfrac{\Gamma_4}{1+\Gamma_4}} \tag{8}$$

which can be simplified as follows:

$$\Gamma_A = \frac{-1 + \Gamma_2\Gamma_3 + \Gamma_2\Gamma_4 + \Gamma_3\Gamma_4 + 2\Gamma_2\Gamma_3\Gamma_4}{2 + \Gamma_2 + \Gamma_3 + \Gamma_4 - \Gamma_2\Gamma_3\Gamma_4} \tag{9}$$

In (9) we just have to replace Γ_3 and Γ_4 by the equivalent reflection coefficients of sub-networks

B, using (4) and (5):

$$\Gamma_2 = e^{-2\gamma L_2} \cdot \Gamma'_2, \quad \Gamma_3 = e^{-2\gamma L_3} \cdot \Gamma'_3, \quad \Gamma_5 = e^{-2\gamma L_5} \cdot \Gamma'_5, \quad \Gamma_6 = e^{-2\gamma L_6} \cdot \Gamma'_6,$$
$$\Gamma_4 = e^{-2\gamma L_4} \frac{-1 + \Gamma_5 + \Gamma_6 + 3\Gamma_5\Gamma_6}{3 + \Gamma_5 + \Gamma_6 - \Gamma_5\Gamma_6}.$$

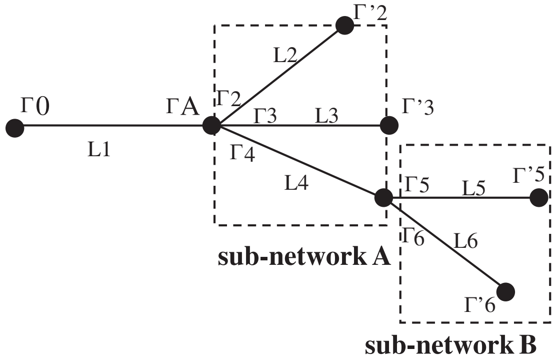

Figure 3: An example of complex network topology.

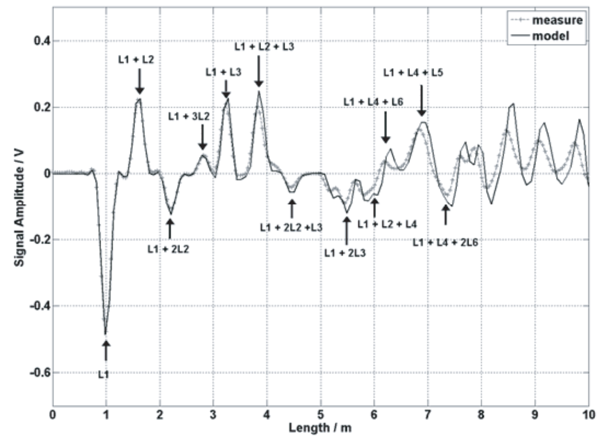

Figure 4: TDR simulation results for a complex network — for simplicity, distances have been divided by two, to better show the line's lengths.

Table 1: Line lengths for the network simulation.

L_1	1.00 m	L_4	4.25 m
L_2	0.60 m	L_5	1.75 m
L_3	2.25 m	L_6	1.00 m

Then, the equivalent reflection coefficient for the entire network is calculated:

$$\Gamma_0 = e^{-2\gamma L_1} \cdot \Gamma_A. \tag{10}$$

Most of these peaks can be recognized on Figure 4, some of them being very close produce larger peaks.

We have compared our model to real measurements, for a complex network made of KX22A coaxial cables referring to the dash-line on Figure 3. TL number 2, 3, 5 and 6 are open-circuited.

The impulse response is deduced from the measurement of the $S11$ parameter with a vector network analyzer (VNA) in frequency domain from 300 KHz to 500 MHz, connecting the ports of the VNA to line number 1.

Figure 4 presents a good agreement between measure and simulation, both for positions and amplitudes of the main peaks, the third order peak being a little bit overestimated by the model, probably due to losses in the connectors.

4. CONCLUSIONS

We have presented a theoretical model that enables to accurately simulate reflectometry signals for any kind of complex wired network topology. This method can handle both time domain and frequency domain reflectometry simulations and provide explicit formulas in both cases. It can be used as a theoretical model to help locate defects in the network (wired network diagnosis). If time domain or frequency domain reflectometry are used and a sudden change in the measurements is observed, this means that one or more defects appeared somewhere in the network and that reflectometry detected these defects. This model can then be used to locate the defects, by comparing the measurements to numerical simulation. An optimization algorithm (such as a genetic algorithm) can then be used to find the new topology of the network.

We provided a linear model up to third order which helps to understand time domain reflectometry results, by explaining the various peaks in terms of multiple paths inside the network. The third order is high enough because the amplitude of the peaks vanish with multiple paths and higher order terms become too weak to be detectable in real measurements.

ACKNOWLEDGMENT

This work is supported by a PREDIT contract called SEEDS (Smart Embedded Electronic Diagnosis Systems), in cooperation between DELPHI, SERMA INGENIEURIE, Monditech, LGEP, INRIA and CEA LIST.

REFERENCES

1. Furse, C., Y. Chung, C. Lo, and P. Pendayala, Invited Paper, "A critical comparison of reflectometry methods for location of wiring faults," *Journal of Smart Structures and Systems.*
2. Pan, T. W., C. W. Hsue, and J. F. Huang, "Time-domain reflectometry using arbitrary incident waveforms," *IEEE Trans. on Microwave Theory and Techniques*, Vol. 50, No. 11, Nov. 2002.
3. Van Hamme, H., "High resolution frequency domain reflectometry," *IEEE Trans. on Instrument and Measurement*, Vol. 39, No. 2, April 1990.
4. Furse, C., Y. C. Chung, and R. Dangol, "Frequency domain reflectometry for on board testing of aging aircraft wiring," *IEEE Trans. EMC*, Vol. 45, No. 2, 306–315, May 2003.
5. Djuric, M. B. and al, "Digital signal processing algorithms for arcing fault detection and fault distance calculation on transmission lines," *Elect. Power Energy Syst.*, Vol. 19, No. 3, 165–170, 1997.
6. Auzanneau, F. and N. Ravot, "Détection et localisation de défauts dans des réseaux filaires de topologie complexe," *Annals of Telecommunications*, Vol. 62, No. 1–2, January–February 2007.
7. Hartebrodt, M. and K. Kabitzsch, "Fault detection in fieldbuses with time domain reflectometry." *Proc. AFRICON2004 7th IEEE Africon Conference*, Vol. 1, 391–396, September 2004.
8. Ravot N., F. Auzanneau, Y. Bonhomme, M. Olivas, and F. Bouillault, "Distributed reflectometry-based diagnosis for complex wired networks," *EMC: Safety, Reliability and Security of Communication and Transportation Syst.*, EMC Workshop, Paris, June 2007.

Effect of Motion of the Scatterers on Localization: Quasi Localization and Quasi Mobility Edge

E. Kogan
Jack and Pearl Resnick Institute, Physics Department, Bar Ilan University
Ramat Gan 52900, Israel

Abstract— We study kinetics of electrons, scattered by heavy particles undergoing slow diffusive motion. In a three-dimensional space we claim the existence of the crossover region (on the energy axis), which separates the states with fast diffusion and the states with slow diffusion; the latter is determined by the dephasing time. In a two-dimensional space the diffusion coefficient for any value of energy is determined by the dephasing time. We discuss relevance of the results obtained for the propagation of light in a disordered medium.

Consider electrons in an inhomogeneous media. When discussing the kinetics of the electrons, the quantity, we usually start from in the theoretical description, is the transport relaxation time τ, calculated in Born approximation. Using Boltzmann equation we can obtain the relation between this relaxation time and the diffusion coefficient

$$D_0 = \frac{1}{3}v^2\tau, \tag{1}$$

where v is the electron velocity. However, the Boltzmann equation is valid provided $E\tau \gg 1$. If we take into account that $1/\tau(E)$ typically decreases slower than the first power of energy when the latter goes to zero, we see that however weak is the scattering, the condition of the applicability of Boltzmann equation is broken near the band bottom. It is well known since the seminal works of N. F. Mott [1], about the existence of the mobility edge E_c, that is the energy which separates the states with finite diffusion coefficient and states with the diffusion coefficient being exactly equal to zero. All this is true provided the disorder is static. Natural question arises: what happens with this picture when the scatterers slowly move.

To answer this question we need some theory of localization. As such we will use the self-consistent localization theory by Vollhard and Wölfle [2]. Of crucial importance in the above mentioned theory are maximally crossed diagrams (the sum of all such diagrams is called Cooperon) for the two-particle Green function. The calculations of these diagrams for the case of moving scatterers were done in the paper by Golubentsev [3]. So in the first part of the present paper we reproduce the results by Golubentsev (plus some additional interpretation). In the second part we use the results for the Cooperon as an input for the self-consistent localization theory, which we modify to take into account the slow motion of scatterers. In the third part we discus the results obtained.

The electrons are scattered by the potential

$$V(r,t) = V\sum_a \delta\left(r - r_a(t)\right). \tag{2}$$

Define the correlator

$$K(r-r', t-t') = < V(r,t)V(r',t') > . \tag{3}$$

In the leading approximation in the scatterers density we have for the Fourier component of the correlator

$$\begin{aligned} K(q,t) &= V^2\left\langle \int \exp\left\{(i\mathbf{q}(\mathbf{r}-\mathbf{r}')\right\} \times drdr' \sum_a \delta\left(\mathbf{r}-\mathbf{r}_a(t)\right)\sum_{a'}\delta\left(\mathbf{r}'-\mathbf{r}'_{a'}(0)\right)\right\rangle \\ &= V^2\sum_a \left\langle \exp\left\{(iq(\mathbf{r}_a(t)-\mathbf{r}_a(0))\right\}\right\rangle = nV^2 f(\mathbf{q},t), \end{aligned} \tag{4}$$

where n is the scatterer density. We consider the case when the scatterers undergo slow diffusive motion. In the ballistic case

$$f(\mathbf{q},t) = \exp\left(-\frac{\mathbf{q}^2}{6} < \mathbf{v}^2 > t^2\right), \qquad |t| \ll \tau_{imp}, \tag{5}$$

In the diffusive case

$$f(\mathbf{q}, t) = \exp\left(-\frac{\mathbf{q}^2}{2} D_{imp}|t|\right), \qquad |t| \gg \tau_{imp}, \tag{6}$$

where $D_{imp} =< v^2 > \tau_{imp}/3$, and τ_{imp} is the scatterers free path time.

For the Cooperon we get [3]

$$C_E(\mathbf{q}) = \int_0^\infty \exp\left\{-D(E)q^2 t - \frac{1}{\tau}\int_0^t (1 - f_{t'})dt'\right\} dt, \tag{7}$$

where E is the energy of each of the two electron lines in Cooperon diagram, and q is the sum their momenta (see Fig. 1). Also

$$\frac{1}{\tau} = nV^2 \frac{k^2}{\pi v}, \tag{8}$$

and

$$f_t = \int \frac{d\mathbf{s}'}{4\pi} f(k_0(s - s'), t) = \begin{cases} y\left(\dfrac{t^2}{\tau_\lambda^2}\right) & |t| \ll \tau_{imp} \\ y\left(\dfrac{|t|\tau_{imp}}{\tau_\lambda^2}\right) & |t| \gg \tau_{imp} \end{cases} \tag{9}$$

where

$$y(x) = \frac{1 - e^{-x}}{x}, \ \tau_\lambda = \left(\frac{2}{3}k^2 < v_{imp}^2 >\right)^{-1/2}. \tag{10}$$

Eq. (7) can be easily understood if we compare diagrams for the Diffuson (the sum of all ladder diagrams) and the Cooperon on Fig. 1. The Diffuson does not have any mass because of Ward identity. In the case of the Cooperon, the Ward identity is broken, and the difference $[1 - f(t)]$ shows how strongly. The interaction line which dresses single particle propagator is given by static correlator, and interaction line which connects two different propagators in a ladder is given by dynamic correlator. The time-reversal invariance in the system we are considering is broken due to

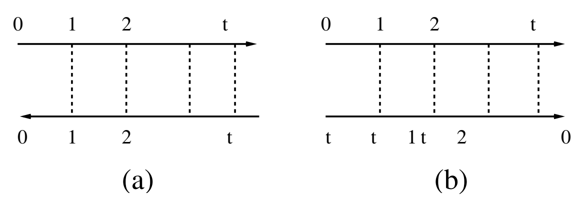

Figure 1: Diagrams for the Diffuson (a) and the Cooperon. (b) Solid line is dressed electron propagator, dashed line connecting points $\mathbf{r}, t$ and $\mathbf{r}', t'$ corresponds to $K(\mathbf{r} - \mathbf{r}', t - t')$.

dephasing; the diffusion pole of the particle-particle propagator disappears, although particle-hole propagator still has a diffusion pole, which is guaranteed by particle number conservation.

In extreme cases, from Eq. (7) we obtain

$$C_E(\mathbf{q}) = \int_0^\infty \exp\left[-D(E)\mathbf{q}^2 t - t^3/\tau_\varphi^3(E)\right] dt, \tag{11}$$

$$\text{at} \qquad \tau_\lambda^2 \tau \ll \tau_{imp}^3, \ \tau \ll \tau_\lambda$$

$$C_E(\mathbf{q}) = \int_0^\infty \exp\left[-D(E)\mathbf{q}^2 t - t^2/\tau_\varphi^2(E)\right] dt, \tag{12}$$

$$\text{at} \qquad \tau_\lambda^2 \tau \gg \tau_{imp}^3, \ \tau\tau_{imp} \ll \tau_\lambda^2$$

where in the ballistic case

$$\tau_\varphi = (3\tau\tau_\lambda^2)^{1/3} \qquad \text{at} \qquad \tau_\lambda^2 \tau \ll \tau_{imp}^3, \tag{13}$$

and in the diffusive case

$$\tau_\varphi = (2\tau\tau_\lambda^2\tau_{imp}^{-1})^{1/2} \qquad \text{at} \qquad \tau_\lambda^2 \tau \gg \tau_{imp}^3. \tag{14}$$

Thus we obtain the crucial parameter — the dephasing time τ_φ.

The results for the dephasing time (up to a numerical factors of order of one) can be understood using simple qualitative arguments. Consider ballistic regime. If a single collision leads to the electron energy change δE, the dephasing time could be obtained using relation [4]

$$\tau_\varphi \delta E \sqrt{\frac{\tau_\varphi}{\tau}} \sim 2\pi, \tag{15}$$

where τ_φ/τ is just the number of scattering acts during the time τ_φ. So in this case

$$\frac{1}{\tau_\varphi^3} \sim \frac{(\delta E)^2}{\tau}. \tag{16}$$

If we notice that $1/\tau_\lambda$ is the averaged electron energy change in a single scattering act δE, we immediately regain Eq. (13).

Inserting Eq. (11) into the self-consistent equation, for the diffusion coefficient D we obtain equation

$$\frac{D_0(E)}{D(E)} = 1 + \frac{1}{4\pi^2 mk} \sum_{\mathbf{q}} C_E(\mathbf{q}) \tag{17}$$

where D_0 is the diffusion coefficient calculated in Born approximation (Eq. (1)) and the momentum cut-off $|\mathbf{q}| < 1/\ell$ is implied, where $l = k\tau/m$ is the mean free path. Thus we obtain

$$\frac{D_0}{D} = 1 + \frac{1}{\pi mk} \int_0^\infty dt \int_0^{1/l} dq\, q^2 \exp\left[-Dq^2 t - g(t)\right], \tag{18}$$

where

$$g(t) = \frac{1}{\tau} \int_0^t (1 - f_{t'}) dt'. \tag{19}$$

(In the particular case of ballistic regime $g(t) = t^3/\tau_\varphi^3$, and in the diffusive regime $g(t) = t^2/\tau_\varphi^2$.) The Eq. (18) can be presented as

$$\frac{D_0}{D} = 1 + X_{IR} \frac{D_0}{D} \cdot \int_0^\infty dx \int_0^1 dy\, y^2 \exp\left[-xy^2 - g\left(\frac{xl^2}{D}\right)\right], \tag{20}$$

where

$$X_{IR} = \frac{3}{4\pi E^2 \tau^2} \tag{21}$$

is the Ioffe-Regel parameter. Further on we will consider Eq. (20) for

$$\tau_\varphi \gg \tau. \tag{22}$$

To solve the equation we take into account that the function is equal to zero for $t = 0$ and assume that it becomes of the order of 1 for $x = D/D_\varphi$, where we introduced $D_\varphi = l^2/\tau_\varphi$. Notice, that the condition (22) can be presented as $D_\varphi \ll D_0$.

Let us analyze the behavior of the r.h.s. of Eq. (20) as a function of D. For $D \gg D_\varphi$ the second term in the exponent in Eq. (20) (which represents dephasing) becomes irrelevant, and we get

$$\text{r.h.s.}(20) = 1 + X_{IR} \frac{D_0}{D}. \tag{23}$$

Substituting this result into Eq. (20) we obtain the solution

$$D = D_0(1 - X_{IR}). \tag{24}$$

This solution is valid, provided that $X_{IR} < 1$, that is $E > E_c$, where the mobility edge E_c is obtained from the equation [2]

$$E_c \tau(E_c) = \sqrt{3/4\pi}, \tag{25}$$

which is just the Ioffe-Regel criterium For $X_{IR} > 1$, thinking in terms of graphical method of solution, we see that the curve, representing the asymptotic formula (23), is above the curve, representing the l.h.s. of Eq. (20), and they never cross. However, Eq. (23) is no longer valid for $D \leq D_\varphi$. In particular, when $D \ll D_\varphi$, it is the first term in the exponent which is irrelevant, and we get

$$\text{r.h.s.} \sim \frac{D_0}{D_\varphi} \tag{26}$$

This equation guarantees the existence of solution for $X_{IR} > 1$. Because the only scale parameter in the r.h.s. is the quantity D/D_φ, the deviations from the asymptotic formula (23) appear only for $D \leq D_\varphi$, and the solution for $X_{IR} > 1$ is

$$D = D_\varphi/\alpha, \tag{27}$$

where α is the solution of equation

$$1 = X_{IR} \int_0^\infty dx \int_0^1 dy\, y^2 \exp\left[-xy^2 - g\left(\alpha x \tau_\varphi\right)\right]. \tag{28}$$

In particular, deep in the "dielectric region" ($E\tau \ll 1$), the solution of the self-consistent equations is

$$D = \frac{4\pi}{\int_0^\infty \exp[-g(z\tau_\varphi)]dz} E^2 \tau^2 D_\varphi. \tag{29}$$

Eqs. (24) and (27) cover the whole region of change of the Ioffe-Regel parameter save the narrow cross-over region near $X_{IR} \approx 1$.

The influence of static disorder in the spaces with dimensionality 2 and 1 is drastically different from that in the space with the dimensionality 3, considered above. In one- and two-dimensional spaces all the states are localized [5] (provided the disorder is static). According to the self-consistent localization theory [2], when the scatterers undergo slow diffusive motion, Eq. (20) for the space of dimensionality d becomes

$$\frac{D_0}{D} = 1 + X_{IR} \frac{D_0}{D} \cdot \int_0^\infty dx \int_0^1 dy\, y^{d-1} \exp\left[-xy^2 - g\left(\frac{xl^2}{D}\right)\right], \tag{30}$$

and the Eq. (1) is $D_0 = \frac{1}{d} v^2 \tau$. Analyzing behavior of the r.h.s., for $D \gg D_\varphi$ we obtain

$$\text{r.h.s.}(30) = 1 + X_{IR} \frac{D_0}{D} \ln\left(\frac{D}{D_\varphi}\right). \tag{31}$$

Again thinking in terms of graphical method of solution, we see that the curve, representing the asymptotic formula (31), is for any X_{IR} above the curve, representing the l.h.s. of Eq. (30), unless $D \sim D_\varphi$. Thus the solution for any value of the Ioffe-Regel parameter is

$$D = \beta D_\varphi, \tag{32}$$

where β is the solution of the equation

$$1 = X_{IR} \int_0^\infty dx \int_0^1 dy\, y \exp\left[-xy^2 - g\left(\beta x \tau_\varphi\right)\right]. \tag{33}$$

CONCLUSIONS

We considered the influence of slow diffusive motion of scatterers on the localization of electrons. In this case, like in the case of purely elastic scattering, the diffusion coefficient drastically differs for the energies below and above the mobility edge, the latter being found from the Ioffe-Regel criterium. Above the mobility edge we have fast diffusion, and the defasing is irrelevant. Below the mobility edge the diffusion coefficient is inversly proportional to the diffusion time.

Now we would like to mention some possible generalization and applications of these ideas. First, they are completely applicable for the case of ballistic motion of scatterers, say to gas, consisting of heavy classical particles and electrons. The results are identical to those obtained above in the ballistic regime. Second, in the previous publication [6], we studied the influence of dephasing on the Anderson localization of the electrons in magnetic semiconductors, driven by spin fluctuations of magnetic ions. There the role of heavy particles was played by magnons; complete spin polarization of conduction electrons prevented magnon emission or absorption processes, and only the processes of electron-magnon scattering being allowed. Finally, the results obtained can be applied for studying kinetics of classical waves, especially light. This last application is particularly appealing, taking into account that the results of Golubentsev [3] were obtained for light waves.

REFERENCES

1. Mott, N. F., *Adv. Phys.*, Vol. 16, 49, 1967.
2. Wölfle, P. and D. Vollhardt, *Anderson Localization*, edited by Y. Nagaoka and H. Fukuyama, Springer, Berlin, 1982.
3. Golubentsev, A. A., *Zh. Eksp. Teor. Fiz.*, Vol. 86, 47, 1984 [*Sov. Phys. JETP*, Vol. 59, 26, 1984].
4. Altshuller, B. L., A. G. Aronov, and D. E. Khmelnitskii, *J. Phys. C*, Vol. 15, 7367, 1982.
5. Efetov, K., *Supersymmetry in Disorder and Chaos*, Cambridge University Press, Cambridge, 1997.
6. Kogan, E. M., M. Auslender, and M. Kaveh, *Eur. Phys. J.*, Vol. 9, 373, 1999.

Multi-layered Fe Films for Microwave Applications

A. V. Osipov, **I. T. Iakubov**, **A. N. Lagarkov**, **S. A. Maklakov**
D. A. Petrov, **K. N. Rozanov**, **and I. A. Ryzhikov**

Institute for Theoretical and Applied Electromagnetics, Moscow, Russian Federation

Abstract— The microwave permeability of multi-layered Fe films is under study. The multi-layer films are found to possess more rigid magnetic structure and larger damping factor of ferromagnetic resonance compared to those of single-layer films. Bulk materials with high microwave permeability may be produced as laminated structures of these multi-layer ferromagnetic films. In the paper, experimental data are presented on the microwave permeability of such laminated regular structures based on Fe films. Possible technical applications of the materials under study include thin wideband radar absorbers and miniaturized patch antennas.

1. INTRODUCTION

For many microwave applications, materials with high microwave permeability values are needed. The frequency dependence of microwave permeability is typically due to the ferromagnetic resonance. In many magnetic materials, the permeability varies slightly with frequency until an abrupt drop appears at the ferromagnetic resonance frequency. Above the resonance, the permeability takes values that are close to unity. Hence, an estimate of microwave permeability of a magnetic material may be made from its static permeability μ_s and resonance frequency f_r. The static permeability characterizes the magnetic performance in the operating frequency band. The resonance frequency is an estimate for the cutoff frequency, above which the material is no more permeable enough and magnetic loss increases greatly. For high microwave permeability be attained, both f_r and μ_s must be as high as possible.

These values often reveal a complex dependence on the material composition, magnetic and crystalline structure, features of manufacturing and processing, etc. However, μ_s and f_r are related closely to each other by well known Snoek's law: an increase of one leads to a decrease of another, with the product of these being dependent only on the saturation magnetization M_s of the material. The anisotropy field or other structure-dependent values are not involved in Snoek's law.

For thin films with in-plane magnetization, μ_s is reciprocal to squared f_r in difference to conventional Snoek's law [1]:

$$(\mu_s - 1)\, f_r^2 = (\gamma 4\pi M_s)^2 \tag{1}$$

where $\gamma \approx 3\,\text{GHz/kOe}$ is the gyromagnetic ratio. Eq. (1), which is referred to as Acher's law in the literature, also has the right-side part depending on the saturation magnetization only. Therefore, Eq. (1) provides a constraint for the microwave permeability of magnetic films that is determined by the composition and is independent of structure, the same as Snoek's law does for bulk materials. When $f_r < \gamma 4\pi M_s$, which is several GHz or several dozens GHz for typical high-permeability films, Eq. (1) produces far higher values of μ_s and, therefore, higher microwave permeability compared to Snoek's law. Therefore, thin ferromagnetic films are promising materials for microwave applications.

However, most applications require bulk samples. With the increase of film thickness, the microwave permeability of the film degrades because of the effect of eddy currents and out-of-plane magnetization. For these effects to be avoided, laminates of thin ferromagnetic layers are useful. Since the thickness of substrate is large compared to that of ferromagnetic film, multi-layer films may be used to obtain high volume fractions of ferromagnetic material in the laminate. Therefore, this study presents experimental data on the microwave performance of both multi-layer thin Fe films and laminates made of such films.

2. EXPERIMENT

Fe films are deposited onto a flexible mylar substrate of 10 or 20 µm in thickness by a RF magnetron sputtering in Ar atmosphere with N_2 admixture. RF magnetron sputtering is employed because it provides high-speed deposition. Fe target is used because Fe has large saturation magnetization that allows good microwave performance to be expected. The mylar substrates are chosen to be as thin as possible to provide the largest volume fraction of Fe in the samples for measurements.

According SEM data [2], the films under study have the columnar morphology. Both the average granule size and the length to width ratio of the granules increase with the film thickness that causes an increase of the effective anisotropy field. The easy magnetic axis is collinear to the larger axis of the elongated granules. Decrease in the granule size diminishes the magnetic anisotropy and therefore increases the low-frequency permeability of the films.

The microwave permeability of flexible films is measured at frequencies of 0.1 to 18 GHz by the technique [3], with a long and narrow film stripe wound into a torus-shaped sample to fit to the 7/3 coaxial line. The measurement setup allows the permeability be measured under magnetic bias of up to 500 Oe. Extensive experimental data are obtained on microwave performance of thin Fe films. A typical measurement results are given in Fig. 1, with a single-layered Fe films. The data are shown in the figure for two samples with different direction of winding, one with sputtered iron outward and mylar inward, and another with opposite geometry. It is seen from the figure that the difference is noticeable in the microwave performance of the two samples, which may be attributed to the effect of magnetostriction.

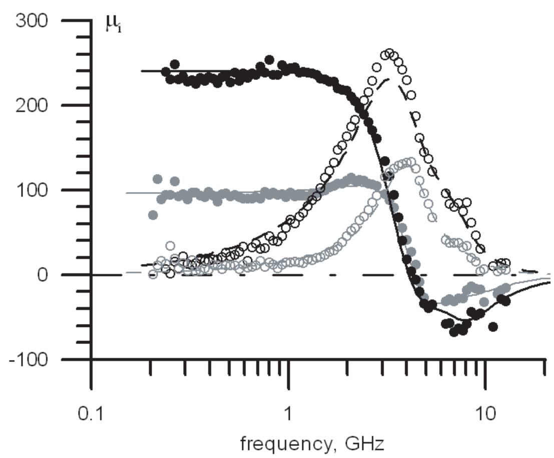

Figure 1: Intrinsic permeability, μ_i, of a single-layer Fe film with inward (black) and outwards (gray) winding: dots are measured data, lines are fitting of the data with the Lorentzian dispersion law.

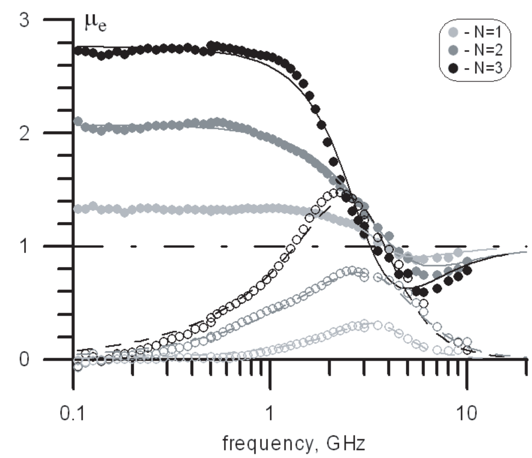

Figure 2: Effective permeability, μ_e, of composites made of multi-layer films with polymer interlayers: dots are measured data, lines are fitting with the Lorentzian dispersion law.

3. RESULTS AND DISCUSSION

Measured magnetic spectra of Fe films are found to agree well to the multiple Lorentzian dispersion law:

$$\mu(f) = 1 + \sum_j \frac{4\pi\chi_{s,j}}{1 - i2\beta_j\left(f/f_{r,j}\right) - \left(f/f_{r,j}\right)^2}, \tag{2}$$

with $x_{s,j}$, β_j, and $f_{r,j}$ being the static susceptibility, damping factor, and resonance frequency of j-th resonance, respectively. The Lorentzian fitting is also plotted in Figs. 1–3 showing a good agreement with the measured data. The physical origin of the resonances, which may be either domain walls motion or magnetic moments precession, may be understood from variations of magnetic spectra under external magnetic bias [4].

Equation (1) is derived for a single-domain film with the in-plane magnetic anisotropy. However, it is shown to provide a good practical estimate for more realistic cases, such as the presence of the stripe domain structure [5], the effect of eddy currents, and inhomogeneity of magnetic film [6]. With representation (2), Eq. (1) is verified for measured permeability of actual films. With the permeability measured under external magnetic bias of 300 to 500 Oe, Eq. (1) is found to be held with a good accuracy. With no external magnetic field, the left part of Eq. (1) is typically 0.3 to 1 of the theoretical limit given by the right part of the equation, which indicates that the directions of easy magnetic axes are distributed in the films under study.

Thickness dependence of microwave permeability of the films is also studied in the thickness range of 0.1 to 1.8 μm. With the thickness increased, the magnetic loss peak width increases rapidly. The static permeability and the resonance frequency depend slightly on thickness below 1 μm. The thickness dependence is conventionally attributed to either the effect of eddy currents or appearing of out-of-plane magnetization at large thickness of a columnar structure. None of these reasons is consistent quantitatively with the measured data. Other reasons for the thickness dependence of microwave magnetic behavior may be larger pore contents and larger surface roughness in thicker films. For further studies, film thickness of 0.25 μm and the nitrogen contents in Fe of 1 to 2 at. % are accepted.

To produce a multi-layer film, several Fe layers are deposited onto a substrate alternated with either polymer or SiO_2 interlayers. Polymer interlayers of 1 to 3 μm thick are deposited making use of a centrifuge. SiO_2 interlayers of 0.25 μm thick are deposited with high-frequency magnetron sputtering. The advantage of the latter is that both film and interlayer are sputtered within a single process. Polymer interlayers require drying, which take time. However, with SiO_2 interlayers the properties of multi-layer film deteriorate noticeably with the number of layers, see below. In both occasions, multi-layer films with the number of layers of up to 10 are produced and studied.

Multi-layer films deposited with thick polymer interlayer reveal more rigid magnetic structure according the magnetostatic measurements and slightly higher damping factor compared with single-layer films, see Fig. 2 [3]. The increase in damping factor may be attributed to the accumulation of inhomogeneities. In other respects, Fe layers in a multi-layer Fe/polymer film may be considered as non-coupled. The multi-layer samples for coaxial measurements are made of the patterned multi-layer films stacked together to comprise a bulk composite. This allows a composite sample to be produced with the permeability of 2.9 and low magnetic loss at frequencies below 1 GHz, with the volume fraction of Fe being as low as 0.77%.

For multi-layer films deposited with SiO_2 interlayers, the change in performance with the number of layers is more pronounced, see Fig. 3. The damping factor increases drastically, which is accompanied by a decrease in intrinsic static permeability of Fe layers. The permeability of the layers in these multi-layer films is not additive. For example, subtraction of the permeability of a single-layer film from the permeability of a two-layer film made with the same technological parameters may produce negative magnetic loss. This may be attributed to smaller thickness of the SiO_2 interlayers, which may not prevent magnetic or structural coupling between adjacent Fe films. Another reason may be large internal stress introduced by the interlayers, which affects the permeability by the magnetostricitve effects.

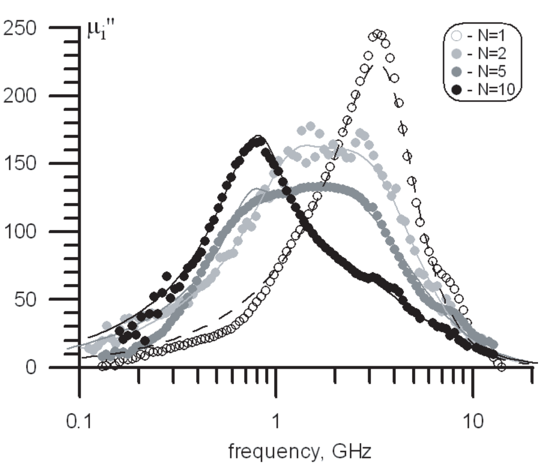

Figure 3: Intrinsic magnetic spectra, μ_i'', of multi-layer Fe films with SiO_2 interlayers: dots are measured data, lines are fitting with the Lorentzian dispersion law.

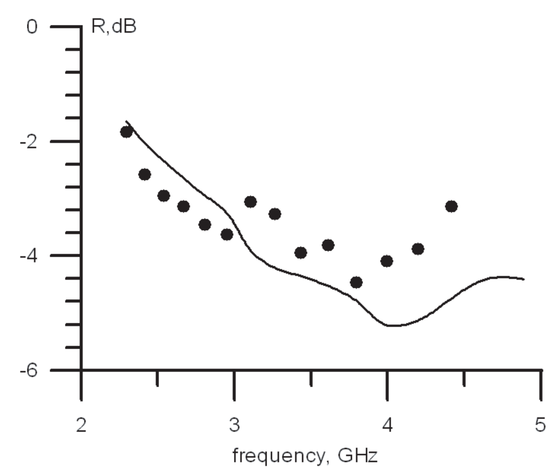

Figure 4: The reflectivity of the bulk laminate as a function of frequency: the dots are obtained by measurement in the rectangular waveguide, the curve shows the prediction based on the coaxial measurement of multi-layered films.

Under magnetic bias up to 480 Oe, single-layered films exhibits fast decrease of β and shift of ferromagnetic resonance to higher frequencies due to saturation in accordance with Kittel's formula. Meanwhile, spectrum of the ten-layered film stays almost unchanged that is an evidence for the escalating rigidness of magnetic structure and, hence, for the magnetic coupling between layers.

By stacking and gluing 10-layer films with SiO_2 interlayers, a laminate sample of 0.9 mm in thickness is produced for measurements of reflectivity in the $72 \times 34\,\mathrm{mm}^2$ rectangular waveguide.

To avoid the effect of conductivity, the sample is cut in stripes of 6.5 mm in width. The sample is light-weight, as the volume fraction of Fe is as low as 5%. The peak of imaginary permeability is 4 at microwaves. In Fig. 4, the reflectivity of the laminate is compared with that predicted on the base of coaxial permeability measurement of the film. The results agree closely.

This closeness justifies also the permeability estimations for a plane film by averaging the permeability measured in wound films with opposite winding directions, Fe/SiO_2 inward and outward.

From the results obtained it may be concluded that multi-layer film laminates are competitive magnetic materials for microwave applications, among other materials, the microwave permeability of which is governed by Eq. (1), namely, hexagonal ferrites and amorphous microwires. Such materials may be of use for many microwave applications, such as magneto-dipole antennas [6] and radar absorbers [7]. The crucial point in selection among these is a width of magnetic loss peak at microwaves: the narrower these are preferred.

ACKNOWLEDGMENT

Authors are grateful to Russian Foundation for Basic Research for partial support of the study according to Agreement No. 05-08-01212.

REFERENCES

1. Acher, O., J. L. Vermeulen, P. M. Jacquart, J. M. Fontaine, and P. Baclet, "Permeability measurement on ferromagnetic thin films from 50 MHz up to 18 GHz," *J. Magn. Magn. Mater.*, Vol. 136, 269–278, 1994.
2. Lagarkov, A. N., I. T. Iakubov, I. A. Ryzhikov, K. N. Rozanov, N. S. Perov, E. P. Elsukov, S. A. Maklakov, A. V. Osipov, M. V. Sedova, A. M. Getman, and A. L. Ulyanov, "Fe-N films: morphology, static and dynamic magnetic properties," accepted for publication in *Physica A*.
3. Rozanov, K. N., N. A. Simonov, and A. V. Osipov, "Microwave measurements of the magnetic film permeability," *J. Communic. Technol. Electron.*, Vol. 47, No. 2, 210–216, 2002.
4. Iakubov, I. T., A. N. Lagarkov, S. A. Maklakov, A. V. Osipov, K. N. Rozanov, I. A. Ryzhikov, and S. N. Starostenko, "Microwave permeability of composites filled with thin Fe films," *J. Magn. Magn. Mater.*, Vol. 300, e74–e77, 2006.
5. Buznikov, N. A. and K. N. Rozanov, "The effect of stripe domain structure on dynamic permeability of thin ferromagnetic films with out-of-plane uniaxial anisotropy," *J. Magn. Magn. Mater.*, Vol. 285, No. 3, 314–326, 2004.
6. Lagarkov, A. N., A. V. Osipov, K. N. Rozanov, and S. N. Starostenko, "Microwave composites filled with thin ferromagnetic films. Part I. Theory," *ICMAT 2005: Proc. of Symp. R*, Singapore, 74–77, July 3–8, 2005.
7. Ikonen, P. M. T., K. N. Rozanov, A. V. Osipov, P. Alitalo, and S. A. Tretyakov, "Magnetodielectric substrates in antenna miniaturization: potential and limitations," *IEEE Trans. Antennas Propag.*, Vol. 54, 3391–3399, 2006.
8. Rozanov, K. N. and S. N. Starostenko, "Influence of permeability dispersion on the bandwidth of magnetic radio absorbers," *J. Communic. Technol. Electron.*, Vol. 48, No. 6, 652–659, 2003.

Modal Analysis of Extraordinary Transmission through Subwavelength Slits in a Silver Plate

G. Ghazi and M. Shahabadi
School of Electrical and Computer Engineering, Photonics Research Lab
University of Tehran, Iran

Abstract— Using eigen-modes of a one-dimensional array of slits together with a mode matching technique, we investigate the extraordinary transmission through subwavelength slits. This modal analysis serves to determine the contribution of various mechanisms of extraordinary transmission. It is shown that surface plasmon polaritons excited on the input interface at certain wavelengths can absorb the incident power and thus reduce the transmitted power.

1. INTRODUCTION

According to the Bethe theory of small apertures [1], it has been believed that optical transmission through subwavelength apertures must be negligible. However, in the recent decade some experiments have shown that an extraordinary optical transmission is possible if there is a periodic array of holes in a metallic film [2]. Because of the potential application of this extraordinary effect in nano-photonic devices, there have been many theoretical and experimental investigations to explain the origin of the high transmission. The explanation of this phenomenon in one dimensional slits smaller than $\lambda_0/2$ is more complicated than in two-dimensional arrays, since there exists a guided mode without cut-off among them. In the one-dimensional case in periodic slit arrays the mechanism of transmission is explained with different viewpoints. Porto et al., using transfer matrix method, believe that it is the surface plasmon polaritons (SPP) which mainly contribute to the transmission [3]. Surface plasmon polariton according to Reather's definition [4] is a localized wave on the interface of metal and dielectric for which the propagation constant along the interface can be obtained from Maxwell's equations as: $k_{sp} = k_0\sqrt{\varepsilon_{rm}\varepsilon_{rd}/(\varepsilon_{rm}+\varepsilon_{rd})}$ where ε_{rm} and ε_{rd} are relative permittivities of metal and dielectric, respectively, and k_0 is the freespace wavenumber. Subsequent theoretical studies of complex band structure of transmission gratings [5] have also proposed the existence of coupled surface resonances and cavity modes. In [6], Lalanne et al., using a rigorous coupled wave analysis (RCWA) concluded that high transmission is due to diffraction and waveguide mode resonances and SPP have negative role in transmission efficiency. Treacy has summarized three physical models in his paper for high transmission and argued that dynamic diffraction theory can explain the transmission mechanism properly [7]. Other analytical works with modal expansion is performed with some simplifications [8, 9] or precisely [10] to explain the interaction of light and gratings. In the latter one, the excitation of the grating modes in a semi-infinite grating and the transfer of power just after interface are considered and it is believed that the guided mode plays an important role in power transmission.

Here, a modal analysis of a periodic slit array in a silver layer characterized by its measured complex permittivity is carried out. The transmission efficiency of such a grating is calculated with matching of the tangential fields on input and output interfaces of the grating. The influence of the excitation of the guided mode on the total transmission and the negative effect of SPP on it will be demonstrated.

2. MODAL EXPANSION IN DIFFERENT REGIONS

Figure 1 shows a periodic array of slits in a metallic layer suspended in air. The array is illuminated by a plane wave propagating in region I. The fields in the air regions (regions I and III) can be expressed as a Rayleigh expansion. In the grating region (region II), Maxwell's equations should be solved with appropriate periodic boundary conditions to obtain the eigen-modes. For this structure, two uncoupled TM_z (Transverse Magnetic to the z direction) and TE_z (Transverse Electric to the z direction) polarization solutions exist. For TM_z, there always exists a guided mode, but for TE_z polarization when the width of the slits is less than $\lambda_0/2$ all the modes are below cut-off. Since TM_z polarization shows extraordinary transmission effect in subwavelength periodic arrays, we will investigate this mode, thus (H_x, E_z, E_y) field components.

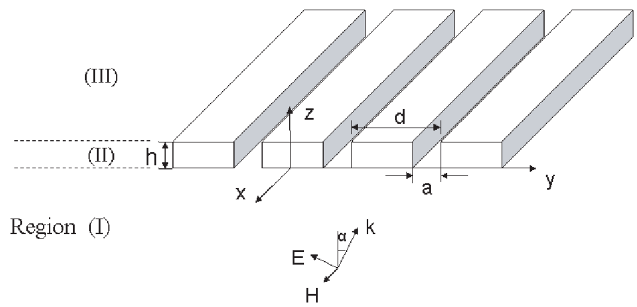

Figure 1: Structure and the polarization of the incident field.

The field expansion in region II of Fig. 1 is expressed by

$$H_x^{(n)II}=\begin{cases}\left[A'_n\cos\left(v_n\left(y+\frac{a}{2}\right)\right)+B'_n\sin\left(v_n\left(y+\frac{a}{2}\right)\right)\right]e^{-jk_{zn}z} & \text{for} \quad -\frac{d-a}{2}\leq y\leq\frac{d-a}{2}\\ \left[C'_n\cos\left(u_n\left(y-\frac{a}{2}\right)\right)+D'_n\sin\left(u_n\left(y-\frac{a}{2}\right)\right)\right]e^{-jk_{zn}z} & \text{for} \quad \frac{d-a}{2}\leq y\leq\frac{d+a}{2}\end{cases}. \tag{1}$$

Here, n is the mode index ($n = 1, 2, 3, \ldots$) and $u_n = \sqrt{k_0^2 - k_z^2}$, $v_n = \sqrt{\varepsilon_{rm}k_0^2 - k_z^2}$ where ε_{rm} is the complex permittivity of the metal at the wavelength of operation. The generation of other field components is straightforward with Maxwells equations. The tangential field components ($H_x^{(n)}$, $E_z^{(n)}$) should be matched on the vertical boundary of metal and the dielectric which is assumed to be air here. The continuity of the fields together with the Bloch condition of the periodic structure yields a linear system of four equations. Existence of a nontrivial solution of the system of equations requires that the determinant of the matrix be zero which results in

$$\frac{u_nv_n}{\varepsilon_{rm}}\cos(k_0d\sin\alpha)-\frac{u_nv_n}{\varepsilon_{rm}}\cos(v_na)\cos(u_n(d-a))+\frac{1}{2}\left(u_n^2+\frac{v_n^2}{\varepsilon_{rm}^2}\right)\sin(v_na)\sin(u_n(d-a))=0. \tag{2}$$

Eq. (2) together with the relation between v_n and u_n with k_{zn}, are solved for k_{zn}.

When the incidence is normal using the symmetries, Eq. (2) can be simplified as

$$v_n\cos\left(u_n\frac{a}{2}\right)\sin\left(v_n\frac{(d-a)}{2}\right)+u_n\varepsilon_{rm}\sin\left(u_n\frac{a}{2}\right)\cos\left(v_n\frac{(d-a)}{2}\right)=0. \tag{3}$$

This equation is solved for a grating of the parameters: $d = 1\,\mu\text{m}$, $a = 300\,\text{nm}$, $\varepsilon_{rm} = -66.63 - j4.86$, when the wavelength of the incident field is $\lambda_0 = 1.2\,\mu\text{m}$. The normalized propagation constants of the modes in the z direction are shown in Fig. 2(a) (they are normalized to k_0). There is one propagating mode whose normalized propagation constant is $1.077 - j0.0028$, while other modes are evanescent. In Fig. 2(b), the normalized magnitude of $H_x(y, z = 0^+)$ for first seven modes in one period of the grating region is illustrated. As is inferred from mode profiles in Fig. 2(b), the first mode resembles the TEM_z (Transverse Electromagnetic to the z direction) mode of a slit in a perfect metal which has no cut-off frequency. The obtained modes are used in a mode matching scheme to find the transmission.

3. MODE MATCHING AND DETERMINATION OF TRANSMISSION

With the modes obtained in the previous section, and the fields of the upper and lower homogeneous regions, we can find the transmitted power. The fields of the air regions can be written as a Rayleigh expansion. H_x components in the two regions are shown to be

$$H_x^I=\sum_{m=-M}^{M}A_me^{-jk_{ym}y}e^{-jk_{zm}z}+B_me^{-jk_{ym}y}e^{jk_{zm}(z-d_1)}, \tag{4}$$

$$H_x^{III}=\sum_{m=-M}^{M}A''_me^{-jk_{ym}y}e^{-jk_{zm}z}. \tag{5}$$

Now, H_x and E_y components of the fields in the three regions are used for mode matching. The modes of the grating region are not orthogonal. Hence, they produce a nondiagonal coefficient matrix in the mode matching equations.

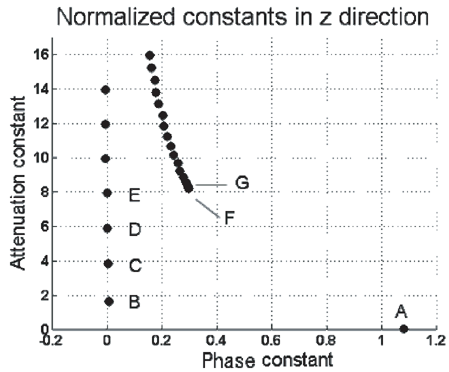

(a)

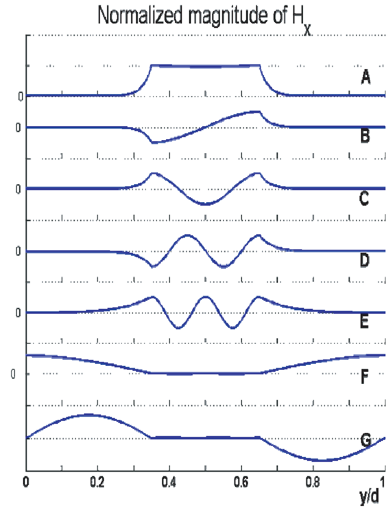

(b)

Figure 2: (a) Normalized propagation constants (the vertical axis is the imaginary part and the horizontal axis is the real part of normalized k_z, (b) Normalized H_x for the first seven modes indicated in (a), in one period of the structure when the slit is in the middle. The parameters of the grating are $d = 1\,\mu\text{m}$, $a = 300\,\text{nm}$, $h = 850\,\text{nm}$, and $\lambda_0 = 1.2\,\mu\text{m}$. Relative permittivity of silver is $\varepsilon_{rm} = -66.63 - j4.86$ from [11].

The transmission efficiency of the zero-order diffracted mode (η_0) shows an amount of 0.799 for the grating introduced in Fig. 1. For this calculation, the parameters are: $d = 1\,\mu\text{m}$, $a = 300\,\text{nm}$, $h = 850\,\text{nm}$, $\varepsilon_{rm} = -66.63 - j4.86$, and 24 modes of the grating region and 50 modes of the air region are considered. When a plane wave is incident to the array, both the propagating and evanescent modes are excited on the entrance boundary. From the ratio of the amplitudes of various modes, one can get some insight into the actual mechanism of transmission. For understanding the origin of high transmission in the mentioned structure, the magnitude of the first seven modes in the grating region is tabulated in Table 1. These magnitudes show obviously that the first propagating mode is excited more than the others, and this propagating mode contributes to a peak in transmission. The field distribution of H_x at a certain time is illustrated in Fig. 3. Here the period of the structure is 1000 nanometer. This amount is far from the SPP wavelength which is obtained from

$$\lambda_{sp} = \lambda_0 \mathrm{Re}\left(\sqrt{\frac{1+\varepsilon_{rm}}{\varepsilon_{rm}}}\right) = 0.9925\lambda_0 \approx 1191\,\text{nm}. \tag{6}$$

This is the cause of the reduced magnitude of evanescent modes in comparison with the guided one. When period of the structure equals the wavelength of SPP, $d = \lambda_{sp}$, the increased relative excitation of evanescent modes at the interface will reduce the transmission. The magnitudes of the higher order modes under this condition are represented in the second row of Table 1. These modes absorb more power whereas the guided mode transfers less power to the output interface. The results of these simulations are in agreement with those obtained by the authors using a Fourier technique [12].

Table 1: Transmission efficiency and magnitude of first seven modes in grating region for two different periods of the structure.

Period	η_0	Grating region mode magnitudes						
		First mode	Second	Third	Forth	Fifth	Sixth	Seventh
1000 nm	0.799	2.4345	0.0001	0.3373	0.0001	0.1171	0.0095	0.0000
1191 nm	6.42e-8	0.0056	0.0006	0.1461	0.0002	0.0335	0.0165	0.0000

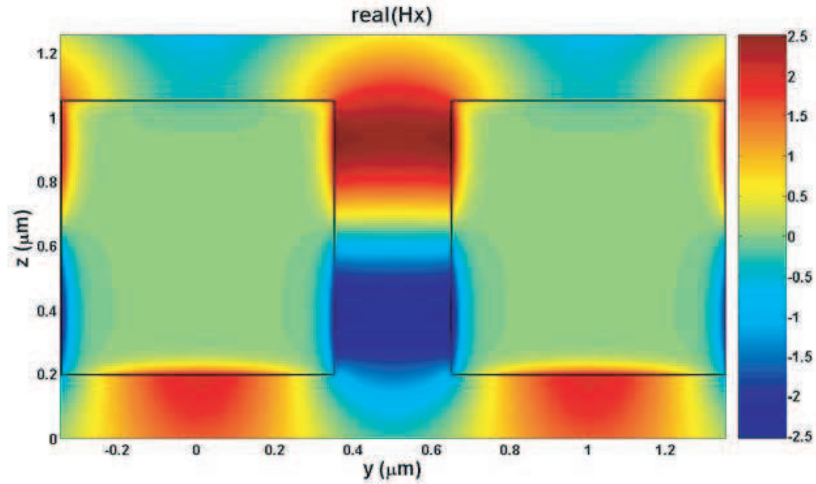

Figure 3: Spatial distribution of H_x component for a grating of $d = 1\,\mu\text{m}$, $a = 300\,\text{nm}$, $h = 850\,\text{nm}$, and $\lambda_0 = 1.2\,\mu\text{m}$.

4. CONCLUSIONS

The effect of the guided mode of the structure on extraordinary transmission has been investigated in one-dimensional periodic arrays. For this purpose, a modal analysis is exploited. The contribution of the guided and evanescent modes, when the SPP is excited, is determined. We conclude that SPP can reduce the overall transmission, whenever they are excited by incident wave.

ACKNOWLEDGMENT

The authors wish to acknowledge the assistance and support of the Iran Telecommunication Research Center (ITRC).

REFERENCES

1. Bethe, H. A., "Theory of diffraction by small holes," *Phys. Rev.*, Vol. 66, 163–182, 1944.
2. Ebbesen, T. W., H. J. Lezec, H. F. Ghaemi, T. Thio, and P. A. Wolff, "Extraordinary optical transmission through subwavelength hole arrays," *Nature*, Vol. 391, 667–669, 1998.
3. Porto, J. A., F. J. Garcia-Vidal, and J. B. Pendry, "Transmission resonance on metallic gratings with very narrow slits," *Phys. Rev. Lett.*, Vol. 83, No. 14, 02845–02849, 1999.
4. Reather, H., *Surface Plasmons on Smooth and Rough Surfaces and on Gratings*, Springer-Verlag, Berlin, 1986.
5. Collin, S., F. Pardo, R. Teissier, and J. L. Pelouard, "Horizontal and vertical surface resonances in transmission metallic gratings," *J. Opt. A: Pure Appl. Opt.*, Vol. 4, S154–S160, 2002.
6. Cao, Q. and Ph. Lalanne, "Negative role of surface plasmons in the transmission of metallic gratings with very narrow slits," *Phys. Rev. Lett.*, Vol. 88, No. 5, 057403-1–057403-4, 2002.
7. Treacy, M. J., "Dynamical diffraction on explanation of the anomalous transmission of light through metallic gratings," *Phys. Rev. B*, Vol. 66, 195105-1–195105-11, 2002.
8. Lalanne, Ph., J. P. Hugonin, S. Astilean, M. Palamaru, and K. D. Moller, "One-mode model and Airy-like formulae for one-dimensional metallic gratings," *J. Opt. A: Pure Appl. Opt.*, Vol. 2, 48–51, 2000.
9. Garcia-Vidal, F. J. and L. Martin-Moreno, "Transmission and focusing of light in one-dimensional periodically nanostructured metals," *Phys. Rev. B*, Vol. 66, 155412-1–155412-10, 2002.
10. Xie, Y., A. R. Zakharian, J. V. Moloney, and M. Mansuripur, "Transmission of light through periodic arrays of sub-wavelength slits in metallic hosts," *Opt. Exp.*, Vol. 14, No. 14, 6400–6413, 2006.
11. Palik, E. D., *Handbook of Optical Constants of Solids*, Academic Press, London, 1985.
12. Ghazi, G. and M. Shahabadi, "Analysis of extraordinary transmission through subwavelength periodic slits," *Proceedings of Iran International Conference on Electrical Engineering*, 1010–1014, Tehran, Iran, May 2007.

Low Frequency Relaxation Oscillations in a Capacitive Discharge Chamber Connected to a Peripheral Grounded Chamber

Zhuwen Zhou[1], **M. A. Lieberman**[2], **Sungjin Kim**[2]
Shiyin Ji[1], **Guangyu Sun**[1], **and Mingsen Deng**[1]

[1]Department of Physics, Guizhou Educational College, Guiyang 550003, China
[2]Department of Electrical Engineering and Computer Sciences-1770
University of California, Berkeley, CA 94720, USA

Abstract— We have observed relaxation oscillations in an argon capacitive discharge connected to a peripheral grounded chamber through a slot with dielectric spacers. The oscillations, observed from time-varying optical emission of the main discharge chamber and the periphery, show, for example, some low frequency (2.72 Hz ∼ 3.70 Hz) relaxation oscillations at 100 mTorr, at higher absorbed power. We interpret the low frequency oscillations using an electromagnetic model of the slot impedance with parallel connection variational peripheral capacitance, coupled to a circuit analysis of the system including the matching network. The model results are in general agreement with the experimental observations, and indicate a variety of behaviors dependent on the matching conditions.

1. INTRODUCTION

A configuration of both theoretical and practical interest is a capacitive discharge connected through a dielectric slot to a peripheral grounded region. A particular configuration, which has been found to have desirable processing applications [1], is a dual frequency capacitive discharge, with the main cylindrical discharge connected to a peripheral cylindrical (pumping) region through an annular slot narrowed with a dielectric. The feedstock gas flows from the main discharge region through the slot, and is pumped in the grounded peripheral chamber, the apparatus is illustrated in Fig. 1. We examined both theoretically and experimentally the conditions [2] for which peripheral ignition occurs, and we determined the conditions required to confine the discharge to the central region.

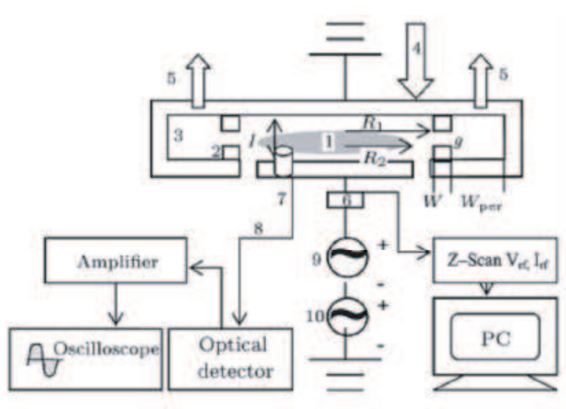

Figure 1: Experimental setup: 1. Central region, 2. Quartz confinement rings, 3. Periphery region, 4. Gas in, 5. Pumping out, 6. Matching network, 7. Optic probe, 8. Fiber, 9. Power V_{rf} (27.1 MHz), 10. Bias $V_{\mathrm{bias}} = 0$.

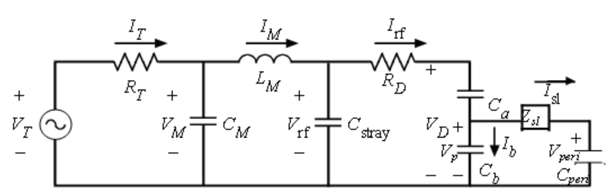

Figure 2: Circuit model of the rf power source, L-type matching network, main discharge region, dielectric slot region and peripheral region.

Unexpected phenomena were the observation of low frequency (hertz range) relaxation oscillations, for conditions when plasma extends beyond the central discharge region. The existence of such oscillations prevents good matching, which is one of the causes of the deterioration of the performance of reactors exhibiting peripheral breakdown. The hertz oscillations occur as spatially moving plasmas with both the slot and periphery ignited. A circuit model of the system is shown in Fig. 2.

2. PHENOMENOLOGICAL DESCRIPTION OF RELAXATION OSCILLATIONS

In Fig. 3, low frequency relaxation oscillations that occur in the discharge are shown. The optical emission in the central region is observed in the 6 mm wide optical slot incorporated in the ground electrode. In the figures, I is the relative optical emission intensity in the main and peripheral discharge regions of the neutral argon emission at 748.7 nm, detected through a notch filter and a fiber optic cable. In Figs. 3 (a), (b), (c), at 100 mTorr and 325 W, 260 W, 176 W absorbed power, the time-varying optical emission from both the main and the periphery discharge shows low frequencies (2.717 Hz, 3.484 Hz, 3.697 Hz) relaxation oscillations. The oscillation visually has spatial motion, typically balls of light rotating around the discharge. In these cases the minimum of the optical emission is close to zero, indicating that the central and periphery discharge electrons producing the emission are cooled or absent.

3. THEORY OF LOW FREQUENCY RELAXATION OSCILLATIONS

Ignition of slot plasma causes the main plasma voltage V_p to drop due to an increase of the grounded area seen by the main discharge. This will extinguish the slot discharge but may leave the main discharge ignited. However, additional detuning of the match and an overall lowering of the circuit Q can result in also extinguishing the main discharge. Because the formation of a slot plasma results in the propagation of a surface wave with significant phase shifts and resistive decays, an electromagnetic analysis in the slot and periphery is relevant. However, this requires some simplifications as described below.

The impedance $Z_{\rm sl}$ of the slot seen at the main discharge is determined by an electromagnetic analysis. The slot plasma is driven at one end (its inner radius) by the rf voltage V_p of the main discharge plasma, with the top and bottom slot surfaces earthed through the quartz confinement rings. As was shown in [2, 4], a transverse magnetic (TM) surface wave that propagates along the quartz-plasma interface is excited at the slot entrance. A rectangular coordinate model is used to determine the propagation and impedance characteristics. We assume open-circuit boundary conditions for the reflection of the wave at the slot exit. We determined the mode characteristics with Maxwell equations detailed discuss in our previous paper [5].

As low frequency oscillation, the plasma density sustained in the slot exceed $n_{\rm sl} = 2\times10^{15}\,{\rm m}^{-3}$ showed in Fig. 5, there are different sustained densities in different frequency oscillations. For example, $n_{\rm sl} = 6\times10^{15}\,{\rm m}^{-3}$ with $f = 3.7\,{\rm Hz}$, $P_{\rm abs} = 176\,{\rm W}$; $n_{\rm sl} = 1.0\times10^{16}\,{\rm m}^{-3}$ with $f = 3.46\,{\rm Hz}$, $P_{\rm abs} = 260\,{\rm W}$; $n_{\rm sl} = 2\times10^{16}\,{\rm m}^{-3}$ with $f = 2.72\,{\rm Hz}$, $P_{\rm abs} = 325\,{\rm W}$; The slot resistance $R_{\rm sl}$ increases with a decrease in $n_{\rm sl}$ and equals or exceeds the capacitive slot reactance down to very low densities. Hence, the slot is mainly resistive at this pressure.

To determine the interaction of the source and matching network with the whole system discharge, we solve the ladder-network shown in Fig. 2 to obtain the source voltage V_T as a function of the plasma voltage V_p on the main discharge. For a linear network, V_T would be a linear function of V_p for any chosen slot density, but the slot and the periphery discharge nonlinearities significantly modify this property. The most important nonlinearities, which we retain in the analysis below, are the voltage-dependent main discharge and the peripheral sheath capacitances $C_a(V_a)$, $C_b(V_p)$ and $C_{peri}(V_{peri})$. Here $V_a = V_D - V_p$ is the voltage across the powered electrode sheath, V_p is the voltagr cross the grounded electrode sheath and V_{peri} is the voltage across the peripheral sheath, $V_{peri} = V_p - I_{\rm sl}Z_{\rm sl}$. We use a collisional (constant mean free path) sheath model [3] to determine these capacitances

$$C_a = \kappa_{cap}A_a/|V_a|^{3/5}; \quad C_b = \kappa_{cap}A_b/|V_p|^{3/5}; \quad C_{peri} = \kappa_{cap}A_{peri}/|V_{peri}|^{3/5} \tag{1}$$

where

$$K_{\rm cap} = 1.25\varepsilon_0\left(\frac{en_su_B}{\varepsilon_0}\right)^{2/5}\left(\frac{M}{e\lambda_i}\right)^{1/5} \tag{2}$$

with n_s the density at the plasma-sheath edge. The sheath edge density was taken to be $n_s = 2\times10^9\,{\rm cm}^{-3}$, consistent with the value of $V_{\rm bd}$ determined from the breakdown model, and the electron temperature was taken to be $T_e = 2\,{\rm V}$. The matching network capacitance was measured just prior to the transition to kilohertz oscillations to be $C_M \approx 2500\,{\rm pF}$. We have chosen the discharge resistance to be consistent with this measurement, obtaining a quite reasonable value $R_D = 1.2\,\Omega$, which is held fixed in the calculation. The procedure for solving the ladder-network of Fig. 2 is as follows: Choosing a real V_p and a slot density $n_{\rm sl}$, then $I_{\rm sl} = V_p/(Z_{\rm sl} + 1/j\omega C_{peri})$, C_b, C_{peri} is determined by (1) for the given V_p, V_{peri}, $I_b = j\omega C_bV_p$, $I_{\rm rf} = I_b + I_{\rm sl}$, and we obtain the equation $|V_a|\omega C_a(|V_a|) = |I_{\rm rf}|$, which can be solved to determine $|V_a|$ and C_a using (1). When the

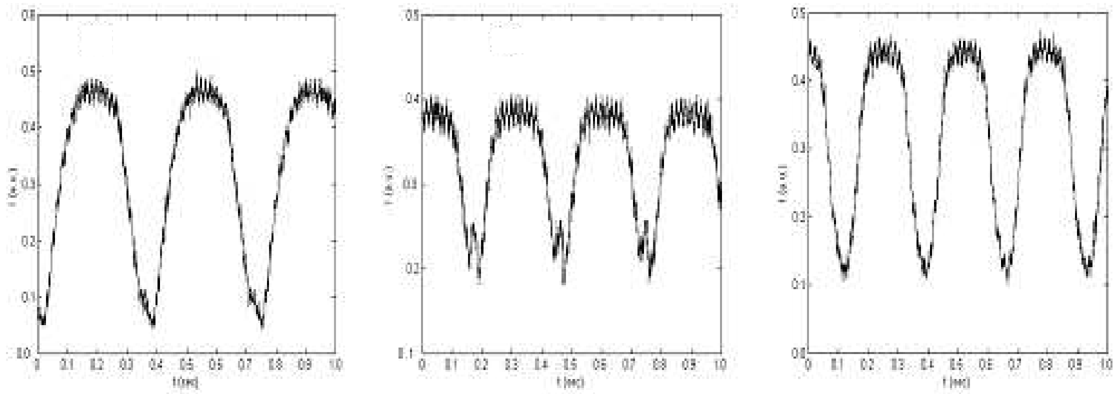

(a) (b) (c)

Figure 3: Time-varying optical emission I from the periphery, showing low frequency relaxation oscillations at $p = 100\,\mathrm{mT}$, (a) $f = 2.717\,\mathrm{Hz}$, $P_{\mathrm{abs}} = 325\,\mathrm{W}$; (b) $f = 3.484\,\mathrm{Hz}$, $P_{\mathrm{abs}} = 260\,\mathrm{W}$; (c) $f = 3.697\,\mathrm{Hz}$, $P_{\mathrm{abs}} = 176\,\mathrm{W}$; the zero of I is not calibrated.

peripheral plasma is ignited, the slot density n_{sl} is too much, Z_{sl} is too small, $V_{peri} \approx V_p$, in another words, C_{peri} can be consider parallel connecting to C_b, $C_p = C_b + C_{peri} = \kappa_{cap}(A_b + A_{peri})/|V_p|^{3/5} = \kappa_{cap}A_{ground}/|V_p|^{3/5}$, where A_{ground} is a total grounded area. With the power increasing, A_{ground} is becoming more, the slot is ignited at high frequency oscillations, further increasing power, the ground area A_{ground} is much more, the periphery is also ignited at low frequency oscillations. Then $V_a = I_{\mathrm{rf}}/j\omega C_a$, $V_D = V_a + V_p$, $V_{\mathrm{rf}} = V_D + I_{\mathrm{rf}}R_D$, $I_M = I_{\mathrm{rf}} + j\omega C_{\mathrm{stray}}V_{\mathrm{rf}}$, $V_M = j\omega L_M I_M + V_{\mathrm{rf}}$, $I_T = j\omega C_M V_M + I_M$, and, finally, $V_T = I_T R_T + V_M$.

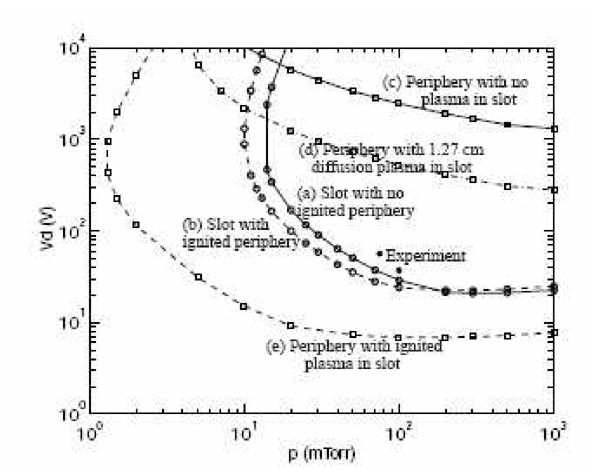

Figure 4: Maintenance curves , stars denote measurements of peripheral plasma ignition. The slot plasma will ignite at about 28 V (curve a). Once the slot ignites, the periphery also ignites, and periphery maintenance voltage at about 6 V with an ignited plasma in the slot (curve e). note: $V_d = V_p$.

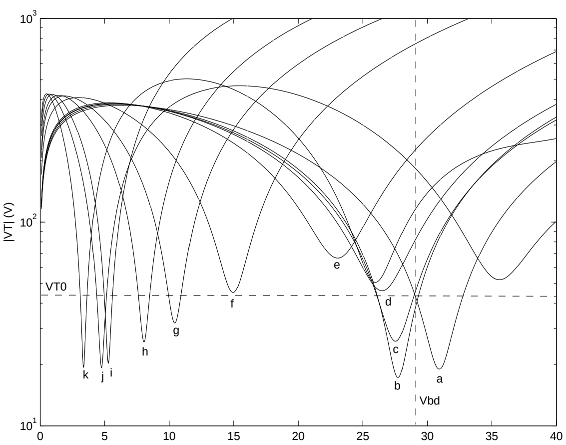

Figure 5: Magnitude of the source voltage $|V_T|$ versus main discharge grounded electrode sheath voltage, for whole processes of low frequency relaxation oscillations at different-density (a: 0.01, b: 0.063, c: 0.186, d: 0.68, e: 1.17, f: 2.0 g: 3.0, h: 4.0, i: 6.0, j: 10, k: 20. ($\times 10^{15}\,\mathrm{m}^{-3}$)) with varying-capacity C_p and varying-impedance Z_{sl}. $p = 100\,\mathrm{mT}$.

Figure 5 shows $|V_T|$ versus V_p for eleven different slot densities, which we use below to provide a plausible explanation for the hertz oscillation that is observed experimentally.

Low frequency relaxation oscillations in the periphery discharges, when the absorbed power increases about 58 W, low frequency oscillations begin, specially, with about a 15% reflected power, $P_{\mathrm{abs}} = 176\,\mathrm{W}$, a low frequency (3.7 Hz) relaxation oscillation occurs at the periphery. Low frequency oscillations increase grounded area when the periphery is ignited, dropping the slot plasma potential (V_p) with respect to ground, as well as dropping the potential below the breakdown voltage ($V_p < V_{\rm bd}$). The density in the slot increases, when the slot density $n_{\rm sl} \approx 6.0 \times 10^{15}\,{\rm m}^{-3}$ (i curve in Fig. 5), in accordance with $P_{\rm abs} \approx 176\,{\rm W}$, the high-Q resonance dips drop just below $V_p = 6\,{\rm V}$, the periphery and slot extinguish (the periphery maintenance voltage is about 6 V, e curve shown in Fig. 4), and then V_p drop rapidly to zero, the main discharge also extinguishes. The slot and the periphery restore the plasma voltage, the slot density decays, the process 'i→h→g→f→e→d→c→b→a' restarts, the main discharge and the slot re-ignite, once the slot is ignited, the periphery is also ignited with absorbed power excess 55 W. V_p re-decreases, the density in the slot re-increase, when the density increases to $2.0 \times 10^{15}\,{\rm m}^{-3}$, V_P does not continue to decrease zero because absorb power is 176 W in this case, the reflected power is 15%, rather than $P_{\rm abs} = 15\,{\rm W}$, the reflected power is 75%. The main discharge and the periphery are still ignited, so the slot density continues to increase, the slot and the periphery are ignited until $n_{\rm sl} \approx 6.0 \times 10^{15}\,{\rm m}^{-3}$, then V_p decreases rapidly to zero, the main discharge plasma extinguishes, the process 'a→b→c→d→e→f→g→h→i' is accomplished. Next step restarts the cycle 'i→a→i'. The absorbed power is 260 W, the reflected power still maintain 15%. A low frequency (3.48 Hz) relaxation oscillation appears in the periphery, the density in slot continues to increase, when the slot density $n_{\rm sl} \approx 1.0 \times 10^{16}\,{\rm m}^{-3}$ (j curve in Fig. 5), in accordance with $P_{\rm abs} \approx 260\,{\rm W}$, the high-Q resonance dips drop at $V_p = 4.9\,{\rm V}$, due to the hysteresis behave below the periphery maintain voltage 6 V, the periphery and slot extinguish, the main discharge also extinguishes when V_p decrease to be zero. The process 'a→b→c→d→e→f→g→h→i→j' is accomplished, and the cycle 'j→a→j' repeat. With the same analysis, another low frequency (2.72 Hz) oscillation presents in the periphery, a new cycle 'k→a→k' shown in Fig. 5 occurs.

From Fig. 5 we can see that each cycle of low frequency oscillations (e.g., 'i→a→i', 'j→a→j', 'k→a→k') has more period than those of high frequency oscillations (e.g., 'f→a→f'). We also see that the period of 'k→a→k' is more than one of 'j→a→j' or 'i→a→i', due to $f_k < f_j < f_i$ ($2.717\,{\rm Hz} < 3.484\,{\rm Hz} < 3.697\,{\rm Hz}$). We explain successfully low frequency relaxation oscillations phenomena.

As the low frequency oscillation in slot plasma density decay, with the timescale determined from diffusion theory to be $\tau_{\rm sl} = \frac{l}{2h_1 u_B}$. Estimate decay time $\tau_{\rm sl} = 48.36\,{\rm ms}$, with a density decay from $n_1 \approx 2 \times 10^{16}\,{\rm m}^{-3}$ to $n_2 \approx 1 \times 10^{13}\,{\rm m}^{-3}$, $f = 1/\tau_{\rm sl} \ln n_1/n_2 \approx 2.72\,{\rm Hz}$.

4. CONCLUSION

We conclude that the low frequency oscillations observed in the central plasma and in the peripheral chamber, at voltages below that at which the peripheral plasma ignites, are essentially understood as an instability induced by the increased resistance and capacitance of the discharge when the slot plasma ignites. A particular tuning of the matching network that we have investigated, both experimentally and theoretically, indicates that the ignition of the slot and the peripheral plasma increases the capacitance of the plasma to ground and lowers the system Q in such a way that the overall equilibrium is lost. This causes the voltage across the discharge to drop dramatically, causing the electron temperature to also drop. The main discharge density correspondingly decays at a slower rate, until the decay of the slot plasma density re-ignites the discharge, repeating the scenario. The oscillation frequencies as well as the shapes of the light emission signal and plasma density, obtained from the model, agree reasonably well with the corresponding experimental observations.

We have explained high frequency relaxation oscillations using an electromagnetic model of the slot impedance coupled to a circuit analysis of system including the match network in previous study. As low frequency relaxation oscillations, although we described some experimental phenomena of low frequency oscillations in previous papers [5–8], we did not further discuss the reason on low frequency oscillations. In this paper we develop the model to be considered various capacitances in the slot and the periphery with increasing absorbed power, the grounded area A_b increases. The capacitance C_b increase with increasing the ground area A_b when the periphery is ignited, corresponding to parallel connect a variation peripheral capacitance C_{peri} with C_b. The matching network dynamics has been found to play an important role in the instability dynamics.

ACKNOWLEDGMENT

We acknowledge the support provided by the Lam Research Corporation, the State of California MICRO Program, National Science Foundation Grant ECS-0139956, and a UC Discovery Grant from the Industry-University Cooperative Research Program (IUCRP). Z. W. Zhou supported by the Science Foundation of the Educational Administration of Guizhou Province in China (Grant No.-2006215).

REFERENCES

1. Tsai, W., G. Mueller, R. Lindquist, B. Frazier, and V. Vahedi, "High selectivity plasma etching of silicon dioxide with a dual frequency 27/2 MHz capacitive radio frequency discharge," *J. Vac. Sci. Technol. B*, Vol. 14, 3276, 1996.
2. Lieberman, M. A., A. J. Lichtenberg, S. Kim, J. T. Gudmundsson, D. L. Keil, and J. Kim, "Plasma ignition in a grounded chamber connected to a capacitive discharge," *Plasma Sources Sci. Technol.*, Vol. 15, 276, 2006.
3. Lieberman, M. A. and A. J. Lichtenberg, *Principles of Plasma Discharges and Materials Processing*, 2nd Ed, 411–413, Wiley, New York, 2005.
4. Lieberman, M. A., J. P. Booth, P. Chabert, J. M. Rax, and M. M. Turner, "Standing wave and skin effects in large area, high frequency, capacitive discharges," *Plasma Sources Sci. Technol.*, Vol. 11, 283, 2002.
5. Kim, S., Z. Zhou, M. A. Lieberman, and A. J. Lichtenberg, "Relaxation oscillations in a capacitive discharge chamber connected to peripheral grounded chamber," *J. Appl. Phys.*, Vol. 100, 103302, 2006.
6. Kim, S., M. A. Lieberman, A. J. Lichtenberg, and J. T. Gudmundsson, "Improved volume-averaged model for steady and pulsed-power electronegative discharges," *Journal of Vacuum Science and Technology A*, Vol. 24, 2025–2040, 2006.
7. Zhou, Z.-W., M. A. Lieberman, and S. Kim, "Instability parameters of optical oscillation frequency in plasma central discharge and peripheral region," *Chin. Phys. Lett.*, Vol. 23, 2251–2254, 2006.
8. Zhou, Z.-W., M. A. Lieberman, and S. Kim, "Review of relaxation oscillations in plasma processing discharges," *Chin. Phys.*, Vol. 16, 758–765, 2007.

RF-ID Tag Location Using RF-over-fibre Techniques

P. V. Brennan, A. J. Seeds, and Y. Huang
University College London, UK

Abstract— Security and efficiency at airports has, in recent years, become a critical issue in the eyes of the general public, security services and politicians alike. This paper presents a high-resolution, indoor location technique, based on RF-over-fibre, that is ideally suited to the monitoring of a high density of people and/or objects in such a situation.

1. INTRODUCTION

The issue of airport security has received increasing attention in recent times with a strong desire to introduce effective security measures that do not unduly inhibit normal airport operations. In addition, the increasing volume of traffic and in some cases larger aircraft have led to a need to improve boarding efficiency in order to reduce the occurrence of flight delays. The Optag project, launched in February 2004, and a further EPSRC-funded project, TINA (The INtelligent Airport), launched in September 2006, are aimed at addressing these issues.

The basic concept [1], illustrated in Figure 1, is for airports to be fitted with a network of combined RF-ID tag readers and high-resolution panoramic cameras, spaced at around 15–20 m intervals, which are used to monitor the movements of people around the terminal building or buildings. Each passenger carries or wears an RF-ID tag, which can allow location to an accuracy of around 1 m, and the video and tag data merged to give a very powerful surveillance capability with a wide range of potential benefits. The tags developed at UCL are transmit-only devices that do not store any data but emit a beacon with a unique ID at frequent, randomised intervals, at least once per second, and this is cross-referenced to passenger information already stored on the system — such as name, flight number and perhaps even biometric data. This gives the effect of intelligence in the tags — passenger information can appear to be 'read' from them though it actually resides on the computer system. The tags and reader infrastructure allow convenient monitoring of passenger flows and identification of late-running passengers.

The system can offer a number of benefits; it can be used to control entry to secure areas, allow the precise automated-tracking of certain individuals, help to evacuate the building in the

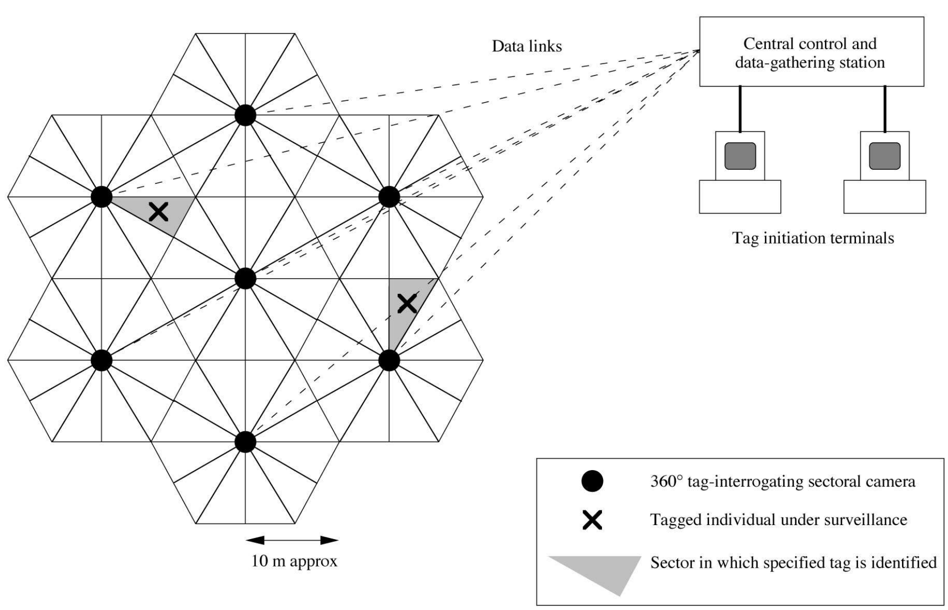

Figure 1: Outline of the Optag/TINA concept — a cellular UDP-based network of combined RF-ID tag readers and panoramic video cameras.

event of an emergency, provide rapid location and imaging of lost children and help to ensure that large aircraft are boarded efficiently by detecting and locating stray passengers. The Optag/TINA consortium have calculated that cost of flight delays due to late-running passengers amounts to some 150 M Euros per year in Europe alone, so considerable savings are possible with a system of this nature. A high degree of functionality can be built in to the system, dependent largely on the ingenuity of the user interface.

2. PROTOTYPE SYSTEM DESCRIPTION

The prototype Optag/TINA camera comprises a cluster of eight 1600×1200 pixel CMOS sensors, producing a 9600×1200 panoramic image. A portion of this image, or a lower-resolution panorama, is streamed to the central monitoring station using gigabit ethernet with the UDP protocol. The camera resolution allows recognition of a human face to 6 m and detection to around 30 m.

The tag system is rather challenging in that it is required to operate at relatively long range [2] (10–20 m), perform location estimates and simultaneously identify large numbers (> 1000) of tagged people or items in any given cell. To meet these challenges, the Optag/TINA team have designed a unique tag protocol that sends short bursts of data, at randomly-varying intervals, with a mean update rate of twice per second. Each tag reader uses direction finding to establish the bearing of the tag and then two or more bearings are used to establish the location. The prototype tag board, operating at 5.8 GHz, is shown in Figure 2. The peak tag output power is 10 mW, but the mean output power is very much lower — around 20 μW, many orders of magnitude below the threshold of emissions that would constitute any conceivable health risk. The prototype tag is a little larger than a credit card, but with miniaturization, could be very compact and easily incorporated in a small card or unobtrusive wristband.

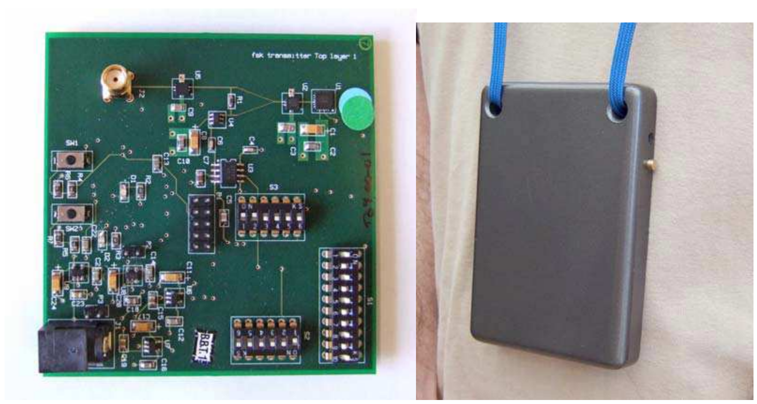

Figure 2: The prototype Optag/TINA 5.8 GHz RF-ID tag.

Figure 3: The prototype RF-ID tag reader/locator and camera cluster.

The tag readers, shown in Figure 3, are based on four antennas and receivers mounted at 90-degree spacings, which perform amplitude-comparison direction finding [3] on each tag burst. This straightforward approach provides a reasonable accuracy of around 1 m within a 10 m radius. However, the effects of reflections, signal blockage in crowded environments and other propagation artifacts are likely to be significant and will most likely diminish the achievable accuracy.

3. TECHNICAL CHALLENGES

An issue of direct relevance to this system is the possibility of data loss due to clashes between the tag bursts. Some such data loss is inevitable, depending on the number of tags in use in a given area and the duration of the data bursts. This has been carefully modeled as follows. The basic arrangement is shown in Figure 4 and consists of a number, N, of far-field RF-ID tags in a single reader cell, each radiating a short data packet of duration τ and with repetition interval, T. The system is asynchronous so that the timing of these data bursts is unrelated and varies randomly from tag to tag.

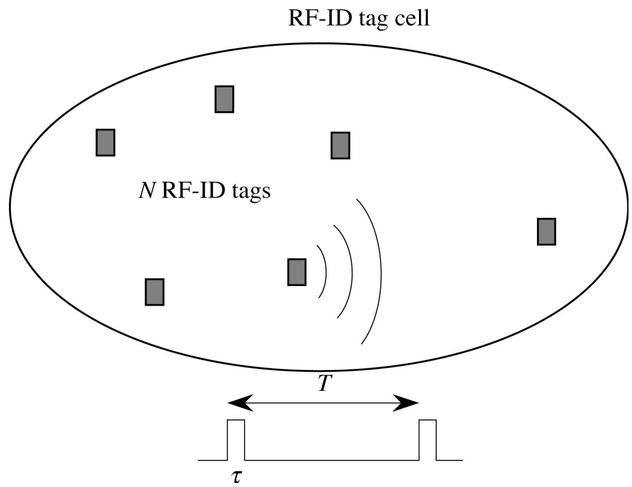

Figure 4: Illustration of RF-ID tag arrangement in a given cell.

Considering one particular tag sending a single data packet; a collision of some degree will occur if any other tag sends a data packet within $\pm\tau$ s of this transmission. The probability that this data packet will avoid the effects of such collisions from any of the other $(N-1)$ tags, thus ensuring there is no resulting data loss, is therefore given by

$$P(\text{no collision}) = \left(1 - \frac{2\tau}{T}\right)^{N-1} \tag{1}$$

The mean update interval, over a population of tags, is clearly increased by this finite probability of interference from neighbouring tags, and taking the worst-case situation in which all collisions result in loss of the data packet, the mean update interval may be expressed as

$$T_{mean} = \frac{T}{\left(1 - \frac{2\tau}{T}\right)^{N-1}} \tag{2}$$

These results are illustrated in Figures 5(a) and 5(b), for our system parameters of 1 Mbit/s data rate, 150 µs packet duration and a tag population of 500–2000. From Figure 5(a), the probability of avoiding data collisions improves with increasing repetition interval and diminishing tag population; however, from Figure 5(b), for a given tag population an optimum repetition interval exists with minimum mean update interval and maximum data throughput. This optimization process may be formulated as follows:

$$\frac{\partial T_{mean}}{\partial T} = \frac{\left(1 - \frac{2\tau}{T}\right)^{N-1} - \frac{2\tau}{T}(N-1)\left(1 - \frac{2\tau}{T}\right)^{N-2}}{\left(1 - \frac{2\tau}{T}\right)^{2N-2}} = 0 \quad \text{at} \quad T = T_{opt} \tag{3}$$

resulting in

$$T_{opt} = 2N\tau \quad \text{and} \quad T_{mean}(\min) = \frac{2N\tau}{(1-1/N)^{N-1}} \to 2eN\tau \equiv eT_{opt} \quad \text{for large} \quad N \tag{4}$$

Taking again the values used in Figures 5(a) and 5(b), for a tag population of 1000, the optimum choice of repetition interval is thus 0.3 s and the corresponding minimum update interval is 0.82 s. For an optimised repetition interval such as this, substituting Equation (3) into Equation (1), the probability that a given data packet suffers no collision is

$$P(\text{no collision, optimised}) = \left(1 - \frac{1}{N}\right)^{N-1} \to 1/e \tag{5}$$

and so, remarkably, maximum data throughput coincides with some 63% loss of data packets due to collisions. The prototype system is designed with a 0.5 s repetition interval equating to a mean update interval of 0.9 s — indicating that the position of all tags can be determined and updated on a second-by-second basis. Thus the system can easily accommodate 1000 tags in any given cell, which is probably close to the limit of the number of people who can possibly be squeezed into a 10 m radius area! In the current design, the tag centre frequency is stabilized by means of a PLL synthesised frequency source [4] with a fourth order loop filter of 50 Hz loop bandwidth, though new receiver techniques are being explored that may relax these requirements and allow for a non-synthesised tag implementation.

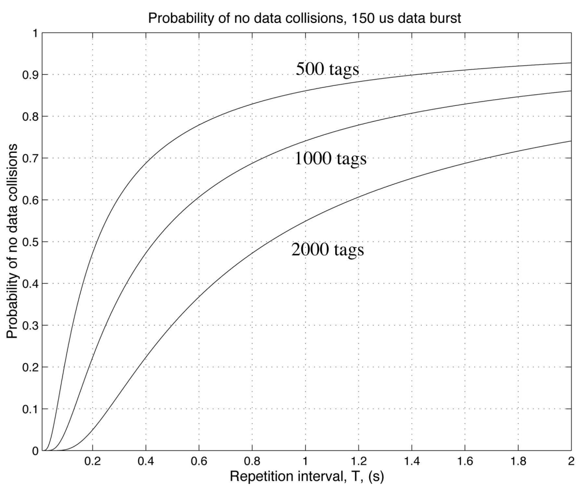

(a)

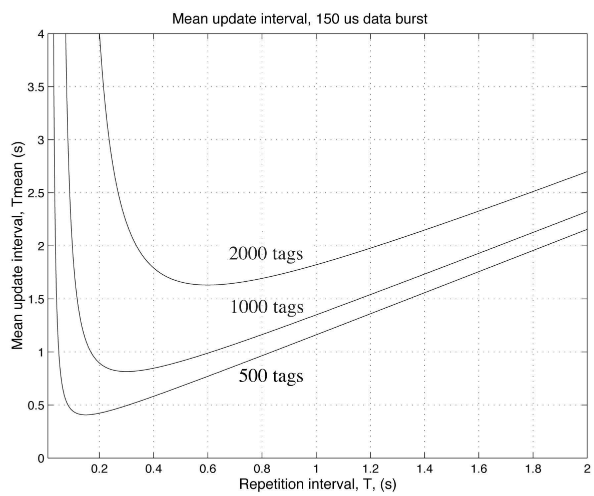

(b)

Figure 5: Modeled (a) tag clash probability and (b) mean update interval with tag population.

As far as propagation effects are concerned, a variety of simulations and trials have been conducted to assess the likely location accuracy in a realistic indoor environment. For illustration, a basic model considers reflections from the walls of a rectangular room, in the absence of any obstacles. The result of such a simulation, assuming a worst-case wall reflectivity of 100%, is given in Figure 6(a). The bearing error varies between zero and 25 degrees, but with a typical value of 6 degrees RMS — equivalent to 1 m error at 10 m range. This model uses a pessimistic value for wall reflectivity, but ignores the effect of the tag antenna pattern, polarisation and obstacles within the building. The location approach adopted in Optag is inherently vulnerable to propagation effects, however an entirely different technique, using wideband chirp tag modulation to measure the time-of-flight (and hence distance) between the tag and readers, rather than the tag bearing, is much more resistant to these multipath effects and is under development in the ongoing TINA project.

A range of trials have been conducted in the departure lounge at Debrecen airport, Hungary. Both the camera and tag systems have been evaluated based on three cells each containing a camera and RF-ID tag reader unit. As far as the tag system is concerned, the location accuracy was assessed with the tag readers mounted both centrally and in the corners of the rooms and with a ‘passenger’ wearing the tag in a variety of locations and facing in several directions. Measurements were repeated in crowd situations in which the tag-wearing person was surrounded by other people. The general conclusions of this trial were that the best positioning of the tag readers is in the corners of the room, location errors are indeed dependent on tag orientation and obstructions due to other individuals, and operating range exceeds expectations — 25 m being easily accomplished even under the most adverse conditions. One of the results obtained with corner-mounted tag readers is shown in Figure 6(b). This indicates the bearing error for different positions of the tag-wearing individual, over a 6×7 grid (with a grid spacing of 801 mm). The mean error is close to zero, indicating that there is no squint in the reader, but there is considerable deviation, dependent on the tag location. The RMS variation in this particular set of result is 16 degrees — equating to 1.4 m of location error at the typical operating range of 5 m.

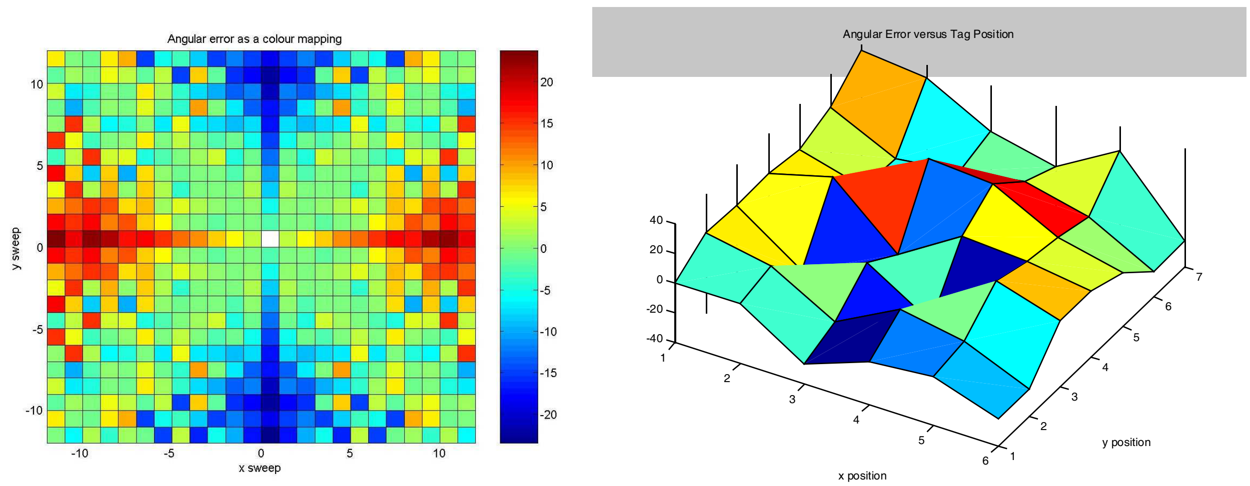

(a) (b)

Figure 6: Modeled (a) and measured (b) bearing errors (corner-mounted reader).

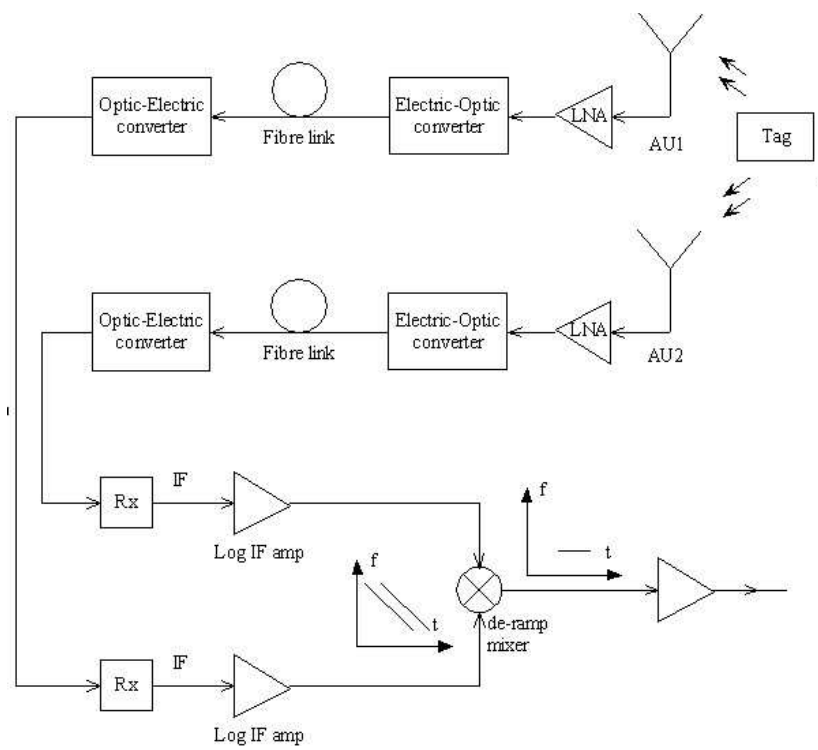

Figure 7: Basic arrangement of the RF-over-fibre TDOA location system.

4. TDOA RF-OVER-FIBRE LOCATION SYSTEM

An alternative location technique, currently under investigation in the TINA project, is to use time difference of arrival (TDOA) estimation with RF-over-fibre. This exploits the very wide bandwidths available in fibre and enables mitigation of multipath effects, thus offering improved location accuracy. The system under development, shown in Figure 7, comprises FM-chirped tags (operating in the 85 MHz wide 2.4 GHz ISM band) with RF-over-fibre interfaces to a central de-ramping block which estimates the time difference between any pair of received signals. Three or more time differences are sufficient to uniquely locate the position of a given tag. The classical resolution limit associated with 85 MHz bandwidth is some 3.5 m, though we hope to obtain up to an order of magnitude greater performance by judicious signal processing design.

5. CONCLUSION

The Optag/TINA projects have demonstrated the feasibility of a combined RF-ID tag and panoramic video monitoring approach in an airport environment, including a proof-of-concept trial in a Hungarian airport building. All indications are that the concept is sound, though any future adoption will require further development and commercialisation, in particular the network infrastructure and associated software to both operate the Optag/TINA system and interface with existing airport computer systems and databases.

The mode of deployment of the tag element of the system is controversial and somewhat critical to certain areas of operation. For instance, in a security context, it would be crucial to ensure that each person carries his/her own tag and does not lose or swap them. One way in which this can be achieved is to incorporate the tag in a wristband that sends an alert code should it be removed. The detection mechanism could be a small capacitively-coupled current across the sealed wristband which is interrupted if it is either cut or removed. With suitable circuit miniaturisation, the wristband could be small and unobtrusive, perhaps made of thin card. However, public acceptance of the use of wristbands for this purpose may well be an issue, so exactly how the tags are deployed remains open at this stage.

Current work is focusing on an alterative tag and reader implementation involving TDOA location exploiting RF-over-fibre transmission, which offers the prospect of significantly improved location accuracy and multipath mitigation Another area that has huge potential for future development is the user interface, where a whole host of features could be incorporated including, for instance, an additional, simple interface at departure gates to alert staff to late-running passengers; an automated monitoring and announcement system to contact such late-running passengers as and when required; extensive archiving facilities to store tag and at least a subset of video data; seamless linking of tag ID, personal data and biometric data and market research analysis of data, to aid the design of airport layouts for instance to optimise passenger flows or to feed into charging models for the various retail outlets. It is clear that, once such an infrastructure is in place, there is huge potential to make use of the capabilities in a variety of different manners, many of which have probably not yet been foreseen. The system may also find application in a range of other arenas, including hospitals (e.g., maternity units), theme parks, exhibition halls and concert venues.

ACKNOWLEDGMENT

The authors would like to thank EPSRC and the European Commission, particularly Jean-Pierre Lentz, for their encouragement and support during this work.

REFERENCES

1. McCoy, T. M., R. J. Bullock, and P. V. Brennan, "RFID for airport security and efficiency," *IEE Seminar on Signal Processing for Homeland Security*, 8/1–8/7, IEE Savoy Place, London, U.K., October 2005.
2. Flores, J. L. M., S. S. Srikant, B. Sareen, and A. Vagga, "Performance of RFID tags in near and far field," *Personal Wireless Communications, 2005, ICPWC 2005*, 353–357, Jan. 2005.
3. Andrews, R. S., "Antenna and other systematic effects on amplitude comparison monopulse systems," *IEE Proc. Electronic Circuits and Systems*, Vol. 3, 103–108, May 1979.
4. Brennan, P. V., *Phase-locked Loops, Principles and Practice*, ISBN 0-333-65571-0, Macmillan, London, ISBN 0-07-007568-9, McGraw-Hill, New York, 1996.
5. Nikitin, P. V., S. Lam, and K. V. S. Rao, "Low-cost silver ink RFID tag antennas," *IEEE Antennas and Propagation Society International Symposium*, Vol. 2B, 353–356, 2005.

Design of New DGS Hairpin Microstrip Bandpass Filter Using Coupling Matrix Method

A. Boutejdar[1], **A. Elsherbini**[2], **A. Balalem**[1], **J. Machac**[3], **and A. Omar**[1]

[1]Microwave and Communication Engineering, University of Magdeburg, 39106 Magdeburg, Germany
[2]Department of Electrical and Electronic Engineering, Ain Shams University, Cairo, Egypt
[3]Faculty of Electrical Engineering, Czech Technical University, Technick 2, 16627 Prague 6, Czech Republic

Abstract— In this paper we present a novel compact Hairpin bandpass (BPF) microstrip filter employing two U-slots etched in the ground plane (DGS) and two $50\,\Omega$ feeds on the top. A new type of microstrip BPF based on coupled DGS resonators is designed using coupling matrix method. The new BPF is very compact, in addition, the filter has a very wide stopband with two transmission zeroes. A good agreement between the measured and simulated results is achieved.

1. INTRODUCTION

THE coupled microstrip bandpass filter (BPF) has been extensively investigated and widely used in many microwave and millimeter-wave systems in order to achieve high performance, small size, and low cost and to comply with strictly required transmission specifications. There are many types of bandpass filter design techniques to meet the above requirements, such as the use of high-permittivity materials, variation of resonator structures, and use of multiple resonant modes. In the conventional microstrip and strip line BPFs having parallel coupled lines, the size is quite large because of use of $\lambda/2$ resonators, while the realization is simple. On the other hand, the BPFs having Hairpin resonator structures, which is a modification of parallel coupled lines, have relatively smaller size than the BPF having parallel coupled lines. However, these filters are of limited utility due to their typically high insertion loss and the practical problem to achieve less than 5% bandwidth. In order to solve these problems, the DGS structures will be used. The stringent requirements of modern microwave communication systems are often met only by high performance and compact filtering structures. Several of such filters have been reported using generic structures called the defected-ground structures (DGS). Since DGS cells have inherently resonant properties, they have been used in filtering circuits to achieve narrow bandwidth, and to suppress these spurious passbands The DGS-resonators have several advantages such as compact size, low radiation loss. Therefore, the DGS-Filters are widely used in the design of filters, oscillators, and antennas.

In this paper, we introduce a new DGS-Hairpin structure in order to suppress higher harmonics and to realize sharp edges by introducing two transmission zeros to filter response [1], and locate them at either sides of the passband. This DGSs operate as two magnetic coupled resonators and also as a stop resonator to suppress harmonics, simultaneously.

2. HAIRPIN-DGS RESONATOR

A defect for the microstrip line, which has been etched in the backside metallic ground plane, disturbs the current distribution in the ground, and increases the effective inductance and capacitance of the microstrip line. Therefore, the DGS is usually modeled as a parallel LC resonance circuit by using a circuit-analysis method. The proposed DGS shape with its dimensions is illustrated in Fig. 1, wile, Fig. 2 shows its equivalent circuit, where L_p and C_p denote the inductance and capacitance, which are the results of the electromagnetic field disturbances in the ground plane. For more accurately modeling the DGS section, capacitance C_1 and inductance L_1 should be considered as a part of the equivalent circuit models, which are result from the fringing field around the discontinuity area. In order to extract the values of the equivalent circuit elements, the S-parameters of a DGS unit at the metallic ground plane should be calculated using an EM-simulator, in addition the relationship between the S-parameter and ABCD-matrix will be used. To confirm the validity of the proposed equivalent circuit model of a DGS unit, shown in Fig. 1, the DGS-Hairpin slot has been simulated using EM simulators Microwave Office. The dimensions of the slot shown in Fig. 3, are as follows: $l_1 = 6\,\text{mm}$, $l_2 = 1\,\text{mm}$, $d = 5\,\text{mm}$, and $w = 1.9\,\text{mm}$.

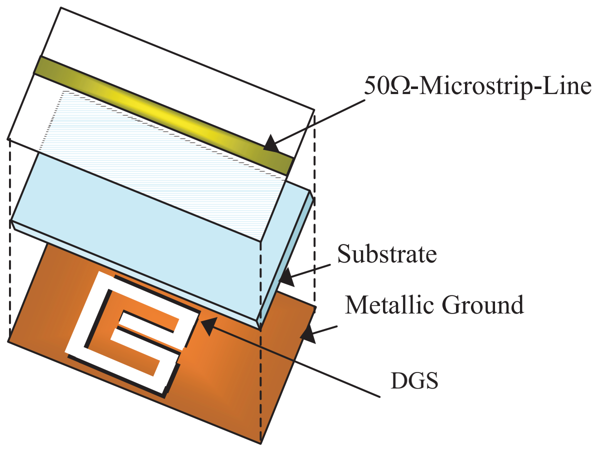

Figure 1: Three-dimensional view of the Hairpin-DGS.

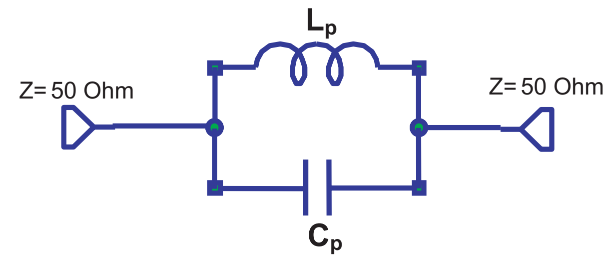

Figure 2: Equivalent circuit of the DGS-Hairpin slot.

3. INFLUENCE OF HAIRPIN DGS DIMENSIONS ON THE ATTENNUATION POLE FREQUENCY

The proposed slot shown in Fig. 1, can provide attenuation pole at certain frequency without any periodic array of DGS. In order to investigate the frequency characteristics of the etched slot, we simulated the DGS unit section using Microwave Office. The placement of the DGS under the microstrip line involves the appearance of a resonance frequency. This effect is due to the decreased the effective permittivity which results with increasing the effective inductance of the microstrip. The variation of the dimensions of the DGS-length shifts the attenuation pole location in the frequency domain. It is well known, a resonant frequency can be generated by a combination of inductive and capacitive elements. Thus, in order to explain the simulated frequency response of the proposed DGS section, we introduced a capacitance in the equivalent circuit. The etched gap area, which is placed under the microstrip line, corresponds to capacitance and the Metallic bridge between the DGS-arms is equivalent to a series inductance. So, the DGS [2] unit is equivalent to a resonant circuit, which is shown in Fig. 2. The parameters of this DGS equivalent circuit have been found using curve-fitting. They are: $C_p = 0.33\,\text{pF}$ and $L_p = 2.33\,\text{nH}$. In order to investigate the effect of the DGS-arm dimensions, the length (d) of intern etched gaps were kept constant at 5mm and the length (l_1) of extern etched rectangular area was varied. The simulated results are illustrated in Fig. 4. As the arm-length (l_1) are increased, both the characteristic impedance and the series inductance of the microstrip line increased, while the cut-off and resonance frequency decrease.

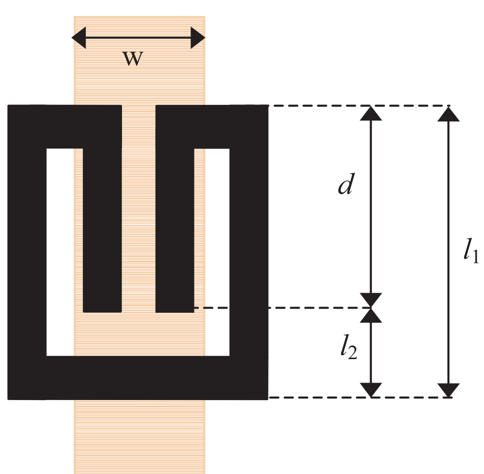

Figure 3: Three-dimensional view of the Hairpin-DGS.

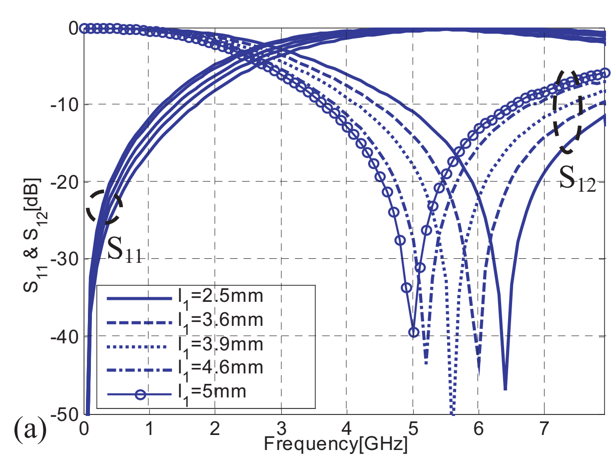

Figure 4: Simulated S-parameters for different values of l_1 of the Hairpin-DGS cell.

4. THE BASIC IDEA

With the modification of the DGS-size it will be possible and easy to shift the resonant frequency band, thus it will be systematically the Filters answer to controlled. The new idea is: how the resonance position will be controlled, while keeping constant the DGS-size? In order to realize that, the length of intern DGS-arm [3] will be simply changed. While d will be increased, the position will be shifted in lower frequency. Thus the compactness will be improved with the length of the intern-DGS-arms. As the Fig. 6 shows.

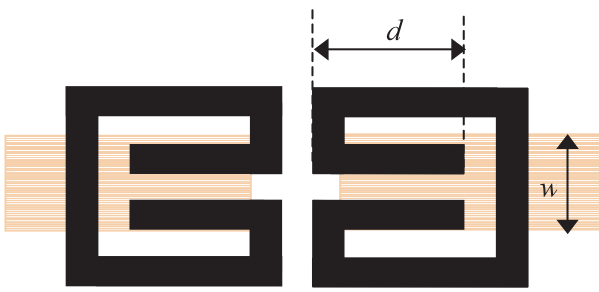

Figure 5: Two-dimensional view of the proposed BPF.

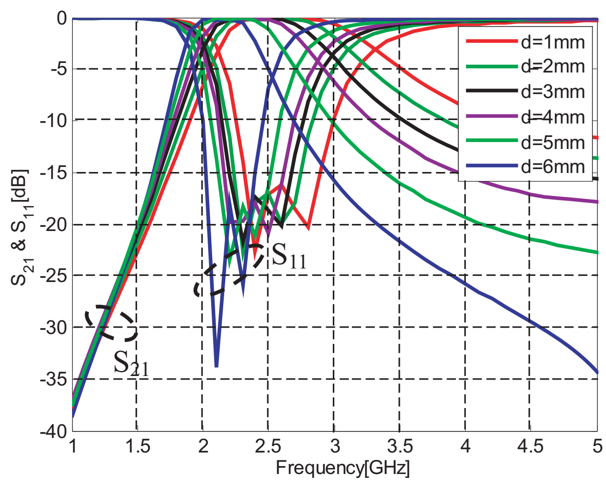

Figure 6: Simulated S-parameters for different values of d of the BPF.

5. THE THEORY OF COUPLING MATRIX METHOD

In order to realize a coupling matrix which conforms to a chosen topology, it is necessary to give first the specifications of the filter. The desired parameters will be then extracted by using an optimization-based scheme [1]. The coupling coefficient and quality factor curves [1] are then used to realize the obtained coupling coefficients In our case the second order filter is with a bandwidth $BW = 500\,\mathrm{MHz}$, return loss $RL = 20\,\mathrm{dB}$, and centre frequency $f_0 = 2.1\,\mathrm{GHz}$. The obtained coupling matrix from the optimization scheme is

$$M = \begin{bmatrix} 0 & 1.236 \\ 1.236 & 0 \end{bmatrix},$$

and the external quality factors are $q_1 = q_2 = 0.8422$.

To realize the normalized coupling matrix and quality factors, we use the required fractional bandwidth $FBW = BW/f_0$, the actual (denormalized) coupling matrix becomes.

$$m = \begin{bmatrix} 0 & 0.231 \\ 0.231 & 0 \end{bmatrix},$$

and $Q_1 = Q_2 = 7$ where $m = FBW \times M$, and $Q = q/FBW$.

The m-coupling coefficients will be inserted in the experimental curve [1] in order to get the optimal distance between the DGS resonators. The unknown distance s is 2 mm. See the Fig. 7.

6. DESIGN AND MEASUREMENT OF THE IMPROVED DGS-BANDPASS FILTER

The optimized DGS has been used to design a BPF, which was fabricated on a $(20 \times 15\,\mathrm{mm}^2)$ substrate with a relative dielectric constant ε_r of 3.38 and a thickness h of 0.813 mm. Photographs of the filter are shown in Fig. 9. Measurements were carried out on an HP8719D network analyser. One can see from Fig. 10 that the measured results show good consistency with both simulations. The fabricated BPF has a center frequency at 2.1 GHz and a suppression level of 20 dB from 2.85 to 8.5 GHz; the insertion loss in the passband is about 0.15 dB. Thus we have demonstrated that the proposed coupled DGS bandpass filter is very favourable than the designed bandpass filters in [1]. The experimental results show excellent agreement with simulated result. Fig. 10 and Fig. 11 show the simulated and measured data of the two layers of the proposed Hairpin-DGS bandpass filter [4].

Fig. 8 shows the field distribution resonant frequency (at the transmission pole), it can be clearly seen that no power it transmitted to port 2.

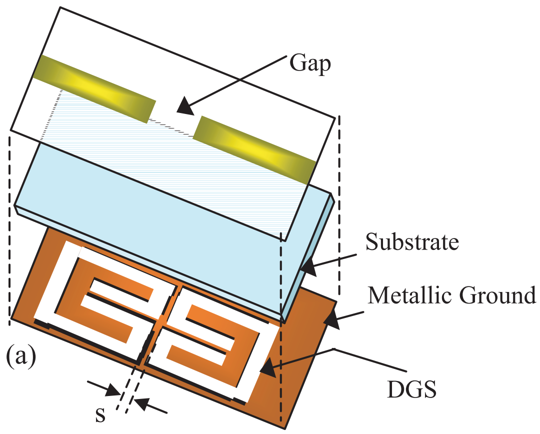

Figure 7: 3D-view of the DGS BPF.

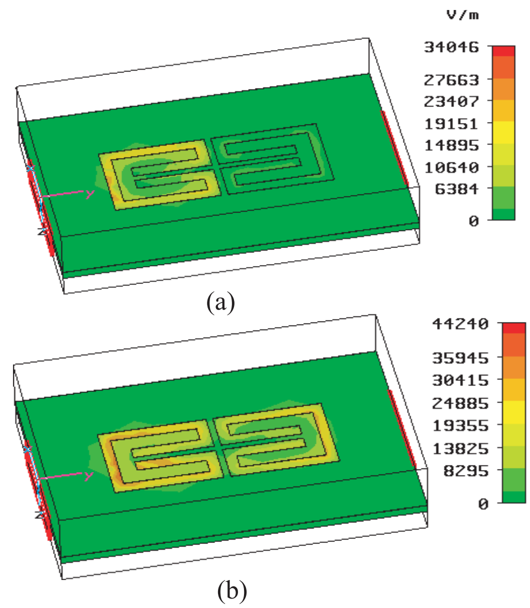

Figure 8: The EM-field distribution (a) at resonance frequency. (b) at center frequency of the DGS-BPF.

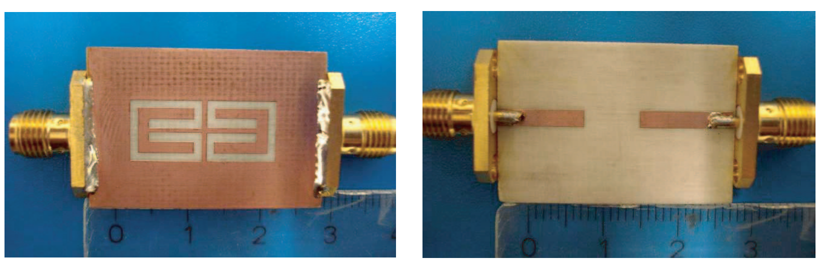

(a) (b)

Figure 9: Fabricated Hairpin-DGS-BPF. (a) Bottom view. (b) Top view.

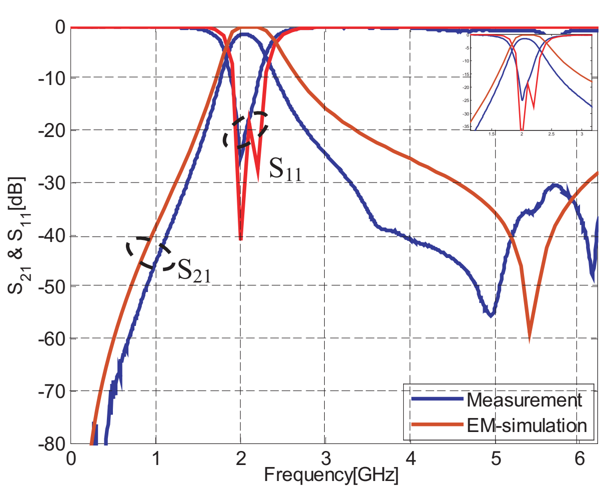

Figure 10: Schematics of the designed DGS-bandpass filter.

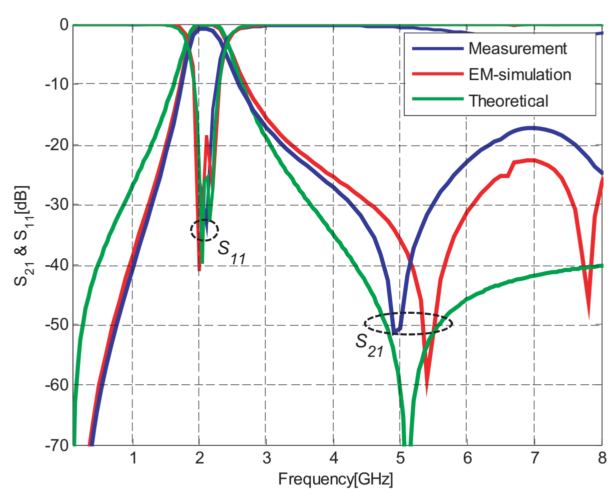

Figure 11: Three-dimensional view of the Hairpin-DGS.

7. CONCLUSION

In this paper we have introduced a new DGS Hairpin resonators and investigated different geometrical modification. Controlling the center frequency and improving the characteristics of the proposed BPF have been addressed. The use of DGS cells shows a good effect on the stopband. The second order filters with quasielliptic response were presented. Controlling the center frequency and archiving a good matching at the passband can be simply realized by changing the length or the width of the investigated structure without changing the area occupied by the filter. The filters were designed, fabricated and measured. Good agreement between simulated and measured results was achieved.

REFERENCES

1. Hong, J.-S. and M. J. Lancaster, *Microstrip Filters for RF/Microwave Applications*, Wiley, New York, 2001.
2. Abdel-Rahman, A., A. R. Ali, S. Amari, and A. S. Omar, "Compact bandpass filters using Defected Ground Structure (DGS) coupled resonators," *IEEE MTT-S International Microwave Symposium*, Honolulu, Hawaii, June 2005.
3. Boutejdar, A., A. Elsherbini, and A. S. Omar, "Improvement of passband and sharpness factor of parallel coupled microstrip bandpass filter using discontinuities correction and DGS cells," *MMS 2007 Mediterranean Microwave Symposium Budapest*, Hungary, May 2007.
4. Awida, M., A. Boutejdar, A. Safwat, H. El-Hannawy, and A. S. Omar, "Multi-bandpass filters using multi-armed split ring resontors with direct feed," *IEEE MTT-S International Microwave Symposium*, Honolulu, Hawaii, June 2007.

Inverse Problem of ECG for Different Equivalent Cardiac Sources

C. G. Xanthis, P. M. Bonovas, and G. A. Kyriacou
Mircowave Lab, Department of Electrical and Computer Engineering
Democritus University of Thrace, Xanthi 67100, Greece

Abstract— An improved solution of the non-linear and ill-posed inverse problem of electrocardiography is presented. The hearts activity is modeled by three different equivalent cardiac sources: 1 moving dipole, 2 and 5 fixed location rotating dipoles. For this purpose a three dimensional volume conductor model of the human body is constructed based on a classical anatomic atlas. This is excited by each one of the cardiac sources. For the inverse problem a Least Squares (LS) optimization scheme is employed, aiming at the matching of the potential distribution calculated on the torso surface to the corresponding distribution measured with the aid of multiple electrodes. The efficiency of the method stems from the employment of arbitrary shaped hexahedral elements within the volume conductor model for the minimization of the required computational resources, while the model realistically reflects the body internal structure. Finally, the algorithm is successfully tested using measured data available online.

1. INTRODUCTION

The objective of electrocardiography in general is the qualitative and quantitative representation of the heart's electrical activity exploiting the information provided by the potentials recorded at the body surface. The inverse electrocardiography (ECG) in particular, refers to a pre-determined modelling of the cardiac activity by a variety of equivalent electric sources as a single or double moving/rotating electric dipole, multiple fixed location dipoles, the epicardial potential distribution and the activation of isochrones on the heart surface, e.g., [1].

The aim of the inverse problem of electrocardiography is to restore the heart activity from a given set of body surface potentials. Its solution provides the researcher with detailed information about the electrophysiological heart activity of a patient and reduces the need for catheter measurements. Moreover, like most inverse problems, the solution of the ECG inverse problem is hindered by two common characteristics. First the non-uniqueness of the solution, namely the same set of measurements could result from more than one source configurations. Second the ill-posed nature of the inverse problem, i.e., an arbitrary small change of the body surface potentials can cause an arbitrary large change of the equivalent source solution. Moreover, like most inverse electromagnetic problems this is a non-linear one.

In the equivalent dipole model approach the activity of the heart is represented by one or multiple moving/rotating current dipoles. The basic underlying principle is to select the amplitudes and coordinates of these dipoles within an appropriate model of the torso such that calculated torso surface potential distribution closely matches the measured body-surface-potential distribution. This source model was used by Gulrajani et al. [2], in some earlier investigations and Guard et al. [3]. Also Armoundas et al. [4], and Bruder et al. [5] used the single moving dipole to simulate the electrical activity of the heart. There are many other research groups, e.g., [6, 7] active in the inverse electrocardiography field which aim at the definition of epicardial potential distribution either by using realistic geometry anisotropic heart models or trying to exploit a priory information. The research status up to 1998 is given in the review paper [1].

Although our previous work [8], based on a single fixed central location but rotating electric dipole, led to relatively successful localizations, this approach in turn involves a compromise in modeling accuracy. For that purpose, the present work implements improvements in the modeling of heart activity using three different equivalent electrical cardiac sources. Firstly, the single cardiac dipole is allowed to move and/or rotate. The use of two fixed location-rotating dipoles constitutes the second step of the current work. Last, the use of multiple static dipoles concludes this work. Each one of these dipoles represents a certain anatomical region of the heart.

The same algorithm for the solution of the inverse ECG problem along with the same finite element (FEM) volume conductor model [9], implemented in our previous work [8], is herein as well. This algorithm is general and can be adapted to the above mentioned or to more general source distributions. Besides the above, the main strength of our approach stems from the appropriately developed body volume conductor model. The latter enables the efficient and fast solution of the inverse problem which is based on multiple solution of the forward problem.

Finally, a series of successfully estimated rotating dipoles tracking the hearts temporal behavior will be presented. High spatial density measured body surface potentials available online by MacLeod et al. [10] are exploited for this purpose.

2. FORMULATION OF FORWARD PROBLEM

2.1. Torso Model — FEM Solution

A three dimensional (3-D) volume conductor modelling is required, which must also be a realistic one, namely accurately reflecting the internal geometrical body structure, in order to get the desirable agreement with the measurements. From previous works the accurate modelling of human torso needs some 400.000 cubic elements or more [11, 12]. In order to use a model in inverse problems it is imperative to minimize the elements number and hence minimize the required computational resources (time and memory). Since, the complexity is mostly due to the curved boundaries between the tissues, the number of elements can be drastically reduced when arbitrary shaped elements are used. For this purpose general hexaedral volume elements are adopted within our effort.

The implemented model, Fig. 1, is based on the Eycleshymer and Shoemaker anatomic atlas [13]. The physiological tissue conductivity values assigned to each general hexahedral element were adopted from Geddes and Baker, [14]. It is constructed into 32 layers (33 cross sections) consisting of totally 8.800 general hexahedral elements and 9.727 nodes. Additional information can be found in previous work [15, 9].

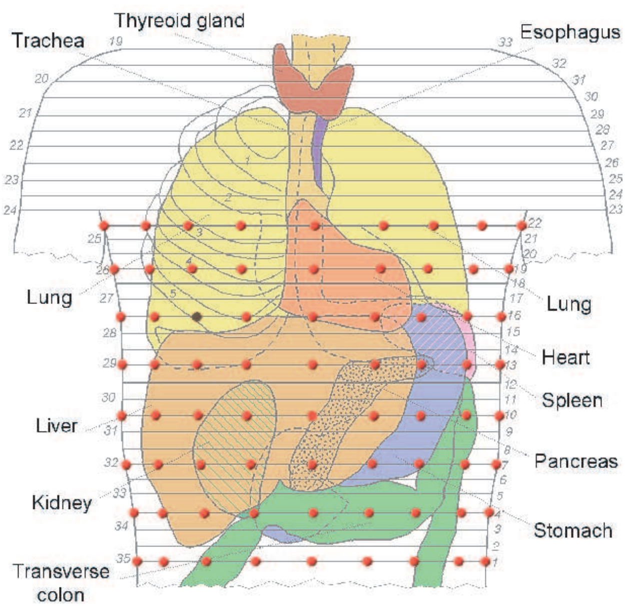

Figure 1: Vertical view of the torso model. Cross sections are numbered according to the atlas [13] on the left and our numbering on the right. The electrode numbered by 67 is painted in black.

2.2. Source Modelling

Focusing on the dipole modeling, the method proposed in [16] is employed. Each of the three different electrical cardiac sources is consisted of an equivalent number of electric dipoles. Every electric dipole is made up of six parameters: 3 for the dipole coordinates (the dipole origin) and 3 for the dipole moment components, $\bar{P} = I \cdot l\hat{p}$ (Fig. 2(a)). Thus, for modeling purposes, a dipole in a 3-D space can be represented by a point current source at $\bar{r} = \bar{r}^+$ and point current sink at $\bar{r} = \bar{r}^-$ providing I and $-I$ A, separated by an infinitesimal distance l, as shown in Fig. 2(b). The Poisson equation in a 3-D space excited by a dipole source follows from the continuity equation [16] and reads:

$$\nabla \cdot \{\sigma(r)\nabla V(r)\} = g(r) = \lim_{l\to 0} I\{\delta(r - r^+) - \delta(r - r^-)\} \quad (1)$$

where $\delta(r - r^\pm)$ denotes the Dirac's delta function centered at $r^\pm$ which defines the points of current source and sink (Fig. 2(b)). With the aid of the variational technique, Eq. (1) along with the boundary conditions is reduced to a functional minimization, e.g., [14, 17].

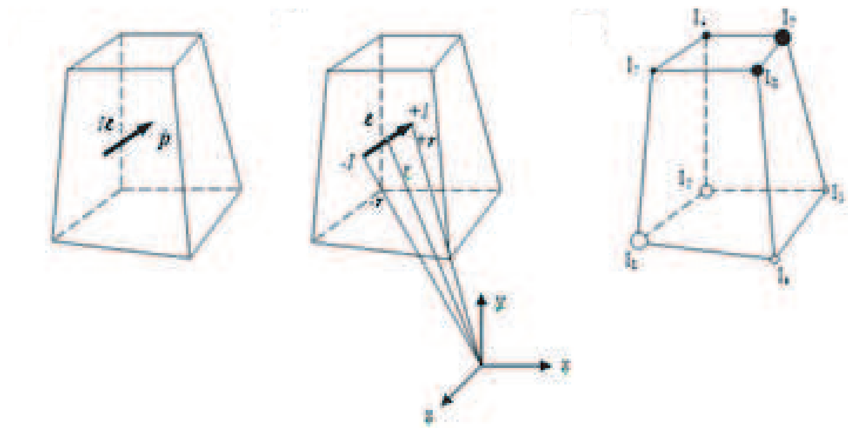

(a) (b) (c)

Figure 2: (a) The original 3-D dipole source with amplitude Il and direction $\hat{p}$ inside a general hexahedral element. (b) The representation of the dipole as a current source and sink. (c) The equivalent 8 nodal current values representing the dipole. The size of the node indicates the current value.

Let us repeat the linear system resulting from the minimization — integration over a specific element containing the dipole this reads $[K]^e \cdot [V]^e = [I]^e$, where $[K]^e$ is an 8×8 matrix that comes from the left hand side of (1), and $[I]^e$ is a vector that comes from the integration of right hand side of (1) after multiplying with the element's interpolation functions. According to [16] the excitation with a dipole source is equivalent to the application of currents I_i on the 8 nodes of each element containing the dipole, Fig. 2(c). In turn, these I_i values will act as the excitation in the final system of equations to be obtained from the FEM master matrix assembly [14, 17].

3. FORMULATION OF INVERSE PROBLEM

The solution of the inverse problem is usually based on iterative solutions of the forward problem. Namely, for a given geometry, a given conductivity distribution and a specified internal source, calculate the body surface potentials. In contrary for the inverse problem the body surface potentials are measured, the conductivity and geometry are assumed known (physiological values) and the internal equivalent source is sought.

Working toward the achievement of better accuracy in the source modelling, a number of different equivalent electric cardiac sources were tested. Every one of these sources is accompanied by a specific number of variables used to minimize the error of fitting the recorded data in the least square sense. Namely, the inverse problem is based on the Least-Squares (LS) Optimization and the nonlinearity is confronted by the implementation of the Levenberg-Marquardt method.

The required measured data set can be obtained from measurements on electrodes positioned equidistantly over the body surface (measured data-V). The algorithm starts with a guess for an equivalent cardiac electric source distribution and the body surface potentials are obtained (calculated data-U), solving the forward problem. Thereafter, the Levenberg-Marquardt optimization scheme is employed for the final equivalent cardiac source estimation. So, the initially assumed equivalent electric cardiac source parameters (e.g., 3 dipole moment components and 3 coordinates of dipole origin for a moving and rotating dipole) are iteratively updated until the differences between the measured and calculated data sets becomes comparable to an acceptable error tolerance. The least squares method minimizes the summed square of residuals. The residual for the ith data point r_i is defined as the difference between the measured potential value V_i and the calculated potential value U_i, and is identified as the error associated with the data:

$$r_i = V_i - U_i \tag{2}$$

The cost function is defined as the summed square of residuals (SSQ) and reads:

$$F = \sum_{i=1}^{n} r^2 = \sum_{i=1}^{n} (V_i - U_i)^2 \tag{3}$$

where n is the number of data points (electrodes on the body surface) included in the fit model.

The algorithm of the inverse problem is programmed in Matlab, while the computationally demanding procedures are implemented as Fortran subroutines. So presently, for the Levenberg-Marquardt scheme we use the functions provided by the Matlab optimization toolbox for the nonlinear least-squares minimization.

4. NUMERICAL RESULTS

The proposed algorithm was applied for the localization of three different equivalent electric cardiac sources and satisfactory results were obtained. Firstly, a single cardiac dipole is allowed to move and/or rotate (six degrees of freedom). For the second model two dipoles are allowed only to rotate about a fixed origin in the heart area, the first located at the sinoatrial node of the heart and the second at the atrioventricular node. Finally, the use of five fixed location dipoles concludes our current work. The first two dipoles maintain the same location as in the previous source type while the third dipole is located in the Bundle of His and the last two in the area of the Purkinje fibers.

The algorithm was tested on real multichannel measured data set available on-line, [10]. According to [10], the body surface potentials were measured from 128 electrodes positioned equidistantly over the body surface (Fig. 1), for three different body poises (aligned-sitting, aligned-right and aligned-lying).

Due to space limitation numerical results will be given only for the 5 dipole model, while results for the other models will be presented at the conference.

Figures 3(a)–(e) presents the moment components (Px, Py, Pz) of the 5 dipoles for each one of the three body poises. Alternatively, the dipole moment vector rotation can be presented in a 3-D view. An example of the 4th dipole's orbit for the sitting and lying poises are presented in the Fig. 3(f).

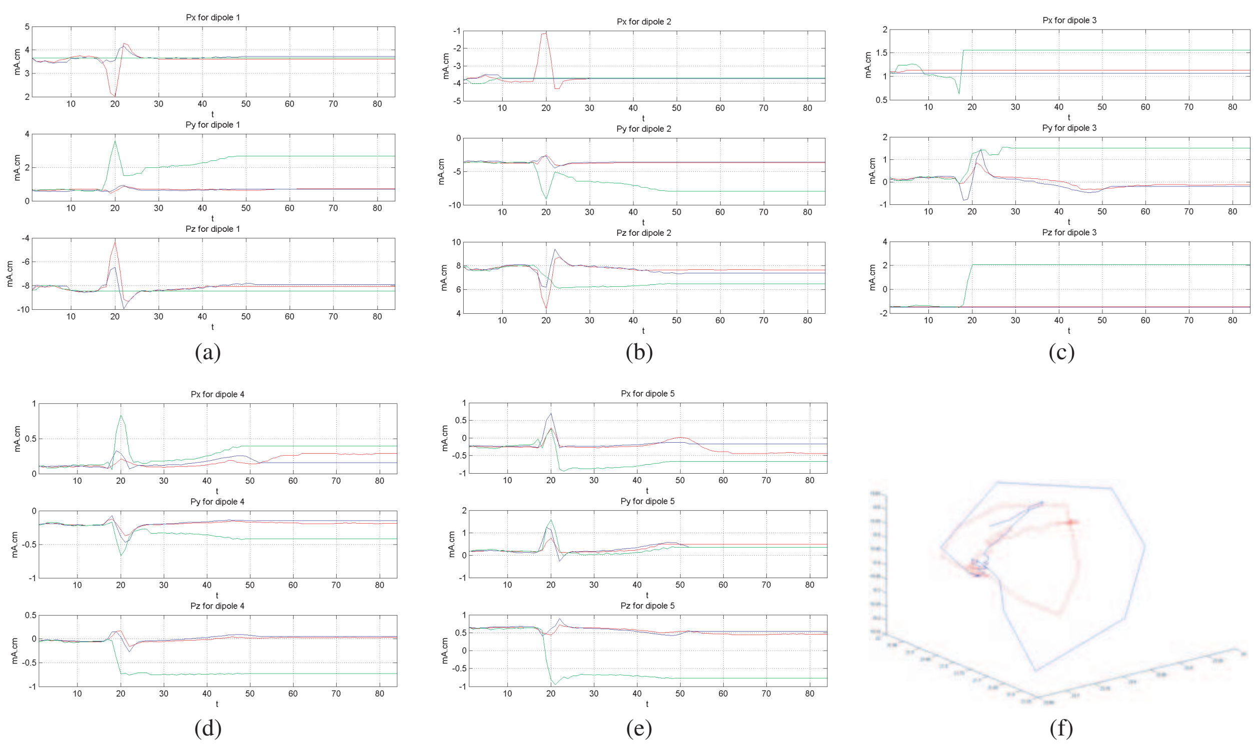

Figure 3: The moments components (Px, Py, Pz) of the five dipoles (a–e) for the three body poises (lying-red, sitting-blue, aligned right-green). Dipole orbit during the whole cardiac temporal period for the 4th dipole for the sitting (blue) and lying (red) poises (f).

The normalized sum of squares error (SSQ/SSQmax) versus number of iterations for the source types of 1 moving dipole and for 2 and 5 fixed location dipoles for the sitting poise is shown in Fig. 4(a). It is obvious that the 5 fixed location dipole model leads to a faster convergence.

Finally, in order to verify the validity of our algorithm, the calculated potential values during the whole cardiac temporal period are compared with the respective values of the measured potentials.

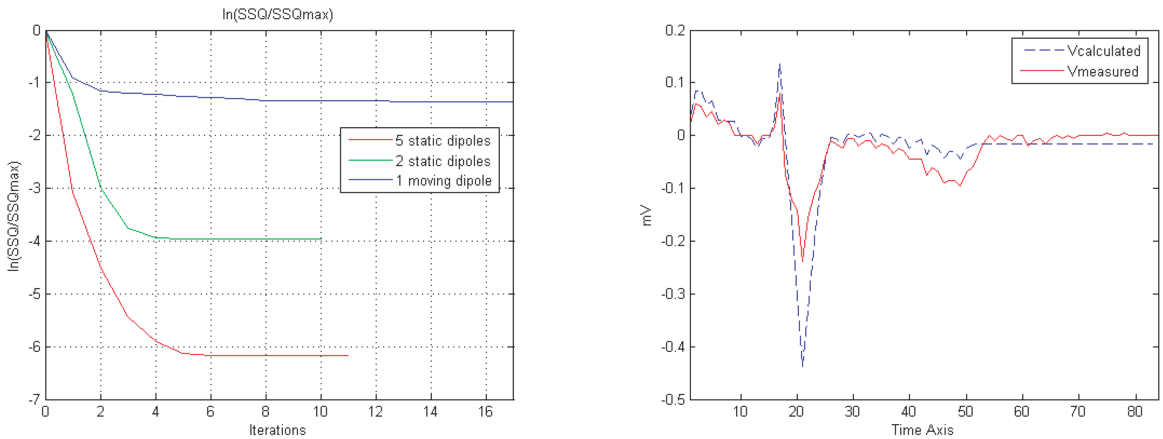

Figure 4: (a) SSQ for three cardiac sources: 1 moving dipole, 2 and 5 fixed location dipoles. (b) Measured and calculated voltages at the electrode 67 for the whole cardiac temporal period and the sitting poise.

This is shown in Fig. 4(b) for the electrode number 67, which is the upper right side electrode shown in Fig. 1 (black dot). As we can see the obtained voltages have almost the same form with small variations in their values.

5. CONCLUSIONS

A method solving the inverse problem of electrocardiography based on three different cardiac electric sources is successfully implemented. As compared to our previous work, the use of 1 moving dipole, 2 and 5 fixed location rotating dipoles leads to a better representation of the cardiac electrical activity. The forward problem future advancements include its "adaptivity" to the measured subject dimensions and separate models reflecting the subject poises (sitting or various lying alignments).

REFERENCES

1. Gulrajani, R. M., "The forward and inverse problems of electrocardiography," *IEEE Engineering in Medicine and Biology*, 84–101, September/October 1998.
2. Gulrajani, R. M., F. A. Roberge, and P. Savard, "The inverse problem of electrocardiography," Macfarlane, P. W. and Lawrie, T. D. Veitch (Eds): *Comprehensive Electrocardiology*, 237-288, Pergamon Press, Oxford, England, 1989.
3. Armoundas, A. A., A. B. Feldman, R. Mukkamala, and R. J. Cohen, "A single equivalent moving dipole model: An efficient approach for localizing sites of origin of ventricular electrical Activation," *Annals of Biomedical Engineering*, Vol. 31, No. 5, 564–576(13), May 2003.
4. Guard, R., B. McA. Sayers, and D. M. Monro, "Evaluation and analysis of the cardiac electrical multipole series based on a two-dimensional fourier technique," *The Theoretical Basis of Electrocardiology*, edited by C. V. Nelson and D. B. Gesselowitz, Chapter 10, 213–256, Oxford, Clarendon Press, 1976.
5. Bruder, H., R. Killmann, W. Moshage, P. Weismuller, S. Achenbach, and F. Bommel, "Biomagnetic localization of electrical current sources in the human heart with realistic volume conductors using the single-current-dipole model," *Phys. Med. Biol.*, Vol. 39, 1994.
6. He, B., G. Li, and X. Zhang, "Noninvasive imaging of cardiac transmembrane potentials within three-dimensional myocardium by means of a realistic geometry anisotropic heart model," *IEEE Trans. Biomed. Eng.*, Vol. 50, 1190–1202, 2003.
7. Farina, D., O. Skipa, O. Dossel, C. Kaltwasser, and W. R. Bauer, "The use of the simulation results as a priori information to, solve the inverse problem of electrocardiography for a patient," *Computers in Cardiology*, Lyon, France, 2005.
8. Xanthis, C. G., D. G. Drogoudis, P. M. Bonovas, D. Mikroulis, and G. A. Kyriacou, "Localization of an equivalent central cardiac electric dipole for electrocardiography applications," *International Special Topic Conference on Information Technology in Biomedicine (ITAB 2006)*, Ioannina, Greece, October 2006.

9. Bonovas, P. M., "Characterization of biological tissues with the use of applied potential method (plethysmography-tomography)," Ph.D. thesis, Dept. of Electrical and Computer Engineering, Demokritos University of Thrace, Xanthi, Greece 2003.
10. MacLeod, R. S., S. Shome, L. Lorenzo, and B. Yilmaz, "ECG measurement and analysis," http://www.cvrti.utah.edu/ macleod/bioen/be6000/labnotes/ecg/data/, March 2005.
11. Jorgenson, D. B., D. R. Haynor, G. J. Bardy, and Y. Kim, "Computational studies and transvenous defibrillation in a detailed 3-D human thorax model," *IEEE Trans. on Biomedical EMG.*, Vol. BME-42, 172–184, 1995.
12. Klepfer, R. N., C. R. Johnson, and R. S. Macleod, "The effects of inhomogeneities and anisotropies on electrocardiographic fields: A 3-D finite-element study," *IEEE Trans. on Biomed. Engin.*, Vol. 44, No. 8, 1997.
13. Eycleshymer, A. C. and D. M. Shoemaker, *A Cross-section Anatomy*, Appleton Century Crofts, New York, 1911.
14. Geddes, L. A. and L. E. Baker, "The specific resistance of biological material — A compendium of data for biological engineer and physiologist," *Med. Biol. Eng.*, Vol. 5, 271–293, 1967.
15. Kyriacou, G. A., P. M. Bonovas, M. A. Alexiou, C. S. Koukourlis, and J. N. Sahalos, "An efficient three dimensional FEM model of the human torso," *Innovation and Technology in Biology and Medicine*, Vol. 18, No. 4, 291–308, 1997.
16. Awada, K. A., D. R. Jackson, J. T. Williams, D. R. Wilton, S. B. Baumann, and A. C. Papanicolau, "Computational aspects of finite elements modeling in EEG source localization," *IEEE Trans. Biomed. Eng.*, Vol. 44, No. 8, 736–752, 1997.
17. Akin, J. E., *Application and Implementation of Finite Element Methods*, Academic Press, New York, 1982.

A Sensitivity Matrix Based Microwave Tomography Exploiting an Adjoint Network Theorem

D. G. Drogoudis[1], **G. A. Kyriacou**[1], **and J. N. Sahalos**[2]
[1]Mircowave Lab, Department of Electrical and Computer Engineering
Democritus University of Thrace, Xanthi 67100, Greece
[2]School of Sciences, Radiocommunications Lab, Department of Physics
Aristotle University of Thessaloniki, Thessaloniki 54124, Greece

Abstract— A reconstruction algorithm for microwave imaging based on the Modified Perturbation Method (MPM) is proposed. Both the object conductivity (σ) and permittivity (ε) are reconstructed. The original Perturbation method developed for static problems was modified in order to apply in time harmonic problem in higher frequency. The Jacobian matrix is now calculated in closed form employing an adjoint network theorem in conjunction with the reciprocity theorem of electromagnetics. A number of successful reconstructions were carried out for different complex permittivity profiles, but all of them based on a computer phantom approach.

1. INTRODUCTION

Microwave tomography is a novel technique with many applications in medical imaging and geophysical prospecting. This is based on the high contrast observed in relative dielectric permittivity and conductivity between physiological and malignant or abnormal tissues, e.g., Pething [1]. Likewise, the geophysical applications are justified by the different σ and ϵ_r properties of different materials-minerals, e.g., Keller [2]. The degree (or contrast) of these changes is large enough to be tomographically reconstructed. These examples demonstrate the significance of microwave tomography (MWT) for biomedical applications as an imaging modality for non-invasive assessment of functional and pathological conditions of tissues.

The basic objective of microwave imaging is the reconstruction of the spatial distributions of permittivity and conductivity of the body under investigation. The body is illuminated by electromagnetic waves from a number of different directions. The reconstruction of σ and ϵ_r is based on these scattered electromagnetic field measurements which are the result of the interaction of the incident wave and the inhomogeneous body. This reconstruction procedure results in a highly nonlinear and ill-posed problem. The degree of the singularity is primarily depended on the data collection strategy, which includes the location of transmitting and receiving antennas.

Iterative approaches are well suited for nonlinear problems, but can be computationally expensive with respect to the multiplicity of field solutions that are required [3]. Numerous iterative methods have been successfully implemented as computer phantom, in-vitro and in-vivo experiments to demonstrate the capabilities of microwave imaging. In simulation, 2-D microwave imaging schemes have been reported by Joachimowicz et al. [3], Meaney et al. [4], and Rekanos et al., [5] among others. Phantom and in-vitro image reconstruction results have also been described by Semenov et al. [6]. In general, these tomographic approaches have been found not to be restricted by wavelength criteria but rather by signal-to-noise limitations.

A common characteristic of these theoretically accurate approaches is their difficulty in handling the inverse problem singularity. Specifically, the involved Hessian matrix inversion, which is usually highly singular asks for specific techniques. This in turn leads to complicated and time consuming algorithms. Our research effort is directed toward a modified perturbation method (MPM) employing an exact sensitivity (Jacobian) matrix. The correction-update at each iteration results from a summation of all available information weighted by the corresponding sensitivity. This makes the method robust and immune against the problems of ill-posedeness. The penalty paid for these advantages is a compromise in the accuracy. Specifically, this work constitutes the first step in the extension of MPM toward microwave imaging and it will be restricted to a two dimensional approach.

For the solution of the forward scattering problem the Finite Element Method (FEM) will be used. As we have to deal with open geometry-problem, absorbing boundary conditions are applied on a fictitious circular surface that encloses the body under investigation. The inverse problem reconstruction algorithm will be based on an extension of the Modified Perturbation Method (MPM) following a dual-mesh scheme. In our previous work, [7, 8], MPM was developed for inverse problems in the area of Electrical Impedance Tomography (EIT). The aim now is its application in imaging at higher frequencies. Within this effort the Jacobian matrix will be calculated in a closed form expression using an Adjoint Network-Field approximation.

2. FORWARD PROBLEM SOLUTION

The geometry of the forward problem is shown in Fig. 1. The object to be imaged is embedded in a lossy homogeneous surrounding medium. Around the geometry there is a PML (Perfect Matching layer) region to truncate the solution domain. This in turn enclosed within a fictitious circular boundary along which absorbing boundary conditions are applied.

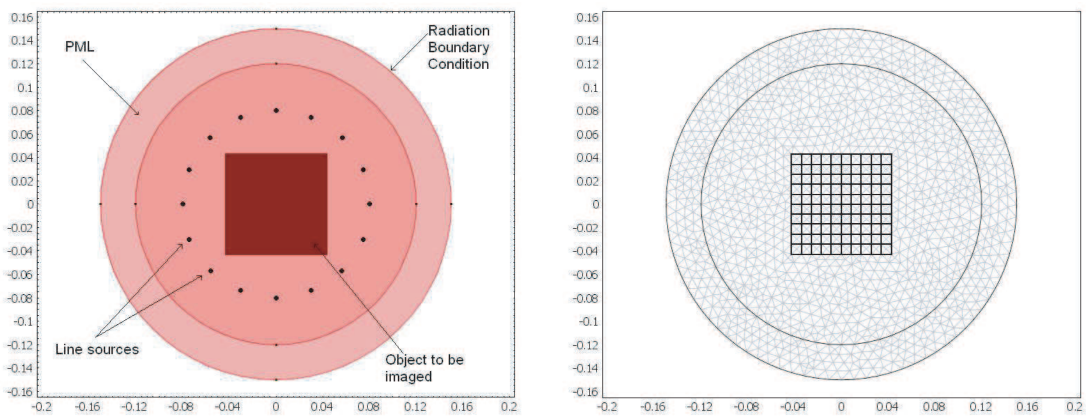

(a) (b)

Figure 1: (a) Geometric configuration of the 2-D scattering problem, and (b) the Dual-Mesh scheme: a reconstruction rectangular mesh and triangular forward mesh.

In order to retain a two dimensional geometry a line source along the $\vec{z}$ direction with $\vec{J} = J_z\vec{z}$ is assumed. This type of source yields only an E_z component for the electric field. So the two- dimensional forward scattering problem is governed by the scalar Helmholtz differential Equation (1) along with the appropriate boundary conditions.

$$\nabla^2 E_z(\vec{r}) + \omega^2\mu_0 \left(\varepsilon(\vec{r}) - j\frac{\sigma(\vec{r})}{\omega}\right) E_z(\vec{r}) = j\omega\mu_0 J_z(\vec{r}) \tag{1}$$

At this point we may define the relative complex permittivity ε_c as:

$$\varepsilon_c(\vec{r}) = \varepsilon(\vec{r}) - j\frac{\sigma(\vec{r})}{\omega} \tag{2}$$

For the solution of Helmholtz equation the Finite Element Method (FEM) is employed. With FEM the body under consideration is split into small elements with constant σ and ϵ_r. So a piecewise homogeneous model is constructed. such that

$$\varepsilon_c(x, y) = \sum_{e=1}^{E} \varepsilon_c^e x^e, \quad x^e = \begin{cases} 1 & \text{within } e\text{th element} \\ 0 & \text{elsewhere} \end{cases} \tag{3}$$

For the Dual-mesh scheme, the field values are defined on the forward (finer) triangular mesh while the material properties σ and ϵ_r are defined on the reconstruction (coarser) rectangular mesh. In this manner voltage values on the reconstruction mesh needs to interpolate from the forward mesh and properties values on the forward mesh needs to interpolate from the reconstruction mesh. For this to be achieved a mapping between the two different meshes needs to be established. To be more specific, each rectangular element from the coarser mesh is divided in four triangular elements and by this way the coarser mesh is constructed. Using this scheme a more realistic model and and an accurate forward solution is obtained,while the number of unknowns in the inverse problem is kept low. We have to notice that the reconstruction mesh is conformal to the forward mesh and each node of the coarse mesh belongs to the finer mesh as well.

The modelling and simulation of our geometry was made using the Electromagnetic module of the Comsol Multiphysics software. A full forward solution requires each antenna to be activated in turn and the scattered electric field to be measured at the location of each receiving antenna. This procedure requires the solution of the scattering problem as many times as the number of the antennas. The ordinary FEM approach is thus employed to yield a linear system of equations as:

$$[K(\epsilon_c)][E] = [B(J_z)] \tag{4}$$

Note that the matrix K is independent of the position of the source antenna. So the global matrix K is assembled only once for every solution, right hand side of Equation (4) is changed accordingly and the linear system is solved. Solving this system the electric fields on the antennas and at all the internal nodes is calculated and stored, to be used later within the reconstruction algorithm.

3. RECONSTRUCTION ALGORITHM

The reconstruction algorithm is based on the modified perturbation method that was developed for the conductivity imaging in Electrical Impedance Tomography. The aim now is its application in imaging at higher frequencies. The new algorithm is based again on the Jacobian matrix. The components of the Jacobian are the partial derivatives (or the sensitivities) of the electric field E_r measured at the rth antenna to the complex permittivity ε_c^e of the eth element-pixel, when the sth antenna (Line source) is activated. This is in turn evaluated through closed form expressions resulting from the reciprocity theorem and the employment of an adjoint problem. For this purpose an approach similar to that given by Oldenburg [9] and the original research referenced therein is adopted. Namely, the two Maxwell Curl equations are written for the source ($\vec{J}_s$) at sth antenna and differentiated with respect to the eth complex permittivity. For the adjoint fields (E_r; H_r) these two curl equations are written considering a source ($\vec{J}_r$) at the rth antenna. The four curl equations are in turn combined following the reciprocity theorem procedure to end up to:

$$\iiint\limits_V \vec{J}_r \cdot \frac{\vartheta \vec{E}_s}{\vartheta \varepsilon_c^e} du = j\omega \iiint\limits_V \vec{E}_r \cdot \vec{E}_s x^e(\vec{r}) du \tag{5}$$

Considering a line source at the rth antenna as $\vec{J}_r = J_z \delta(\vec{r} - \vec{r}_r)$, the left hand side of (5) is identically reduced to the (s, r, e) entry of the Jacobian-Sensitivity matrix as:

$$J(s, r, e) = \frac{\vartheta E_i}{\vartheta \varepsilon_c^e} = \frac{j\omega}{J_z} \sum_{\ell=1}^{L} S_\ell E_{s(\ell)} E_{r(\ell)} \tag{6}$$

To this end, E_s and E_r are the electric field values on the nodes of the triangular elements (forward mesh) that are in the region of the eth rectangular element (reconstruction mesh) when the active antenna is at point s and r respectively. These field distributions have already been calculated during the forward solution. The constants S_ℓ are the weights arising from the finite element formulation and the integral of the basis function that are used within FEM.

Considering the field distribution as an analytical function Cauchy-Riemann conditions apply, which can be written as:

$$\frac{\vartheta E_{real}}{\vartheta \varepsilon_c^{real}} = \frac{\vartheta E_{imag}}{\vartheta \varepsilon_c^{imag}} \quad \text{and} \quad \frac{\vartheta E_{imag}}{\vartheta \varepsilon_c^{real}} = -\frac{\vartheta E_{real}}{\vartheta \varepsilon_c^{imag}} \tag{7}$$

In view of (7) the complex Jacobian matrix calculated from Equation (6) can be decomposed into four sub-matrices by separating the electric field and the complex permittivity into real and imaginary parts as:

$$J = \frac{\vartheta E}{\vartheta \varepsilon_c} = \frac{\vartheta E_{real}}{\vartheta \varepsilon_c^{real}} + j \frac{\vartheta E_{imag}}{\vartheta \varepsilon_c^{real}} = \frac{\vartheta E_{imag}}{\vartheta \varepsilon_c^{imag}} - j \frac{\vartheta E_{real}}{\vartheta \varepsilon_c^{imag}} \tag{8}$$

The above approach greatly simplifies the reconstruction problem be reducing it to the application of our original MPM [8] once for each sensitivity, similar to our previous quasi-static work [7].

Finally the reconstruction algorithm updating the complex permittivity distribution of the eth element takes the following form:

$$\varepsilon_{cn} = \left[\varepsilon_c^{real(n-1)} + k_1 W_1 \varepsilon^{real(n-1)_c}\right] + j\left[\varepsilon_c^{imag(n-1)} + k_2 W_2 \varepsilon^{imag(n-1)}\right] \tag{9}$$

$$W_1 = \frac{\sum_{i=1}^{M} \frac{E_{m\,i}^{real}-E_{ci}^{real}}{E_{m\,i}^{real}} \frac{\vartheta E_i^{real}}{\vartheta \varepsilon_c^{real}}}{\sum_{k=1}^{M} \left|\frac{\vartheta E_k^{real}}{\vartheta \varepsilon_c^{real}}\right|} + \frac{\sum_{i=1}^{M} \frac{E_{m\,i}^{imag}-E_{ci}^{imag}}{E_{m\,i}^{imag}} \frac{\vartheta E_i^{imag}}{\vartheta \varepsilon_c^{real}}}{\sum_{k=1}^{M} \left|\frac{\vartheta E_k^{imag}}{\vartheta \varepsilon_c^{real}}\right|} \tag{10}$$

$$W_2 = \frac{\sum_{i=1}^{M} \frac{E_{m\,i}^{real}-E_{ci}^{real}}{E_{m\,i}^{real}} \frac{\vartheta E_i^{real}}{\vartheta \varepsilon_c^{imag}}}{\sum_{k=1}^{M} \left|\frac{\vartheta E_k^{real}}{\vartheta \varepsilon_c^{imag}}\right|} + \frac{\sum_{i=1}^{M} \frac{E_{m\,i}^{imag}-E_{ci}^{imag}}{E_{m\,i}^{imag}} \frac{\vartheta E_i^{imag}}{\vartheta \varepsilon_c^{imag}}}{\sum_{k=1}^{M} \left|\frac{\vartheta E_k^{imag}}{\vartheta \varepsilon_c^{imag}}\right|} \tag{11}$$

where M is the total number of linear independent measurements, E_{mi} and E_{ci} are the measured and calculated fields at the ith antenna and $k_{1,2}$ are the relaxations factors that may provide faster convergence. The optimum values of k_1, k_2 can be obtained through a numerical investigation.

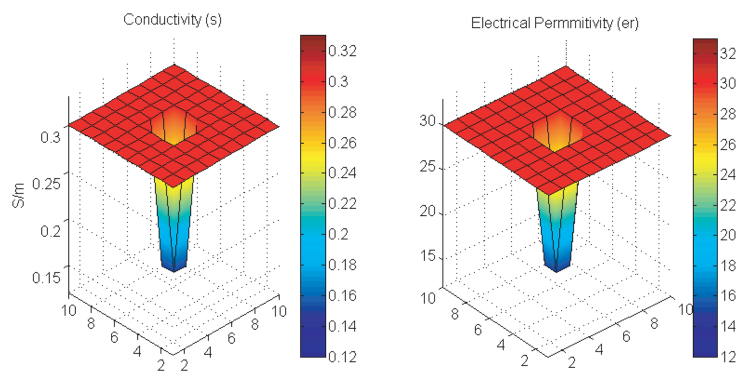

(a) (b)

Figure 2: Target model for (a) conductivity profile, (b) permittivity profile.

4. NUMERICAL RESULTS

The so called "computer phantom" is assumed. Namely, first the forward problem was solved for a target model and the results are stored, labeled as "measurements". In turn the reconstruction algorithm starts from a homogeneous model and the desired complex permittivity profile is sought. Successful imaging of many different conductivity and permittivity distributions and satisfactory results were performed on computer phantoms only. Only one example for a common anomaly distribution of human tissue is presented herein due to space limitations.

The target model simulated as a computer phantom is presented is Fig. 3. A total number of 16 antennas (line sources) were used, where only 11 are exploited as receivers for each projection

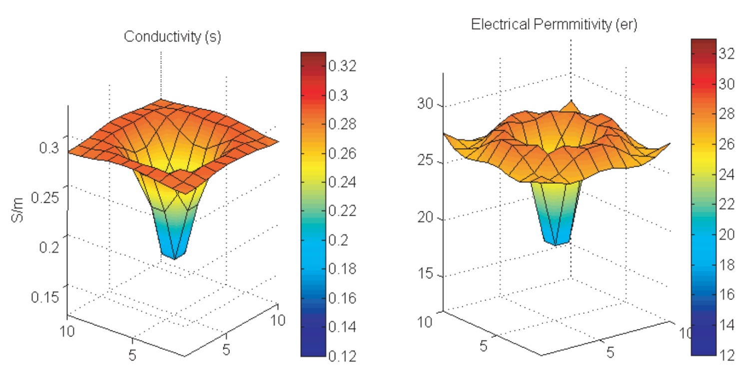

(a) (b)

Figure 3: Reconstructed profiles for (a) conductivity and (b) permittivity distributions after 6 iterations.

angle. An anomaly with conductivity $\sigma = 0.15\,\mathrm{S/m}$ and permittivity $\varepsilon_r = 15$ was introduced in a homogeneous background of ($\sigma = 0.3\,\mathrm{S/m}$) and $\varepsilon_r = 30$. The frequency of operation was assumed as $f = 1\,\mathrm{GHz}$. The image reconstructed after 6 iterations is presented in Fig. 3 for the conductivity and the permittivity profile respectively. The correct location of the anomaly as well as its σ and ϵ_r peak values are obtained, but some artefacts of the order of 6% are caused. More results will be presented at the conference along with a number of new phantoms that need investigation.

5. CONCLUSION

A lot of successful reconstructions are carried out and the method seems to work well. A further investigation of the optimum relaxation factors as well as data collection strategies is required. As future plan we will try to combine MPM with Levenberg-Marquardt or simple Gauss-Newton to take advantage of fast convergence of MPM during its future plan we will try to combine MPM with Levenberg-Marquardt or simple Gauss-Newton to take advantage of fast convergence of MPM during its first few iterations and the better accuracy of Gauss-Newton.

ACKNOWLEDGMENT

This work is implemented in the framework of Measure 8.3 through the O.P. Competitiveness 3rd Community Support Programme and is co-funded by: (75%) of the Public Expenditure from the European Union — European Social Fund, (25%) of the Public Expenditure from the Hellenic State — Ministry of Development — General Secretariat for Research and Technology, and Private Sector (INTRACOM SA).

REFERENCES

1. Pethig, R., "Dielectric properties of biological materials: Biophysical and medical applications," *IEEE Transactions on Electrical Insulation*, Vol. EI-19, 453–474, Oct. 1984.
2. Keller, G. V., "Electrical properties of rocks and minerals," *Handbook of Physical Constemts*, S. P. Calrk, ed., 553–770, N. Y. Geological Society of America, 1988.
3. Joachimowicz, N., C. Pichot, and J. Hugonin, "Inverse scattering: an iterative numerical method for electromagnetic imaging," *IEEE Transactions on Antennas and Propagation*, Vol. 39, 1742–1753, Dec. 1991.
4. Meaney, P., K. Paulsen, and T. Ryan, "Two-dimensional hybrid element image reconstruction for tm illumination," *IEEE Transactions on Antennas and Propagation*, Vol. 43, 239–247, March 1995.
5. Rekanos, I. T., M. S. Efraimidou, and T. D. Tsiboukis, "Microwave imaging: Inversion of scattered near-field measurements," *Trans. Magnetics*, Vol. 37, 3294–3297, September 2001.
6. Semenov, S., R. Svenson, A. Bulyshev, A. Souvorov, A. Nazarov, Y. Sizov, A. Pavlovsky, V. Borisov, B. Voinov, G. Simonova, A. Starostin, V. Posukh, G. Tatsis, and V. Baranov, "Three-dimensional microwave tomography: experimental prototype of the system and vector born reconstruction method," *IEEE Transactions on Biomedical Engineering*, Vol. 46, 937–946, Aug. 1999.
7. Drogoudis, D. G., G. Trichopoulos, G. Kyriacou, and J. N. Sahalos, "A modified perturbation method for three-dimensional time harmonic impedance tomography," PIERS Online, Vol. 1, No. 2, 147–150, 2005.
8. Kyriacou, G., C. Koukourlis, and J. Sahalos,"A reconstruction algorithm of electrical impedance tomography with optimal configuration of the driven electrodes," *IEEE Transactions on Medical Imaging*, Vol. 12, 430–438, Sept. 1993.
9. Oldenburg,D. W., "Practical strategies for the solution of large-scale electromagnetic inverse problems," *Radio Science*, Vol. 29, 1081–1099, 1994.

Identification of Multiple Cylindrical Targets Located above Perfectly Conducting Flat Surface by Artificial Neural Networks

A. Kızılay[1,2] **and S. Makal**[1,2]

[1]Electrical-Electronics Faculty, Yıldız Technical University, Turkey
[2]Electronics and Communications Engineering Department
Yıldız Technical University, Turkey

Abstract— The radar target identification performance of neural networks is analyzed in this paper. The image technique formulation and Moment Method (MoM) are used for deriving a set of features utilized by artificial neural network. This work aims to find the radiuses of the targets and the distance between the targets located above perfectly conducting flat surface from the scattered field values.

1. INTRODUCTION

There are many approaches to recognition of radar targets and especially recognition from their scattered signals is a complicated task in electromagnetics [1, 2]. Because of their ability to learn and generalize, artificial neural networks are attractive for numerous engineering applications [3–5].

Two cylindrical targets with a radius of r_{t1} and r_{t2} are located at a distance h_{t1} and h_{t2} from the flat surface. The incident electromagnetic field E_i is illuminating the target with the incidence angle ϕ_i measured from the horizontal as shown in Figure 1.

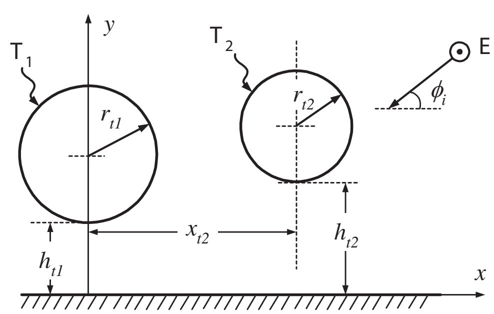

Figure 1: Cylindrical targets.

The data set used is obtained by using the image technique solution for scatterers above a Perfectly Electrical Conducting (PEC) flat surface. The PEC flat surface is chosen to be infinitely long to avoid direct and indirect reflections from edges.

The method of images can be used to replace the infinite flat surface with images of the incident field and the cylinder as shown in Figure 2.

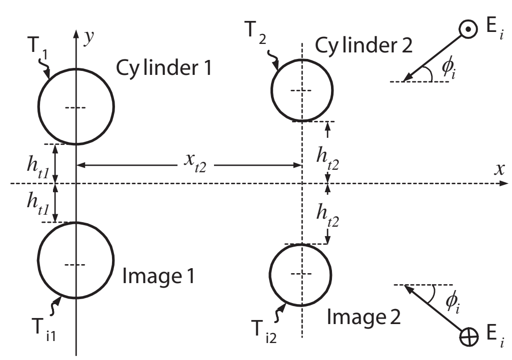

Figure 2: Cylinders above an infinite flat surface.

The incident electric field (E-Field) is the sum of a TM (transverse magnetic) plane wave and its reflection. The sum is a standing wave in the y-direction and a propagating wave in the x-direction, and can be expressed as

$$\vec{E}^i(x,y) = 2jE_0 e^{jk_0(x\cos\phi_i)}\sin(k_0 y\sin\phi_i)\hat{z} \tag{1}$$

The scattered field can be written as

$$E_z^s(\vec{\rho}) = M_\Gamma(\vec{\rho},\vec{\rho}\,')K_z(\vec{\rho}\,') \tag{2}$$

where $\vec{\rho}$ and $\vec{\rho}\,'$ are the position vectors of the field points and the source points, respectively. $M_\Gamma(\vec{\rho},\vec{\rho}\,')$ is an operator defined as

$$M_\Gamma(\vec{\rho},\vec{\rho}\,')K_z(\vec{\rho}\,') = -\frac{k_0\eta_0}{4}\int\limits_\Gamma K_z(\vec{\rho}\,')H_0^{(2)}(k_0|\vec{\rho}-\vec{\rho}\,'|)dl' \tag{3}$$

where, K_z is the unknown induced surface current, k_0 is the free-space wave number and $H_0^{(2)}$ represents the Henkel function of the second kind.

The scattered E-field can be rewritten in terms of the induced current on the cylinders and the images current as

$$\begin{aligned} E_z^s(\vec{\rho}) &= E_z^{T_1}(\vec{\rho}) + E_z^{T_{i1}}(\vec{\rho}) + E_z^{T_2}(\vec{\rho}) + E_z^{T_{i2}}(\vec{\rho}) \\ &= M_{T_1}(\vec{\rho},\vec{\rho}\,')K_z^{T_1}(\vec{\rho}\,'_1) + M_{T_{i1}}(\vec{\rho},\vec{\rho}\,'_1)K_z^{T_{i1}}(\vec{\rho}\,'_1) + M_{T_2}(\vec{\rho},\vec{\rho}\,'_2) + M_{T_{i2}}(\vec{\rho},\vec{\rho}\,'_2)K_z^{T_{i2}}(\vec{\rho}\,'_2) \end{aligned} \tag{4}$$

This is the integration path for the image currents; the relation between this path and the integration path for the cylinder currents are

$$\begin{aligned} M_{T_{i1}}(x,y|x'_1,y'_1) &= M_{T_1}(x,y|x'_1,-y'_1) \\ M_{T_{i2}}(x,y|x'_2,y'_2) &= M_{T_2}(x,y|x'_2,-y'_2) \end{aligned} \tag{5}$$

After using this relation

$$\begin{aligned} K_z^{T_{i1}}(\vec{\rho})|_{T_{i1}} &= -K_z^{T_1}(\vec{\rho})|_{T_1} \\ K_z^{T_{i2}}(\vec{\rho})|_{T_{i2}} &= -K_z^{T_2}(\vec{\rho})|_{T_2} \end{aligned} \tag{6}$$

The scattered E-field becomes

$$E_z^s(\vec{\rho}) = M_{T_1}(\vec{\rho},\vec{\rho}\,'_1)K_z^{T_1}(\vec{\rho}\,'_1) + M_{T_{i1}}(\vec{\rho},\vec{\rho}\,'_1)K_z^{T_{i1}}(\vec{\rho}\,'_1) + M_{T_2}(\vec{\rho},\vec{\rho}\,'_2)K_z^{T_2}(\vec{\rho}\,'_2) + M_{T_{i2}}(\vec{\rho},\vec{\rho}\,'_2)K_z^{T_{i2}}(\vec{\rho}\,'_2) \tag{7}$$

A set of coupled Electric-Field Integral Equations (EFIEs) for the induced currents can be found by using the boundary condition of zero tangential component of total E-field over the first and the second target. Applying the boundary condition on the first target gives the first EFIE

$$\begin{aligned} -E_z^i(x_1,y_1) &= \left[M_{T_1}(x_1,y_1|x'_1,y'_1) - M_{T_1}(x_1,y_1|x'_1,-y'_1)\right]K_z^{T_1}(x'_1,y'_1) \\ &\quad + \left[M_{T_2}(x_1,y_1)|x'_2,y'_2 - M_{T_2}(x_1,y_1|x'_2,-y'_2)\right]K_z^{T_2}(x'_2,y'_2) \end{aligned} \tag{8}$$

where x_1, y_1 define the points on the first target, and x_2, y_2 define the points on the second target. Applying the boundary condition on the second target gives the second EFIE

$$\begin{aligned} -E_z^i(x_2,y_2) &= \left[M_{T_1}(x_2,y_2|x'_1,y'_1) - M_{T_1}(x_2,y_2|x'_1,-y'_1)\right]K_z^{T_1}(x'_1,y'_1) \\ &\quad + \left[M_{T_2}(x_2,y_2)|x'_2,y'_2 - M_{T_2}(x_2,y_2|x'_2,-y'_2)\right]K_z^{T_2}(x'_2,y'_2) \end{aligned} \tag{9}$$

The moment method is used to solve the EFIEs to obtain the induced currents on the targets. Then, the induced currents are used to calculate the scattered E-field from the two cylinders located above a ground plane. Frequency data points belonging to the sum of the electric fields are obtained by calculating electric fields in particular frequency steps [6].

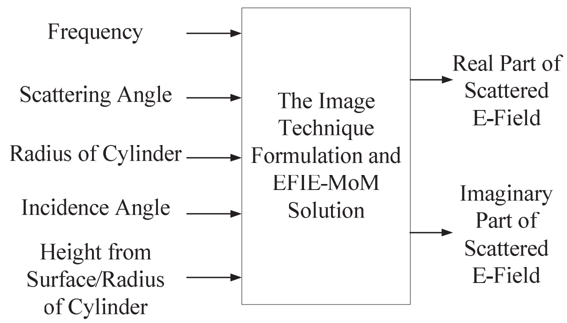

Figure 3: Block Diagram of inputs and outputs of the image technique formulation and EFIE-MoM solution.

2. METHOD

In this target identification technique, some target features from the available database of electromagnetic scattered signals are extracted. These features are obtained by using EFIE-MoM solution of the image technique formulation [6]. Frequency data points consist of the real and the imaginary parts of the scattered E-field are obtained by calculating fields at the frequencies between 1 GHz–30 GHz and then transformed into the time domain using the inverse Fourier Transform. The maximum amplitude values of the time domain scattered E-field are found. The data set including these amplitude values and time is obtained by using cylindrical targets having various radiuses and distances between each other.

An MLP (Multilayer Perceptron) and GRNN (General Regression Neural Network) are designed and applied to the group of test targets which are at the same height from the infinite flat surface. The dataset has two groups including two targets. According to the scattering angles, a portion of the database is used to train the network and the rest is used to test the performance of the neural network for target identification. The angles used for training are 10, 20, 30 degrees and the angle used for testing is 40 degree. Namely, the values calculated at 40 degree show the performance of the neural network.

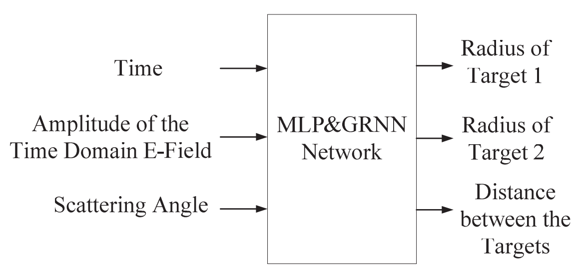

Figure 4: Block Diagram of the inputs and outputs of MLP and GRNN Network.

3. MLP

Multilayer perceptions (MLPs) are feedforward neural networks trained with the standard backpropagation algorithm. They are supervised networks so they require a desired response to be trained. They learn how to transform input data into a desired response, so they are widely used for pattern classification. With one or two hidden layers, they can approximate virtually any input-output map. The basic MLP building unit is a simple model of artificial neuron. This unit computes the weighted sum of the inputs plus the threshold weight and passes this sum through the activation function. In a Multilayer Perceptron, the outputs of the units in one layer form the inputs to the next layer. The weights of the network are usually computed by training the network using the backpropagation algorithm [8, 9].

4. GRNN

The General Regression Neural Network (GRNN) is a neural network architecture that is often used for function approximation. The learning process is to find a surface in a multidimensional space that provides a best fit to the training data and the generalization is equivalent to the use of this multidimensional surface to interpolate the test data. GRNN has three layers having different roles. The inputs are applied in the input layer. A nonlinear transformation is applied on the data from the input space to the hidden space in the hidden layer. The outputs are produced in the linear output layer [10].

5. SIMULATION AND RESULTS

The training dataset has 201 values obtained at four angles and 49 of them are used for testing of the neural network. The input layer of the neural networks is designed to have 3 neurons including the time, the amplitude of the time domain E-field and the scattering angles. The output layer has three neurons corresponding to the first radius, the second radius and the distances between the two targets. An MLP network with four layers (the input layer, two hidden layers, and the output layer) of neurons is trained. Logarithmic-sigmoid function is used at hidden layers and pure-linear transfer function is used at output layer. The hidden layers are chosen to have 7 and 5 neurons. After 100 iterations, the classification rate with the testing data is 93.8% and the classification rate with the training data is 100% as shown in Table 1. A GRNN network having a spread value of 0.5 is trained. Both the classification rate with the testing data and the classification rate with the training data are 100% as shown in Table 1.

Table 1: Training and testing rate.

	MLP	**GRNN**
Testing rate (%)	93.8	100
Training rate (%)	100	100

6. CONCLUSION

In this work, a neural network solution is proposed for target identification which gives reasonably good results. MLP and GRNN are used and exact classification rates of testing and training were given. It is shown that the accuracy of GRNN is higher than MLP and the Electric field features for a target can be extracted from its radar returns that are independent of such radar parameters as target range, loss, antenna gain, etc. They are determined only by the time, the amplitude values of time domain E-field and the scattering angles. These results are very useful in practical applications especially relating to target identification.

REFERENCES

1. Chen, S., "Radar target identification with relative amplitudes and unknown target aspect angles," *IEEE Aerospace and Electronics Conference*, Vol. 1, 1990.
2. Chen, S., "Relative amplitudes and phase features for resonance-region radar target identification," *IEEE Aerospace and Electronics Conference*, Vol. 1, 1989.
3. Turhan, G., K. Leblebicioglu, and T. İnce, "Electromagnetic target classification using time-frequency analysis and neural networks," *Microwave and Optical Technology Letters*, Vol. 21, No. 1, April 5, 1999.
4. Chakrabarti, S. and E. K. Miller, "A fuzzy neural network model for aspect independent target identification," *Antennas and Propagation Society International Symposium*, Vol. 1, 1994.
5. Joung, I., F. D. Garber, and S. C. Ahalt, "Classification of radar targets using synthetic neural network," *IEEE Transaction on Aerospace and Electronic Systems*, Vol. 29, No. 2, April 1993.
6. Kizilay, A., "A perturbation method for transient multipath analysis of electromagnetic scattering from targets above periodic surfaces," Ph.D. Dissertation Thesis at Michigan State University, 2000.
7. Daqing, C. and B. Zheng, "High range resolution radar target identification using multilayer feedforward neural network," *CIE International Conference of Radar*, 215–218, 1996.
8. Haykin, S., *Neural Networks: A Comprehensive Foundation*, Macmillan College Publishing, New York, 1994.
9. Schalkoff, R. J., *Artificial Neural Networks*, McGraw-Hill Inc., Singapore, 1997.

10. Popescu, I., A. Kanatas, P. Constantinou, and I. Nafornita, "Applications of general regression neural networks for path loss prediction," *Proceedings of International Workshop "Trends and Recent Achievements in Information Technology"*, Cluj-Napoca, May 16–18, 2002.

A Dynamic Simulation Approach for Electrostatic Force Microscopy on Inhomogeneous Sample Material

M. Greiff, U. B. Bala, and W. Mathis

Leibniz University of Hanover, Germany

Abstract— This paper is dedicated to a high quality simulation approach for electrostatic force microscopes. In order to take into account the multi-scale aspect of the problem, the electrostatic field is obtained by using a hybrid simulation approach which consists of a boundary element method (BEM) and an augmented finite element method (FEM). The electrostatic force is calculated by integrating the Maxwell stress tensor over a surface. An arbitrary Eulerian Lagrangian method (ALE) is used for the mesh update.

1. INTRODUCTION

The electrostatic force microscope (EFM) is able to scan electrostatic fields with nearly atomic resolution. Basically it consists of a tip at the end of a cantilever, which is moved over the sample under investigation [1]. A laser beam which is reflected on the back of the cantilever is detected by a photo diode array. The output voltage of the photo diodes can therefore be used to measure the cantilever deflection. The measurement process itself consists of two steps, the first of which is the detection of the sample topography. In this step the tip is in contact with the sample. During the second step, in which the electric field is measured, the tip is moved over the sample without touching it. Though the working principle of an EFM is quite simple, the design of a numerical model turns out to be complicated. Firstly both, the mechanical and the electrical behavior as well as their coupling have to be taken into account. Furthermore, since there is a large difference in size of cantilever and tip, a special multi-scale simulation approach is necessary in order to get accurate results.

2. ELECTROSTATIC SIMULATION MODEL

From a physical point of view the EFM can be separated into a mechanical and an electrical part (Fig. 1). Since the governing equations for both parts are different, they must be modelled separately. However, a simulation model has to take into account the coupling between them. In this work this is achieved by passing the electrostatic forces from the electrical to the mechanical part and vice versa, passing the deformations from the mechanical to the electrical part. This coupling process has to be carried out iteratively. The paper at hand focuses on the electrostatic part.

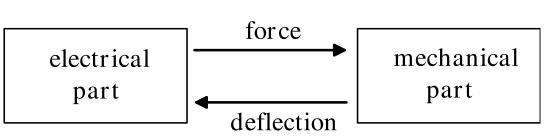

Figure 1: Electro-mechanical simulation model.

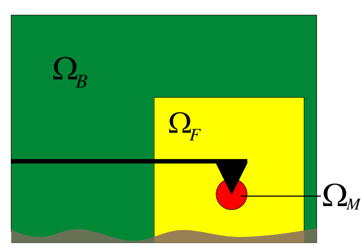

Figure 2: Hybrid simulation approach.

The electrostatic potential u in regions holding a volume charge ρ can be found by solving the Poisson equation

$$\nabla(\varepsilon\nabla u) = -\rho \tag{1}$$

and taking into account the given boundary conditions. It is known that the solution u minimizes the energy related functional

$$W = \frac{1}{2}\int_{\Omega}\varepsilon(\nabla u)^2 d\Omega - \oint_{\Gamma_N}\varepsilon u\frac{\partial u}{\partial n}d\Gamma_N, \tag{2}$$

where $\rho \equiv 0$ is assumed. For a numerical solution the potential u has to be approximated by

$$u = u\left(a_1, a_2, \ldots, a_n\right), \tag{3}$$

where $a_1, a_2, \ldots$ is a finite function space. The minimum of (2) can then be found by solving

$$\frac{\partial W}{\partial a_i} = 0, \tag{4}$$

where the quality of the approximation of u depends on the function space used. In order to find a convenient set of ansatz functions a closer look at the calculation domain is beneficial. Since the behavior of the electric field very close to the tip (Ω_M) is mainly determined by the tip itself, special ansatz functions can be used in this region (Fig. 2). At a greater distance (Ω_F) the influence of the tip vanishes and the potential can be approximated by linear ansatz functions. Therefore the approximation for the electrostatic potential is chosen as [2]

$$u = \sum_j u_j \psi_j(x, y, z) + A(r) \sum_k c_k f_k(r, \theta, \phi), \tag{5}$$

where the cut-off function

$$A(r) = \begin{cases} 1, & 0 < \rho < \frac{R}{2} \\ \frac{1}{2}\left(1 + \cos\left(\frac{2}{R}r - 1\right)\pi\right), & \frac{R}{2} < r < R \\ 0, & \text{otherwise} \end{cases} \tag{6}$$

ensures the vanishing of the singular functions [3]

$$f_k = r^\nu P_\nu^m(\cos\theta) \sin m\phi \tag{7}$$

outside the tip's scope and P_ν^m are the Legendre polynomials [4]. This leads to the set of linear equations

$$\frac{\partial W}{\partial u_i} = \sum_{j=1}^{n} u_j \int_\Omega \varepsilon \nabla\psi_i \nabla\psi_j d\Omega + \sum_{k=1}^{m} c_k \int_\Omega \varepsilon \nabla\psi_i \left(\nabla A f_k + A \nabla f_k\right) d\Omega = 0 \tag{8}$$

and

$$\frac{\partial W}{\partial c_i} = \sum_{j=1}^{n} u_j \int_\Omega \varepsilon \left(A f_i + A \nabla f_i\right) \nabla\psi_j + \sum_{k=1}^{m} c_k \int_\Omega \varepsilon \left(\nabla A f_i + A \nabla f_i\right)\left(\nabla A f_k + A \nabla f_k\right) d\Omega = 0 \tag{9}$$

which can also be written as

$$\begin{pmatrix} M & B^T \\ B & F_{NN} \end{pmatrix} \begin{pmatrix} c_m \\ u_F \end{pmatrix} = \begin{pmatrix} b_m \\ b_F \end{pmatrix}. \tag{10}$$

On the FEM-BEM coupling interface [5] $\Gamma_T = \Gamma_B \cap \Gamma_F$, $u_B = u_F$ and $\frac{\partial u_B}{\partial n} + \frac{\partial u_F}{\partial n} = 0$. Using the Gauss theorem on $\Omega_{FM} = \Omega_F \cup \Omega_M$ one obtains

$$\int_{\Gamma_F} \frac{\partial u_{FM}}{\partial n} v d\Gamma = \int_{\Omega_{FM}} \operatorname{div}\left(\nabla u_{FM} \cdot v\right) d\Omega = \int_{\Omega_{FM}} \triangle u_{FM} \cdot v d\Omega + \int_{\Omega_{FM}} \nabla u_{FM} \cdot \nabla v d\Omega \tag{11}$$

i.e., for all $v \in H^1_{D,0}\left(\Omega_{FM}\right) := \left\{v \in H^1\left(\Omega_{FM}\right) : v|_{\Gamma_D \cap \Gamma_F} = 0\right\}$

$$a\left(u_{FM}, v\right) := \int_{\Omega_{FM}} \nabla u_{FM} \cdot \nabla v d\Omega = \int_{\Omega_{FM}} f \cdot v d\Omega + \int_{\Gamma_F} \frac{\partial u_{FM}}{\partial n} v d\Gamma =: (f, v)_{\Omega_{FM}} + \left\langle \frac{\partial u_{FM}}{\partial n}, v \right\rangle_{\Gamma_F} \tag{12}$$

where u_{FM} includes c_m and u_F. The representation formula of the Laplace's equation for the solution of u_B inside Ω_B is

$$u_B(x) = \int_{\Gamma_B} \left\{ \frac{\partial}{\partial n(y)} G(x, y) u_B(y) - G(x, y) \frac{\partial u_B}{\partial n(y)} \right\} d\Gamma, \quad x \in \Omega_B \tag{13}$$

with the fundamental solution of the Laplacian in 3D given by

$$G(x,y) = \frac{1}{4\pi}|x-y|^{-1}. \tag{14}$$

For Poisson's problem the two boundary integral equations on the BEM region are

$$V\frac{\partial u_B}{\partial n} = (I+K)u_B - N_0 f \tag{15}$$

$$Wu_B = (I-K')\frac{\partial u_B}{\partial n} - N_1 f \tag{16}$$

where the single layer potential V and the hypersingular operator W are symmetric and the double layer potential K has the dual K' [6]. The integral operators N_0 and N_1 are defined by

$$N_0 f(x) := \int_{\Omega_B} G(x,y)f(y)dy, \quad N_1 f(x) := \frac{\partial}{\partial n_x} N_0 f. \tag{17}$$

The saddle point formulation of the problem for all $(w,v,\psi) \in \tilde{H}^{1/2} \times H^1_{D,0}(\Omega_{FM}) \times \tilde{H}^{-1/2}$ is

$$2a\left(u_{FM}, v\right) + \langle Wu_B, v\rangle_{\Gamma_T} + \left\langle (I+K')\varphi, v\right\rangle_{\Gamma_T} = 2(f,v)_{\Omega_{FM}} + 2\langle t_0, v\rangle_{\Gamma_N\cap\Gamma_F} - \langle N_1 f, v\rangle_{\Gamma_T} \tag{18}$$

$$\langle Wu_B, w\rangle_{\Gamma_B\cap\Gamma_N} + \langle (I+K')\varphi, w\rangle_{\Gamma_B\cap\Gamma_N} = 2\langle t_0, w\rangle_{\Gamma_B\cap\Gamma_N} - \langle N_1 f, w\rangle_{\Gamma_B\cap\Gamma_N} \tag{19}$$

$$\langle (I+K)u_B, \psi\rangle_{\Gamma_B} - \langle V_\varphi, \psi\rangle_{\Gamma_B} = \langle N_0 f, \psi\rangle_{\Gamma_B} \tag{20}$$

If the bases are introduced as $\mathrm{span}\{v_1,\ldots,v_F\} = X_F$, $\mathrm{span}\{w_1,\ldots,w_F\} = X_B$ and $\mathrm{span}\{\psi_1,\ldots,\psi_F\} = Y_B$, the basis functions of X_F and X_B are supposed to be ordered such that

$$\mathrm{span}\{v_1,\ldots,v_F\} = X_F \cap H^1_{D,0}(\Omega_F)$$

$$\mathrm{span}\{w_1,\ldots,w_B\} = X_B \cap H^{1/2}(\Omega_B).$$

This system corresponds to a matrix formulation which can be written as

$$\begin{pmatrix} M & B^T & 0 & 0 & 0 \\ B & F_{NN} & F_{NC} & 0 & 0 \\ 0 & F_{CN} & F_{CC}+W_{CC} & W_{CN} & \left(K^T+I\right)_C \\ 0 & 0 & W_{NC} & W_{NN} & \left(K^T+I\right)_N \\ 0 & 0 & (K+I)_C & (K+I)_N & -V \end{pmatrix} \begin{pmatrix} u_M \\ u_F \\ u_T \\ u_B \\ \varphi \end{pmatrix} = \begin{pmatrix} b_m \\ b_F \\ b_\Gamma \\ b_B \\ b_\varphi \end{pmatrix} \tag{21}$$

where the subscript C means contribution from the coupling nodes and N means contribution from the non-coupling nodes. Finally the blocks W, V, $K+I$, and K^T+I provide the coupling between the two ansatz spaces X_F and X_B. Here u_F and u_B are the nodal potentials inside the FE domain and on the boundary of the BE domain respectively, u_T are the nodal potentials on the FE-BE coupling interface and φ are the normal components of the electric field distribution on the boundary of the BE domain. The vector b includes the corresponding boundary conditions and the charge distribution. As the matrix in (21) is not positive definite, a specific algorithm such as the MINRES algorithm is required for the solution.

3. FORCE CALCULATION

The electrostatic forces are used as input for the calculation of the cantilever deflection. Since the electrostatic field is singular on corners or edges, the results obtained by numerical calculation will lack accuracy in those regions. By using the Maxwell stress tensor

$$\mathbf{T} = \varepsilon_0 \begin{pmatrix} E_x^2 - \frac{E^2}{2} & E_xE_y & E_xE_z \\ E_xE_y & E_y^2 - \frac{E^2}{2} & E_yE_z \\ E_xE_z & E_yE_z & E_z^2 - \frac{E^2}{2} \end{pmatrix} \tag{22}$$

the force $\mathbf{F}$ acting on parts of the probe can be obtained by evaluating

$$\mathbf{F} = \int_V \mathrm{div}\mathbf{T}dV = \oint_A \mathbf{T}d\mathbf{A}, \tag{23}$$

where V is a volume including the part of the cantilever under investigation and A is the surface enclosing V [7]. Therefore the use of inaccurate field results very close to the cantilever can be avoided in the force calculation. In this work the volume V was chosen as the union of all mesh elements next to the part of the cantilever where the force is calculated. The forces are calculated by evaluating the surface integral in (23) where the electric field on A is found by calculating the average field of the neighboring elements. The forces can be divided into three different groups which are forces acting on smooth parts of the cantilever, forces acting on edges and forces acting on tips or corners (Fig. 5). The first group (a) can easily be calculated by using the adjacent element of the tetrahedral mesh as volume V. For the calculation of the second group (b) the volume V can be defined by the union of all mesh elements sharing the edge where the force is calculated. For the third group (c) the volume V is the union of all mesh elements sharing the node where the force is calculated. The forces are then calculated by integrating the Maxwell tensor over the surface A enclosing V. The resulting forces can be seen in Figs. 6 and 7. As expected the forces acting on corners or edges are greater than the ones acting on the smooth parts of tip and cantilever. This is in line with the experience that most of the force between probe and sample acts via the tip. The force distribution also shows that the edges and corners of the cantilever contribute noticeable to the cumulative force and therefore will have an influence in EFM measurements. Since the mesh near the tip is much finer than in the other regions, the force on the tip is related to a smaller surface than the forces acting on the corners of the cantilever. For this reason the latter appear to be greater than the tip force in Fig. 7. The resulting forces are in line with previous investigations [8].

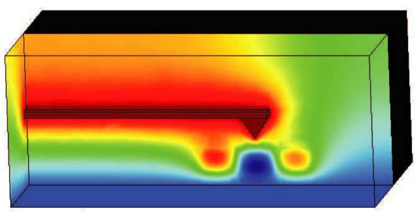

Figure 3: Electrostatic potential.

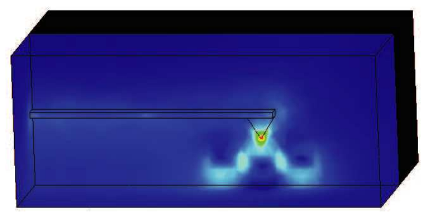

Figure 4: Electrostatic field.

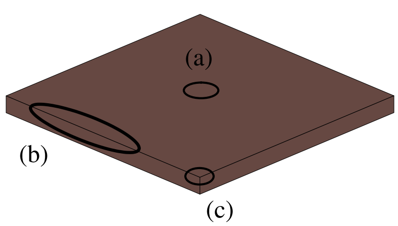

Figure 5: Force types.

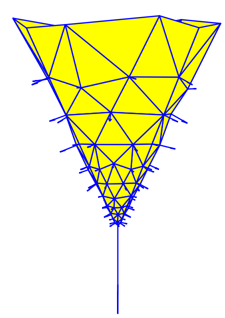

Figure 6: Forces on tip.

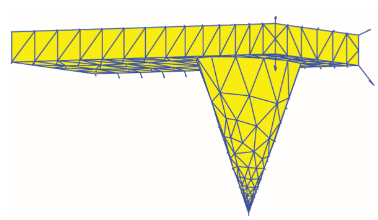

Figure 7: Forces on cantilever.

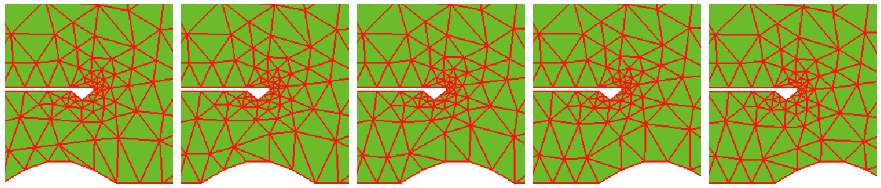

Figure 8: Mesh deformation by ALE.

4. MESH DEFOMATION

The mechanical deformation of the cantilever has to be taken into account in the next electrostatic simulation step. Therefore the FEM mesh has to be adapted to the changing geometry. This can be done by running the mesh generator again, but in order to save calculation time, another approach is used in this work. The mesh is treated as a massless elastic which is deformed by the changing boundaries [9]. In this arbitrary Langrangian Eulerian (ALE) approach the vector Laplace equation

$$\triangle \mathbf{v} = \mathbf{0} \tag{24}$$

is solved for the mesh deformation $\mathbf{v}$ by using a linear FEM, where the movement of sample and probe is brought in as Dirichlet boundary condition

$$\mathbf{v} = \mathbf{v_0}. \tag{25}$$

On the interface between FEM and BEM the normal component of $\mathbf{v}$ is fixed while the tangential components v_t are kept loose and therefore treated as Neumann boundary condition, which leads to

$$v_n = 0, \quad \frac{\partial \mathbf{v_t}}{\partial \mathbf{n}} = \mathbf{0}. \tag{26}$$

The deformation of the mesh during a simulation is shown in Fig. 8.

5. CONCLUSION

The simulation of electrostatic force microscopes is difficult though necessary for their efficient development. In this paper a hybrid simulation approach consisting of an augmented finite element method and a boundary element method for the calculation of the electrostatic field has been presented. Furthermore an electrostatic force calculation approach which uses the Maxwell stress tensor has been applied. Its use avoids the inclusion of inaccurate field results near edges and corners in the force calculation. The changing shape of the configuration and therefore the mesh is considered by using an arbitrary Langrangian Eulerian approach. The simulated fields as well as the resulting forces are in line with previous investigations.

REFERENCES

1. Morita, S., R. Wiesendanger, and E. Meyer, *Noncontract Atomic Force Microscopy*, Springer, 2002.
2. Strang, G. and G. J. Fix, *An Analysis of the Finite Element Method*, Prentice-Hall, 1973.
3. Van Bladel, J., "Field singularities at the tip of a cone," *Proc. IEEE*, Vol. 71, No. 7, 901–902, 1983.
4. Jackson, J. D., *Classical Electrodynamics*, Wiley, 1975.
5. Bala, U. B., M. Greiff, and W. Mathis, "Hybrid numerical simulation of electrostatic force microscopes in 3D," *Proceedings of Progress in Electromagnetic Research Symposium*, Tokyo, August 2006.
6. Stephan, E. P., "Coupling of boundary element methods and finite element methods," *Encyclopedia of Computational Mechanic*, Vol. 01, Chapter 13, 375–412, 2004.
7. Hui, C. Y., J. L. Yeh, and N. C. Tien, "Calculation of electrostatic forces and torques in MEMS using path-independent integrals," *J. Micromech. Microeng.*, Vol. 10, 477–482, 2000.
8. Jacobs, H. O., P. Leuchtmann, O. J. Homan, and A. Stemmer, "Resolution and contrast in Kelvin probe force microscopy," *Journal of Applied Physics*, Vol. 84, No. 3, 1998.
9. Belytschko, T., K. W. Liu, and B. Moran, *Nonlinear Finite Elements for Continua and Structures*, Wiley, Sussex, 2004.

Controlled Approximation of the Coefficient Matrix of the Finite Network Method

A. Eppler, A. Farschtschi, and M. Pfefferkorn
Chemnitz University of Technology, Germany

Abstract— A method is presented for electrostatic field calculations in unlimited three-dimensional space with boundary conditions on the surface of electrodes. The method is based on surface discretization of electrodes and charge loading on electrode patches. The realization of boundary conditions yields a system of equations to calculate the charges. The structure of the referring coefficient matrix is analyzed and afterwards one algorithm is applied to compute a controlled element-wise approximation of this matrix in order to save time while not losing accuracy for the solution.

1. INTRODUCTION

The electrostatic field computations to be explained in this paper are implemented with the help of the **Finite Network Method (FNM)**. In a volume V, n electrodes with their electrode surfaces $\Gamma_j(V)$ $(j = 1 \dots n)$ and given potentials φ_{Dj} are assumed. Therefore the volume V is three-dimensional and unlimited with $\varepsilon_r = 1$. Calculating the potential $\varphi(x)$ in the domain Ω outside the electrodes means to solve the Laplace equation on Ω with Dirichlet Boundary Conditions.

$$\begin{aligned} \Delta\varphi &= 0 \quad \text{on } \Omega \\ \varphi &= \varphi_{Dj} \quad \text{on } \Gamma_j(V) \quad j = 1 \dots n \end{aligned} \tag{1}$$

2. FNM

In order to solve (1) we take in consideration the fundamental solution $E(x, y) = \frac{1}{4\pi} \frac{1}{||x-y||}$ for Laplace equation in 3D. We use this to approximate the unknown function $\varphi(x)$ by a linear combination of functions

$$\varphi(x) \approx \varphi_h(x) := \sum_{i=1}^{N} \varphi_i(x), \text{ where} \tag{2}$$

$$\varphi_i(x) := \frac{1}{|F_i|} \left(\int_{F_i} \frac{1}{4\pi\varepsilon_0} \frac{Q_i}{||x-y||} d\Gamma_y \right). \tag{3}$$

The Q_i may be regarded as the *constant* charge on disjoint elements $F_i \subset \Gamma$. By $|F_i|$ the area of the element F_i is denoted. To fulfill boundary conditions using Galerkin-method one comes up with a $N \times N$ system of equations for computing the charges Q_i : $A\underline{Q} = \underline{b}$ with

$$A = (a_{k,i}) = \frac{1}{|F_k|} \frac{1}{|F_i|} \frac{1}{4\pi\varepsilon_0} \int_{F_k} \int_{F_i} \frac{1}{||x-y||} d\Gamma_y d\Gamma_x \tag{4}$$

$$\underline{b} = (b_k) = \frac{1}{|F_k|} \int_{F_k} \varphi_D \, d\Gamma_x = \varphi_{D|_{F_k}} = \varphi_D(x_k), \tag{5}$$

and x_k being centre of F_k.

In this case FNM can be classified as **indirect Galerkin-BEM with constant ansatz functions**.

Remark 0.0.1. *From the contribution of the Charges Q_i other field sizes than $\varphi(x)$ may be computed. If one omits the factors $\frac{1}{|F_k|}\frac{1}{|F_i|}$ in (4) one comes up with a system for calculating the constant charge densities.*

3. NUMERICAL EXAMPLE

In the following example example we used three electrodes as shown in Figure 1 where electrodes got potentials from left to right of $\varphi_{D1} = 0.25$ V, $\varphi_{D2} = 0.5$ V and $\varphi_{D3} = 1.0$ V.

In Figure 1 the computed charges Q_i are plotted on a uniform mesh of 3000 elements.

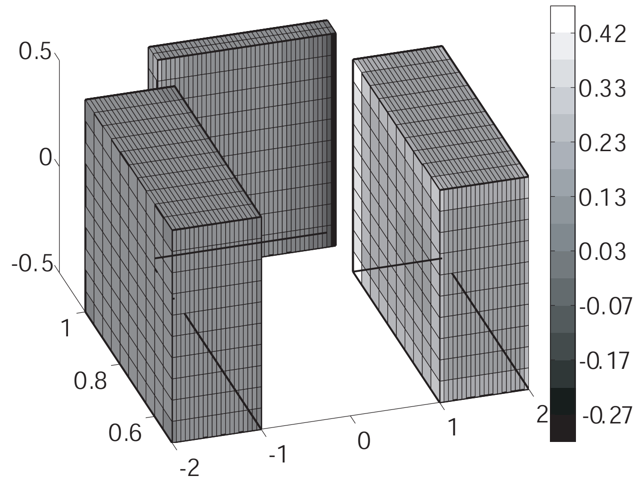

Figure 1: Computed charges Q_i in $10^{-12}C$ with 3000 rectangular elements.

4. COMPUTATION OF THE SYSTEM MATRIX

To compute matrix entries demonstrated in (4) for this task one have to solve integrals on rectangles. One only has to distinguish if the elements F_i and F_k are parallel or orthogonal to each other. We solve these integrals using primitives in an analytically way. One comes up with only two different formulas according to the position of the two panels. (For details see [1] or [2]) Thus FNM refers as a *hybrid method*.

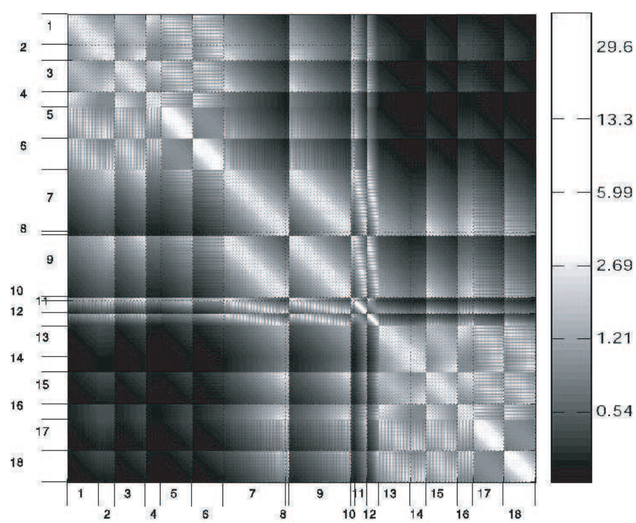

Figure 2: Plot of the coefficient matrix with $N = 3000$ elements.

Each matrix coefficient $a_{k,i}$ represents the interaction between two elements F_k and F_i. Therefore we get a symmetric, dense and positive definite matrix. Picture 2 shows the 18×18 block structure of the matrix caused by the interactions of the 18 electrode surfaces. The blocks along the blockdiagonal contain the larger entries compared to the other blocks corresponding to the interaction of electrode surfaces to themselves. Moreover the largest entries may be found along the main diagonal representing the effects of elements to themselves.

5. CONTROLLED APPROXIMATION

5.1. Basic Concept

Coefficients on the main diagonal and close to main diagonal are important and need to be calculated exactly. So matrix entries a_{ii} are always calculated exactly using formula (4). For increasing distances of the elements F_i and F_k for $k \neq i$ the matrix coefficient $a_{k,i}$ approaches more and more to

$$\tilde{a}_{k,i} = \frac{1}{4\pi\varepsilon_0} \frac{1}{||x_k - x_i||}, \tag{6}$$

with x_i and x_k being centres of F_i and F_k.

Let $r_{ki} := ||x_k - x_i||$ and h_i the longest edge of F_i. If

$$r_{ki} < C \max\{h_k, h_i\} \tag{7}$$

holds for some approximation parameter $C \geq 0$, we say the elements are *close to each other* and calculate $a_{k,i}$. Otherwise we call the elements *far enough away* and calculate $\tilde{a}_{k,i}$ instead of $a_{k,i}$.

Remark 0.0.2. *In fact (6) can be considered as the simplest 1-point quadrature formula on each element.*

5.2. Controlled calculation of C

The parameter C affects how many matrix entries are computed exactly. Raising C means a lower percentage of approximated matrix entries by formula (6). We calculate a value C^* in advance to get a certain percentage within an given intervall of approximated entries. Starting with $C = 1$ we test if the percentage lies within the desired range. If not we double the value of C as long as the percentage lies obove the upper bound of the intervall. From now on we find a value C^* causing a percentage lying inside the desired intervall by *bisection algorithm.* We computed for 9 given intervalls each of length 1% one refering C^* for 6 different meshes using $N = 750$ up to $N = 3000$ elements. All calculations were done using a 64 bit machine with AMD-Opteron-244 processor with 1800 MHz and 16 GB RAM. The results for $N = 3000$ are shown in Table 1.

Table 1: Results for given approximation intervals for $N = 3000$ elements.

given interval	90–91%	80–81%	75–76%	70–71%	60–61%	50–51%	40–41%	20–21%	0%
calc. percentage	90.13	80.28	75.33	70.50	60.95	50.70	40.96	20.01	0.00
C^*	5.5	7.75	8.75	9.75	12.0	15.5	19.5	28.0	128.0
# iterations C^*	6	7	9	9	5	8	10	7	7
time C^* in sec	1.13	1.31	1.69	1.678	0.94	1.50	1.87	1.31	1.31
time matrix in sec	5.58	11.42	14.40	17.43	23.35	29.71	35.79	48.63	60.29

One can see that using the algorithm described above the number of iterations does not depend on the position of the interval and also the number is reasonably small. The second fact that can be investigated is that the time for computing a matrix approximation depends linearly on the percentage of exact calculated matrix entries. One can conclude that the time for calculating $\tilde{a}_{ki}$ is negligible in comparison to a_{ki}.

Table 2: Comparison of times.

N	750	1068	1442	1952	2448	3000
time/iteration in sec	0.0117	0.0237	0.0425	0.0754	0.1232	0.1866
time full matrix in sec	3.6775	7.4975	13.7725	25.3925	40.1825	60.4775
ratio	0.0032	0.0032	0.0031	0.0030	0.0031	0.0031

In Table 2 the time for one iteration of testing a certain value C is shown in camparison to the time one needs to calculate the full exact system matrix. In the second line the mean value of all 9 times per iteration is used. Since both times depend quadratically on N the ratio becomes constant. One can see that testing a certain C only takes 0.3% of the time for computing the full matrix. If you take in consideration that about 10 iterations (the maximum was 12) are needed to find C^* it is about 3% of the time one needs for the full matrix. Calculating C^* in advance makes sense.

5.3. Influence to the Computed Potential Distribution

In order to compare results of different meshes we computed in a second step the potential in $61 \times 61 = 3721$ points in the symmetry plane $z = 0$ and chose the solution on our finest mesh with 3000 elements and exact calculated matrix as reference solution.

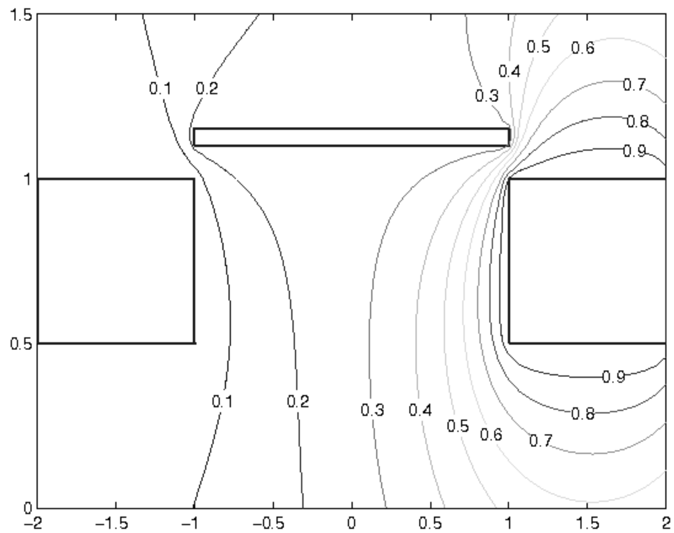

Figure 3: Potential distribution in plane $z = 0$ with $N = 3000$ exact matrix.

Afterwards we compared the Euclidean norm of the potential vectors from all our calculations with the reference solution. The results are plotted in Figure 4.

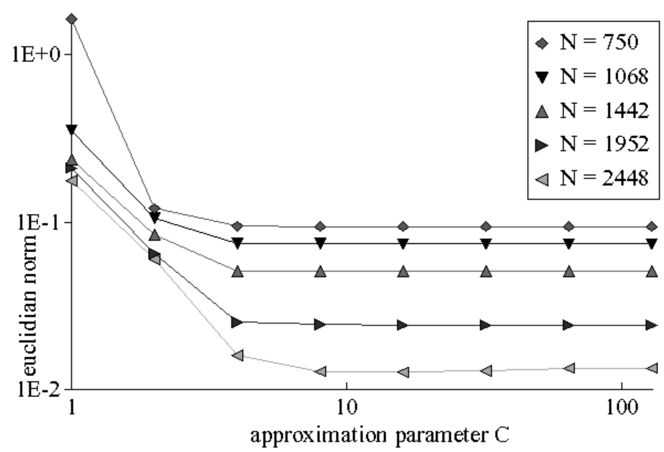

Figure 4: Difference of the potential vectors to our reference solution.

The ordinate axis is scaled logarithmically to investigate the order of the error. One can see that the error is decreasing when using finer mesh. For small values of C the error is relatively high and decreases with higher C refering to more exact computed matrix entries. At a certain value of C an increase does not lead to a better solution. One can see for $C = 8$ being enough to result in accurate solution. It is not necessary to compute the full matrix exactly in order to save time.

6. CONCLUSION

We investigated a controlled element-wise approximation of the system matrix arising by the use of **Finite Network Method**. This approximation is reasonable saving time and not losing accuracy of our solution. We were able to determine in advance the percentage of the matrix beeing approximated. In our example it was enough only to compute about 20% up to 50% of matrix entries with exact formula. In genral this depends on geometry and the desired precision one wants to gain.

REFERENCES

1. Farschtschi, A. and J. Plontke, "Anwendung eines Hybridverfahrens zur Feldberechnung bei vorgegebenen Randbedingungen nach Dirichlet, Neumann oder Cauchy," *Frequenz*, Vol. 54 No. 9–10, 203–208, 2000.
2. Eppler, A., "Berechnungen elektrostatischer Felder mit der Finiten Netzwerkmethode," Abschlussarbeit im Modellierungsseminar, Technische Universität Chemnitz, 15 Juni, 2006.